Unravelling the evolution of the Galactic stellar disk & bulge

Ly Duong

A THESIS SUBMITTED FOR THE DEGREE OF

DOCTOR OF PHILOSOPHY

OF THE AUSTRALIAN NATIONAL UNIVERSITY

Australian National University

RESEARCH SCHOOL OF ASTRONOMY AND ASTROPHYSICS
CANBERRA, AUSTRALIA

JULY 2018

For the fools who dream.

Declaration

This thesis is an account of research undertaken between March 2014 and February 2018 at the Research School of Astronomy and Astrophysics of The Australian National University. Part of this research was conducted at the Munich Institute for Astro- and Particle Physics, Garching; and the Max Planck Institut für Astronomie, Heidelberg. Except where acknowledged, the material presented in this thesis is, to the best of my knowledge, original and has not been submitted in whole or part for a degree in any university.

Part of Chapter 3 was adapted for and appears in the paper 'The GALAH survey: Second Data Release' by Buder, S., et al., 2018, published in *Monthly Notices of the Royal Astronomical Society*. The text in this chapter was written solely by the candidate.

Chapter 4 is the paper 'The GALAH survey: properties of the Galactic disk(s) in the solar neighbourhood' by Duong, L., et al., 2018, published in *Monthly Notices of the Royal Astronomical Society*. As this paper made use of the GALAH survey infrastructure, the author list adheres to GALAH publication policies.

Chapter 5 is the paper 'HERBS I: Metallicity and alpha enhancement along the Galactic bulge minor axis' by Duong, L., et al., 2018, submitted to *Monthly Notices of the Royal Astronomical Society*. The target selection was done by the candidate and David Nataf using ARGOS data provided by Melissa Ness. The data acquisition was carried out by the candidate, Martin Asplund, Ken Freeman and David Nataf.

Chapter 6 is the paper 'HERBS II: Detailed chemical composition of Galactic bulge stars' by Duong, L., et al., 2018, submitted to *Monthly Notices of the Royal Astronomical Society*.

The analysis and written text in chapters 4, 5 and 6 are the work of the candidate alone. However, the co-authors provided valuable discussions and suggestions that helped to improve these publications. Further acknowledgements are made at the end of each chapter.

Ly Duong
13.07.2018

Acknowledgements

Throughout my schooling years, I never thought that I would continue to study science beyond high school. Along the way, I was fortunate enough to have met dedicated educators who nurtured my curiosity and believed in me. It is a happy coincidence that these people, Ms Sandulache and Dr Wilson, are both formidable lady physicists. I am most thankful for their presence in my life, for without their mentorship and guidance, I would not be where I am today. I must also thank the late Professor Harry Messel, AC, CBE, and his legacy – The International Science School. Meeting Harry and participating in the programme was a pivotal moment in my life, and gave me the much needed encouragement to pursue science.

Even though the PhD was a rewarding experience, it can be slow-moving, confusing and oftentimes stressful. I am grateful for my supervisors, Ken and Martin, for the many hours they spent with me during these difficult moments. Their ideas, expertise and advice were indispensable to my research. Above all, their humility and passion for astronomy have been a constant source of inspiration.

I would like to extend my sincere gratitude to Martin for his assistance in the final stages of my PhD. His commitment to helping me deliver this thesis was of equal importance to the hard work he put into it, if not more so.

I am indebted to the researchers I have had the privilege of collaborating with: David, Jane, Karin, Katie, Luca, Melissa and Sven. I thank the entire GALAH survey team for being so accommodating and helpful in the past few years. Each member of my supervisory panel had generously spent time assisting and teaching me essential skills for my research, and I thank them for their much-appreciated effort. My fellow students Bonnie, Sarah, Dongwon, Wladimir, Anshu, Fan, Melanie, Mayuri, Anish, Mari & Johanna, it has been wonderful getting to know you and being your friend.

In every adventure I choose to take part, my family and friends have always given me their unconditional love and support. I thank Dad for being the exemplary scientist that I can always look up to; Mum for her constant encouragement; my brother, god-daughter and Huyen for keeping me grounded so that I never get (too) lost in my work. My long-time confidantes: Ting, Hayley and Andrew, thank you for being available always and for our long talks about everything and anything.

Last but not least, I owe a great deal to my best friend, who had stood by me throughout this wild ride. At every difficult turn you gave me your unfaltering support, and not once did you let me give up, nor did you give up on me. Thank you for the friendship, the laughter, the love.

Unravelling the evolution of the Galactic stellar disk & bulge

Abstract

The formation and evolution of spiral galaxies is a research topic central to modern Astronomy. In this context, the Milky Way offers a unique opportunity for astronomers to study a spiral galaxy in detail, and thus informs many aspects of galaxy formation theory. The observational signatures of Galactic stellar components provide clues to its assembly history. This thesis is focused on two main components of the Galaxy: the stellar disk and bulge. In particular, we examine the chemical properties of these components and their implications for Galactic evolution. The data in this thesis were obtained with HERMES, a new high-resolution optical spectrograph on the Anglo Australian Telescope.

The disk sample consists of over 3000 giant-branch stars, extending up to 4 kpc in height from the Galactic plane. The thin disk (low-α population) exhibits a steep negative vertical metallicity gradient, a signature observed in galaxy evolution models where radial migration plays an important role. The thick disk (high-α population) has a weaker vertical metallicity gradient, which could have arisen from a settling phase of the primordial disk. The [α/Fe] ratios of the thin and thick disk populations are distinct and nearly constant with height. This indicates the two populations were formed in very different conditions, and although the high-α population likely experienced a settling phase, its formation timescale was fast still, in the order of a few Gyrs.

To investigate the chemistry of the Galactic bulge and its connection to the disk, we obtained abundance ratios of 18 elements for more than 800 red giants. The [α/Fe] abundance ratios show vertical variations that are consistent with the distribution of bulge metallicity components: at high latitudes [α/Fe] is enhanced as the metal-poor component dominates; closer to the plane, the metal-rich components contribute lower [α/Fe]. However, at fixed metallicity, all elements show uniform abundance ratios with latitude. We observe normal [Na/Fe] ratios that do not vary as a function of latitude at fixed metallicity, indicating that the bulge does not contain strongly helium-enhanced populations as observed in globular clusters.

By comparing our results with that of the GALAH survey, we conclude that there are similarities between the bulge and disk in terms of their chemistry. However, the more metal-poor bulge population ([Fe/H] $\lesssim -0.8$) shows enhanced abundance ratios compared to the disk for some light, alpha, and iron-peak elements that are associated with core-collapse supernovae (SNeII). This population may have experienced a different evolution to bulge stars of disk origin. Moreover, the [La/Eu] abundance ratios suggest higher *r*-process contribution in the bulge, which indicates that overall the bulge experienced a higher star formation rate than the disk.

Contents

Listing of figures

Listing of tables

All my life through, the new sights of Nature made me rejoice like a child.

Marie S. Curie

1 Introduction

Galaxy assembly and evolution within a Λ-cold-dark-matter (ΛCDM) universe remains a puzzle that modern cosmology is yet to solve. Within the orthodox ΛCDM framework, structures are formed hierarchically: small dark matter halos form first via gravitational collapse and coalesce to form massive halos, in which galaxies eventually form after radiative cooling of baryons. The proto-galaxy then evolves through interactions with its environment such as accretion of satellites and mergers with other galaxies (de Vaucouleurs 1970, Peebles 1970, Press & Schechter 1974, White & Rees 1978, White & Frenk 1991, Springel et al. 2005). Other environmental factors that affect a galaxy's evolution include star formation, accretion of baryons (cold flows) and accretion of dark matter.

Since its inception, hierarchical structure formation steadily became the standard theory, and has successfully reproduced large-scale observations (e.g., measurements by the Planck collaboration, Ade et al. 2016). However, inconsistencies still exist between ΛCDM predictions and small-scale observations. These issues include: the missing satellite problem (observed number of satellites around galaxies are much lower than predicted); the cusp-core problem (measured density and density profile do not match predictions); the too-big-to-fail problem (too few galaxies with dark halo mass $\approx 10^{10} \mathcal{M}_{\odot}$, or stellar mass of $\approx 10^{6} \mathcal{M}_{\odot}$ are observed; they may have failed to form stars, however, it is believed that they are too massive to have failed), all of which are discussed in detail by Bullock & Boylan-Kolchin (2017).

From the galaxy formation point of view, cosmological models have, for a time, struggled to reproduce observed properties of present-day galaxies (e.g., Scannapieco et al. 2009, 2012). Recent advances in galaxy modelling within a cosmological framework have been successful at producing Milky Way-like galaxies, including realistic satellite populations, structural details such as a thick disk (Wetzel et al. 2016, Ma et al. 2017), and even chemi-

cal abundance ratios resembling that of Milky Way stars (Grand et al. 2017). To this end, the Milky Way has served as a benchmark system that theoretical galaxy evolution models can be tested against, as it is currently the only spiral galaxy in which sub-structures and stellar populations can be studied in great detail. A comprehensive understanding of the formation and evolution of the Milky Way is therefore critical to our effort to understand how realistic galaxies form within a ΛCDM universe.

The most effective way to unravel the assembly history of the Milky Way is to study its stellar populations. In particular, the surface chemical compositions of stars are preserved throughout their lifetimes, and thus hold vital clues to the condition in which the Galaxy was formed and how it has evolved (Freeman & Bland-Hawthorn 2002). By studying the chemical abundance ratios of stellar populations in the Milky Way, we may be able to trace their birth location and epoch in order to reconstruct the events that shaped our Galaxy. This concept is at the core of Galactic Archaeology, the aim of which is to establish Galaxy evolution history through the study of signatures embedded in stars.

1.1 Galactic Archaeology

Stellar populations have been observed in our Galaxy from as early as 1926 by Oort (1926), who classified populations based on their kinematics. After the discovery of two distinct populations (Pop I and II) in Andromeda some 20 years later, it was realised that there are other physical implications associated with stellar populations (Baade 1944). Population II was thought to be older and more metal-poor than Population I, which was thought to be recently formed stars (Russell 1948). The oldest, first stars to have formed in the universe is referred to as Population III stars, although it is still unclear if any have survived to the present day (e.g., Frebel & Norris 2015).

Eggen, Lynden-Bell and Sandage (Eggen et al. 1962) were amongst the first to show the importance of stellar populations in Galactic studies. By comparing the kinematics of halo and disk stars, they proposed that the Milky Way formed via the dissipational collapse of a uniform proto-cloud. However, observations of globular clusters by Searle & Zinn (1978) showed that there is a wide range of metal abundances independent of distance from the Galactic centre. They suggested that the Galactic halo actually resulted from the build up of independent, small fragments instead of uniform collapse. At this time, the hierarchical formation theory was gaining momentum, and the scenario suggested by Searle & Zinn (1978) seemed fitting in this context. More importantly, it was apparent from these studies that the properties of stellar populations can give insights to the process of galaxy formation.

The study of abundance ratios, ages and kinematics of Galactic stars from early epochs to understand Galaxy formation is referred to as Galactic Archaeology (for a review, see Bland-Hawthorn & Gerhard 2016). The advent of massive photometric and spectroscopic stellar surveys has ushered the field into a new era, where the chemistry and kinematics can be measured for an unprecedentedly large number of stars. On-going surveys such as

Gaia-ESO (Gilmore et al. 2012), APOGEE (Majewski et al. 2015) and GALAH (De Silva et al. 2015) collectively yield information for ≈700 000 stars to date; other planned surveys such as WEAVE (de Jong et al. 2011) and 4MOST (Dalton et al. 2016) will significantly increase this number. Combined with precise distances and proper motions from the *Gaia* space mission, results from these surveys can alleviate the uncertainties and conflicting conclusions surrounding earlier works, some of which are brought to focus in Sections 1.3 and 1.4. They will also provide more stringent constraints on the formation and evolution of the Milky Way. In the next section, we introduce some of the ongoing and upcoming massive spectroscopic surveys.

1.1.1 Large-scale spectroscopic surveys

Spectroscopic surveys have varying scientific goals, and as a result there are large differences in target selections and observing strategies. The details of each survey are outlined below.

RAVE

RAVE (RAdial Velocity Experiment)[1] (Steinmetz et al. 2006) is a Southern hemisphere spectroscopic survey conducted on the 1.2m UK Schmidt Telescope of the Australian Astronomical Observatory. RAVE's primary aim was to derive the radial velocity of Galactic stars. The survey largely overlaps with the *Tycho-Gaia* astrometric survey (Michalik et al. 2015), which provides many RAVE stars with accurate proper motions that are important for kinematic studies. At the end of its observing campaign (2013), RAVE had obtained spectra for 483 330 stars within magnitude range $8 < I < 12$.

The spectral region covered by the RAVE spectrograph (8410–8794 Å) and its resolving power ($\mathcal{R} \equiv \lambda/\Delta\lambda \approx 7000$) enable measurements of stellar effective temperature, surface gravity, metallicity, as well as the abundance ratios of 6 elements (Mg, Al, Si, Ca, Ti, and Ni). The radial velocities can be measured to a precision better than 1.5 km s^{-1} (Kunder et al. 2017). In addition to the official RAVE spectroscopic data release, Casey et al. (2017) provides a catalogue of stellar parameters and abundances derived using data-driven techniques, which are calibrated on stellar parameters and abundances from the APOGEE survey.

LAMOST/LEGUE

The LAMOST telescope[2] has a 4m mirror with extremely high multiplexity (4000 fibres can be positioned at a time) (Luo et al. 2015). The project has two main science objectives, one focused on extragalactic objects (galaxies, quasars), and the other focused on the Milky Way, called the LAMOST Experiment for Galactic Understanding and Exploration (LEGUE).

[1] www.rave-survey.org

[2] www.lamost.org

The spectrograph can observe stars up to a magnitude $r = 19$ at resolving power $\mathcal{R} = 1800$. The LAMOST pilot survey was launched on Oct 24 2011. By mid-2017, LAMOST has observed ≈8.2 million stars of its 10^7 stars target.

The public data releases from LAMOST contain spectroscopically derived effective temperature, surface gravity, metallicity and α-abundance ratio. It has been shown by Ho et al. (2016) that data-driven techniques can be used to improve the accuracy and precision of LAMOST results by cross-calibrating with a survey that has higher resolving power and signal-to-noise ratio (in this case the APOGEE survey).

APOGEE

The Apache Point Observatory Galactic Evolution Experiment (APOGEE)[3] is a high resolution, high signal-to-noise spectroscopic survey. The survey also operates on the Sloan Foundation 2.5m telescope. APOGEE uses a near-infrared spectrograph covering wavelengths between 1.51–1.70 μm, with resolving power of $\mathcal{R} = 22\,500$. Due to its infrared wavelength coverage, APOGEE has an advantage when observing regions obscured by dust. The survey observed over 150 000 giants in the Galactic bulge, disk and halo, covering a large range of Galactocentric radius in the Northern hemisphere. APOGEE targets are bright giants from the 2MASS catalogue (Skrutskie et al. 2006) with H-band magnitudes between $11 < H < 12.2$. The signal-to-noise ratio for APOGEE spectra are therefore very high, typically much greater than 100. As the result, APOGEE is able to derive precise radial velocity, stellar parameters and abundance ratios for up to 15 elements, with uncertainties < 0.1 dex (Holtzman et al. 2015).

APOGEE completed its observations between late-2011 to mid-2014. Following its completion, a twin spectrograph was installed on the Du Pont Telescope at Las Campanas Observatory, Chile. This instrument will be used for APOGEE-2 South, an extension of the APOGEE survey, which focuses on the Southern hemisphere, particularly the Galactic bulge. In addition, the APOGEE-2 North survey will continue observing the Milky Way disk until 2020 as part of SDSS-IV.

***Gaia*-ESO**

Gaia-ESO[4] is a high-resolution spectroscopic survey that uses the FLAMES instrument on the VLT. The survey targets 10^5 stars, covering the Galactic halo, disk and bulge. The main spectrograph used is GIRAFFE, which has $\mathcal{R} = 16\,500$ at $\lambda = 8484$–9001 Å, and $\mathcal{R} = 19\,800$ at $\lambda = 5339$–5619 Å. A small number of stars are observed with the UVES spectrograph (which only allows 8 objects to be observed at a time) at $\mathcal{R} = 47\,000$, $\lambda = 4700$–6840 Å. The first *Gaia*-ESO observations began in late December 2011.

[3] www.sdss3.org/surveys/apogee.php

[4] www.gaia-eso.eu

Gaia-ESO observes distant field stars, down to a faint magnitude limit of $V \approx 20$. The predicted radial velocity precision for this data set is 0.1–5 km s^{-1} (Gilmore et al. 2012). Depending on the instrumental setup, the survey can provide accurate abundances for the elements Na, Mg, Si, Ca, Ti, V, Cr, Mn, Co, Sr, Zr, Ba in addition to effective temperature, surface gravity and metallicity.

GALAH

The GALAH (GALactic Archaeology with HERMES)[5] survey, the most recent high resolution spectroscopic survey to come online, began operating in early-2014. GALAH uses the HERMES spectrograph on the 4m Anglo Australian Telescope. The primary science goal of GALAH is chemical tagging (Section 1.1.2) - for which a large number of stars and elemental abundances is required (Ting et al. 2012).

The HERMES spectrograph covers four optical wavelength ranges and has nominal resolving power of 28 000. This wavelength coverage and resolving power allow up to 28 elemental abundances to be measured, along with precise radial velocities and stellar parameters. The main GALAH targets are disk stars (giants and dwarfs) between magnitude $12 < V < 14$, and some brighter targets of magnitude $9 < V < 12$ from the *Tycho-Gaia* catalogue. GALAH will only observe a small fraction of halo stars, and an even smaller fraction of bulge stars. The survey aims to observe a total of 10^6 stars, and to date has acquired spectra for ≈500 000. The results in Chapter 4 of this thesis is based on data from the GALAH survey, which will be discussed further in Chapter 2.

WEAVE

WEAVE[6] is a high-multiplexity spectrograph built for the 4.2m William Herschel telescope at the La Palma Observatory, which can observe up to 1000 objects in a single exposure (Dalton et al. 2016). The WEAVE Galactic Archaeology survey will target the Northern Galactic halo, disk (in particular the outer disk) and open clusters using both the high and low resolving power modes ($\mathcal{R} = 20\,000$ or $\mathcal{R} = 5000$). WEAVE will provide radial velocities for stars fainter than $V = 15.5$ and elemental abundances for stars with V-magnitude fainter than 12. Millions of stars will be observed by the survey, which is due to start in 2018.

SDSS-V: Milky Way Mapper

SDSS-V[7] has been proposed as an all-sky survey that will provide coverage of the Milky Way and Local Group objects in both hemispheres (Kollmeier et al. 2017). The Milky Way

[5] www.galah-survey.org

[6] www.ing.iac.es/weave

[7] https://www.sdss.org/future/

Mapper (MWM) program within SDSS-V is particularly important for Galactic Archaeology. SDSS-V MWM aims to observe 4–5 million Galactic stars from the Las Campanas and Apache Point observatories. The program commences in 2020, and will likely be conducted using the same instruments as the APOGEE survey (2.5m telescope; wavelength 1.51–1.70 μm; $\mathcal{R} = 22\,000$).

4MOST

The 4-Meter Multi-object Spectroscopic Telescope[8] is a high-multiplex telescope with at least 1500 fibres in low resolution mode, and more than 800 fibres in high-resolution mode. The instrument has $\mathcal{R} = 20\,000$, covering wavelength regions 395–456.5 nm and 587–673 nm (de Jong et al. 2011). The survey will provide complementary Southern sky coverage to the WEAVE survey, targetting the Galactic disk and bulge. 4MOST aims to deliver chemical abundances for two million stars, which complements the astrometric information provided by the *Gaia* space mission. 4MOST is estimated to begin operations in 2021.

1.1.2 Chemical tagging

The large number of stars and chemical abundance ratios from the current and future high-resolution spectroscopic surveys outlined above will enable the (re)grouping of stellar clusters that have been spatially dispersed throughout the Galaxy since birth, otherwise known as chemical tagging.

The concept of chemical tagging was first discussed by Freeman & Bland-Hawthorn (2002), more recently by Bland-Hawthorn et al. (2010), Ting et al. (2015), and it is the main scientific driver of the GALAH survey. A star's chemical composition should remain largely constant throughout most of its life, and reflect its location and epoch of formation. As such, stars that are from the same cluster/star forming aggregate (co-natal) should have very similar abundance ratios, even after being dispersed from their parent clusters over time. Tracking likely cluster members and their present location may reveal their birth place and migratory pattern during the evolution of the Galaxy (Mitschang et al. 2014, Quillen et al. 2015, De Silva et al. 2015). Many methods exist to group cluster candidates in chemical space where they lie in close proximity, including: principal component analysis (PCA) (Ting et al. 2012), k-means clustering (Hogg et al. 2016) and t-distributed stochastic neighbour embedding (t-SNE) (Kos et al. 2018).

The premise chemical tagging is the belief that stellar clusters have unique and homogeneous chemistry. De Silva et al. (2006, 2007) showed, for the Hyades and Collinder 2061 clusters, that the scatter in abundance ratios are consistent with measurement uncertainties, suggesting little to no intrinsic variation between cluster members. This has also been supported by numerical simulations implying negligible abundance variation within an open

[8] www.4most.eu

cluster (Feng & Krumholz 2014). However, very precise differential abundance analysis by Liu et al. (2016) revealed inhomogeneity in the Hyades, as the overall scatter was 1.5–2 times larger than measurement uncertainties. Further challenges for chemical tagging were noted by Ness et al. (2018), who found a large number of field stars (1%) with identical chemical signatures but are *unlikely birth siblings*. The use of abundance ratios to identify stars of common birth must therefore be treated with caution.

However, chemical tagging can still be performed in a limited capacity to identify unique stellar populations. Using abundances from the *Gaia*-ESO survey, Lind et al. (2015) found a halo star with aluminium and magnesium abundances indicating that it may have originated from the globular cluster ωCentauri. Similary, the nitrogen abundance ratios from the APOGEE survey revealed a group of nitrogen-rich stars, which could be members of dissolved globular clusters in the Galactic bulge (Schiavon et al. 2017). A large inventory of chemical abundance ratios is therefore extremely valuable for disentangling Galactic subcomponents described in the next section.

1.2 The Galactic structure

The Milky Way appears to be a large spiral galaxy, with components typically observed in external disk galaxies. The stellar mass of the Milky Way is estimated to be approximately $5 \pm 1 \times 10^{10} \mathcal{M}_{\odot}$, similar to that of Andromeda (Bland-Hawthorn & Gerhard 2016, Kafle et al. 2018). Like other disk galaxies, it also contains an invisible dark matter halo (Freeman 1970, Rubin & Ford 1970). The gravitational effects of the dark halo on stellar kinematics are visible, and it contributes the largest Galactic mass fraction, at ≈90% of the total Galactic mass (Freeman & Bland-Hawthorn 2002). For the rest of this thesis, however, we will mainly focus on the visible matter in Galaxy.

Of the visible components, the Galactic disk contains the largest baryon fraction. It is generally accepted that the Milky Way has an exponential disk (van der Kruit & Freeman 2011), which can be further divided into the 'thin' and 'thick' disks. The thin disk has a scalelength of $\approx 2.6 \pm 0.5$ kpc, and the thick disk scalelength is $\approx 2 \pm 0.2$ kpc (Bland-Hawthorn & Gerhard 2016). Towards the Galactic centre lies the bulge, a bright region with high stellar density. The Galactic halo is the most diffuse stellar component, and contains primarily old and metal-poor stars. These components are indicated in the edge-on infrared image of the Milky Way, Fig. 1.1.

1.2.1 The stellar halo

The diffuse stellar halo (≈1% of the total Galactic mass) surrounding the Galaxy is likely to have formed through merger and accretion episodes, as proposed by Searle & Zinn (1978). The accretion history of the Milky Way is contained in the substructure of the halo, such as tidal tails, streams and over-densities from accreted satellites.

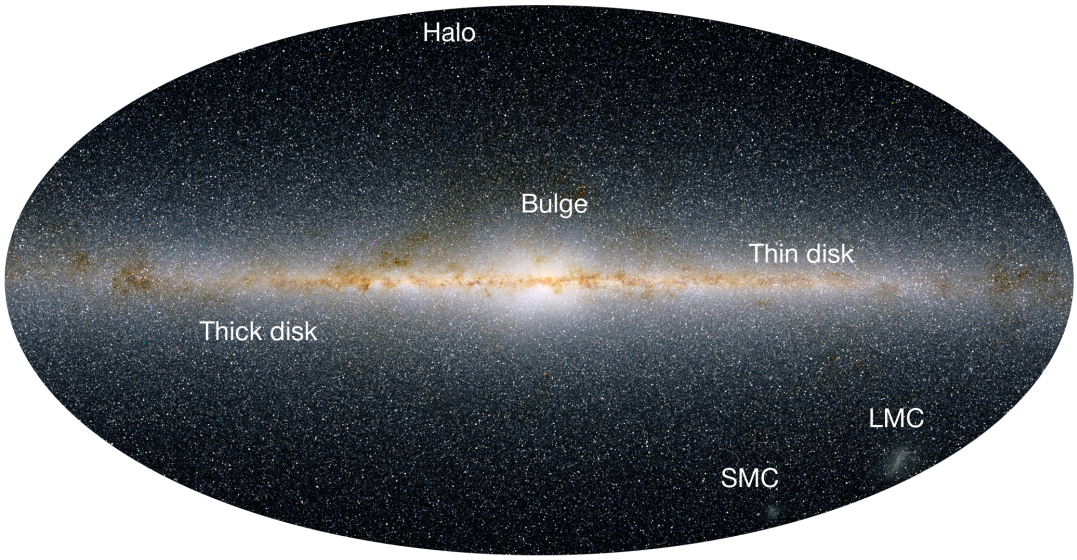

Figure 1.1 The visible components of the Milky Way. The stellar disks, bulge, and halo are typical of disk spirals in the local group. Two Milky Way satellites, the Large and Small Magellanic Cloud, can also be seen. Image credit: 2-Micron Sky Survey (2MASS) collaboration (Skrutskie et al. 2006).

The stellar halo's properties indicate that its evolution is probably unrelated to that of the disk and bulge: its stars are much more metal-poor and has many times higher velocity dispersion in comparison. Carollo et al. (2007) (also Beers et al. 2012) argued for a double halo structure in the Milky Way: an inner and outer halo that were formed via different channels. The inner halo was thought to have formed *in situ*, whereas the outer halo was primarily built up by mergers and accretion. Schönrich et al. (2011) question the kinematics evidence for a dual halo presented in Carollo et al. (2007), however there is evidence from chemical abundances suggesting that there are two halo sub-populations (e.g., Nissen & Schuster 2010).

1.2.2 The disk

The disk of the Milky Way is thought to have formed by redshift of $z \approx 1$, based on age estimates of the oldest disk stars placing them at 10–12 Gyr (e.g., Haywood et al. 2013). The scaleheight of the thinner disk component is well established and estimated to be ≈300 pc (Gilmore & Reid 1983, Jurić et al. 2008, Bovy et al. 2012b, 2016). Many disk galaxies exhibit a second disk component which is more diffuse and has larger scaleheights, known as the thick disk. Thick disks were first seen in external galaxies through surface photometry (Tsikoudi 1979, Burstein 1979), and is now thought to be common in most disk galaxies (Dalcanton & Bernstein 2002, Yoachim & Dalcanton 2006, Comerón et al. 2015). An image of the thick disk of the galaxy NGC891, a Milky Way analogue, is shown in Fig 1.2. In general, thick disks have relatively constant scaleheights as a function of radial distance (Ibata et al. 2009, Comerón et al. 2015).

The thick disk of the Milky Way was discovered by Gilmore & Reid (1983), using stellar

density measurements as a function of vertical height. Gilmore & Reid (1983) estimated the Galactic thick disk scaleheight to be ≈1350 pc. Numerous authors have since attempted to measure the scaleheight of the thick disk. The most recent results place the thick disk scaleheight at smaller values than originally reported, but the scatter of thick disk scaleheight measurements is larger than that of the thin disk (Jurić et al. 2008, Kordopatis et al. 2011, Bovy et al. 2012b, 2016). By analysing a compilation of literature studies, Bland-Hawthorn & Gerhard (2016) estimated the thick disk scaleheight to be 900 ± 180 pc, and its surface brightness relative to the thin disk is ≈12%. The ratio of these scaleheights are comparable to that observed in spirals with similar circular velocity to the Milky Way (V_c = 210 km s^{-1}) (Yoachim & Dalcanton 2006).

The Galactic thick disk appears to be older (≈13 Gyr) and more metal-poor than the thin disk (e.g., Haywood et al. 2013, Bensby et al. 2014). The origin and nature of the thick disk has been a widely debated topic, and will be explored further in the next sections. Nonetheless, the old age of the thick disk means that it contains a snap-shot of the conditions in the early Galaxy, making it an important component for Galactic Archaeology and chemical tagging.

Figure 1.2 An example of the thick disk component in an external galaxy - NGC891. The edge-on profile of NGC891 is similar to that of the Milky Way, where the bulge, thin and thick disk components can be seen. The thick disk of NGC891 has scaleheight of 1.44 ± 0.03 kpc (Ibata et al. 2009). Image credit: Robert Gendler and Adam Block, data taken with the Subaru (NAOJ) and *Hubble* Space Telescope (NASA).

1.2.3 The bulge

The bulge is the second most massive visible component, containing ≈30% of the total stellar mass in the Galaxy (Portail et al. 2015). The bulge was first thought to be a spheroidal, or classical bulge, postulated to have formed via rapid collapse early on in the Galaxy's

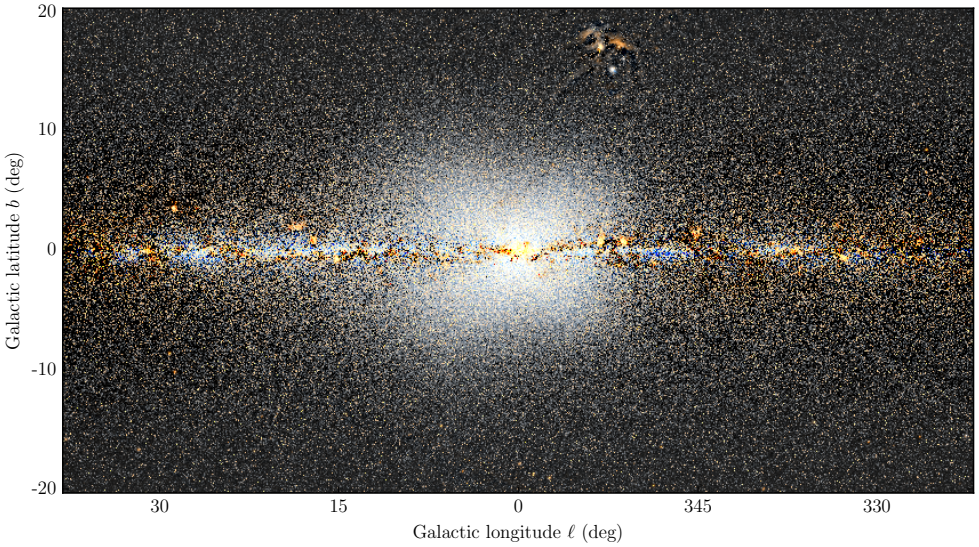

Figure 1.3 A close up of the Milky Way's central region, indicating the X-shape structure of the Galactic bulge. Figure from Ness & Lang (2016).

formation (Kormendy & Kennicutt 2004). The observed vertical metallicity gradient of the bulge, and colour-magnitude diagrams from the *Hubble Space Telescope* suggesting that the bulge is exclusively old both support the classical bulge picture (e.g., Matteucci & Brocato 1990, Minniti et al. 1995, Clarkson et al. 2008, 2011). It was estimated by Clarkson et al. (2011) that less than 3.5% of bulge stars are younger than 5 Gyr.

In recent years, multiple studies of photometry, age, and kinematics of bulge stars gave evidence against the Galactic bulge being a primarily classical one. Infra-red images of the Milky Way bulge showed that it is a boxy/peanut/X-shape (Dwek et al. 1995, Ness & Lang 2016), which can be seen in Fig. 1.3. The X-shape morphology can also be inferred from the double red-clump as shown by photometric studies of bulge stars (Ness et al. 2012, Wegg & Gerhard 2013, Nataf et al. 2015, Gonzalez et al. 2015a). In addition, the bulge exhibits cylindrical rotation, consistent with it being a pseudo-bulge (Kunder et al. 2012, Ness et al. 2013b, Zoccali et al. 2014, Ness et al. 2016b), formed via disk instability (e.g., Martinez-Valpuesta & Gerhard 2013, Di Matteo et al. 2014). The fraction of young stars in the bulge is also larger than previously estimated: over 20% of the microlensed bulge dwarfs and subgiants from Bensby et al. (2017) are younger than 5 Gyr. It is currently unclear whether a spheroidal/classical component exists in the Milky Way. While the bulge contains mostly metal-rich stars, it may host some of the oldest stars in the Galaxy (Tumlinson 2010, Howes et al. 2015). Kunder et al. (2016) found that the metal-poor, old RR Lyrae stars do not show cylindrical rotation, which may be indicative of a classical population. However, the fraction of the classical component should be small, at maximum 25% of the total bulge mass (Shen et al. 2010).

The evolution of the different Galactic stellar components is evidently complex and intrinsically linked. Certain similarities should exist between the stellar disk, and bulge, for

example, if the bulge is indeed a product of disk instability. This thesis will focus on the Milky Way disk (in particular, the thick disk) and bulge, the largest stellar components of the Galaxy and their evolution history. The sections that follow discuss the chemical evolution of the Galactic disk and bulge in detail.

1.3 Chemical evolution of the Milky Way disk

Numerous studies of stellar populations in the nearby thin and thick disks have been conducted. The thick disk is more metal-poor on average than the thin disk, with a large metallicity range: $-2.2 \leq$ [Fe/H] ≤ -0.5 (e.g., Chiba & Beers 2000). However, most thick disk stars are between $-1 \leq$ [Fe/H] ≤ -0.5; those with [Fe/H] < -1 are quite rare, and is referred to as the metal-weak thick disk. The thin disk in the solar neighbourhood has metallicity range $-0.7 \leq$ [Fe/H] ≤ 0.5. At the solar annulus, a clear dichotomy is observed in abundances of the alpha-elements (typically O, Mg, Si, Ca, Ti). The ratio of [α/Fe] at a given [Fe/H] is much more enhanced for stars that belong to the thick disk, compared to those of the thin disk (e.g., Prochaska et al. 2000, Adibekyan et al. 2012, Bensby et al. 2014, Fuhrmann et al. 2016). Although using [α/Fe] ratios has been recently advocated as the more accurate method to separate the thin and thick disks; kinematics has also been used, amongst other criteria. Different separation methods can lead to varying interpretations of the thick disk's properties. Sections 4.5.2 and 4.6 revisit this discussion in detail.

The enhanced α-abundance ratios of thick disk stars have important implications. One is the formation time-scale: it is likely that the thick disk has been enriched primarily by supernovae type II, before the contribution of iron-peak elements from supernovae Type I took effect. The formation time-scale of the thick disk should therefore be $\approx$1–3 Gyr (Gratton et al. 2000, Mashonkina et al. 2003), although Haywood et al. (2013) suggested a slightly longer formation timescale of 4–5 Gyr.

It was shown by Haywood et al. (2013) and Bensby et al. (2014) that α-rich thick disk stars are much older than α-poor thin disk stars. Thick disk stars also have a narrow age range - between 8–13 Gyr (Haywood et al. 2013), whereas the age spread in the thin disk is large - between 0–8 Gyr (Casagrande et al. 2011). The thin/thick disk chemical dichotomy is shown in Fig. 1.4. There are also older, more α-enhanced stars at the super-solar metallicity regime, the so-called 'hαmr' (high-α metal-rich) stars (Adibekyan et al. 2011). These stars may not be associated with the thick disk, but are thought to have migrated from the inner disk (e.g., Schönrich & Binney 2009).

There has been intense debate over whether the thick disk is a 'distinct' Galactic component since its discovery (Gilmore & Reid 1983, Norris 1987, Nemec & Nemec 1993). Earlier evidence favoured a merger-origin (therefore 'distinct') thick disk, such as the lack of vertical metallicity gradient (e.g., Gilmore et al. 1995, Allend Prieto et al. 2006) and kinematics properties resembling that of a 'satellite debris' (Wyse et al. 2006). However, Bovy et al. (2012a) controversially argued that the Galaxy has no distinct thick disk using low resolu-

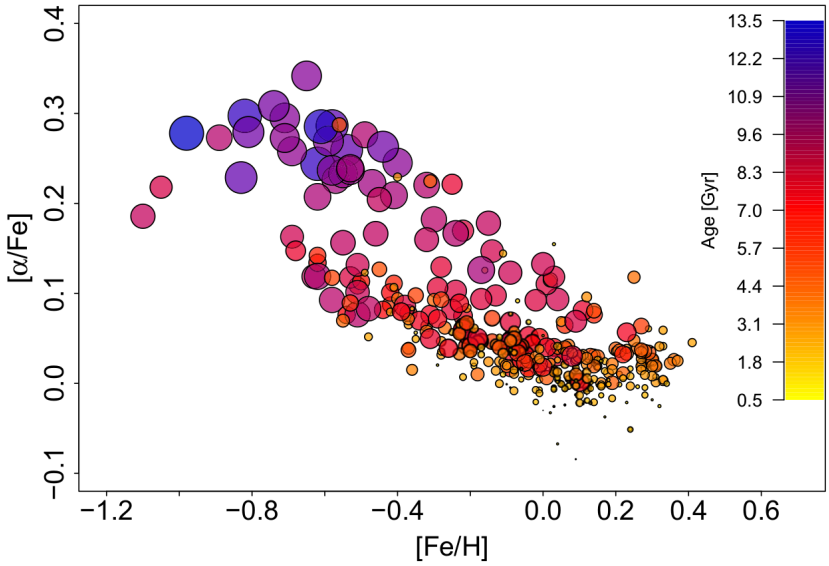

Figure 1.4 The [α/Fe]-metallicity-age distribution of disk stars from Haywood et al. (2013), for a sample of HARPS planet search stars. The stellar parameters and abundances are from Adibekyan et al. (2012). Stars with high [α/Fe] at a given [Fe/H] tend to be the oldest stars and are associated with the thick disk.

tion SEGUE/SDSS data of a non-local sample (several kpc distant). The authors find, after correcting for the selection effects of their stellar sample, that the dichotomy in [α/Fe]–[Fe/H] plane disappears. Furthermore, Bovy et al. (2012a) showed that the scaleheight distribution of the disk is not bi-modal as suggested by Gilmore & Reid (1983). Multiple recent spectroscopic studies of the thick disk concluded that it likely has a vertical metallicity gradient (e.g., Katz et al. 2011, Kordopatis et al. 2011, Ruchti et al. 2011, Mikolaitis et al. 2014).

Results from the APOGEE survey confirmed the smooth vertical distribution of the disk: stars with higher α-abundance ratios and older ages lie at progressively larger scaleheights (Bovy et al. 2016, Mackereth et al. 2017). At the same time, chemical abundances from *Gaia*-ESO and APOGEE also show that the disk does indeed have two distinct α-abundance sequences (Recio-Blanco et al. 2014, Nidever et al. 2014, Hayden et al. 2015). Large scale abundance maps from the APOGEE survey demonstrate that two clear tracks in [α/M] vs [M/H] are observed at all galactocentric radii, although the stellar densities of the two sequences vary with position in the Galaxy. In the inner Galaxy ($3 < R_{\rm GC} < 5$ kpc), and at large heights above the Galactic plane, the high-α sequence dominates, but its density decreases beyond galactocentric radius $R_{\rm GC} \approx 9$ kpc (Hayden et al. 2015).

The mechanism(s) that gave rise to an old, α-enhanced population residing at larger scaleheights in the disk have been explored by many authors. While much progress has been made, a general consensus is still not reached. Below we discuss the main galaxy formation and evolution models that have been put forward to explain the Galactic thick disk.

1.3.1 Thick disk formation

Thick disks may arise from external heating processes such as dwarf satellite accretion or minor merger events. Accretion models, as discussed by Abadi et al. (2003), predict that galaxies are assembled by direct accretion of dwarf satellites. The thick disk is postulated to have been deposited as a debris of an accretion event, thus comprised of a unique component. This results in a lack of vertical and radial chemical gradients.

In the case of thick disk formation by minor merger events (Quinn & Goodman 1986, Quinn et al. 1993, Kazantzidis et al. 2008, Villalobos & Helmi 2008, Bekki & Tsujimoto 2011), the pre-existing thin disk is heated by mergers with smaller satellites, creating a thicker component that is kinematically hotter than the thin disk. Vertical or radial chemical gradients could be preserved in the thick disk after the merger events, and reflect the condition of the early disk, if such gradients existed in the first place. Flaring of the thin disk, where the thin disk scaleheight increases at larger radii, is also expected in minor merger models (Minchev et al. 2015, 2016).

A different merger scenario, where thick disk stars are formed *in situ*, was proposed by Brook et al. (2004). Instead of direct accretion of stars into the thick disk, they suggest that the stars formed at the epoch of gas mergers at high redshift can be associated with the simulated galaxy's thick disk. This simulation shows that the thick and thin disk remain separated in their α-abundances, which is in agreement with observations (Brook et al. 2005).

In a similar vein to Brook et al. (2004, 2005), Bournaud et al. (2009) showed that thick disks matching observed properties (such as constant thick disk scaleheights seen in external galaxies) can be formed when clumps of the early disk merge and scatter gas away from the disk plane. This formation scenario by clumpy, unstable gaseous disks model predict that the thick disk and the bulge form together within about 1 Gyr. Thick disk stars in this model are also formed *in situ*. It is important to note that the gas-rich merger (Brook et al. 2004) and clumpy disk scenarios both predict a fairly uniform vertical metallicity distribution in the thick disk.

Radial migration of stars (Sellwood & Binney 2002), a secular evolution mechanism that could have formed the thick disk, is perhaps the most discussed in recent literature (Schönrich & Binney 2009, Minchev & Famaey 2010, Loebman et al. 2011, Roškar et al. 2013, Loebman et al. 2016, Schönrich & McMillan 2017). It was argued by Schönrich & Binney (2009) that the stars at co-rotation with the spiral arm or bar can be transported outwards, where they experience less gravitational potential and hence gain vertical velocity and height, provided the vertical action is conserved. This model results in a disk that has smooth changes in its star formation, chemical and dynamical properties. Chemical similarities between the bulge and the local thick disk are also expected, as thick disk stars in the solar neighbourhood would have migrated outwards from the inner galaxy, while stars from the inner disk migrated inwards to the bulge region (Schönrich & Binney 2009).

Observational evidence are largely in favour of radial migration being an important process in the evolution of the disk, especially the thin disk. The existence of metal-rich, more α-enhanced stars in the solar neighbourhood can be explained by the migration of old, inner thin disk stars to outer radii (Adibekyan et al. 2011). The age-metallicity relation of the nearby thin disk is essentially flat, which is a signature of radial mixing (Haywood 2008, Casagrande et al. 2011). Hayden et al. (2015) observed that the metallicity distribution of thin disk stars are skewed towards metal-rich values at larger radii, a migration signature corroborated by Loebman et al. (2016) in their simulation. Schlesinger et al. (2014) measured a vertical metallicity gradient of $-0.24^{+0.04}_{-0.05}$ dex kpc^{-1} for the disk overall from a sample of volume complete SEGUE sample, which is in agreement with migration model predictions from Schönrich & McMillan (2017).

However, there are doubts that radial migration alone is responsible for the formation of the Galactic thick disk. In their numerical models of radial migration, Roškar et al. (2013) find that the thick disk produced is thinner than what is observed for the Milky Way. They suggest that perhaps radial migration is not the only mechanism to produce the thick disk - that external perturbations may also be involved. Furthermore, the 'gap', or under-density observed in the α-abundances versus metallicity plane, is at odds with Schönrich & Binney (2009)'s prediction of a continuous distribution. Haywood et al. (2013) also question the role of radial migration in the formation of the thick disk, as all stars residing at large vertical heights ($Z_{\rm max}$) in their stellar sample are old (ages $\geq$ 8 Gyr).

Cosmological models, such as that of Brook et al. (2012) and Bird et al. (2013) found that radial migration had little effect on the final configuration of their simulated galaxies. Instead, they proposed that the proto-disk was born thick, and settled over time into progressively thinner configuration - this is illustrated in Fig. 1.5. Brook et al. (2012) suggests that the dichotomy of the α-enhancement in the disk could have been caused by a decrease in star formation rate in at some point during the galaxy's evolution, similar to the model proposed by Chiappini et al. (1997). This idea was explored further in Haywood et al. (2016), who found that the star formation rate in the Milky Way may have decreased from $\approx$9 Gyr by fitting their chemical evolution model to APOGEE α-abundances. The exact reason for this decreased star formation rate is not yet clear, and further observational evidence need to be considered in the context of these models.

The current theories on the formation of thick disks in spiral galaxies are, in some ways, conflicting. An additional layer of complexity is added if one also considers the possible connection between the evolution of the thick disk and bulge. The chemical properties of the disk, in particular, the thick disk, should therefore be examined concurrently with that of the bulge.

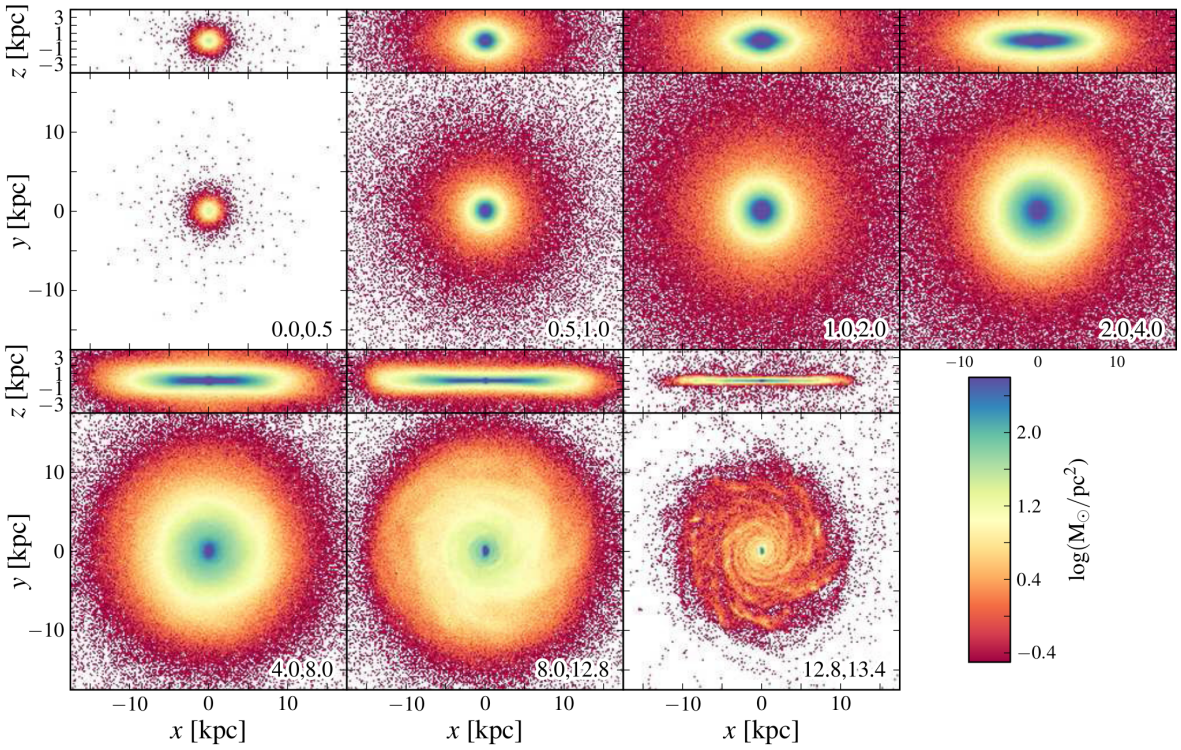

Figure 1.5 The temporal evolution of a Milky Way-like galaxy in the 'upside-down' and 'inside-out' formation scenario. The first two rows show spatial projections on the *xz* (edge-on) and *xy* (face-on) axes of the galaxy at time intervals (after the Big Bang) 0–0.5 Gyr; 0.5–1 Gyr; 1–2 Gyr and 2–4 Gyr. The bottom two rows show the same projections at time intervals 4–8 Gyr, 8–12.8 Gyr and 12.8–13.4 Gyr. The colour scale indicates the logarithm surface density. Over time, the stars settle into progressively thinner configurations. The present-day thick disk of this galaxy is an old component that was born thick. Figure from Bird et al. (2013).

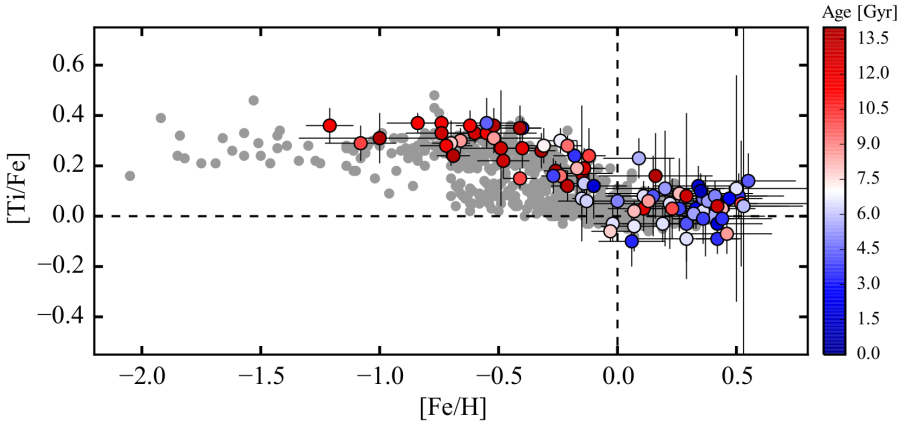

Figure 1.6 The [Ti/Fe] abundance trend of microlensed bulge dwarfs (colour-coded by their ages) compared to nearby disk stars (grey circles, Bensby et al. 2014). The α-abundance trends in the bulge is similar to that of high-α, or thick disk stars. There is a significant fraction of young stars in the bulge, and some are α-enhanced . Figure from Bensby et al. (2017).

1.4 Chemical evolution of the Milky Way bulge

Early detailed abundance studies of bulge giants reported enhanced α-abundances for elements such as oxygen, silicon and titanium, but especially so for magnesium (Zoccali et al. 2006, Lecureur et al. 2007, Fulbright et al. 2007). The magnesium abundances from Fulbright et al. (2007) plateaued at [Mg/Fe] = 0.3 dex even at super-solar metallicity, indicating that the bulge had a different chemical enrichment to the nearby disk. This was seen as evidence for a rapid bulge formation. In addition, the bulge clearly exhibits a vertical metallicity gradient (e.g., Minniti et al. 1995, Zoccali et al. 2008). The conclusion that the bulge is exclusively old from *Hubble* colour-magnitude diagrams (e.g., Clarkson et al. 2011) corroborated the widely held view that the bulge formed rapidly, via mergers or dissipational collapse (e.g., Matteucci & Brocato 1990).

Our understanding of the bulge slowly changed as evidence of a disk-bulge connection began to emerge. Meléndez et al. (2008) noticed that the oxygen abundance ratios of bulge red giants were similar to those of the local thick disk, also at the super-solar metallicity regime. Alves-Brito et al. (2010) corroborated these findings in their reanalysis of Fulbright et al. (2007). This similarity has since been firmly established by many other high-resolution chemical studies of the bulge (e.g., Gonzalez et al. 2011, Johnson et al. 2014, Ryde et al. 2015, Bensby et al. 2017, Rojas-Arriagada et al. 2017). Fig 1.6 shows α-abundance trends for bulge stars. Bensby et al. (2017) suggested that the bulge may have experienced a slightly faster formation than the thick disk in the solar neighbourhood, as the 'knee' for the α-abundances (where the abundance ratios begin to decrease near solar metallicity) is located at slightly lower [Fe/H] value for the bulge.

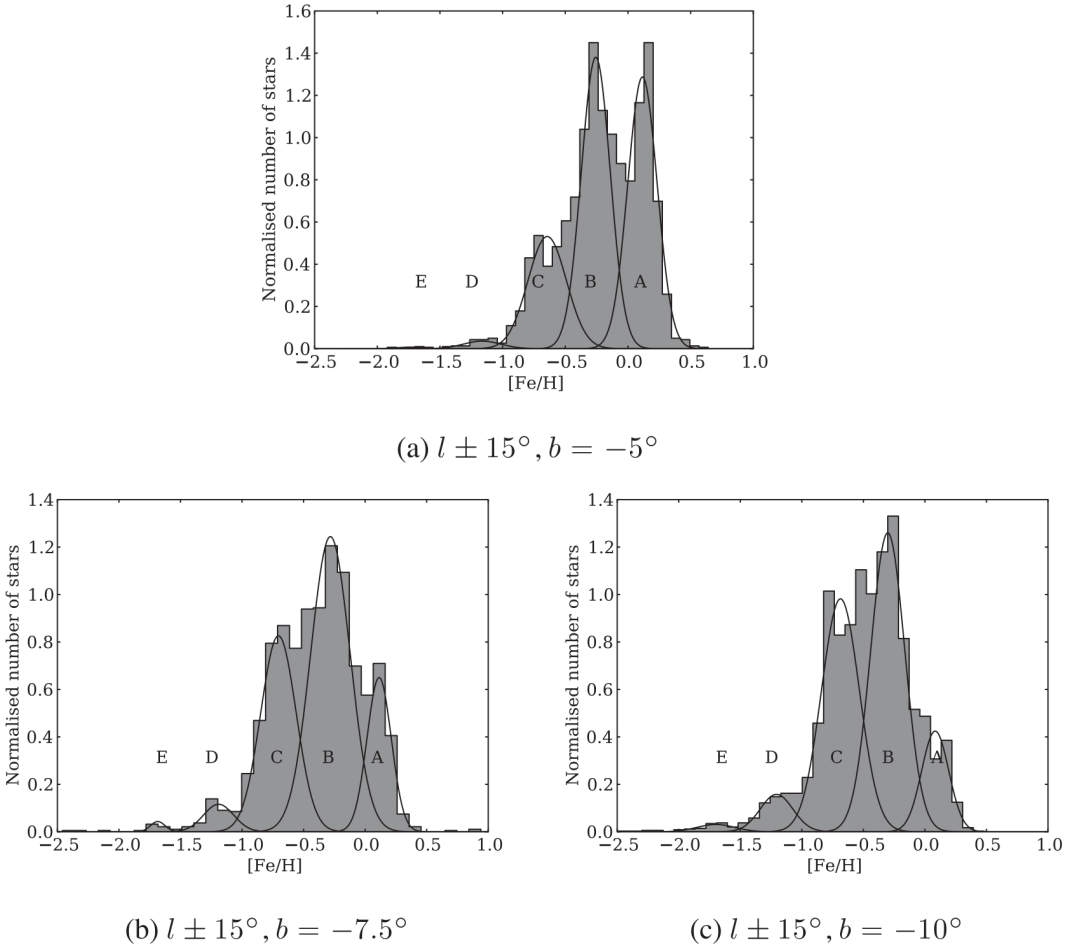

(a) $l \pm 15^\circ, b = -5^\circ$

(b) $l \pm 15^\circ, b = -7.5^\circ$

(c) $l \pm 15^\circ, b = -10^\circ$

Figure 1.7 Metallicity distribution function (of fields with the same latitude combined) for Galactic bulge stars, at $l \pm 15^\circ$ and $b = -5^\circ$. The components are labelled from A–E, with A being the most metal-rich. Components A, B and C may have originated from the disk. Components A and B are thought to be associated with the inner thin disk of the early Galaxy, and component C associated with the inner thick disk. Components D resembles the metal-poor extension of the thick disk, and component E is thought to be halo stars. Figure from Ness et al. (2013a).

The metallicity distribution function (MDF) of the bulge shows that it has multiple components, at least two and up to as many as five (Babusiaux et al. 2010, Ness et al. 2013a, Zoccali et al. 2017, Rojas-Arriagada et al. 2017). The bulge MDF from the ARGOS survey by Ness et al. (2013a) (Fig. 1.7) saw many different stellar populations, which they named A–E. Three of these populations - A, B and C - have metallicity similar to the disk in the solar vicinity. Population A has high mean metallicity and low α-enhancement, population B has intermediate metallicity and α-enhancement. These two populations are likely associated with the early inner thin disk of the Galaxy. Population C is metal-poor and α-rich, much like the local thick disk. The metal-poor components D and E are thought to be the metal-poor extension of the thick disk and the halo, respectively.

Ness et al. (2013a), along with other authors, showed that the vertical metallicity gradient in the bulge is due to the changing fraction of each component at different heights (e.g., Babusiaux et al. 2010, Rojas-Arriagada et al. 2017). This can also be seen in Fig. 1.7, where the most metal-rich component (labelled A) contributes the most near the plane, and significant less away from the plane. Thus, the bulge vertical metallicity gradient cannot be interpreted as a signature of merger or dissipative collapse bulge formation.

Bensby et al. (2017) found five peaks in their MDF for a much smaller sample of microlensed bulge dwarfs and subgiants, four of which matched the ARGOS MDF peaks fairly well. Their stellar age distribution also contains multiple peaks that could be interpreted as star formation episodes in the bulge. Bensby et al. (2017) proposed that the peaks at 11 and 8 Gyr could be the onset of the thick and thin disks; and at 6 and 3 Gyr could be associated with the the thin disk or Galactic bar. In contrast to Clarkson et al. (2011), Bensby et al. (2017) estimated over 20% of their bulge stars are younger than 5 Gyr. Some of these young stars are enhanced in α-abundance ratio (see also Chiappini et al. 2015, Martig et al. 2015). This is a rather unusual finding, as α-enhancement is typically associated with older stars. There is currently no consensus on the interpretation of this result, which potentially implies further complications for the evolution of the bulge. The reader is referred to Barbuy et al. (2018) for a detailed discussion.

The most recent evidence all point to the Galactic bulge forming primarily as a result of secular evolution (Kormendy & Kennicutt 2004) via disk instability (Athanassoula 2005, Martinez-Valpuesta & Gerhard 2013). The three bulge components A, B and C have been shown by Di Matteo et al. (2014), in a dissipationless N-body simulation, to have originated from the disk. Shen et al. (2010) and Li & Shen (2012) find that a model of the Milky Way without a merger-induced bulge successfully reproduce kinematics information from the BRAVA survey and X-shape morphology of the bulge.

However, there remain multiple questions regarding the evolution of the Galactic bulge. It is still not clear whether the 'knee' in the α-abundance is offset from the local thick disk. Many authors have discussed this issue but have not reached a definitive conclusion, which may be due to possible systematic offsets in different analyses or types of stars observed (Bensby et al. 2017, Rojas-Arriagada et al. 2017). Although it has been established

that the Milky Way does not have a purely classical bulge component, the existence of a classical bulge population cannot be ruled out. It is possible that the Milky Way has a composite bulge, like other spiral galaxies in the Local Group (Kormendy et al. 2010, Fisher & Drory 2011). Some evidence for a classical bulge component can be seen in the kinematics of RR Lyrae stars (Kunder et al. 2016), but such a component may be very small, and difficult to detect (Saha 2015). To this end, the abundance ratios of elements belonging to the all nucleosynthesis channels can provide valuable insights on the nature of the bulge, but measurements for non-alpha elements are still relatively scarce (Johnson et al. 2014, Van der Swaelmen et al. 2016, Schiavon et al. 2017).

1.5 Thesis outline

In this thesis, I attempt to understand the still ambiguous or unknown aspects of the Galactic disk evolution, and explore its connection to the bulge. I made use of data products from the GALAH survey for the disk study, and high-resolution observations from the HERMES spectrograph to obtain a detailed chemical inventory for the bulge.

Chapter 2 describes the HERMES spectrograph and spectra, which are used throughout this work. Here I introduce and discuss details of the GALAH survey, and the dedicated Galactic bulge survey with the HERMES spectrograph (HERBS). This chapter also outlines the observation and data reduction procedures. Chapter 3 details the spectroscopic analysis pipeline of the GALAH survey, which must be automated for large, high resolution samples. An introduction to spectroscopy and its changing landscape, along with terminologies relevant to this thesis, are explained in this chapter. The GALAH analysis pipeline, or a modified version of it, was used for analysis in Chapters 4, 5 and 6.

The Galactic disk study focuses on its most controversial component, the thick disk. I analyse data from the GALAH survey pilot project and present the results in Chapter 4. I discuss the implications of these results for the formation of the Galactic thick disk. Results from the Galactic bulge survey HERBS are presented in Chapters 5 and 6. In Chapter 5, I focus on the metallicity and α-enhancement along the minor axis of the Galactic bulge, which gives insights on how chemical properties of the bulge components vary with distance from the plane. Chapter 6 details the elemental abundance ratios for the HERBS sample, which comprises $\approx$830 bulge giants. This sample includes a larger percentage of metal-poor stars ([Fe/H] ≤ -1) than other studies, so to better understand the chemical signatures of all bulge metallicity populations. Finally, Chapter 7 provides concluding remarks and directions for future work.

My dear Kepler, what would you say of the learned here, who… have steadfastly refused to cast a glance through the telescope? What shall we make of this? Shall we laugh, or shall we cry?

Galileo Galilei

2 Observations

The spectra analysed in this thesis were obtained as part of the GALAH survey (Chapter 4) and a dedicated high-resolution survey of the Milky Way bulge (HERBS, Chapters 5 and 6), all taken with the HERMES spectrograph. The two surveys have different goals, however they are designed to be complementary: the spectra are taken with the same spectrograph and analysed with a similar spectral synthesis pipeline (Chapter 3). In this chapter, the spectral properties, observational details and data reduction process of each survey are described.

2.1 The HERMES spectrograph

The HERMES[1] spectrograph is an instrument built for the 2dF system on the Anglo Australian Telescope. 2dF is a robotic fibre-fed 2 degree field plate consisting of 400 fibres in total, ≈360 of which can be used to observe science objects simultaneously. The remaining fibres are dedicated to sky spectra (a minimum of 25 sky fibres are recommended for all HERMES observations) and bright guide stars to maintain field position accuracy (8 fibres). It takes ≈30 minutes for the 2dF robot to position all fibres for a typical field configuration. 2dF has two observing plates and two sets of fibres, so that one plate can be configured while the other is observing. The width of each fibre is 2 arcseconds, and the positioning precision of 2dF is 0.3 arcseconds. Apart from HERMES, 2dF also feeds the AAOmega spectrograph, which has resolving power of ≈11 000.

HERMES was conceived with the goals of chemical tagging in mind: to deliver as many high-precision elemental abundances as possible for a large number of stars (Freeman & Bland-Hawthorn 2002, Bland-Hawthorn et al. 2010, Ting et al. 2012). To this end, the

[1]High Efficiency and Resolution Multi-Element Spectrograph

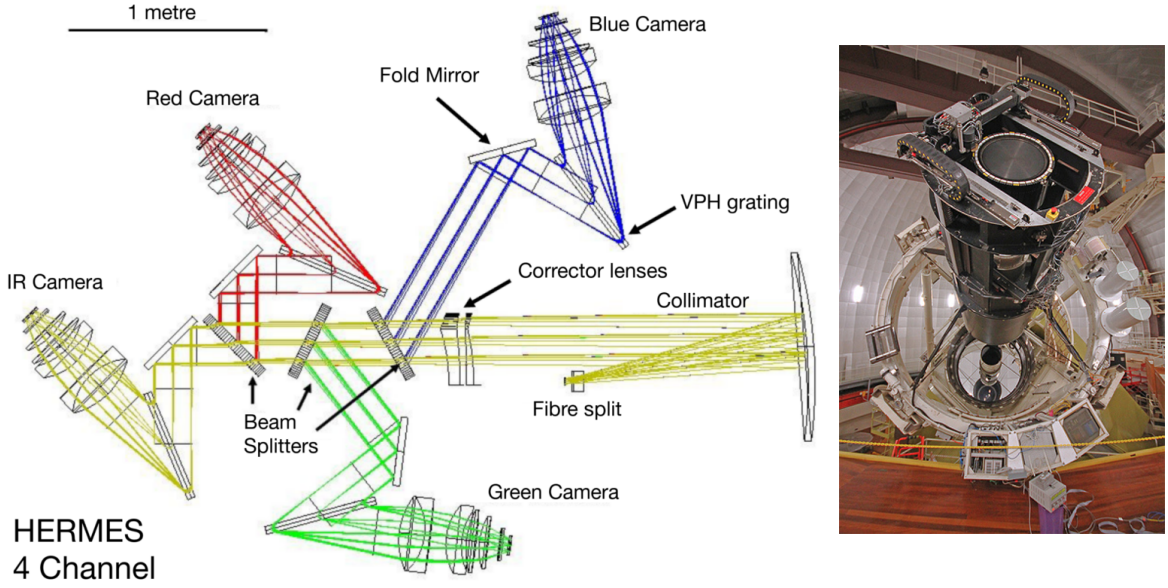

Figure 2.1 A schematic of the HERMES four-channels split design and an image of the 2dF system. Left panel: The 'blue', 'green', 'red' and 'IR' cameras correspond to wavelengths 4713–4903 Å; 5648–5873 Å; 6478–6737 Å and 7585–7887 Å, respectively. Right panel: the 2dF fibre-fed system (at the very top) mounted on the prime focus of the AAT.

spectrograph was designed to include four optical cameras at wavelengths 4713–4903 Å; 5648–5873 Å; 6478–6737 Å; 7585–7887 Å, covering a total of 1000 Å. The nominal resolving power ($\mathcal{R} = 28\,000$) and wavelength coverage of HERMES can deliver abundance ratios for the light elements Li, Na, Al, K; α-elements O, Mg, Si, Ca; iron-peak elements Sc, Ti, V, Cr, Mn, Co, Ni, Cu, Zn and neutron-capture elements Y, Zr, Ba, La, Nd, Eu. These elements include all of the major nucleosynthetic production channels. Fig 2.1 shows the HERMES four-channel design.

Each HERMES camera feeds a 4096 $\times$ 4112 pixels CCD. The `FAST` readout mode has a gain of $\approx$3 e^-/ADU and up to 5 e^- readout noise. This is the standard mode for most HERMES observations. The `NORMAL` readout mode, used for the HERMES Bulge Survey, has a gain of $\approx$2 e^-/ADU and less readout noise (3 e^-), is more suitable for very faint stars. The level of dark current is negligible, between 1.5–3.0 e^-/pixel/hour. After 60 minutes of integration, the spectrum of a star with Johnsons-Cousin V magnitude of 14 is expected to reach signal-to-noise ratio (SNR) of at least 100 per resolution element[2], provided all other conditions are optimal. The spectrograph was commissioned in late 2013, and at this time primarily observed targets from the GALAH survey.

[2] At HERMES resolving power, a resolution element is approximately 4 wavelength pixels.

2.2 The GALAH survey

The GALAH[3] survey is an on-going, new generation massive spectroscopic survey. The survey aims to unravel the formation history of the Galaxy, using the stellar chemical signatures - or abundance ratios. The ultimate scientific goal that motivated this survey is identifying clusters that have dispersed over the evolution of the Milky Way, using chemical tagging. In order to achieve this goal, GALAH is to observe ≈1 million Galactic stars with the HERMES instrument, delivering abundance ratios for up to 28 elements for each star.

In addition to chemical tagging of various disk populations, GALAH offers the opportunity for many other science projects, such as chemically peculiar candidates, metal-poor stars, young and active stars, and characterising planet-hosting candidates. This is further serviced by the overlap between GALAH and the asteroseismic survey K2 (via the K2-HERMES/TESS-HERMES programs, Sharma et al. 2018), and the astrometric survey *Gaia* (Brown et al. 2016), which provide accurate ages, parallaxes and proper motions for a large number of stars. For a comprehensive discussion of GALAH scientific motivations, the reader is referred to De Silva et al. (2015). GALAH officially began operations in February 2014, and so far has observed over half a million stars.

GALAH targets are primarily disk stars in the southern sky with $V \approx 12$–14. In addition, targets of magnitudes $V \approx 9$–12 from the *Tycho*-2 catalogue were observed to take advantage of the *Tycho-Gaia* astrometric measurements (Michalik et al. 2015). Open and globular clusters and *Gaia* benchmark stars have also been observed as part of the GALAH pilot survey. Results from the pilot survey project aimed at determining the properties of the Galactic thin and thick disks are presented in Chapter 4. Fig 2.2 shows the spatial coverage, in ecliptic coordinates, of GALAH observations as of November 2017.

The low magnitudes of GALAH targets allow observations in bright time, although this requires accurate sky-subtraction (see Section 2.4). Observations are split into sets of three exposures to minimise the effects of cosmic rays; typical fields are integrated for 1 hour in 3×20 minutes exposures and bright fields are integrated for 18 minutes in 3×6 minutes exposures. The magnitude limits and observing times of GALAH are designed such that the survey can be completed in a reasonable time frame. For this reason, faint targets belonging to the Galactic bulge and halo are not specifically targeted by GALAH.

2.3 The HERMES-Bulge Survey

The Galactic bulge is one of the most complex and least understood components in the Milky Way, as outlined in Section 1.4. Bulge stars are typically faint at optical wavelengths as they are distant and suffer from significant reddening; their observations at high resolution in the optical regime are therefore extremely time consuming. These issues can be

[3]GALactic Archaeology with HERMES

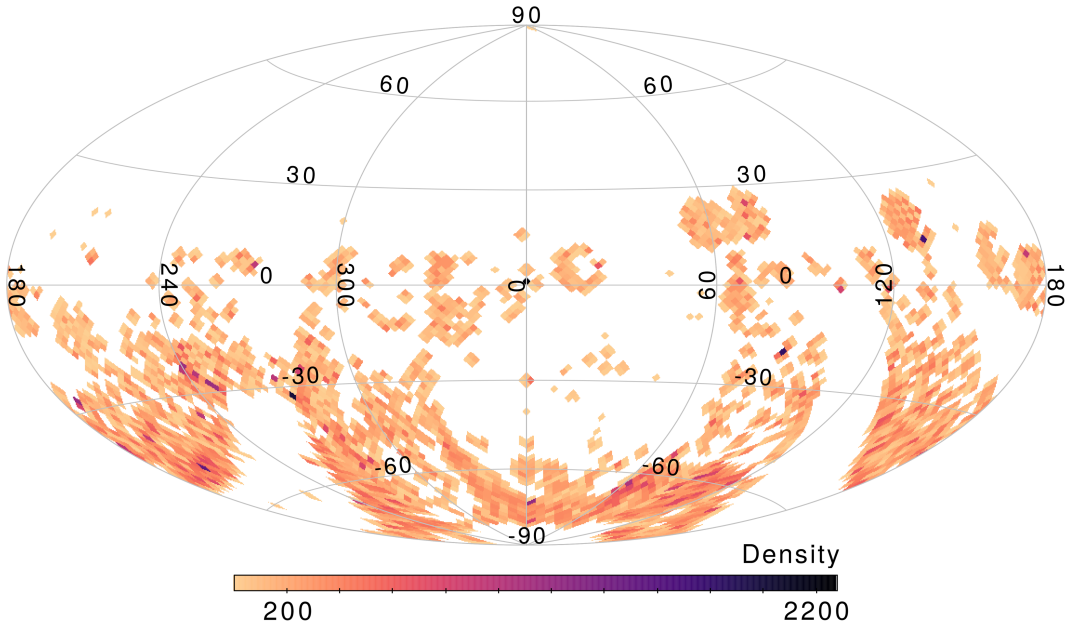

Figure 2.2 Map of observed GALAH and K2-HERMES targets as of November 2017. The K2 fields can be seen along the ecliptic. The density scale shows total number of objects within an area of ≈4 square degrees. Note that some repeat observations are included.

resolved by either observing bulge targets in the infrared wavelengths, or observe during micro-lensing events where their luminosities are amplified (Bensby et al. 2017). However, micro-lensing events are quite rare, and at infrared wavelengths, less chemical information are available. For example, the APOGEE survey can deliver high fidelity spectra and precise abundance ratios for 15 elements at resolving power of 22 500 (or up to 21 elements with much less reliable atomic information, Hawkins et al. 2016). As the result, bulge studies have typically contained small stellar samples, and most have only examined the abundance trends of α-elements.

Bulge observations with the HERMES spectrograph can provide accurate abundance ratios for many more elements than most current bulge studies in the literature. Furthermore, such a sample would enable a consistent comparison to GALAH disk stars if analysed in the same manner. The HERMES Bulge Survey (HERBS) was designed to first obtain a large high quality sample of bulge stars to characterise abundance trends in the Galactic bulge, and second to understand its evolution in relation to the disk. To maximise the number of stars that actually belong to the bulge in our sample, we chose to follow up ARGOS survey targets, which have pre-determined bulge membership. The ARGOS pre-selection helps to avoid foreground star contamination, which is ≈30% (Freeman et al. 2013). The details of target selection can be found in Section 5.2.1.

As previously mentioned, the faint magnitude of targets and high extinction in the bulge region pose difficulties for optical observations (see also, Jönsson et al. 2017). To reach ad-

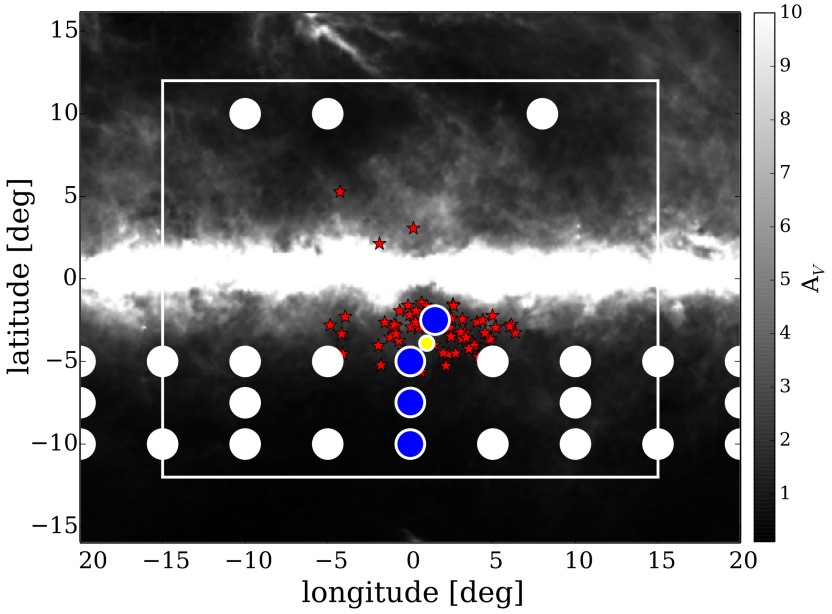

Figure 2.3 Locations of the fields observed by the HERBS survey (shaded blue). Three minor-axis fields are chosen. The field at $(\ell, b) = (3, -3)$ was observed because it is within the K2 Campaign 9 footprint, which will provide stellar ages once the data becomes available. The white circles are ARGOS fields, the yellow small circle is Baade's window and the red stars that are spread out over the inner bulge region are micro-lensed stars from Bensby et al. (2017). The grey scale indicates the extinction level (A_V), which increases greatly towards the mid-plane.

equate SNR for abundance ratio measurements, bulge observations with HERMES require tens of hours of integration time per field. For this reason, we could only select a few ARGOS fields to follow up in order to complete observations within the time frame of this PhD thesis. The fields chosen are those along the minor axis of the bulge to allow characterisation of abundance trends as a function of latitude. We also selected a field within the K2 survey's footprint for which ages can in principle be derived through asteroseismic measurements. The exact locations of the fields are shown in Fig 2.3.

The observations were carried out primarily in dark time, with the exception of the brightest field at $(\ell, b) = (0, -10)$, which was observed for a few hours in grey time. This maximises the SNR for our faint targets, and minimises errors caused by imperfect sky subtraction. Similar to the GALAH survey, observations are split into multiple 30-minutes exposures to avoid the effects of cosmic rays. Typically, a field is observed over many nights; the total integration time depends on the estimated magnitude of clump giants in the field. We discuss the observation outcomes further in Section 5.2.2.

2.4 Data reduction

The original goal of the HERBS survey was to reduce, and analyse spectra in exactly the same manner as the GALAH survey. Due to the different setup and requirements of the

two surveys, it was more practical to reduce HERBS observations independently. For example, to co-add HERBS spectra, the effect of barycentric velocity offset between observations taken at different epochs has to be corrected. As GALAH typically observes objects at a single epoch, multi-epoch co-adding was not implemented in its reduction pipeline until recently. An effort was made to adopt the GALAH analysis pipeline for the HERBS survey, however the results were far from satisfactory. Since the GALAH pipeline is complex, and contains many steps that have been calibrated manually for GALAH data, it was difficult to pinpoint the issues.

We therefore used the HERMES-specific 2dF reduction package 2dfdr v6.46[4], which is publicly available, for the HERBS project. Post-reduction requirements, such as co-adding, were done in PYTHON. The GALAH reduction software is based on IRAF routines, with a custom PYTHON-based sky, fibre cross-talk subtraction modules, and incorporates ESO's telluric removal software `Molecfit` (Smette et al. 2015).

The HERMES spectrograph is prone to some unique issues, as detailed in Martell et al. (2017) and Kos et al. (2017). The first is vertical streaks in the blue, green and red CCDs, as shown in Fig 2.4. These artefacts are intrinsic to the spectrograph, caused by radiation from the material used in the camera's field-flattening lens (Martell et al. 2017). The streaks appear to be widest and most saturated at the first pixel they strike, but continue to saturate adjacent pixels in the same column at lower intensities. At the originating pixel, the streaks are typically cannot be removed fully; away from this pixel, they can be removed with standard cosmic ray rejection methods. Work is under way to replace the camera's field lens with one that does not contain radioactive material by 2019.

The second issue is the tilted point spread function (PSF) (Kos et al. 2017). As observed in arc spectra, the HERMES PSF is circular at the CCD centre, but elliptical towards the corners. This reduces the signal ($\approx$5%) and the resolution at CCD corners (up to $\approx$15%) (Kos et al. 2017). Bland-Hawthorn et al. (2017) are developing a photonic comb that can map and correct for the PSF variation.

These issues affect the data reduction process of each survey, which are summarised and discussed below. Calibration frames such as fibre flat and Thorium-Xenon (ThXe) arc spectra referred to are the same for both GALAH and HERBS surveys, bar the different readout modes.

2.4.1 The GALAH reduction pipeline

The GALAH reduction steps for each 20 minutes GALAH exposure are outlined here; for a more detailed discussion, the reader is referred to Kos et al. (2017).

- **De-biassing**: All biases taken throughout the night are median combined to create a master bias, which is subtracted from all science frames. If the bias level of the master

[4]www.aao.gov.au/science/software/2dfdr

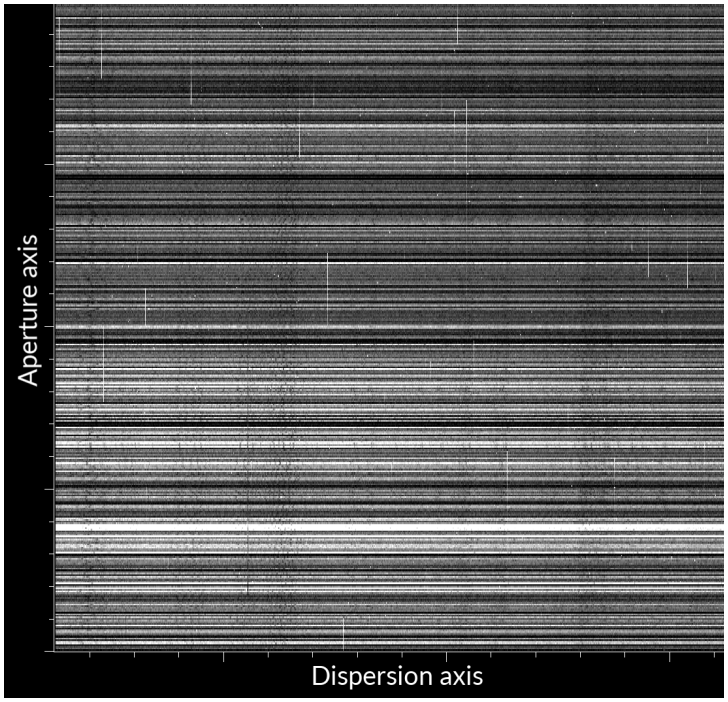

Figure 2.4 Vertical streaks in a raw image from the green HERMES CCD. The streaks start off with high intensity and bleed into adjacent pixels at lower intensities. Although these vertical streaks fade, they can affect tens of fibres at a time.

frame is different from the overscan on the image, then the overscan is used for bias subtraction instead.

- **Flat fielding**: Two flat spectra (one for each observing plate) are created for each CCD by averaging all flat field spectra taken in a given night. Science frames are divided by the flat spectrum corresponding to the same observing plate.

- **Fibre tracing**: The averaged flat field spectra are used to trace fibres with IRAF routine `center1d`. This requires a manually generated template with the corresponding image pixels for each fibre. The fibre traces from each flat field spectrum can be shifted by a global value against the template, and an additional shift of 3 pixels per fibre.

- **Extraction**: The fibre width used for extraction is fixed at 6 pixels, centred on the fibre trace.

- **PSF correction**: The tilt of the PSF is corrected by dividing each arc frame aperture into sub-apertures, transforming (along the dispersion axis) the sub-aperture line centres so that they match the globally measured values, i.e., the line centres measured using the full aperture. This uses the IRAF routines `geomap` and `geotran`. A single transformation is applied to all frames observed in the same night.

- **Scattered light subtraction**: Measured and subtracted using IRAF routine `apscatter`.

- **Fibre cross-talk subtraction**: Light from adjacent apertures can contribute to either one's signal, which is called fibre cross-talk. The cross-talk level in GALAH observations is low (≈0.5%). It has been measured using the gaps between fibre bundles, where no light is expected. The cross-talk values measured from the gaps are used scale and subtract adjacent spectra from each fibre.

- **Wavelength Calibration**: An initial wavelength solution, done manually for a large number of spectra is used to ensure correct arc lines are identified. Using the IRAF `center1d` routine, central wavelengths of ThXe arc lines are calculated and matched with the linelist. Lines that deviate more than 2.5σ from the initial solution are rejected (but no more than 15% of the entire linelist is rejected at any time). The final wavelength calibration is performed on the remaining lines.

- **Sky subtraction** Fibre throughputs are measured from an averaged flat field, and spectra are normalised by their throughputs. The flux in each sky fibre is measured and modelled as a function (3D plane) of position on the plate. For each science object, the model sky flux is calculated according to its location on the plate and subtracted from the object spectrum.

To subtract cosmic rays and vertical streaks, a PYTHON version of the routine LaCosmic is used (van Dokkum 2001). A rejection threshold is set manually for each signal-to-noise level (i.e., the threshold is different for bright fields and normal fields). The red CCD suffers from telluric absorption bluewards of Hα. This affects the lines of some alpha and neutron capture elements. The telluric absorption in the IR CCD may affect the potassium and magnesium lines. It is therefore important that the telluric absorption is dealt with. This is done by by generating a telluric spectrum based on the average airmass for a given field, using ESO's `Molecfit` software. The telluric spectrum is then divided from the object spectrum. Finally, the combined GALAH reduced frame is a simple sum of the three 20-minute exposures.

2.4.2 HERBS data reduction

The reduction process of the HERBS survey follows roughly the same steps as the GALAH survey, with a few important differences as dictated by the setup of our observations. We observed the same field all night and over many nights to reach the required integration time. Both observing plates were used to observe the same stars, as the fields must be reconfigured throughout the night to maintain fibre position accuracy. The fibre allocation also changes subtly when moving between the two plates. In contrast to GALAH spectra, the final co-added HERBS spectra are therefore a product of observations from different plates, fibres, and epochs.

The 2dfdr reduction software subtracts the bias using only the overscan region. After a rough mapping of the fibre traces has been established using the first exposure, the fibre flat

is reduced. The traces are matched to the fibre flat data to determine fibre positions. The fibre extraction is done by fitting a Gaussian profile (rather than a fixed 6-pixels width as in the GALAH pipeline) to each fibre, which helps to minimise cross-talk between fibres. There is no separate module to correct for fibre cross-talk. Prior to fibre extraction, the scattered light is subtracted. Fibre flats are then divided from object spectra. Each observing block, which is between one hour (2×30 minutes exposures) and two hours (4×30 minutes exposures), has a unique fibre flat frame.

The wavelength calibration is done using the same ThXe arc lines as in the GALAH reduction pipeline. However, the *whale shark* pattern matching algorithm (Arzoumanian et al. 2005)[5] is used to fit arc lines. Arc spectra from all fibres are combined to produce a high SNR spectrum, which is then matched against the ThXe atlas using the *whale shark* algorithm. Finally, the fibre throughputs are computed using strong skylines in the red and IR arms of HERMES. The flux from each fibre is then normalised by the throughputs, and the median-combined sky spectrum is subtracted. We do not include a PSF tilt correction, nor do we implement `Molecfit` telluric corrections.

`Molecfit` is partially successful at correcting telluric absorption. Thorough inspection of many GALAH spectra reveal that earlier implementations of `Molecfit` was not able to remove telluric absorption in the red arm at all, while residuals can still be seen in the current implementation. This is likely due to the highly variable atmospheric conditions at the observing site. For the HERBS survey, we deemed it more prudent to 'mask' regions of the spectrum where telluric absorption is expected by increasing the errors at these wavelength points by a large fraction. First, all frames observed within the same night and on the same plate are averaged, weighted by the variance. The weighted average spectrum is given by:

$$flux = \frac{\sum_{i=1}^{n} \left(f_i \sigma_i^{-2} \right)}{\sum_{i=1}^{n} \sigma_i^{-2}} \tag{2.1}$$

The corresponding variance of the combined spectrum is given by:

$$variance = \frac{1}{\sum_{i=1}^{n} \sigma_i^{-2}} \tag{2.2}$$

Here f_i and σ_i are the flux and error of an individual spectrum, and n is the number of spectra to be combined. Thereafter, the barycentric correction is computed and applied to each spectrum. The NOAO telluric atlas is convolved to HERMES resolving power, and scaled to match the absorption level of HERMES spectra, as it is much stronger at Siding Spring than at Kit Peak. The telluric atlas is shifted by the barycentric correction of each star, and the errors of wavelength points corresponding to telluric lines are increased by the

[5]This algorithm was developed to match the spotted patterns on whale sharks with archived photos in order to identify and track them, hence the name. In the application of fitting arc lines, the central wavelength of the lines and their intensities are compared to the ThXe atlas.

inverse of the line absorption level. We do this separately for each object, for each night, as the barycentric velocity changes at different epochs. As the final combined spectra is also a weighted average, the regions affected by tellurics have relatively much larger errors, and consequently smaller weights when spectra are analysed.

For a given field, the spectra from each night, each plate are interpolated onto a common wavelength grid and combined using equations 2.1 and 2.2. The weighted average is very robust against cosmic rays, vertical streaks and bad pixels. While they are not completely eliminated and residuals are present in final spectra, their effects are minimised.

Finally, the fact that we do not correct the tilted PSF is perhaps the most significant difference between the HERBS and GALAH reductions. This means that both the signal to noise ratio and resolution towards the CCD edges of HERBS spectra are slightly decreased. We discuss how this difference affects the stellar parameters in Appendix A.

2.5 Radial velocity and initial parameter estimates

Having good estimates for the radial velocity and initial parameters significantly speeds up the subsequent spectroscopic analysis. For this purpose, we use the GUESS code[6], which is also implemented in the GALAH survey for radial velocity measurements, and has been shown to provide accurate initial parameters (see Kos et al. 2017). Only the blue, green and red HERMES CCDs are used in this step; the IR CCD is excluded as it does not have as many parameter-sensitive lines and is severely affected by telluric absorption.

The GUESS code has two separate modules to compute radial velocity and stellar parameters. Radial velocities are calculated via cross-correlation with a grid of 15 AMBRE models (de Laverny et al. 2012). The models have $\log g = 4.5$, [Fe/H] = 0 and spans 4000–7500 K in $T_{\rm eff}$, at 250 K intervals. Prior to cross-correlation, a crude normalisation is done by fitting a spline function over observed spectra, omitting regions around Hα and Hβ lines. The observed normalised spectrum is then cross-correlated with all 15 models, one at a time. The cross-correlation peak is fitted with a quadratic function, the maximum of which is adopted as the cross-correlation coefficient. The coefficients range from 0 to 1, higher values indicate a better match between model and observation. To improve accuracy, model spectra that return coefficients less than 0.3 are excluded. The radial velocity is an average of values from accepted models, weighted by their cross-correlation coefficient. Each HERMES CCD goes through this process independently, and the final radial velocity is an average of all three CCDs, the uncertainty being the standard deviation between CCDs.

Estimates of stellar parameters ($T_{\rm eff}$, $\log g$, [Fe/H]) are derived after the radial velocity determination using a grid of 16783 AMBRE models. Spectra are shifted to rest with radial velocities from the previous step, and normalised by fitting 3rd order (for the blue and green

[6] https://github.com/jlin0504/GUESS

arms) and 4th order (for the red arm) polynomials to pre-determined continuum regions. These regions were determined by inspection of high resolution spectra of the Sun, Arcturus and μLeo. The polynomial orders are kept low to avoid poorly constrained continuum fits, and appear to work well in the majority of cases. After normalisation, observed spectra are interpolated onto the same wavelength grid as the models, and the L^2 norm (distance in Euclidean space) between them are computed. For each star, the ten models closest in Euclidean space to the observed spectrum are combined to give initial parameters estimate. These were used as starting models in the spectral synthesis analysis described the next chapter.

Classifying the stars has helped materially in all studies of the structure of the universe.

Annie J Cannon

3 Stellar spectroscopy

Part of this chapter appears in Buder, S., Asplund, M., Duong, L., et al., 2018, The GALAH survey: Second Data Release, Monthly Notices of the Royal Astronomical Society, 478:4513. The text that appears below was written entirely by the candidate.

Stellar spectroscopy is instrumental in the studies of Galactic formation and evolution. Abundance ratios of stellar populations obtained with spectroscopy allow astronomers to trace their birth locations and epochs, so to track their spatial and chemical evolution over time. In the case of the oldest stars, stellar abundances allow one to probe conditions in the nascent universe (e.g., Frebel & Norris 2015, Howes et al. 2015). Spectroscopy is a well established field, but at the same time it is constantly evolving with improved computational capabilities and advances in stellar and atomic physics. The advent of massive spectroscopic surveys in the last few years have also prompted the development of new methods to deal with drastic increases in sample size. The spectral analysis of surveys such as *Gaia*-ESO, GALAH and APOGEE, is typically an involved process and requires multiple methods or tools to achieve the desired accuracy and efficiency. This chapter aims to describe the GALAH spectroscopic analysis pipeline, as it was used in full, or in part, to obtain the results presented in this thesis. The methodology is summarised in subsequent chapters, and discussed here in detail. In addition, part of this chapter is dedicated to providing relevant terminology and background information on stellar spectroscopy.

3.1 Stellar spectroscopy: an introduction

A star's physical properties are embedded in the light emitted by its photosphere: absorption features (or emission features in hot stars) correspond to atomic transitions of different

elements present in the star. Absorption line strengths and profiles are dictated by conditions in the photosphere, such as the temperature, pressure and density of each chemical element. Indeed, absorption features have been used since the 19th century to classify stars in the work of Maury & Pickering (1896) and Cannon & Pickering (1901). Together, they established the foundation upon which the modern day Morgan-Keenan spectral classification system is built on (Morgan & Keenan 1973).

Stars are classified by their atmospheric parameters, in particular the temperature, surface gravity, and the metal content[1]. Measuring stellar atmospheric parameters does not necessarily require spectroscopy. Photometric methods, such as colour index calibrations (e.g., Alonso et al. 1999, Carney et al. 2005) and the infra-red flux method (IRFM) (e.g., Blackwell et al. 1979, Casagrande et al. 2010), are commonly used to determine effective temperature. Specially designed photometric filter sets can also estimate the iron content of stars to efficiently identify rare objects, such as extremely metal-poor stars (Bessell et al. 2011). For nearby stars, surface gravity can be inferred using distances from parallax measurements in conjunction with absolute magnitudes, extinction and bolometric correction (e.g., Bensby et al. 2014). Asteroseismology offers yet another technique to infer $\log g$, using internal stellar oscillations. Fundamental scaling equations relating oscillations and effective temperature to stellar mass and radius can be used to determine surface gravity (Kjeldsen & Bedding 1995, Hekker et al. 2013, Stello et al. 2017). Non-spectroscopic methods can serve as external benchmarks for spectroscopic results, as they offer a more accurate solution in some cases (see Section 3.6.1). However, at the present time these non-spectroscopic techniques can only be applied to a small number of stars due to observational constraints.

Measuring equivalent widths (EWs) is perhaps the most popular method via which stellar properties can be determined (e.g., Meléndez et al. 2008, Yong et al. 2012, Liu et al. 2014, Bensby et al. 2014). Equivalent width is essentially a measurement of line strength: it is defined as the width of a rectangle whose area is equal to that of the absorption line, and whose length the full depth of the continuum. Effective temperature and surface gravity are typically determined using excitation potential of and ionisation balance of neutral and singly ionised Fe lines[2]. The effective temperature is found by requiring that all Fe I lines yield the same abundance, while the correct surface gravity should result in the same abundance ratios for Fe I and Fe II lines. Elemental abundances can be measured using the 'curve of growth', which relates EWs to the number density of atoms.

The equivalent width method is susceptible to broad/blended line profiles for which EWs cannot be accurately measured; or lines that experience substantial broadening due to atomic effects such as hyperfine splitting. In these cases, line profile fitting using spectral

[1]The term 'metal' indicates elements heavier than hydrogen and helium.

[2]It is typical to use Fe lines as they are most numerous and easily measured. However, other species such as Ti and Sc can also be used.

synthesis is preferred (e.g., Brewer et al. 2015, García Pérez et al. 2016). As the name suggests, spectral synthesis spectroscopy compares models against observed spectra to find the best-fit model corresponding to the global minimum χ^2. Given accurate atomic or molecular data; and including blending lines, spectral synthesis can be fully automated with relative ease. This approach is used throughout this work for both stellar parameter and abundance determination. As with any method, assumptions and caveats exist at each analysis step, and are outlined in the sections below. This analysis is specific to GALAH/HERMES spectra, which cover four optical wavelength bands: 4713–4903 Å; 5648–5873 Å; 6478–6737 Å and 7585–7887 Å; and has nominal spectral resolving power of $\mathcal{R} \approx 28\,000$.

3.2 Model atmospheres

Stellar spectroscopy is heavily model-dependent, and all spectroscopic methods require model predictions to interpret observed line properties. Many different atmospheric models exist in the literature, but they normally follow the same basic assumptions: ***one dimensional geometry*** (either plane-parallel or spherical); ***hydro-static equilibrium***; ***mixing length theory*** and ***local thermodynamic equilibrium*** (LTE). The mixing length theory assumes that convective parcels traverse over a distance equal to the mixing length, which is proportional to the pressure scale height (Böhm-Vitense 1958). The mixing length parameter that describes this proportionality is adjustable, and typically calibrated on the Sun.

While 1D models have many limitations due to their simplistic assumptions (e.g., Asplund 2005), they are close approximations of stellar photospheres and are used in almost all spectroscopic analyses to date. Full 3D hydro-dynamical models or time-averaged 3D (denoted $\langle$3D$\rangle$) models, such as the Stagger grid (Magic et al. 2013), provide realistic descriptions of temperature stratification and convective transport in stellar photospheres without parametrisation. As the result, they are able to match observations better than 1D models (e.g., Asplund et al. 2000, 2009, Pereira et al. 2013), as shown in Fig 3.1. However, developing 3D model grids require much more time and computing resources. As such, they still lack the extensive parameter space coverage of 1D grids, and are not yet suitable for the analysis of data sets containing many different stellar types, such as the GALAH data set. For this reason, we used 1D model atmospheres in our analysis, in particular the marcs 2012 grid (Gustafsson et al. 2008).

3.3 The fundamental parameters: $T_{\rm eff}$, $\log g$ and [M/H]

A stellar photosphere is defined by its effective temperature – $T_{\rm eff}$; the surface gravity in logarithmic scale – $\log g$; and the abundance of metals, or metallicity – [M/H]. These are often referred to as the fundamental parameters.

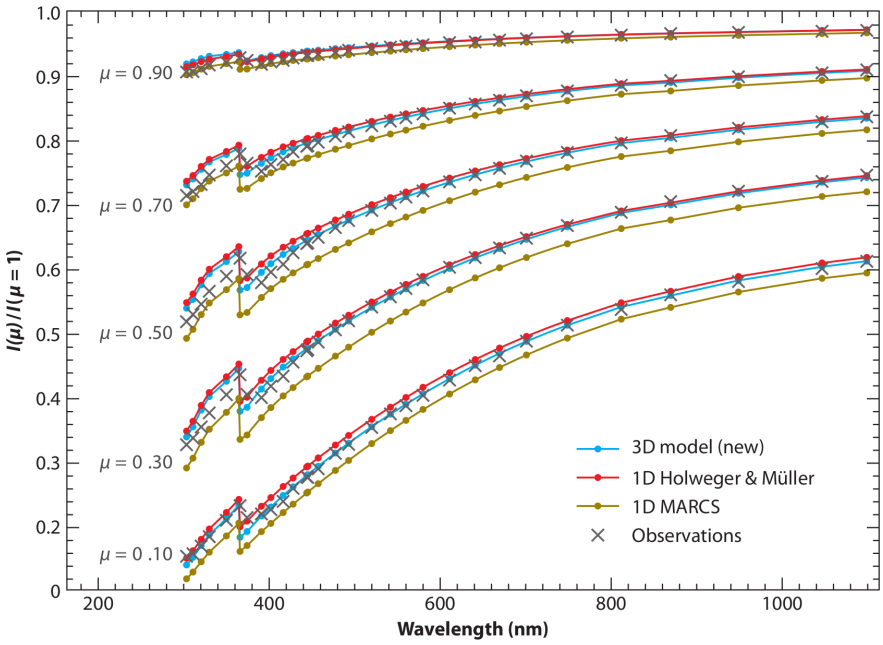

Figure 3.1 Solar centre-to-limb intensity variation as a function of wavelength at different viewing angles μ, where $\mu = 1$ is at disk centre. In most cases the 3D model is a better fit to the data compared to 1D models. Figure from Asplund et al. (2009).

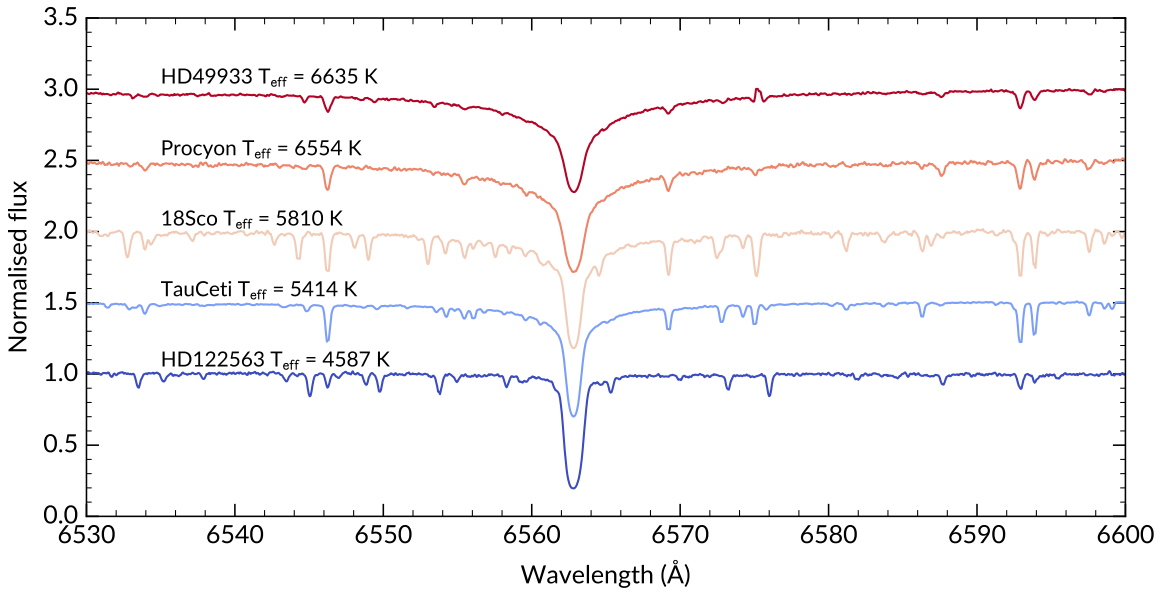

Figure 3.2 The sensitivity of Hα line profiles to effective temperature. The wings of hydrogen lines increase in width with increasing $T_{\rm eff}$. Shown are HERMES observations of standard stars HD122563 (F giant); TauCeti (G subgiant); 18Sco (solar twin/G dwarf); Procyon (F dwarf) and HD49933 (F dwarf), with reference effective temperatures from Heiter et al. (2015a).

3.3.1 Effective temperature

The effective temperature is defined in relation to the total stellar flux, following the Steffan-Boltzman equation for a black-body radiator:

$$F = \sigma T_{\rm eff}^4; \tag{3.1}$$

The luminosity, or power emitted by a star can thus be related to its effective temperature through the surface area:

$$L = 4\pi R^2 \sigma T_{\rm eff}^4 \tag{3.2}$$

Effective temperatures can be measured spectroscopically by leveraging the profiles of hydrogen lines, which are sensitive to effective temperature changes. The wings of hydrogen lines typically become broader with increasing temperatures and have little dependence on surface gravity. The Hβ (4861 Å) and Hα (6563 Å) lines in HERMES spectra are used as primary temperature indicators. Fig 3.2 shows the hydrogen line profile sensitivity to effective temperature for HERMES observations of *Gaia* benchmark standards (Jofré et al. 2014, Heiter et al. 2015a).

Hydrogen line profiles can only be used to accurately determine $T_{\rm eff}$ within a certain temperature range. For the resolution and wavelength coverage of HERMES spectra, this is ≈4000–6500 K. At the hot end degeneracy occurs between temperature and gravity; at the cool end HERMES spectra become dominated by molecular absorption lines and hydrogen

profiles lose sensitivity to effective temperature changes. For hot stars, this method can underestimate the effective temperature by up to 200 K (Sharma et al. 2018).

3.3.2 Surface gravity

The surface gravity is defined by stellar mass and radius as:

$$g = \frac{G\mathcal{M}}{R^2}; \tag{3.3}$$

where G is the gravitational constant.

The line profiles of some metal species are sensitive to gravity changes. An example is the wings of Ca II triplets in the infrared wavelengths, which is a commonly used gravity indicator. Singly ionised lines of Fe and Ti are also sensitive to gravity in late type stars, i.e. when they are the dominant ionisation stage (e.g., Gray 2005). These are used in the GALAH analysis pipeline to determine $\log g$. However, there are few unblended ionised lines of suitable strength in HERMES spectra, making surface gravity determination a challenge. This is especially apparent for dwarf stars cooler than 4000 K, which tend to converge at surface gravities similar to giant stars, causing an 'up-turn' in the lower main sequence. Here the titanium dioxide molecular lines begin to dominate and ionised lines become increasingly blended, rendering the ionisation balance ineffective. The lower main sequence up-turn could also be attributed to the break down of 1D LTE analysis.

The issues concerning $\log g$ accuracy are not unique to HERMES/GALAH spectra. Surface gravity is notoriously difficult to determine spectroscopically, even for spectra at higher resolving power and signal-to-noise ratio (e.g., Bensby et al. 2014). When available, external calibrations from parallaxes or asteroseismic measurements are often necessary to constrain surface gravity (e.g., Pinsonneault et al. 2014). Section 3.6.1 explores further the application of external gravity constraints in the GALAH analysis pipeline.

3.3.3 Metallicity

Stellar metallicity, denoted [M/H], is formally defined as the relative mass fraction of all elements other than hydrogen and helium, relative to the Sun on a logarithmic scale. However, the iron abundance [Fe/H] is often used as a metallicity indicator. The abundance scale is defined such that the Sun has metallicity $[\mathrm{Fe/H}]_\odot = 0$:

$$[\mathrm{Fe/H}] \equiv \log_{10}\left(\frac{N_\mathrm{Fe}}{N_\mathrm{H}}\right)_\mathrm{star} - \log_{10}\left(\frac{N_\mathrm{Fe}}{N_\mathrm{H}}\right)_\mathrm{sun}; \tag{3.4}$$

where $N_\mathrm{Fe}/N_\mathrm{H}$ is the density ratio of iron to hydrogen atoms.

By equation 3.4, a star with metallicity -1 has 10 times less iron relative to hydrogen than the Sun. In the GALAH analysis pipeline, both Fe I and Fe II lines are used as the primary metallicity indicators.

3.4 Velocity fields

Stellar rotation and the motions of gas in the photosphere cause broadening in all spectral lines. In 1D model atmospheres, these effects are accounted for with 'velocity' parameters, namely: micro-turbulence v_{mic} (also ξ_t); macro-turbulence v_{mac}; and projected rotational velocity $v \sin i$ (Gray 2005). It has been shown that micro- and macro-turbulence are not necessary in 3D models, but they are needed in 1D analyses to compensate for motions that cannot be accounted for by mixing length theory (Asplund et al. 2000, Magic et al. 2013).

For spectra with $\mathcal{R} \leq 30\,000$ and SNR ≈ 100 such as that of HERMES, it is not trivial to separate all three broadening parameters. Solving for all three without constraints will only cause additional scatter in the result, as there is not enough information in the spectra to break degeneracies. However, micro- and macro-turbulence show systematic variations with atmospheric parameters, and can be calibrated with $T_{\rm eff}$ and $\log g$ (e.g, Valenti & Fischer 2005).

In our analysis, we set all macro-turbulence values to zero, essentially combining it with $v \sin i$, since the spectra are not of sufficient resolving power to determine both. $v \sin i$ is optimised simultaneously with the fundamental parameters. While micro-turbulence ξ_t is updated in every iteration, it is dictated by the empirical formulas that has been calibrated for the *Gaia*-ESO survey (Smiljanic et al. 2014), as shown below.
For main sequence stars ($T_{\rm eff} \leq 5500$K; $\log g \geq 4.2$):

$$\xi_t = 1.1 + 1.6 \times 10^{-4} \times (T_{\rm eff} - 5500) \tag{3.5}$$

For evolved and warmer stars ($T_{\rm eff} \geq 5500$K; $\log g \leq 4.2$):

$$\xi_t = 1.1 + 1.0 \times 10^{-4} \times (T_{\rm eff} - 5500) + 4 \times 10^{-7} \times (T_{\rm eff} - 5500)^2 \tag{3.6}$$

3.5 Elemental abundances

The absolute abundance scale is defined relative to hydrogen:

$$A(\mathrm{X}) = \log\left(\frac{N_{\rm X}}{N_{\rm H}}\right) + 12; \tag{3.7}$$

where $N_{\rm X}$ is the density of element X, and $N_{\rm H}$ is the density of hydrogen atoms.

Following equation 3.4, other elemental abundances can also be presented in bracket notation as [X/H]. Similarly, abundance ratios relative to iron can be defined as:

$$[\mathrm{X/Fe}] = [\mathrm{X/H}] - [\mathrm{Fe/H}] \tag{3.8}$$

In this work, the bracket notation [X/Fe] is most often used for abundance ratios.

3.5.1 Non local-thermal-equilibrium effects

Often the line formation of species in stellar atmospheres deviate from the assumptions of LTE, which only take into account local density and temperature variations (see Asplund 2005, Asplund et al. 2009 and references therein). Due to its success in approximating observations of solar-type stars and the complexity of non-LTE computations, LTE is the default mode of abundance analyses. However, departures from LTE can have large effects on the line strengths of certain species, manifesting as systematic errors in measured abundance ratios (Mashonkina et al. 2003, Lind et al. 2013, Amarsi et al. 2016a). Extremely metal-poor stars in particular are affected by departures from LTE, due to lower opacities that lead to stronger radiation fields relative to the black-body Planck function. Fig 3.3 shows non-LTE effects on some elements for the most metal-poor star SMSS0313-6708. The iron abundance requires a larger non-LTE correction (0.8 dex) compared to other elements (Nordlander et al. 2017).

Non-LTE effects have significant implications for Galactic chemical evolution studies, and should be taken into account where possible. In the GALAH survey abundances pipeline, non-LTE corrections are currently applied to abundances of the elements Li (Lind et al. 2009), Al (Nordlander & Lind 2017), Na (Lind et al. 2011), Mg (Osorio & Barklem 2016), O (Amarsi et al. 2016a), Si (Amarsi & Asplund 2017) and Fe (Amarsi et al. 2016b), with more elements to be considered in the near future.

3.6 The GALAH analysis pipeline

The spectral synthesis method requires 20 minutes on average to analyse a HERMES spectrum for stellar parameters on a single CPU. The most time consuming aspect here is synthesising spectral lines (including blending lines), and the processing time increases with the number of lines present in a spectrum. It can take hours to analyse a spectrum of a metal-rich giant, excluding ancillary procedures such as reading linelists and input data tables. For a survey that has collected spectra for more than 500 000 stars, and aims to observe a total of 1 million, spectral synthesis alone is not the ideal solution. The computation costs for such a pipeline is too great, especially when re-analysis is required to incorporate improvements or rectify errors. This calls for data analysis solutions that are much less computationally taxing than 'traditional' techniques.

The Cannon is a data-driven modelling techniques that is extremely fast, requires modest computing resources and has been successfully applied to the APOGEE (Ness et al. 2015), LAMOST (Ho et al. 2016) and RAVE (Casey et al. 2017) surveys. *The Cannon* works by creating a flexible model as a function of flux pixels based on known stellar parameters (or *labels*) for a reference set of stars (the *training set*). This model alone can be used to determine labels for other survey stars, without further use of atomic data or model atmospheres. An underlying assumption of this approach is that different stars with the same stellar parameters should have identical observed spectra. *The Cannon* is a powerful, but

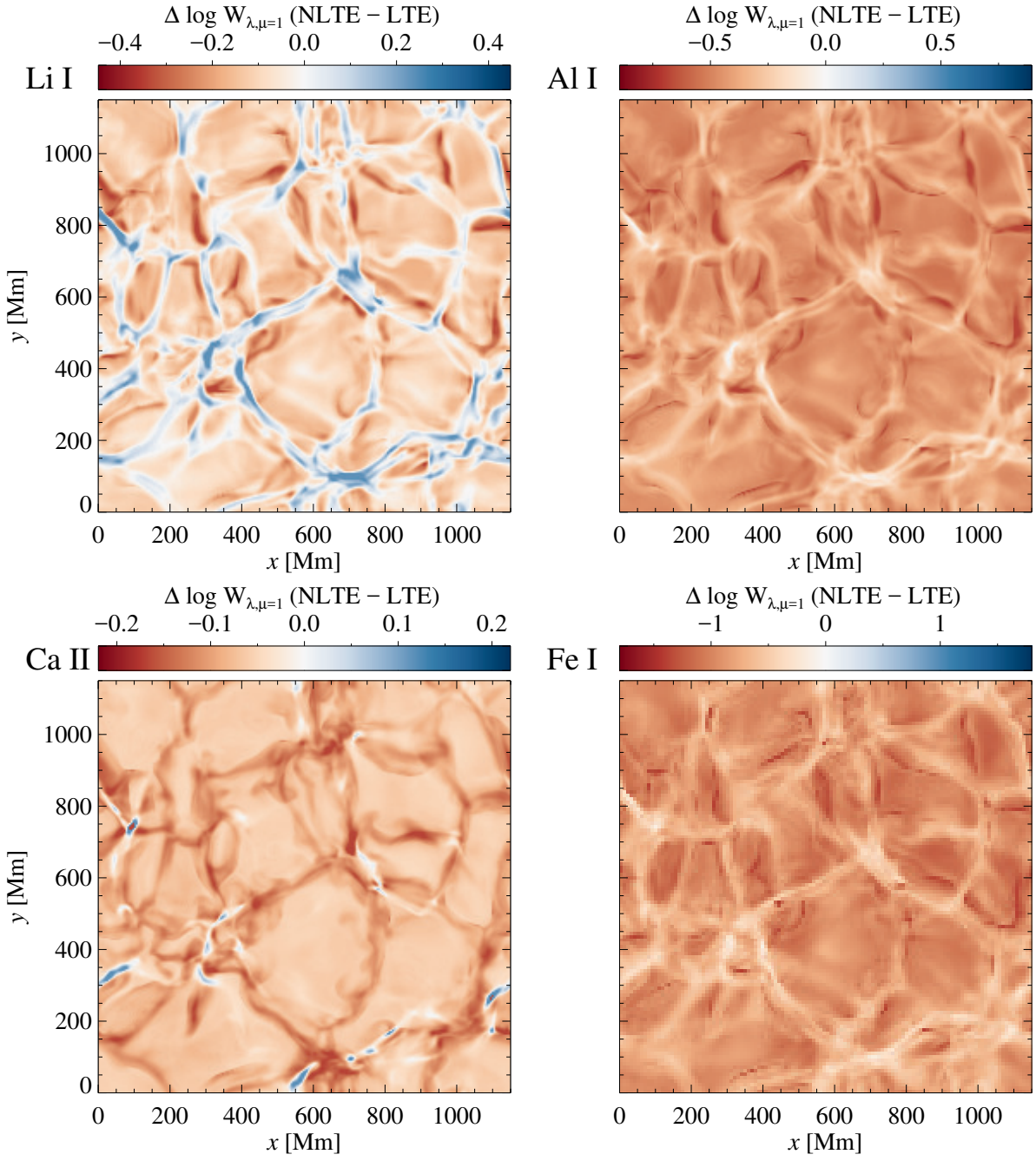

Figure 3.3 Departures from LTE in 3D for the lines Li I 6707 Å, Al I 3961 Å, Ca II 3933 Å, and Fe II 3719 Å of the most iron deficient star known to date - SMSS0313-6708. The colour bars indicate the scale of non-LTE effects on equivalent width measurements. The stellar surface is shown at disk centre intensity. Figure from Nordlander et al. (2017).

not a stand-alone method as it still requires traditional techniques to determine training set parameters.

The GALAH analysis pipeline combines the advantages of both model-driven and data-driven methods to provide accurate parameters and abundances efficiently. Below we outline the analysis steps and configuration of the pipeline.

3.6.1 Spectral synthesis: Spectroscopy Made Easy

For the model-driven analysis, we use the spectral synthesis code SME (*Spectroscopy Made Easy*) v360 (Valenti & Piskunov 1996, Piskunov & Valenti 2017). The atomic data is based on the *Gaia*-ESO survey linelist (Heiter et al. 2015b). However, some background blending lines have slightly different oscillator strength ($\log gf$) values compared to the *Gaia*-ESO linelist. When possible, experimental oscillator strengths are used, but for many background (blending) lines, we have to resort to uncertain theoretical transitional probabilities.

To determine stellar parameters, spectra are divided into several ≈10 Å wide segments containing the relevant lines. These lines are Hα, Hβ and neutral/ionised lines of Sc, Ti and Fe. SME first synthesises the initial model based on estimated stellar parameters and radial velocity from the software GUESS (see Chapter 2). Typically there are two iteration cycles, unless a star does not have initial GUESS parameters, in which case there are three cycles (the second cycle is repeated).

In the first cycle, each segment is normalised using a linear function, which is adequate for the short wavelength intervals used here. SME then creates synthetic spectra based on selected (masked) regions. The free parameters $T_{\rm eff}$, $\log g$, [M/H][3], ξ_t (micro turbulence) and $v \sin i$ (rotational velocity) are simultaneously determined. Radial velocity ($v_{\rm rad}$) is also solved for at each iteration. This is necessary to correct for local variations due to uncertainties in wavelength calibration, and is done separately from parameter optimisation. In addition to providing a formal solution of the radiative transfer, SME uses the Levenberg-Marquardt algorithm to find parameters that correspond to the minimum χ^2. The χ^2 value is computed for regions with line masks following the formula:

$$\chi^2 = \frac{\sum \left(\frac{spectrum-model}{variance}\right)^2 \times spectrum}{N_{\rm lpts} - N_{\rm free} - N_{\rm seg}}; \tag{3.9}$$

where the sum is over the difference between observed and model spectra; $N_{\rm lpts}$ is the number of line pixels; $N_{\rm free}$ is the number of free parameters and $N_{\rm seg}$ is the number of segments.

Final parameters from the first cycle are used to synthesise the initial model in the second cycle and re-normalise each segment. SME goes through the same iteration process,

[3]SME returns the iron abundance of the model atmosphere during the parameter determination stage, which is called metallicity, or [M/H]. This is not to be confused with the metallicity definition explained in Section 3.3.3.

optimising χ^2 until convergence is achieved (when χ^2 changes by less than 0.01%). The number of iterations necessary to reach convergence varies from star to star. Typically more metal-rich and cooler stars take longer to converge, but in less than 20 iterations. During the parameter determination, we implement non-LTE corrections from Amarsi et al. (2016b) for Fe I lines.

The telluric correction and sky subtraction steps in the data reduction process do not always provide optimal results, and have been shown to affect both abundance and stellar parameters determination. We therefore increase the errors of all wavelength points where skylines have been subtracted, and where telluric absorption is expected.

While the nominal resolving power of HERMES is $\mathcal{R} \approx 28\,000$, it is known to vary from fibre to fibre, and as a function of wavelength (Kos et al. 2017). For the GALAH survey, this issue is resolved by interpolating the observed spectrum with pre-computed resolution maps from Kos et al. (2017) to estimate a median resolution for each segment. The GALAH survey is currently implementing a photonic comb, which will map the aberrations and point-spread-function across the full CCD images (Bland-Hawthorn et al. 2017).

External surface gravity constraints

Section 3.3.2 outlined the difficulties with surface gravity determination in spectroscopy, which requires external constraints to improve accuracy. The GALAH survey observed fields that are in the Hipparcos and *Tycho-Gaia* (TGAS) catalogues and within the K2 footprint, providing spectra with parallax and asteroseismic information that can be used to aid surface gravity determination (Perryman et al. 1997, Brown et al. 2016, Stello et al. 2017).

For stars with asteroseismic information, surface gravity is not strictly a free parameter, but is determined at each iteration with respect to solar values using the scaling relation (Kjeldsen & Bedding 1995):

$$\nu_{\rm max} = \nu_{\rm max,\odot} \frac{g/g_\odot}{\sqrt{T_{\rm eff}/T_{\rm eff,\odot}}} \tag{3.10}$$

Here $\nu_{\rm max}$ is the measured frequency at maximum oscillation.

Likewise, for stars with parallax information, $\log g$ is updated at each iteration using the fundamental relation derived from equations 3.2 and 3.3 (Nissen et al. 1997, Zhang & Zhao 2005):

$$\log \frac{g}{g_\odot} = \log \frac{\mathcal{M}}{\mathcal{M}_\odot} - 4 \log \frac{T_{\rm eff}}{T_{\rm eff,\odot}} + 0.4\,(M_{\rm bol} - M_{\rm bol,\odot}) \tag{3.11}$$

$$\text{where } M_{\rm bol} = K + BC - 5 \log d + 5 \tag{3.12}$$

Here the mass $\mathcal{M}$ of each star is estimated using 2MASS photometry (Skrutskie et al. 2006), and the age estimation code ELLI (Lin et al. 2018). For the absolute bolometric magnitude $M_{\rm bol}$, bolometric corrections (BC) from Casagrande & VandenBerg (2014) are applied to

the 2MASS *K*-band. For all stars of the Hipparcos catalogue, the distance d is computed by the transformation $d = 1/\varpi$ (with ϖ being the parallax). For all stars of the *Tycho-Gaia* catalogue, Bayesian distances from Astraatmadja & Bailer-Jones (2016) are used.

Comparison of spectroscopically-determined $\log g$ from the SME analysis pipeline with *Gaia* benchmark stars (Heiter et al. 2015a) shows an offset of ≈ -0.15 dex, in the sense that SME underestimates surface gravity (Sharma et al. 2018). The same offset is found when spectroscopic and asteroseismic results are compared. We therefore adjust the SME-based $\log g$ by +0.15 dex for stars in *The Cannon* training set (Section 3.6.2).

Abundance determination and solar abundance normalisation

After the atmospheric parameters have been established, they are fixed for abundance determination. The lines of each element are synthesised, and line blending is modelled using the atomic information provided. The blended wavelength points are excluded from the line mask. For the GALAH survey, all available lines for each element are synthesised (as opposed to line-by-line synthesis).

Abundance ratios are given in bracket notation as [X/M]. To minimise systematic errors (such as uncertain $\log gf$ values) and calibrate the zero point, we analysed a HERMES Solar spectrum with the SME pipeline and rescale the abundances such that:

$$[\mathrm{X/M}] = [\mathrm{X/M}] - [\mathrm{X/M}]_{\mathrm{HERMES},\odot} \tag{3.13}$$

Where [X/M] are the unscaled abundances, and $[\mathrm{X/M}]_{\mathrm{HERMES},\odot}$ are the abundances of the HERMES solar spectrum.

3.6.2 Data-driven modelling: *The Cannon*

From Ness et al. (2015), the general form of *The Cannon*'s spectral model can be written as:

$$f_{n\lambda} = \theta_\lambda^T \cdot \ell_n + \mathrm{noise} \tag{3.14}$$

Where $f_{n\lambda}$ is the flux at every pixel, θ_λ the model coefficients and ℓ_n is a function of the labels. For *The Cannon* analysis of HERMES spectra, ℓ_n is a quadratic function of the labels, as shown in Equation 8 of Ness et al. (2015). In contrast to Casey et al. (2017), who used different models for the main-sequence and giant branch, the same model is used here for all stars. The fluxes of all spectra are normalised and shifted to rest for *The Cannon* analysis.

The Cannon determines coefficients θ_λ from the known fluxes and spectroscopic labels of a reference (or training) set. It is crucial that the spectra and parameters of the training set are of high fidelity, as any systematic errors in either one would translate to the full sample. To reduce random errors, it is desirable to have high signal to noise training spectra. As such, all stars in the GALAH reference set have SNR > 50 per pixel in the blue HERMES CCD (4713–4903 Å). The training set was chosen to consist of stars with external surface gravity

constraints from parallaxes (TGAS catalogue, Michalik et al. 2015) and asteroseismology (K2 campaigns, Stello et al. 2017), as well as *Gaia* benchmark stars and well studied open and globular clusters. In addition, only stars with relative parallax errors smaller than 30% are included.

Prior to the training step, we perform a validation test for spectroscopic parameters $T_{\rm eff}$, $\log g$ and [M/H] against that of *Gaia* benchmark stars (Jofré et al. 2014, Heiter et al. 2015a). For surface gravity an additional test against asteroseismic measurements is carried out. The comparisons show that HERMES/GALAH surface gravities are typically underestimated by $\approx$0.15 dex, and [M/H] systematically underestimated by 0.1 dex. These biases are corrected for in the reference set where applicable, and *The Cannon* is trained on corrected $\log g$ and [M/H] values.

For stellar parameter determination, the *The Cannon* model includes primary labels $T_{\rm eff}$, $\log g$, [M/H], ξ_t and $v \sin i$, and an auxiliary label $A(K_s)$ extinction, to minimise the effect of reddening and diffuse interstellar bands on abundance determination (e.g., Ho et al. 2016). Extinction values for the training set was estimated with the RJCE method (Majewski et al. 2011). We used 2MASS H-band and WISE 4.5 μm photometry (Wright et al. 2010), following procedures outlined in Zasowski et al. (2013). In general, *The Cannon* reproduces SME results without bias, and to precisions of 47 K in $T_{\rm eff}$, 0.1 dex in $\log g$ and 0.05 dex in [M/H] (Sharma et al. 2018). Fig 3.4 shows a side-by-side comparison of the GALAH training set and *The Cannon*-derived parameters for the full survey sample. Here the limitations of *The Cannon* can also be appreciated: the lack of gians cooler than 4000 K and dwarfs cooler than 4500 K, and the artefact near 7000 K are due to the sparse sampling of training stars in these regions.

The Cannon models can also be built with additional labels [X/M] for each of the 28 elemental abundances measurable with HERMES spectra. The [α/M] abundance ratio has been successfully derived for the APOGEE, LAMOST and GALAH surveys (Ness et al. 2016a, Ho et al. 2016, Duong et al. 2018). Casey et al. (2017) were able to compute abundance ratios of six elements for the RAVE survey using *The Cannon*. However, data-driven abundance measurements for as many as 28 elements have not been explored previously. Complications inevitably arise as some elements can only be measured for certain types of stars, which results in incomplete parameter space coverage. The treatment, or identification of chemically peculiar stars is also an important point of discussion for *The Cannon* and similar methods. The GALAH survey has succeeded, for the most part, in their effort to use *The Cannon* to determine stellar abundances for over 20 elements. Due to the limitations of training data, the method currently works best for FGK dwarfs and giants (Buder et al. 2018). While the details of data-driven abundance determination are outside the scope of this work, we refer the reader to Buder et al. (2018) for a comprehensive discussion of the procedure and caveats.

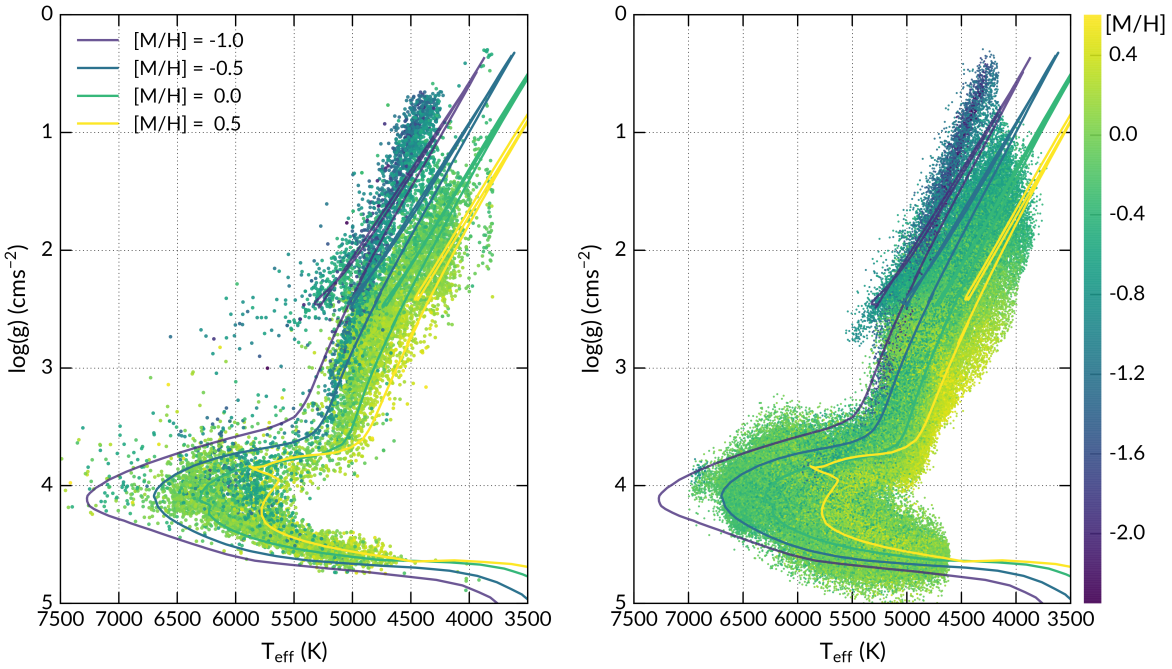

Figure 3.4 Comparison of the training set (SME-derived) and *The Cannon*-derived stellar parameters for GALAH survey objects. Left panel shows the training set of ≈13 000 stars, and the right panel shows *The Cannon* results for ≈420 000 GALAH stars (without reduction/analysis flags). *The Cannon* reproduces training set parameters accurately, even with a common model for dwarfs and giants. Data courtesy of the GALAH Collaboration.

There are no solved problems, there are only problems that are more or less solved.

Henri Poincaré

4

Properties of the Galactic disk near the solar neighbourhood

This chapter has been published as Duong, L., Freeman, K., Asplund, M., et al., 2018, The GALAH survey: properties of the Galactic disc(s) in the solar neighbourhood, Monthly Notices of the Royal Astronomical Society, 476:5216.

Using data from the GALAH pilot survey, we determine properties of the Galactic thin and thick disks near the solar neighbourhood. The data cover a small range of Galactocentric radius ($7.9 \lesssim R_{\rm GC} \lesssim 9.5$ kpc), but extend up to 4 kpc in height from the Galactic plane, and several kpc in the direction of Galactic anti-rotation (at longitude $260^\circ \leq \ell \leq 280^\circ$). This allows us to reliably measure the vertical density and abundance profiles of the chemically and kinematically defined 'thick' and 'thin' disks of the Galaxy. The thin disk (low-α population) exhibits a steep negative vertical metallicity gradient, at $\mathrm{d[M/H]}/\mathrm{d}z = -0.18 \pm 0.01$ dex kpc^{-1}, which is broadly consistent with previous studies. In contrast, its vertical α-abundance profile is almost flat, with a gradient of $\mathrm{d}[\alpha/\mathrm{M}]/\mathrm{d}z = 0.008 \pm 0.002$ dex kpc^{-1}. The steep vertical metallicity gradient of the low-α population is in agreement with models where radial migration has a major role in the evolution of the thin disk. The thick disk (high-α population) has a weaker vertical metallicity gradient $\mathrm{d[M/H]}/\mathrm{d}z = -0.058 \pm 0.003$ dex kpc^{-1}. The α-abundance of the thick disk is nearly constant with height, $\mathrm{d}[\alpha/\mathrm{M}]/\mathrm{d}z = 0.007 \pm 0.002$ dex kpc^{-1}. The negative gradient in metallicity and the small gradient in $[\alpha/\mathrm{M}]$ indicate that the high-α population experienced a settling phase, but also formed prior to the onset of major SNIa enrichment. We explore the implications of the distinct α-enrichments and narrow $[\alpha/\mathrm{M}]$ range of the sub-populations in the context of thick disk formation.

4.1 Introduction

The Milky Way is believed to have a thick disk, similar to those observed photometrically in external disk galaxies (Tsikoudi 1979, Burstein 1979, Dalcanton & Bernstein 2002, Yoachim & Dalcanton 2006, Comerón et al. 2015). The ubiquity of thick disks indicates that they are an integral part of disk galaxy evolution. The Galactic thick disk was originally discussed as a distinct structural component by Gilmore & Reid (1983)[1], who showed that the vertical stellar density profile at the Galactic South pole was best described by two exponentials. Much debate has since ensued over the origin and properties of the Galactic thick disk. Most notably some authors have argued that it may not be a discrete component (Norris 1987, Nemec & Nemec 1993, Schönrich & Binney 2009, Bovy et al. 2012a).

The chemical properties of the local thick disk have been well characterised by multiple spectroscopic studies. The consensus is that it is older (e.g., Wyse & Gilmore 1988, Haywood et al. 2013, Bensby et al. 2014), kinematically hotter (Chiba & Beers 2000), and more metal-poor and α-rich than the thin disk (Prochaska et al. 2000, Fuhrmann 2008, Bensby et al. 2014, Fuhrmann et al. 2016). The enhanced α-abundances indicates that thick disk stars were enriched by SNe Type II over a short period of time, before SNe Type Ia contribution of iron-peak elements took effect in earnest. The thick disk is thought to have formed within $\approx$1–3 Gyr (Gratton et al. 2000, Mashonkina et al. 2003), although Haywood et al. (2013) suggested a slightly longer formation timescale of 4–5 Gyr.

At the solar annulus, many authors have observed a gap between thin and thick disk stars in the α-abundance ([α/M]) vs metallicity ([M/H]) plane. This is widely interpreted as evidence that the thick disk is a distinct component. In recent literature, the 'thick disk' is often defined chemically as the α-enhanced population. Large scale abundance maps from the APOGEE survey show that two distinct sequences in [α/M] vs [M/H] are observed at all galactocentric radii, although the fractions of stars in the two sequences varies greatly with position in the Galaxy. In the inner Galaxy ($3 < R_{\rm GC} < 5$ kpc), and at large heights above the Galactic plane, the high-α sequence dominates. Beyond galactocentric radius $R_{\rm GC} \approx 9$ kpc, its density decreases significantly (Hayden et al. 2015). This observation is in line with the short scale length of about 2 kpc for the chemical thick disk (Bensby et al. 2011, Cheng et al. 2012, Bovy et al. 2012b, 2016). The concentration of the older, α-enhanced population to the inner disk indicates that the thick disk formed inside-out (Matteucci & François 1989, Burkert et al. 1992, Samland & Gerhard 2003, Bird et al. 2013). In contrast to the chemically defined thick disk of the Milky Way, the photometrically defined thick disks of external galaxies are more extended, with scale lengths comparable to thin disk scale lengths (e.g., Yoachim & Dalcanton 2006, Ibata et al. 2009).

While its scale length is fairly well constrained, the scale height of the thick disk is still contentious (see Bland-Hawthorn & Gerhard 2016, and references therein). Gilmore & Reid (1983) estimated the thick disk exponential scale height to be 1.35 kpc from star counts,

[1]See also Yoshii (1982).

similar to measurements made by photometric decomposition of Milky Way analogues (e.g., Ibata et al. 2009). More recent estimates find the thick disk scale height to be significantly shorter, and there is still some scatter in the measurements (Jurić et al. 2008, Kordopatis et al. 2011, Bovy et al. 2012b, 2016). Furthermore, results from high-resolution spectroscopic surveys have raised doubts on the existence of a structurally distinct thick disk, even if there are clearly two populations with distinct α-enhancements. Bovy et al. (2016) finds a smooth transition in scale-heights for mono-abundance populations, as does Mackereth et al. (2017) for mono-age populations, where more α-enhanced and older stars populate increasingly greater heights. Martig et al. (2016b) also showed that, due to flaring of the disk (Rahimi et al. 2014, Minchev et al. 2015, Kawata et al. 2017), the geometrically thick part of the disk has a large age dispersion, whereas the chemical 'thick disk' (high-α population) has a narrow age range. This may also explain why the chemically defined thick disk of the Milky Way has a short scale length, while surface brightness measurements of geometrical thick disks in external galaxies indicate that they are radially much more extended.

Several theoretical models have been proposed for thick disk formation and explain its observed properties. Thick disks may arise from external heating processes such as dwarf satellite accretion (Abadi et al. 2003) or minor merger events (Quinn & Goodman 1986, Quinn et al. 1993, Kazantzidis et al. 2008, Villalobos & Helmi 2008). The fast internal evolution of gravitationally unstable clumpy disks at high red-shift (Bournaud et al. 2009, Forbes et al. 2012) or gas-rich mergers at high red-shift (Brook et al. 2004, 2005) could form a thick disk. The turbulent interstellar medium observed in disk galaxies at high red-shift may also be associated with thick disk formation (e.g.Wisnioski et al. 2015). Radial migration of stars (Sellwood & Binney 2002), where stars are transported outwards and gain vertical height to form a thick disk, is another possibility that has been extensively discussed (Schönrich & Binney 2009, Minchev & Famaey 2010, Loebman et al. 2011, Roškar et al. 2012, Schönrich & McMillan 2017). Although there is evidence for radial migration in the thin disk, such as the presence of very metal rich low-α stars in the solar neighbourhood (Haywood 2008, Casagrande et al. 2011) and the skewness of metallicity distribution functions at different Galactic radii (Hayden et al. 2015, Loebman et al. 2016), the role of radial migration in thick disk formation is still unclear, and is not supported by some observed properties of the thick disk (high-α) population (e.g., Haywood et al. 2013, Recio-Blanco et al. 2014, Bovy et al. 2016). Vera-Ciro et al. (2014) showed in their simulation that radial migration can have strong effects on the thin disk, but not the thick disk. Aumer et al. (2016) found that in their standard model, outwardly-migrating stars are not responsible for the creation of the thick disk, but thick disks can form in models with high baryon fractions. However, in their high-baryon models, the bar is too long, the young stars are too hot and the disk is strongly flared.

Observational evidence to discern thick disk formation scenarios is still inconclusive. Earlier results, such as the lack of thick disk vertical metallicity gradient observed by Gilmore et al. (1995) and orbital eccentricity distributions by Sales et al. (2009), Dierickx et al. (2010)

favoured merger scenarios. More recent studies, most of which separate thin and thick disk stars by their metallicity or kinematics, indicate that the thick disk does have a vertical metallicity gradient (Chen et al. 2011, Katz et al. 2011, Kordopatis et al. 2011, Ruchti et al. 2011), but the gradients measured by these studies vary greatly due to their different methods of isolating the thick disk. Few studies report on the vertical abundance profile of the disk, although an accurate measurement of the metallicity and abundance profile as a function of distance from the Galactic plane can provide important constraints for the evolution history of the disk.

This work is motivated by the current uncertainty about the formation and properties of the Galactic thick disk. The thick disk is important because its formation is a seemingly ubiquitous feature of disk galaxy evolution; its rapid formation and old population means that it provides a detailed snap-shot of the conditions in the early Galaxy. Understanding how the thick disk formed and evolved will be central to chemical tagging efforts of current and future high resolution massive spectroscopic surveys such as 4MOST (de Jong et al. 2011), *Gaia*-ESO (Gilmore et al. 2012), APOGEE (Majewski et al. 2015), GALAH (De Silva et al. 2015), and WEAVE (Dalton et al. 2016).

We have used data from the first GALAH survey internal release to study the properties of the Galactic thick disk. We show that at the solar circle, the thick disk exhibits a non-negligible vertical metallicity gradient, and the thin disk shows a steep vertical metallicity gradient. We find that the mean α-element abundance does not vary significantly with height in either of the chemically and kinematically defined thick and thin disks.

The paper is structured as follows: Section 4.2 describes the stellar sample used in the analysis, including field and colour selection. Section 4.3 explains the methods of obtaining stellar parameters, abundances and the distances, as well as how thin and thick disk components were defined. Section 4.4 explores the possible effects of our selection and how they were corrected for. Section 4.5 presents the results of metallicity and the α-abundance variation with vertical height are described in section 4.6. We discuss the implications of our results for the formation and evolution of the thick disk in Section 4.7, and summarise the work in Section 4.8.

4.2 Sample selection

We present in this paper results from the GALAH survey internal data release v1.3. The data acquisition and reduction are described in Martell et al. (2017) and Kos et al. (2017), respectively. The stellar parameter and abundance determination is summarised in Section 4.3.1. Briefly, GALAH spectra cover four optical bands, at wavelengths located within the Johnson-Cousins B, V, R, I passbands, with resolving power $\lambda/\Delta\lambda \approx$28 000 (De Silva et al. 2015). The GALAH main-survey selects stars according to a simple magnitude criterion: $12 < V_{JK} < 14$, where the V_{JK} magnitude is estimated from 2MASS (Skrutskie et al. 2006)

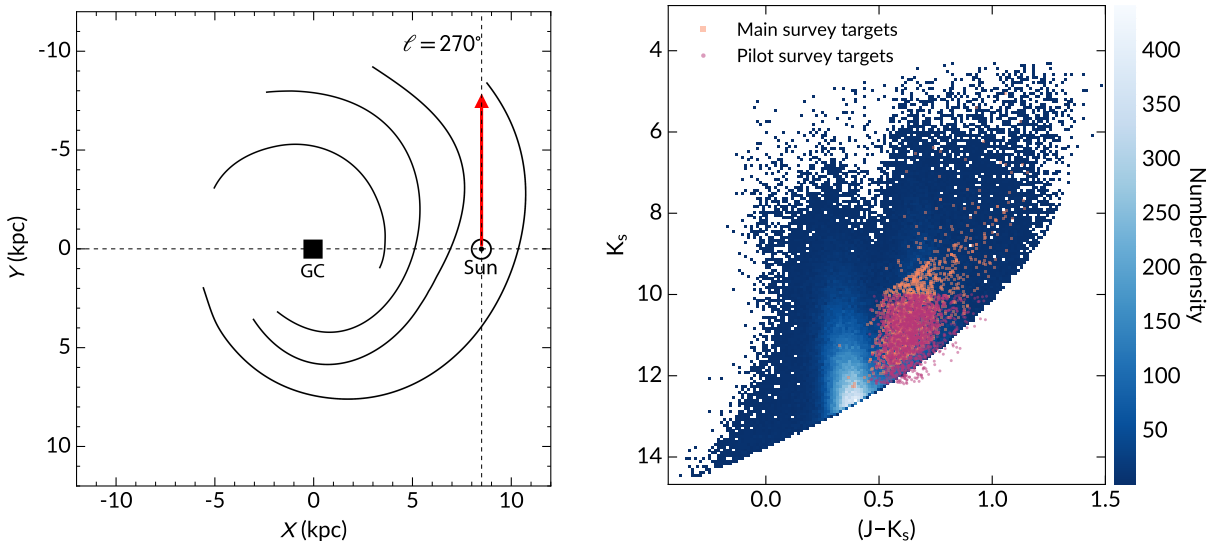

Figure 4.1 The location of observed fields and colour-magnitude selection of GALAH main and pilot survey targets. Left panel: a schematic view of the Milky Way, illustrating the targeted line-of-sight. We observe along $\ell \approx 270°$ and at five latitudes below the plane. The spiral arms are shown as traced by H II gas, from Drimmel & Spergel (2001). Right panel: Colour-magnitude selection of the stars in this analysis is shown against all GALAH input catalogue targets within the observed region (including special bright targets). The pilot survey has a simple magnitude cut, at bright and faint limits of $K_s = 10$ and 12, respectively. The main GALAH survey magnitude selection $12 < V_{JK} < 14$ appears as a stripe in the $(J - K_s)$ vs K_s plane. The pilot survey extends slightly fainter than the main survey, and the handful of stars falling outside of the main survey selection are from a bright field.

photometry via the transformation:

$$V_{JK} = K_s + 2(J - K_s + 0.14) + 0.382\, e^{(J-K_s-0.2)/0.50} \tag{4.1}$$

The above equation is discussed further in Sharma et al. (2018) (see their Fig. 1). The magnitude selection in V_{JK} manifests as a $(J - K_s)$ colour dependence when plotted as function of other magnitudes, as shown in Fig. 4.1, right panel. In addition to normal survey fields which follow the V_{JK} magnitude limit described above, GALAH also observed special fields, such as pilot survey fields (which included benchmark stars and clusters), and bright stars selected from the *Tycho*-2 catalogue (Martell et al. 2017), most of which also appear in the *Gaia* DR1 catalog (Brown et al. 2016).

As part of the GALAH pilot survey, we conducted a study of the chemical properties and distribution of the Galactic thin and thick disks. Fields were chosen towards Galactic longitude $\ell = 270°$, as shown in Fig. 4.1, left panel. This longitude was chosen to maximise the asymmetric drift component between thin and thick disk stars (Gilmore et al. 2002, Wyse et al. 2006), thus making it easier to distinguish them by their kinematics. We observed fields at five latitudes: $b = -16°, -22°, -28°, -34°$ and $-42°$. Fig. 4.2 shows the

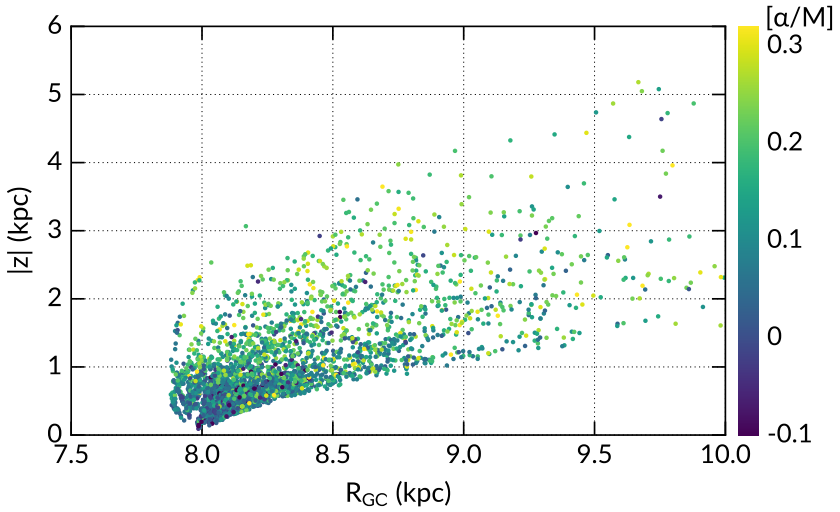

Figure 4.2 The distribution in Galactocentric radius and height below the plane for the entire sample, adopting $R_{\mathrm{GC},\odot}$ = 8 kpc. There are a few stars (not shown) outside the limits $|z| > 6$ kpc and $R > 10$ kpc. Stars are colour-coded by α-abundances: low-α stars lie typically closer to the plane whereas α-enhanced stars are found at greater distances from the plane.

distribution of observed stars in Galactic coordinates R_{GC} and $|z|$ (distances are derived as per Section 4.3.2). Adopting $R_{\mathrm{GC},\odot} = 8$ kpc, most of the stars are concentrated around the solar radius, between $R_{\mathrm{GC}} = 8 - 8.5$ kpc, and up to about 4 kpc in height below the Galactic plane. Since our longitude range is between $\ell = (260, 280)$, we also observed stars with $R_{\mathrm{GC}} < 8$ kpc. We chose to use only giants in this study to include a larger range of distances and heights from the plane. The magnitude limits of the main GALAH survey result in giants making up only about 25% of stars observed. In order to increase the fraction of giants, a colour cut at $(J - K_s) > 0.45$ was imposed for the pilot survey prior to observations, which excludes turn-off stars and some dwarfs. We also extended the faint V_{JK}-magnitude limit of the pilot survey to 14.5 in order to observe a larger fraction of clump giants. Also included in this analysis are giants from the GALAH main-survey that fall within the same Galactic longitude–latitude range described above. The colour and magnitude selection for all stars included in the analysis is shown in Fig. 4.1.

4.3 Data analysis

4.3.1 Stellar parameters and alpha abundances

The GALAH stellar parameters and abundances pipeline will be described in detail elsewhere; here we seek to give a brief summary. The pipeline is a two-step process, involving spectral synthesis using SME (*Spectroscopy Made Easy*) (Valenti & Piskunov 1996, Piskunov & Valenti 2017) and the data-driven generative modelling approach of *The Cannon* (Ness et al. 2015). We identify a sample of stars with high signal-to-noise ratio, each visually inspected to be free of irregularities like unexpected continuum variations and large cosmic

ray residuals. This set of stars serves as the training set, the labels of which are propagated to all other survey stars. The training set includes *Gaia* benchmark standards (Jofré et al. 2014, Heiter et al. 2015a) whose parameters have been determined by non-spectroscopic methods; globular and open clusters and stars with accurate asteroseismic surface gravity from K2 Campaign 1 (Stello et al. 2017). In total there are ≈2500 training stars.

In the first step, stellar parameters for the training set are obtained with SME. Here we use the MARCS model atmospheres (Gustafsson et al. 2008), and non-LTE corrections for Fe (Lind et al. 2012). SME syntheses of Hα and Hβ, neutral and ionised lines of Ti, Sc and Fe are used to determine $T_{\rm eff}$, $\log g$, [M/H][2], v_{mic} (micro turbulence) and $v \sin i$ (rotational velocity), converging at the global minimum χ^2. The stellar parameters are fixed when individual abundances are computed for the α-elements Mg, Si, Ti. The weighted average of these elements gives [α/M], and all abundances are scaled according to the Solar chemical composition of Grevesse et al. (2007).

Although the GALAH wavelength range includes lines of the α-elements Ca and O, they are currently omitted from the weighted average because the Ca lines fall within problematic spectral regions (due to bad CCD pixels and/or sub-optimal data reduction), and the O I triplet at 7772–7775 Å is subjected to large non-LTE effects (Amarsi et al. 2015, 2016a), which are not yet accounted for in the GALAH analysis pipeline. Relative to *Gaia* benchmark standards, SME produces accurate results with offsets in $\log g$ and [M/H] of -0.15 and -0.1 dex respectively, in the sense that it underestimates these values. The same surface gravity offset is also observed when SME results are compared to asteroseismic $\log g$ obtained with oscillations from Stello et al. (2017). The offsets are constant across the HR diagram, and are corrected by simply adding 0.15 and 0.1 dex to all $\log g$ and [M/H] values of the training set prior to parameter propagation with *The Cannon* (Sharma et al. 2018).

In the second step, *The Cannon* learns the training set parameters and abundances (*labels*) from SME, and builds a quadratic model at each pixel of the normalised spectrum[3] as a function of the labels (Ness et al. 2015). This model is then used to determine stellar parameters and abundances for all other survey spectra. In addition to the six primary labels described above, *The Cannon* uses a seventh label, extinction $A(K_s)$, to minimise the effect of reddening and diffuse interstellar bands on [α/M] determination. The extinction for each star of the training set was estimated with the RJCE method (Majewski et al. 2011). We used 2MASS H-band and WISE 4.5 μm photometry (Wright et al. 2010), following procedures outlined in Zasowski et al. (2013). Parameter errors are estimated by cross-validating the input (SME) and output labels (*The Cannon*) for the training set. Cross-validation was

[2]We use [M/H] to denote metallicity to differentiate it from the actual iron abundance [Fe/H]. The metallicity reported in this data release is the iron abundance of the best-fit atmospheric model and mostly measured from Fe lines. However, [M/H] values are close to the true iron abundances, and GALAH results presented elsewhere have used [Fe/H] to denote metallicity, which is equivalent to the [M/H] used here.

[3]The normalisation method is described in Kos et al. (2017).

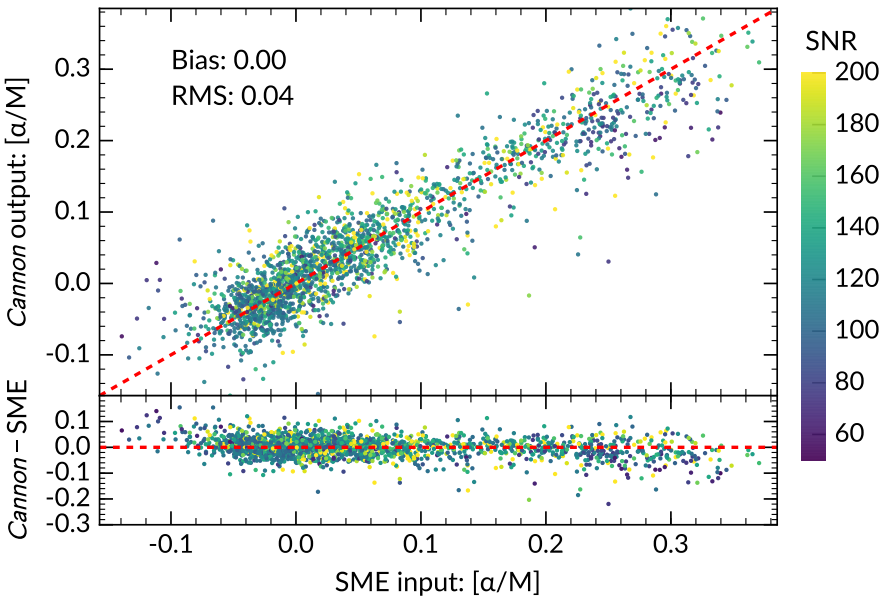

Figure 4.3 Cross-validation of *The Cannon* output against SME input for the label [α/M]. Stars are colour coded by signal-to-noise ratios in the 'green' arm of HERMES, the wavelength of which lies within the Johnson-Cousins V-band. The top panel shows the 1:1 relation between SME input and *The Cannon* output. The bottom panel shows the distribution of the difference. *The Cannon* reproduces the SME input without bias, and to 0.04 dex precision.

done by partitioning the reference set into unique sub-samples, each consisting 20% of the full set. Five tests were performed, each time a 20% sub-sample is left out of the training step, and used only to validate the results. Fig. 4.3 shows the combined cross-validation outcomes of all five tests for label [α/M]. The training set results have also been successfully applied to the TESS-HERMES survey, and the error estimation of stellar labels except for [α/M] is shown in Fig. 5 of Sharma et al. (2018). Overall, *The Cannon* achieves internal precisions of 47 K in $T_{\rm eff}$, 0.13 dex in $\log g$, 0.05 dex in [M/H] and 0.04 dex in [α/M], which are typical of the errors reported in this data release.

Fig. 4.4 shows *The Cannon*-derived stellar parameters for the full sample of giants selected for analysis. We have excluded most sub-giants, turn-off and main-sequence stars. *The Cannon* is able to reproduce the accuracy and precision of SME such that all parameters follow the PARSEC isochrone tracks (Marigo et al. 2017) without further calibrations. The [α/M]–[M/H] plot is shown in Fig. 4.5 for a sub-sample of stars with signal-to-noise ratio $\geq$ 80 per resolution element. We observe the two distinct α-tracks in the [α/M]–[M/H] plane: a low-α track extending from [M/H] $\approx$ 0.4 to $-$0.6, usually defined as the chemical thin disk, and a high-α track extending from [M/H] ≈ -0.2 to -1, usually defined as the chemical thick disk. The typical precision of the [α/M] measurements is 0.04 dex, similar to that of [M/H].

We do not include stars with [M/H] ≤ -1 dex here, because few metal-poor stars could be used in the training set (they stars are rare, and typically have low SNR), rendering *The Cannon* results for metal-poor stars significantly less accurate. *The Cannon* has limited ab-

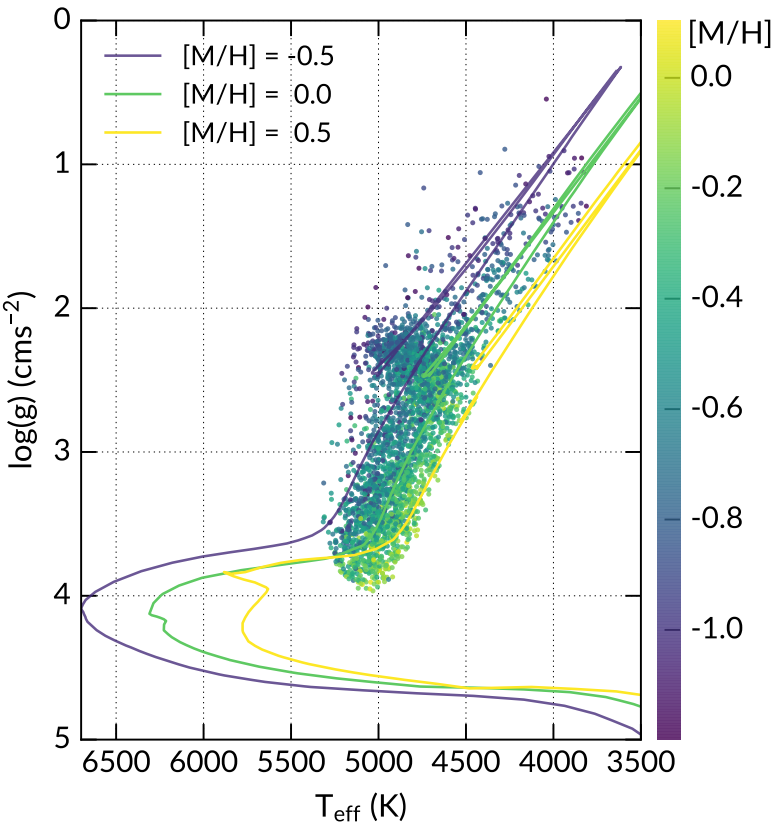

Figure 4.4 The *Kiel* diagram from *The Cannon* for the sample of stars in this analysis, colour coded by [M/H]. Over plotted are 4 Gyr PARSEC isochrones at metallicities indicated in the figure legend. The stellar parameters behave as predicted by the evolutionary tracks after bias corrections to *The Cannon* training set (see text for details).

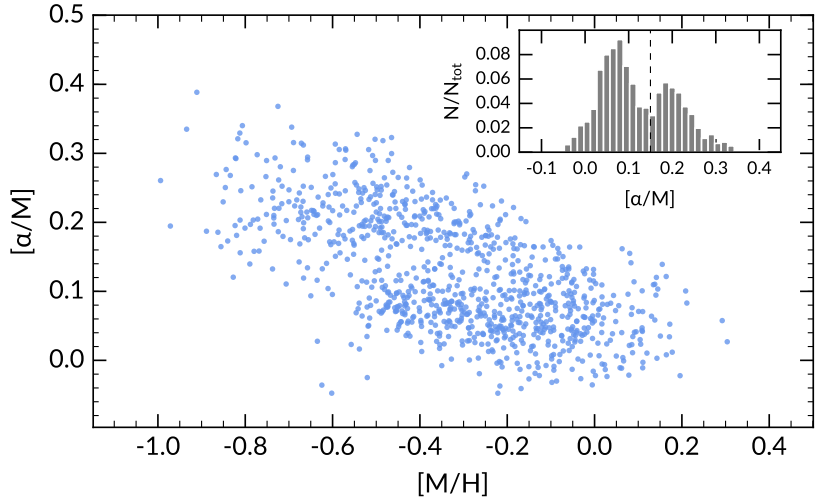

Figure 4.5 α-abundances as a function of metallicity for a sub-sample with signal-to-noise ≥ 80 per resolution element. There are two distinct abundance sequences corresponding to the thin disk (low-α) and the thick disk (high-α). Inset: histogram of the [α/M] distribution, the dotted line indicate [α/M] = 0.15, where the two populations appear to separate.

ility to extrapolate, which is evident in the comparison to *Gaia* benchmarks: stars with [M/H] < -1 have larger deviations from reference values (Sharma et al. 2018). This does, however, exclude the metal-weak thick disk from our analysis. We find that other studies which include the metal-poor extension of the thick disk, such as Katz et al. (2011), Ruchti et al. (2011) reported similar results to ours (see detailed discussion in Sections 4.5.2 and 4.6). Furthermore, there are few stars with [M/H] ≤ -1 dex to begin with (2% of the full sample), so their exclusion may have small effects on the vertical gradients derived in later sections, but this is unlikely to have a major impact on our conclusions.

4.3.2 Distance determination

Distances are typically determined by isochrone fitting methods using the fundamental stellar parameters $T_{\rm eff}$, $\log g$ and [M/H] and photometry. Theoretical constraints, such as stellar evolution and initial mass functions (IMF) have been included by Zwitter et al. (2010) and Burnett & Binney (2010), respectively, to obtain more accurate distances for the RAVE survey (Steinmetz et al. 2006). Isochrone distances are dependent on all fundamental parameters, but a strong dependence on [M/H] can cause correlated errors when trying to assess the metallicity distribution as a function of distance from the Galactic centre or above the plane (Schlesinger et al. 2014, Anguiano et al. 2015). In this section we describe an empirical method of distance determination that does not have such a strong dependence on inferred [M/H], which may be advantageous for our measurements of metallicity vertical gradients in Section 4.5.

To determine the distance, we exploit the relationship between stellar surface gravity and radius R using *Kepler* asteroseismic data from Casagrande et al. (2014). Fig. 4.6 shows

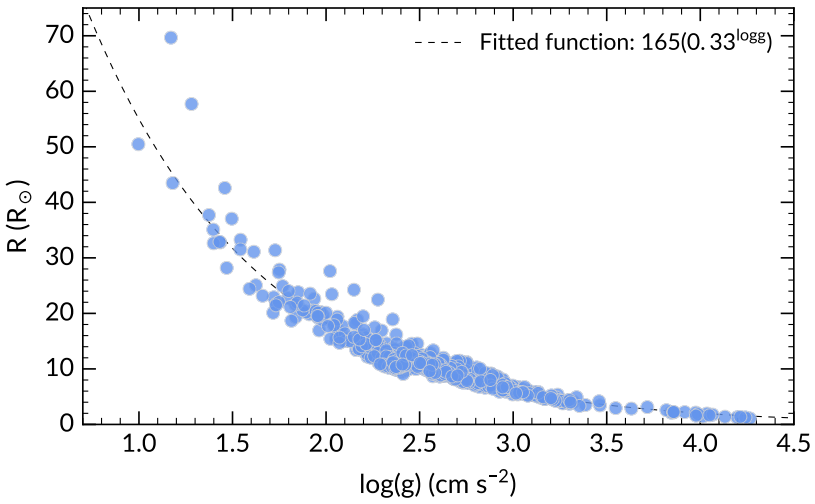

Figure 4.6 The correlation between stellar surface gravity and radius, data from the *Kepler* sample of Casagrande et al. (2014). The stellar radius as a function of $\log g$ is best described by an exponential.

the $\log g - R$ correlation and the exponential function that best fits the data. Using spectroscopically determined $\log g$, we compute for each GALAH star a radius (in solar radii) using the function:

$$R_* = 165(0.33^{\log g}) \tag{4.2}$$

Note that starting from the definition of $g = GM/R_*^2$, where G is the gravitational constant, and M the mass of the star, we arrive at the formula:

$$R_*/R_\odot = 10^{0.5(\log g_\odot - \log g)}, \tag{4.3}$$

which is equivalent to $165.59 * 0.316^{\log g}$, assuming that $M = M_\odot$ and the solar $\log g$ is 4.438068 cm s^{-2} . However, the function used to fit the data in Fig 4.6 returns the minimum reduced-χ^2 (perhaps due to differences in the stellar mass compared to the assumed solar value), and is used instead[4].

The absolute luminosity is estimated using the effective temperature and radius relation:

$$L = 4\pi R_*^2 \sigma T_{\rm eff}^4 \tag{4.4}$$

Finally, we interpolate the stellar parameters $T_{\rm eff}$, $\log g$, [M/H] over a grid of synthetic spectra to determine the correction that needs to be applied to 2MASS J, H, K_s photometry to derive the bolometric flux $\mathcal{F}_{bol}$[5]. We correct for extinction using the Schlegel et al. (1998) map to de-redden the observed 2MASS magnitudes. This is done using extinction

[4]The typical difference between distances derived using $165.59 * 0.316^{\log g}$ and equation 4.3 is 13%, which is comparable to the distance uncertainties (Section 4.3.2).

[5]Although [M/H] is used, the dependence of $\mathcal{F}_{bol}$ on this parameter is minimal (Casagrande et al. 2010)

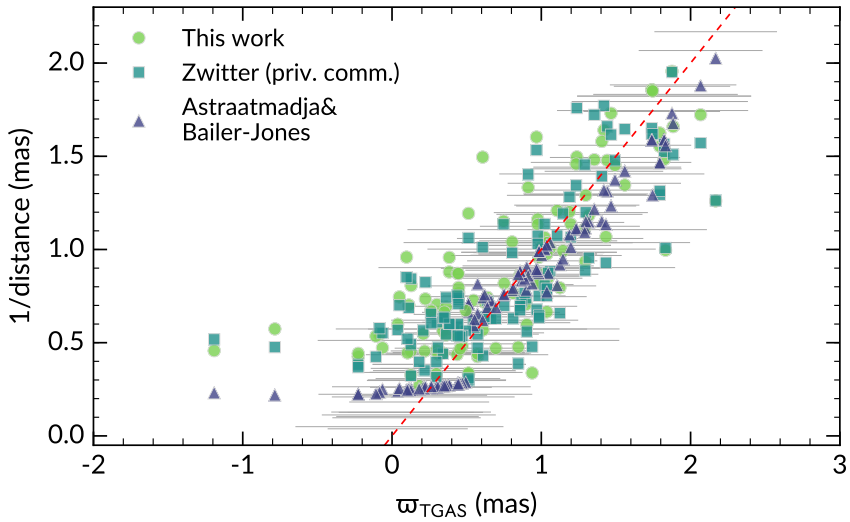

Figure 4.7 Comparison of distances derived from GALAH stellar parameters (this work/Zwitter) and Bayesian TGAS distances (Astraatmadja & Bailer-Jones). On the x-axis are TGAS parallaxes, and the grey horizontal bars indicate reported uncertainties (including systematic errors). There is a break in the Astraatmadja & Bailer-Jones (2016) values because a different prior is used for $\varpi < 0.5$ mas, which according to the authors is more accurate for large distances (see text for details). The y-axis shows inferred parallaxes from the three distance methods. The dashed line is the 1:1 correlation. As the parallax decreases, TGAS fractional errors become very large, and in some cases negative parallaxes are reported. Compared to TGAS, distances derived from GALAH stellar parameters have an overall scatter of ≈ 0.37 mas, which is within the typical TGAS uncertainty of 0.3 mas. For $\varpi < 0.5$ mas, there is a systematic offset between TGAS and IRFM/Zwitter distances of ≈ 0.3 mas.

coefficients computed on-the-fly for the set of stellar parameters adopted (Casagrande et al. 2010). The distance is then simply:

$$D = \left(\frac{L}{4\pi \mathcal{F}_{bol}} \right)^{1/2} \tag{4.5}$$

As is evident from Fig. 4.6, the $\log g$–stellar radius relation is poorly constrained for $\log g \leq 1.5$, because we have few seismic data points in this region and the scatter is larger. There are however relatively few stars with $\log g < 1.5$ in our sample (see Fig. 4.4).

Distance error estimate

We tested the accuracy and precision of our distance determination method by comparing our results to the first *Gaia* data release (Brown et al. 2016, TGAS), which provides accurate parallaxes (ϖ) for bright stars in the *Tycho*-2 catalogue (Michalik et al. 2015). Because of the brighter magnitude limit of *Tycho*-2, we only have a small overlap of about 100 stars for comparison. We also compare our distances to those of Astraatmadja & Bailer-Jones (2016), who computed Bayesian distances using TGAS parallaxes and Milky Way density models. Finally, we include a comparison between our method and that of Zwitter et al.

(2010), which computes the distance modulus by fitting stellar parameters to their most likely isochrone counterparts.

Fig. 4.7 compares the unaltered TGAS parallaxes with the inferred parallaxes from the three distance methods. Distances from Astraatmadja & Bailer-Jones (2016) are median values of the posterior from their Milky Way density model. However, they note that the Milky Way model under-estimates distances for $\varpi < 0.5$ mas when compared to Cepheid distances, as the model assumes that a star is more likely to be in the disk and photometric information is not used. Thus, the distances used here for $\varpi < 0.5$ are the median of the posterior from their exponentially decreasing density model with scale length $L = 1.35$ kpc (Astraatmadja & Bailer-Jones 2016).

The comparison shows no systematic discrepancy for $\varpi_{\rm TGAS} > 0.5$ mas. The distances computed from our IRFM and the Zwitter et al. (2010) isochrone fitting method using the same spectroscopic parameters agree to within ≈15%. Compared to TGAS, both the IRFM and isochrone fitting method have a standard deviation of 0.3 mas, which is well within the typical errors quoted for TGAS parallaxes. We noticed that the Bayesian distances from Astraatmadja & Bailer-Jones (2016) are slightly over-estimated compared to TGAS between $\varpi_{\rm TGAS}$ = 1–2 mas.

We do find an offset between all distance methods and the TGAS parallaxes for $\varpi_{\rm TGAS}$ = 0–0.5 mas, where the TGAS values may be underestimated. For stars with $\varpi_{\rm TGAS} > 0$, the offset is 0.33 mas for the spectroscopic distances. Stassun & Torres (2016) found a similar offset, between TGAS and inferred parallaxes derived from eclipsing binaries, however their results are applicable only to smaller distances, which is not seen in our results (see also Huber et al. 2017). A likely reason for the GALAH-TGAS offset is that TGAS uncertainties becomes very large at $\varpi < 0.5$ mas, so for a magnitude-limited sample, TGAS systematically scatters to smaller values.

In summary, we find that our distances are accurate compared to TGAS parallaxes and the Bayesian distances of Astraatmadja & Bailer-Jones (2016), albeit with an offset for $\varpi_{\rm TGAS} < 0.5$ mas. Overall the standard deviation between the two spectroscopic methods is 17%. Since both our method and the isochrone fitting method used the same set of stellar parameters, the comparison between them is indicative of their intrinsic uncertainties. Assuming that both methods contribute equally to the overall scatter, the internal uncertainty of each method is 12%. This is the value we adopted as the our distance errors.

4.3.3 Separating the thin and thick disk populations

High resolution spectroscopic studies show that the α-enhancement of local disk stars follow two distinct tracks (e.g., Bensby et al. 2014, Adibekyan et al. 2011). The high-α population is typically associated with the thick disk and has high velocity dispersion; the low-α stars are associated with the thin disk, with low velocity dispersion. The thick disk also has a larger rotational lag compared to the thin disk.

The thick disk can also be defined geometrically by star counts (Jurić et al. 2008, Chen et al. 2011), or by metallicity and kinematics (Katz et al. 2011, Kordopatis et al. 2011). The thin and thick disks do overlap in their spatial, metallicity and kinematical distributions. Because of the two distinct sequences in [α/M]-[Fe/H] space, definition of the thick disk by its enhanced α-abundances relative to thin disk stars of the same metallicity is currently widely used (Adibekyan et al. 2013, Bensby et al. 2014, Haywood et al. 2015) . However, the adopted dividing line between the high and low-α populations differs from author to author. Furthermore, some stars with thick disk chemistry have thin disk kinematics, and there are stars that lie in the intermediate region between the two [α/M] sequences. The 'thick disk' population that we are interested in is the stellar fossil of the turbulent epoch of fast star formation at high-z. Following this definition, we want to exclude the flaring outer thin disk, which contributes to the geometrical thick disk, and metal-rich stars which may have migrated from the inner thin disk.

To this end, we chose to separate the two components by fitting a mixture of Gaussian distributions using the Expectation-Minimisation algorithm (Dempster et al. 1977). We use three variables: [M/H] and [α/M] and the radial velocity (RV), which, to the best of our knowledge, has not been done previously. At $\ell = 270°$, the component of the rotational lag between the thin and thick disk along the line-of-sight is maximised for most of our fields, such that RV is a good proxy for V velocity (see also Kordopatis et al. 2017). Instead of using the Cartesian V space velocity component, which has significant proper motion errors, we use the precise GALAH radial velocity to help separate the two populations (98% of our survey stars have RV uncertainty < 0.6 kms^{-1} according to Martell et al. 2017).

The PYTHON `scikit-learn` (Pedregosa et al. 2011) module `GaussianMixture` was used to perform the fitting. we assume that the data cube can be described by 2 multivariate Gaussians, each characterised by its three means and 3×3 covariance matrix: $\theta_j = (\mu_j, \Sigma_j)$, where $j = \{1, 2\}$, to represent the low and high-α sequences. Note that Rojas-Arriagada et al. (2016) argue the [α/M] vs [M/H] distribution could be described by five components, but here we are not concerned with finding sub-components of the two α-sequences.

Given a set of data $(x_1, x_2, ..., x_n)$, the likelihood function is defined as:

$$\mathcal{L}(\theta; x) = \prod_{i=1}^{n} \sum_{j=1}^{2} w_j f(x_i; \mu_j, \Sigma_j), \tag{4.6}$$

where f is the probability density function of a multi-variate normal distribution and w_j is the weight of each distribution. The algorithm initialises with random guesses for $\theta = (w_j, \mu_j, \Sigma_j)$ and iterates until the log-likelihood is at minimum. The probability that a data point x_i belongs to component j is given by:

$$P_j\,(x_i \,|\, \theta) = \frac{w_j f(x_i; \mu_j, \Sigma_j)}{w_1 f(x_i; \mu_1, \Sigma_1) + w_2 f(x_i, \mu_2, \Sigma_2)} \tag{4.7}$$

where

$$P_1(x_i) + P_2(x_i) = 1 \tag{4.8}$$

Fig. 4.8 shows projections in the [α/M]–[M/H] and the RV–[α/M] planes, where two Gaussian components centred at [α/M] = 0.05 and [α/M] = 0.2 can be seen, each with a distinctive median radial velocity. Stars are colour-coded by their thick disk probability. As expected, the high-α stars have much higher thick disk probability than the low-α stars. It is also apparent that stars with [M/H] between -0.4 and 0 are likely to be designated thin disk membership, because their radial velocities and metallicity more closely resemble that of thin disk stars. This is perhaps the most important distinction between our 'thick disk' definition and that of other studies: that the overall more α-enhanced population does not include the high metallicity, high-α population. This places important constraints on subsequent analyses and the interpretation of our results with respect to models of disk formation, as here we are assuming that the thick disk is almost exclusively old by excluding more metal-rich stars.

Furthermore, Fig 4.8 indicates that there are 'transition stars', which have higher [α/M] than thin disk stars at the same metallicity and kinematics that lie between the two disks, making it is difficult to assign them to either population. We therefore assigned thin disk membership only to stars that have thick disk probability ≤ 0.1, which have [α/M] ≤ 0.15, consistent with the location of the 'gap' between high and low α populations for our data set. The majority of stars with thick disk probability between 0.1–0.5 have [α/M] values between 0.15–0.3 dex. These 'transition' stars are omitted from the analysis to minimise contamination in each defined population. Approximately 13% of the overall sample are in the 'transition' category.

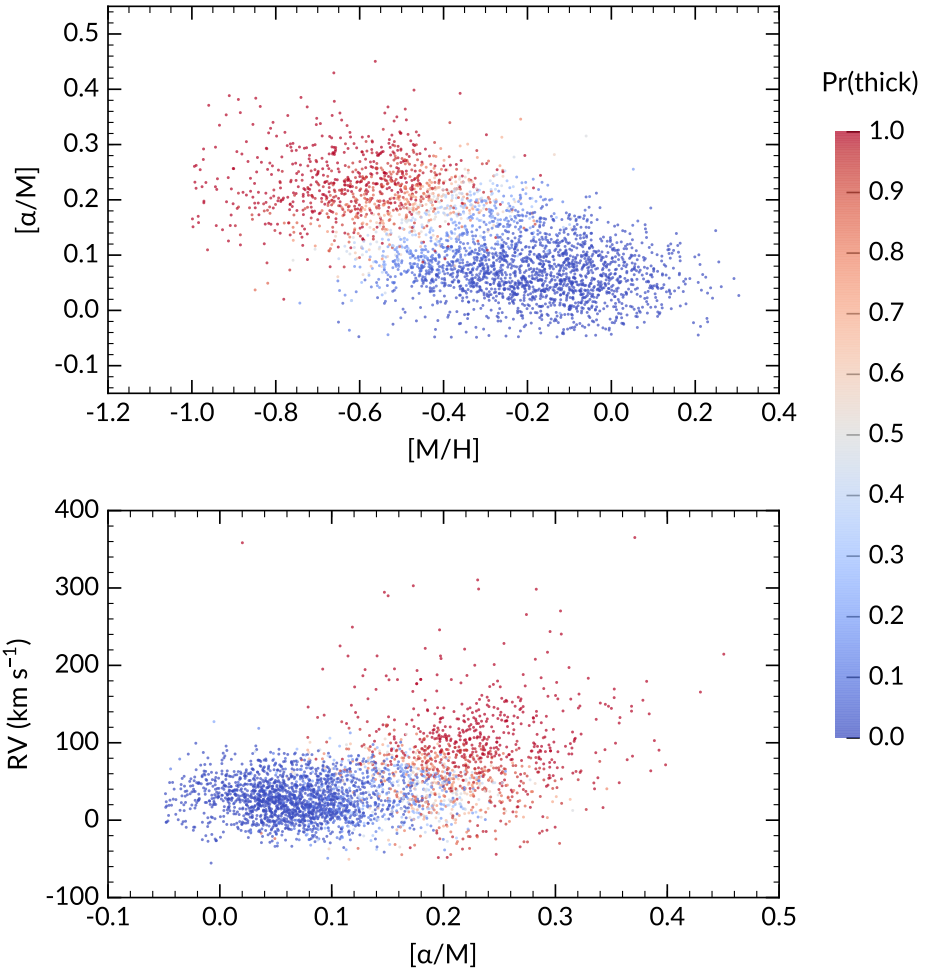

Figure 4.8 Results of the Gaussian mixture decomposition. Top panel: projection along the [α/M]–[M/H] plane. Bottom panel: projection along the [α/M]–RV plane, both colour-coded by the probability of a star belong to the thick disk. We can see that there are two well defined populations in both projections, however there are also plenty of stars that are difficult to place in either population. These stars have chemistry and kinematics that could belong to either of the classically defined 'thin' and 'thick' disk. Stars that are typically defined as thin disk by chemistry have Pr(thick) ≤ 0.1. Stars with typical thick disk chemistry however have a higher velocity dispersion and therefore a larger spread in probability, ranging from $0.6 \leq$ Pr(thick) < 1.

4.4 Selection bias

Fig. 4.1, right panel, shows that the pilot survey has a simple magnitude cut, $10 < K_s < 12$, while the main survey colour-magnitude selection appears to be a stripe in the $(J-K_s)_0$ vs K_s plane, from the criterion that $12 < V_{JK} < 14$. The main survey also observed some bright stars that fall outside the lower magnitude limit. In addition, the pilot survey purposely observed a larger fraction of stars at higher latitudes, which means that the population at low latitudes is under-represented. These selection biases affect the resulting metallicity, distance (and therefore vertical height) distributions of the observed population. In this section we aim to correct for these effects so that the underlying Galactic population can be correctly recovered.

4.4.1 Correcting for selection effects

Field selection bias

The first selection effect that we corrected was the bias from targeting particular fields. We purposely observed a larger relative fraction of stars at higher latitudes to target the thick disk, and thus biased against low latitude stars.

To correct for this, we determined for each field the number of stars present in the observed sample compared with the number of photometric targets available for that field in the GALAH input catalogue, within the same magnitude limit, e.g.:

$$w_{field} = \frac{N_{observed}\ (12 < V_{JK} < 14)}{N_{targets}\ \ (12 < V_{JK} < 14)}$$

We dealt with the magnitude ranges of the pilot and main surveys separately. The limits used are $12 < V_{JK} < 14$ for main survey fields; $12 < V_{JK} < 14.5$ for pilot fields and $9 < V_{JK} < 12$ for the bright field.

Magnitude and colour selection bias

Following Casagrande et al. (2016), we assessed the magnitude and colour selection bias by creating a synthetic population using BaSTI isochrones (Pietrinferni et al. 2004). From a data cube that spans 0.5 to 10 Gyr in age, -3 to 0.5 dex in metallicity and 10 to 10000 pc in distance, each point in the age and metallicity plane is populated on the isochrones according to the Salpeter (1955) IMF, with the distances providing apparent magnitudes for each population. We then applied the same apparent colour and magnitude cut as shown in Fig. 4.1 to obtain the ratio of stars observed with our selection function compared to the total number of stars that populate a given point in the age, metallicity and distance cube. As in the previous section, the pilot and main survey selection functions are taken into account separately. Because there is no age information available for this sample, we integrated the observed probabilities over all ages for each point in the distance–metallicity

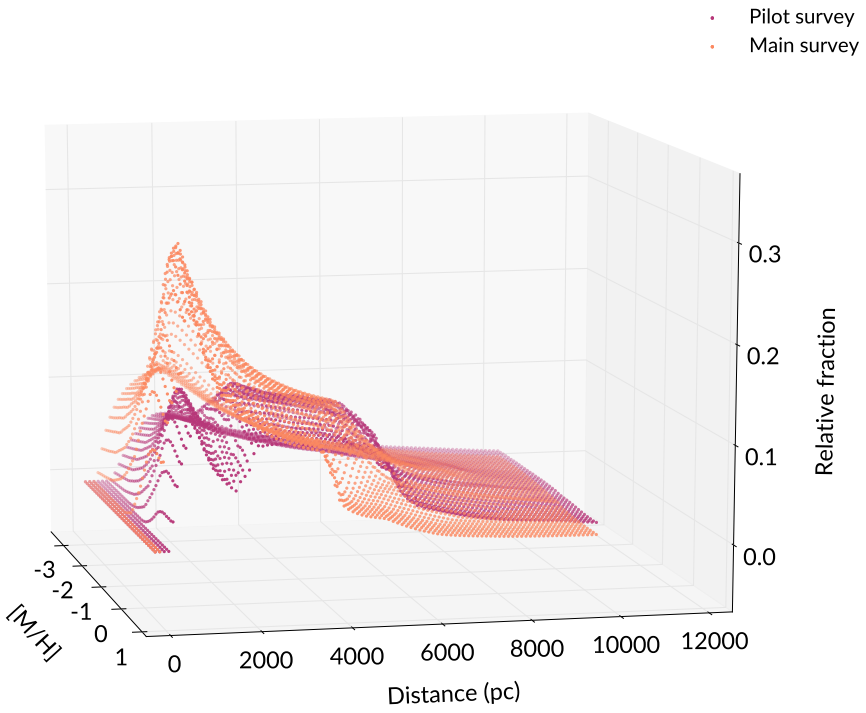

Figure 4.9 The relative probability of observing a particular star in the metallicity-distance plane given the colour-magnitude selection of GALAH pilot and main surveys. While we show the metallicity distribution up to [M/H]=−3 dex, we do not have any stars with [M/H] < -1 in our sample. The distance distribution is most affected by the colour-magnitude selection of the two surveys, with the pilot survey favouring more distant stars. The metallicity of both surveys peaks around solar, but compared to the main survey, the pilot survey has a larger fraction of stars that are more metal-poor.

plane. This implicitly assumes that the age distribution is flat in the solar neighbourhood (e.g., Edvardsson et al. 1993, Ting et al. 2015). With this method, the effects of different evolutionary time-scales of each stellar population on the HR diagram are also taken into account via the IMF.

Fig. 4.9 shows the relative fraction of stars observed after the colour-magnitude selection is applied. The most metal-poor and metal-rich stars are slightly biased against, similarly so for both the pilot and main survey selections. The distances, on the other hand, are very different for the pilot and main surveys. The main survey is biased against stars more distant than 1.5 kpc, especially at lower metallicities. The pilot survey observes relatively more distant (and thus larger $|z|$) stars as intended. In addition, the pilot survey colour and magnitude limit particularly targetted red clump stars, which primarily contributed to the second peak in its selection function.

The relative ratios obtained from this population synthesis method are dependent on the choice of stellar models and IMF, however we note that we are only using these numbers in the relative sense, to gauge the importance of one star compared to another. In this sense, we do not expect the selection effects to change qualitatively.

4.4.2 Effects of bias correction

The final weight is determined by combining the fraction from field selection bias and the isochrone population synthesis. Since the fraction indicates how likely a star is observed, the weights are computed as

$$w_{final} = \frac{1}{w_{field} \times w_{isochrone}}$$

so that stars less likely to be observed are given higher weights.

Overall, the corrections mean that more metal-poor and distant stars are weighted more heavily. Effects of the weights on the [M/H] and $|z|$ distributions are shown in Fig. 4.10.

4.4.3 Halo contamination

To assess the halo contamination in our low and high-α samples, we used the *Galaxia* code (Sharma et al. 2011), based on the *Besançon* models (Robin et al. 2003) to synthesise the stellar population within our observed region. We applied the same colour-magnitude limits (in 2MASS J, K_s photometry as shown in Fig. 4.1) for the pilot and main survey samples separately. The simulation shows that within our metallicity range ($-1 \leq$ [M/H] ≤ 0.4), the contamination of halo stars is extremely small, at 0.5% for both of the pilot and main surveys. Therefore, any effects of halo stars on our results would be negligible.

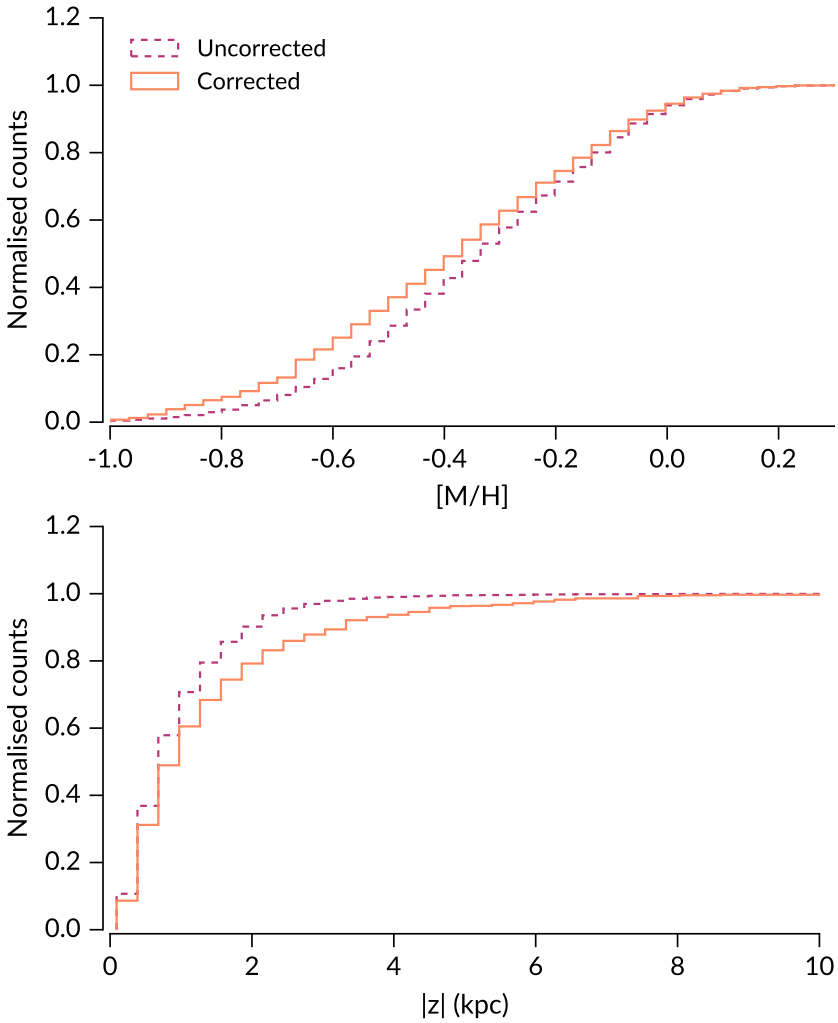

Figure 4.10 Cumulative histograms showing bias-uncorrected and corrected metallicity and height $|z|$ distributions. Top panel: [M/H] distribution. Bottom panel: height distribution. Typically the corrections account for the bias against stars that are more metal-poor and further from the plane.

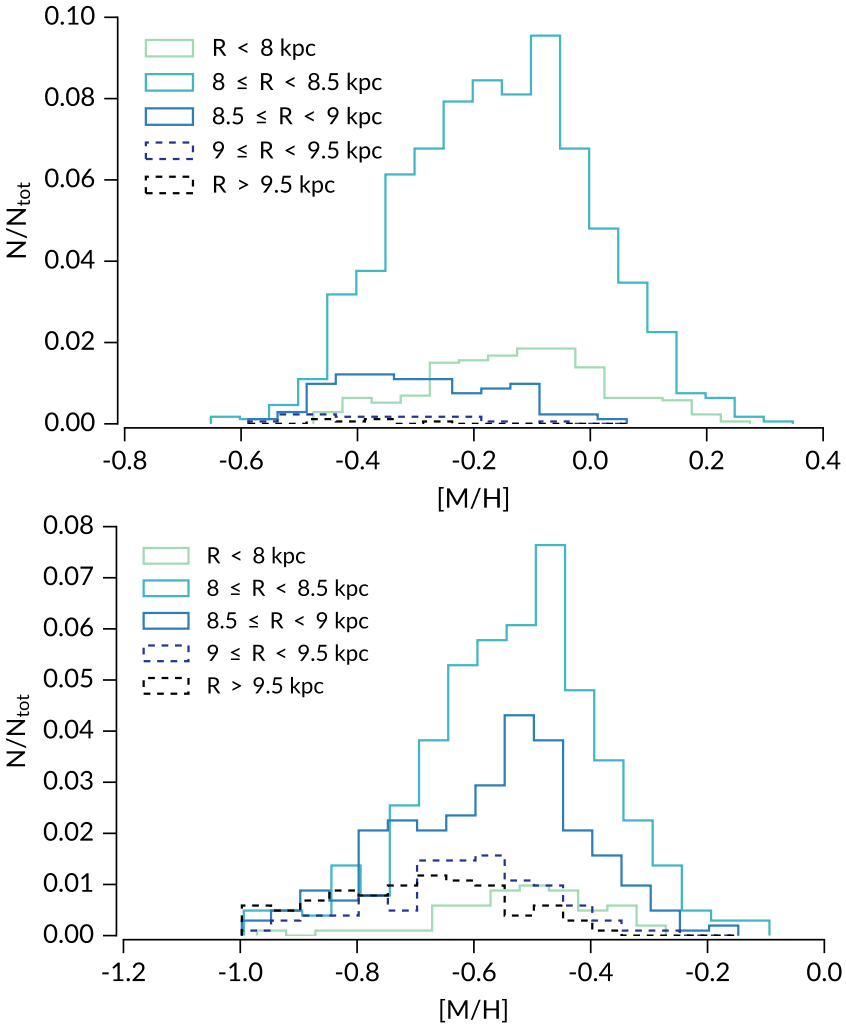

Figure 4.11 Radial distribution of the thin (low-α) and thick (high-α) disks, after correcting for selection effects. Top panel: the thin disk's mean metallicity changes rapidly as a function of radial distance. This is due to both the radial metallicity gradient observed in the thin disk, and that the average vertical height increases with increasing radial distance. Bottom panel: The thick disk, on the other hand, does not show a strong change in shape nor median value with radial distance.

4.5 Metallicity profiles

4.5.1 Radial metallicity profiles

In figure 4.11 we show the MDF of the thin and thick disks in radial distance bins of 500 pc. Within the small range that we cover, no metallicity gradient is observed for the thick disk. The MDF remains constant in shape and median value across all radial distances up to 9 kpc, which is consistent with Hayden et al. (2015). Beyond 9 kpc, we notice that the MDF skews slightly towards more metal-poor values, but we interpret this as an effect caused by observing progressively larger median $|z|$ as we move further from the Galactic centre (see Fig. 4.2) rather than the thick disk having a radial metallicity gradient.

For the low-α population, we observe only a small number of stars at radial distances

Table 4.1 The mean (and standard error), dispersion and skewness of the metallicity distributions at different radial bins for the low-α population.

Radial range kpc	Median [M/H] dex	Standard deviation dex	Skewness
$R < 8$ kpc	-0.12 ± 0.01	0.15	$+0.01 \pm 0.02$
$8 \leq R < 8.5$ kpc	-0.16 ± 0.004	0.16	-0.02 ± 0.01
$8.5 \leq R < 9$ kpc	-0.30 ± 0.01	0.13	$+0.30 \pm 0.02$
$9 \leq R < 9.5$ kpc	-0.37 ± 0.03	0.17	$+1.50 \pm 0.07$
$R > 9.5$ kpc	-0.42 ± 0.05	0.13	-0.30 ± 0.07

Table 4.2 The mean (and standard error), dispersion and skewness of the metallicity distributions at different radial bins for the high-α population.

Radial range kpc	Median [M/H] dex	Standard deviation dex	Skewness
$R < 8$ kpc	-0.52 ± 0.02	0.13	-0.79 ± 0.04
$8 \leq R < 8.5$ kpc	-0.53 ± 0.01	0.15	-0.27 ± 0.01
$8.5 \leq R < 9$ kpc	-0.57 ± 0.01	0.15	-0.26 ± 0.02
$9 \leq R < 9.5$ kpc	-0.61 ± 0.01	0.14	-0.36 ± 0.03
$R > 9.5$ kpc	-0.70 ± 0.02	0.15	-0.07 ± 0.04

further than 9 kpc. The distribution is roughly Gaussian at all locations, but skews towards metal-poor with increasing R. In Fig. 4.2, it is evident that the majority of α-poor stars (thin disk) are confined to the plane. At $R_{\rm GC} = 8.5$ kpc, most of the stars lie above $|z| = 1$ kpc, so here we are likely to be observing only the metal-poor tail of the thin disk. The shift towards lower metallicity at large R is likely due to the radial metallicity gradient of the thin disk (Cheng et al. 2012, Genovali et al. 2014, Hayden et al. 2015), and the vertical gradient discussed in the next section.

We provide the median, standard deviation and skewness of each radial bin of each population in tables 4.1 and 4.2. These support our conclusions that the MDFs of both populations within our $R_{\rm GC}$ range is close to Gaussian, and that there is little change in the median metallicity and shape of the high-α population. We caution that the statistics is more uncertain for bins $R_{\rm GC} > 9$ kpc for the low-α population due to the low number of stars, likewise for the bin $R_{\rm GC} < 8$ kpc for the high-α population.

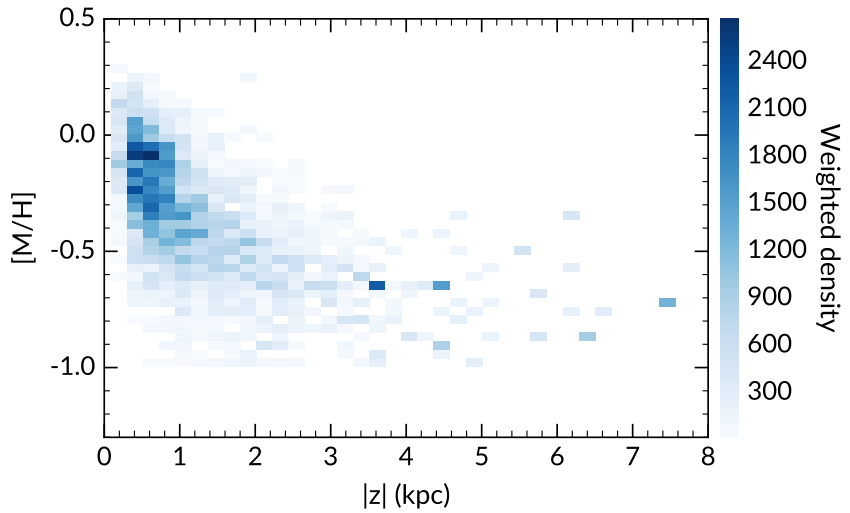

Figure 4.12 Variation of metallicity with distance from the Galactic plane for all stars independently of their alpha assignment (the 'transition' stars mentioned in Section 4.3.3 are also included). The density was weighted using bias correction fractions described in Section 4.4. The metallicity decreases smoothly with increasing height, however the gradient appears to flatten at $|z| = 2$ kpc.

4.5.2 Vertical metallicity profiles

The vertical gradients were measured using an orthogonal linear least squares regression to all data points, taking into account each data point's uncertainties in [M/H] and vertical height. Each point is then weighted by the selection bias correction described in Section 4.4. We do this by decreasing the uncertainty of each data point by the square root of the correction factor. In this section we report the gradients measured for the disk as a whole, and for each α sub-population. The gradients measured are summarised in Table 4.3.

Fig. 4.12 shows a density plot of the metallicity as a function of height above the plane for all stars, including those that were omitted from the individual α-subpopulation, as explained in Section 4.3.3. The density was weighted to correct for selection biases using relative fractions described in Section 4.4. We observe that the metallicity decreases smoothly as $|z|$ increases. The vertical gradient for the disk overall is $\mathrm{d[M/H]}/\mathrm{d}z = -0.22 \pm 0.01$ dex kpc^{-1}, and appears to flatten at larger $|z|$, from about $|z| = 2$ kpc. The gradient value is in good agreement with overall disk gradients measured by Schlesinger et al. (2014) for a sample of volume-complete SEGUE dwarfs.

For each of the sub-populations, we also found a metallicity gradient, as shown in Fig. 4.13. Over-plotted in each panel are averaged values of metallicity at different $|z|$ bins for clarity, but these binned values have no effect on the data fitting. We discuss the vertical gradients below.

The low-α population

The low-α population, or thin disk, is known to have a radial metallicity gradient d[M/H]/dR of ≈ -0.08 dex kpc^{-1}, which flattens at progressively higher $|z|$ (Cheng et al. 2012, Hayden et al. 2014). The radial metallicity gradient can be seen in the left panel of Fig. 4.11, where the median metallicity shifts to lower values at larger $R_{\rm GC}$. The small $R_{\rm GC}$ range that we cover does not allow us to reliably measure radial metallicity gradients, so we corrected for this effect by estimating the metallicity of each star at $R = 8$ kpc using radial gradients specified in Cheng et al. (2012) for height bins $0.25 < |z| < 0.5$ kpc; $0.5 < |z| < 1$ kpc and $1 < |z| < 1.5$ kpc. The data set of Cheng et al. (2012) did not extend beyond $|z| = 1.5$ kpc, so for all heights above this value, we assumed the same radial gradient as at $1 < |z| < 1.5$. Overall, the radial gradient correction caused a change of -0.01 dex kpc^{-1}in the vertical gradient. The final weighted vertical gradient of the low-α population d[M/H]/d$z = -0.18 \pm 0.01$ dex kpc^{-1}.

Studies that were conducted prior to recent large spectroscopic surveys typically reported steeper negative gradients than our value. Bartašiūtė et al. (2003) separated thin disk stars by rotational lag and measured -0.23 ± 0.04 dex kpc^{-1}. Marsakov & Borkova (2006) used both space velocities and orbital eccentricities restrictions to select thin disk stars and reported a gradient of -0.29 ± 0.06 dex kpc^{-1}. It is highly likely that separating the thin disk purely based on kinematics would result in contamination of thick disk stars, which explains why these gradients are in agreement with our overall disk gradient, but steeper than the gradient of the low-α population.

Few studies of disk vertical metallicity gradients separated the thin/thick disk using chemistry. The only recent studies that identified the thin disk by their α-abundances are Schlesinger et al. (2014) (SEGUE), Hayden et al. (2014) (APOGEE) and Mikolaitis et al. (2014) (*Gaia*-ESO). Hayden et al. (2014) found a low-α gradient of -0.21 ± 0.02 dex kpc^{-1} at the solar circle for the APOGEE DR10 sample, which is slightly steeper than our value. Hayden et al. (2014) also correct for the radial metallicity gradient, using values similar to that of Cheng et al. (2012) used here. The small discrepancy could arise from our different definitions of the thin disk, as Hayden et al. (2014) made a straight-line cut at [α/M] = 0.18. In Fig. 6 of Hayden et al. (2014), their low-α population extends to [M/H] = -2 dex while ours extends to only [M/H] = -0.6 dex. The low-α, very metal-poor stars seen in APOGEE data could belong to the halo (Nissen & Schuster 2010, Adibekyan et al. 2013), and this contamination would steepen the gradient.

Schlesinger et al. (2014) also computed a gradient for the low-α population of SEGUE dwarfs. They measured, for the disk as a whole, a vertical metallicity gradient of $-0.24^{+0.04}_{-0.05}$ dex kpc^{-1}, in agreement with our measurement. While their low-α population has a gradient consistent with zero: d[M/H]/d$z = -0.01^{+0.09}_{-0.06}$ dex kpc^{-1}, the intermediate α subpopulation with $0.2 <$[α/M]< 0.3 has d[M/H]/d$z = -0.17^{+0.08}_{-0.07}$ dex kpc^{-1}, which agrees with our low-α metallicity gradient. We thus conclude that the discrepancy between our

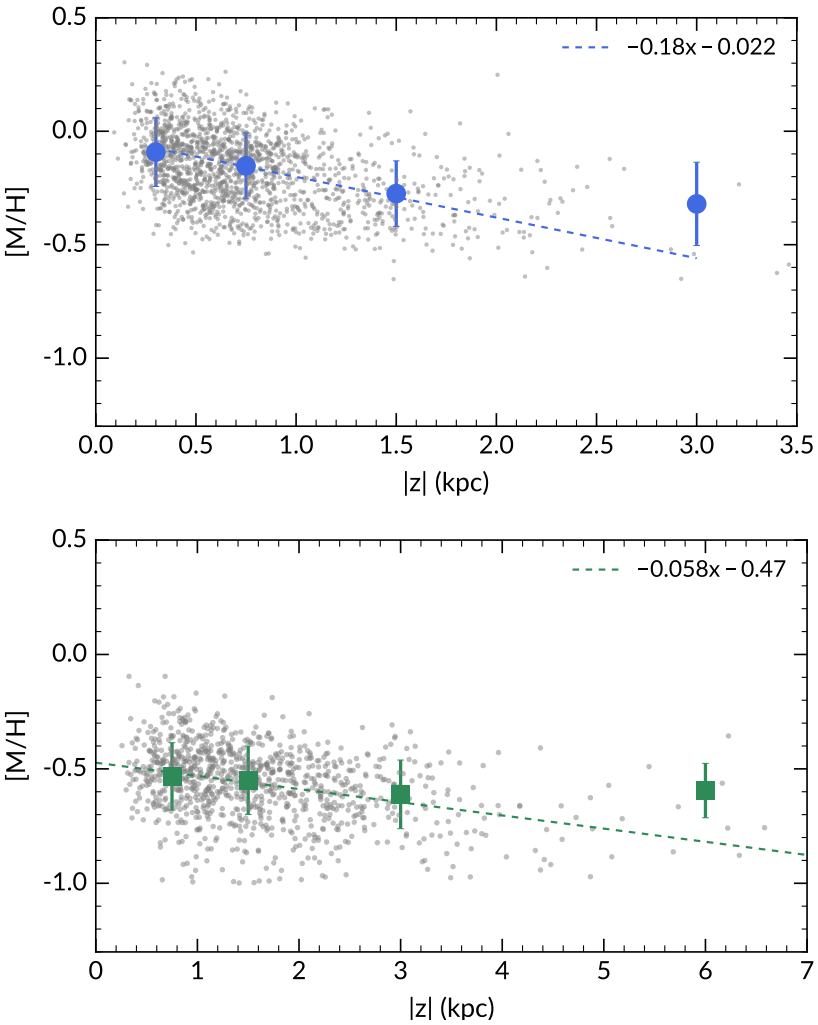

Figure 4.13 Variation of metallicity with distance from the Galactic plane for each α sub-population. Top panel: the thin disk has a steep negative gradient, which is consistent with what many authors have observed previously. Bottom panel: the thick disk has a shallower gradient. The trends are fitted over grey data points, over-plotted are averaged values of four height bins and their one sigma error bars. It is important to note that the binned values were not used in the gradient fitting.

result and that of Schlesinger et al. (2014) is largely due to the chemical separation criteria (also see Ciuca et al. 2018, who found an age-dependence for the thin disk vertically metallicity gradient, such that the youngest population has a flatter gradient).

Mikolaitis et al. (2014) measured a slightly shallower gradient of $\mathrm{d[M/H]/d}z = -0.11 \pm 0.01$ for *Gaia*-ESO dwarfs and giants. The *Gaia*-ESO sample is more metal-poor overall and Mikolaitis et al. (2014) separated thick disk stars by the location of under-densities in their [Mg I/M] histograms (their Fig. 3). The dividing line is at different values of [Mg I/M] for different metallicity regimes. In Fig. 10 of Mikolaitis et al. (2014), it is clear that their sample is biased against metal-rich stars, such that there are very few stars with [M/H]> 0 (also see Stonkutė et al. 2016).

The high-α population

The vertical metallicity distribution of the thick disk (high-α) stars, is relatively flat compared to the low-α population, at -0.058 ± 0.003 dex kpc^{-1}. Several authors have measured the vertical gradient for the thick disk, using different methods to define this population. Earlier studies, such as Gilmore et al. (1995) and Allend Prieto et al. (2006), reported no vertical metallicity gradient in the thick disk (Allend Prieto et al. 2006 quoted an upper limit of d[M/H]/dz = 0.03 dex kpc^{-1}). More recently, Boeche et al. (2014) concluded that the vertical metallicity gradient of the thick disk is consistent with zero, based on a sample of RAVE giants. However, other studies, using a combination of metallicity or kinematics to separate the thick disk have reported a shallow metallicity gradient.

Katz et al. (2011) observed sub-giants at two lines of sight: $(l, b) = (51°, 80°)$ and $(5°, 46°)$ at low resolution. Their metallicity distribution functions show signs of bimodality, and the thick disk was defined as stars centred around [M/H] ≈ -0.5 dex. The vertical gradient measured by Katz et al. (2011) is -0.068 ± 0.009 dex kpc^{-1}, consistent with our value.

Ruchti et al. (2011) observed a number of metal-poor thick disk candidates at high resolution using the MIKE, FEROS and UCLES spectrographs ($\lambda/\Delta\lambda \approx 35,000 - 45,000$). They classified their stars based on a Monte Carlo simulation of space motion U, V, W, assuming Gaussian errors on the velocities and distances. By further restricting their α-enhanced sample with thick disk kinematics to metal-poor stars only ([M/H]≤ -1.2), they avoid most thin disk contamination. The measured gradient is -0.09 ± 0.05 dex kpc^{-1}, which also agrees with our results.

Kordopatis et al. (2011) observed stars using the VLT/GIRAFFE spectrograph ($\lambda/\Delta\lambda \approx$ 6500) at almost the same Galactic longitude as the GALAH pilot survey ($\ell = 277°$), and the same latitude as our highest fields ($b = 47°$). They reported a gradient of -0.14 ± 0.05 dex kpc^{-1} for stars at heights $1 < |z| < 4$ kpc, where the thick disk is dominant, which does not agree with our result. Selecting the thick disk based only on height above the plane will certainly include thin disk contaminants and thus cause their gradient to be steeper.

Chen et al. (2011) selected a sample of SDSS stars at $1 < |z| < 3$ kpc to represent the thick disk and measured a vertical gradient of -0.22 ± 0.07 dex kpc^{-1}. From the separation by chemistry shown in this paper and elsewhere, thin disk stars exist at $|z|$ up to at least 2 kpc, so a thick disk definition based on vertical height alone is not very accurate. Chen et al. (2011) provides another estimate of -0.12 ± 0.01 dex kpc^{-1} for the gradient after they have modelled and subtracted thin disk contaminants using the Besançon model, which is closer to our value. However, neither of these thick disk vertical metallicity gradients is in agreement with our value.

Comparing our measurement of the vertical gradient for the high-α population with the gradient from the APOGEE DR10 (Hayden et al. 2014) reveals a large discrepancy, as they found a steep negative gradient of -0.26 ± 0.02 dex kpc^{-1} at the solar circle. However, APOGEE DR10 suffered from systematic errors in the alpha abundance determinations,

particularly for cooler stars. This may have caused errors in their measured abundance gradients, and thus the discrepancy between our results (M. R. Hayden, private communication). The gradient measured for the same stars using APOGEE DR13 is -0.09 ± 0.01 dex kpc^{-1}which, although not in agreement with our result, is much more similar (M. R. Hayden, private communication). Gradients measured for APOGEE stars are restricted to $|z| \leq 2$ kpc, which could explain why their measurement is steeper than ours, as we see that the vertical metallicity gradient flattens at larger heights.

4.5.3 The effects of excluding 'transition' stars

As mentioned in Section 4.3.3, we omitted all stars that lie between the low and high-α populations in terms of abundances and radial velocities so to minimise possible contaminations. In a purely chemical separation, however, they would contribute to the vertical gradients. We explored the effects of excluding them by separating the two populations by [α/M] only, making a cut at [α/M] = 0.15, where the 'gap' is located and repeated our analysis of the gradients. As expected, the vertical metallicity gradients for both sub-populations steepened compared to our probability-based thin/thick disk separation using the [M/H]–[α/M]–RV distribution described in Section 4.3.3. The low-α population changes to $\mathrm{d[M/H]}/\mathrm{d}z = -0.21 \pm 0.01$, and the high-$\alpha$ population to $\mathrm{d[M/H]}/\mathrm{d}z = -0.11 \pm 0.004$. For the high-$\alpha$ population, we would then be in better agreement with APOGEE DR13 and Kordopatis et al. (2011).

4.6 [α/M] profiles

Within the 1.5 kpc R_{GC} range of our sample, we do not observe any significant radial changes in [α/M] for either of the defined populations. Studies of the high-α population's radial abundance gradients show that there is no variation, but there may be small positive radial [α/M] gradients in the low-α population (e.g., Mikolaitis et al. 2014, Bergemann et al. 2014). Genovali et al. (2015), however, found a negative radial abundance gradient for the α-element Ca. Boeche et al. (2014) also found modest radial gradients for the α-elements. The fact that we do not observe a radial abundance gradient in the low-α population is likely due to our limited radial coverage, which prevents us from assessing [α/M] variation with R_{GC}.

The vertical α-abundance profile of the entire sample is shown in Fig. 4.14, presented as a density plot similar to Fig. 4.12. The median [α/M] increases as a function of height, as noted previously by Schlesinger et al. (2014) and Mikolaitis et al. (2014). However, unlike the metallicity, we find that the α-abundance profile does not vary smoothly with $|z|$. The α-abundance vertical gradient for the entire disk is $\mathrm{d[\alpha/M]}/\mathrm{d}z = 0.038 \pm 0.001$ dex kpc^{-1}. For the low and high-α populations, the [α/M] vertical gradients are both slightly positive, as shown in Fig. 4.15. The gradients are $\mathrm{d[\alpha/M]}/\mathrm{d}z = 0.008 \pm 0.002$ dex kpc^{-1} for the low-α, and $\mathrm{d[\alpha/M]}/\mathrm{d}z = 0.007 \pm 0.002$ dex kpc^{-1} for the high-α population. As in Section

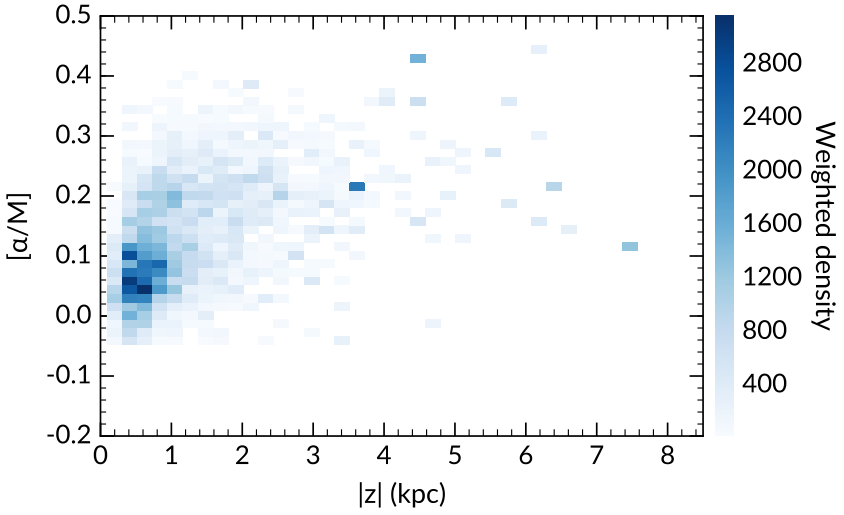

Figure 4.14 Variation of [α/M] with distance from the Galactic plane for all stars. The density is weighted by selection bias fractions as described in Section 4.4. The over densities at high $|z|$ are due to a few data points with large weights. Unlike metallicity, [α/M] does not vary smoothly with increasing height. There appears to be a break in the distribution at $|z| \approx 1$ kpc.

4.5.3 above, we also analysed the two α populations with the 'transition stars' included. This did not change the slope measured for the low-α population, but increased the slope of the high-α population to $\mathrm{d}[\alpha/\mathrm{M}]/\mathrm{d}z = 0.014 \pm 0.001$ dex kpc^{-1}, which is higher than the value measured without transition stars. The transition stars contribute primarily at low $|z|$ (≤ 1 kpc), which is why their addition affected the high-α population more: as defined in Section 4.3.3, this population is mainly located at $|z| \geq 1$ kpc.

For the high-α population, Ruchti et al. (2011) showed that individual α-abundances [Mg/Fe] and [Si/Fe] have vertical gradients 0.03 ± 0.02 and 0.02 ± 0.01 dex kpc^{-1}, respectively. Meanwhile, the vertical abundance gradients of [Ca/Fe] and [Ti I,II/Fe] decrease to -0.01 ± 0.01 and -0.02 ± 0.02 dex kpc^{-1}. While we do not have α-enhanced stars with [M/H] < -1 as in their study, this result is in agreement with the flat gradients we observe. Mikolaitis et al. (2014) also provide vertical gradients for the averaged [α/M] abundances, as well as vertical gradients for individual α-elements using *Gaia*-ESO iDR1. They found similar vertical abundance profiles for the low and high-α stars. Both populations have averaged and individual vertical α-abundance gradients of 0.04–0.05 dex kpc^{-1}, with errors < 0.01 dex kpc^{-1}. These values are not in agreement with our measured vertical gradient for the α sub-populations, as we find that both populations have rather flat abundance distributions as a function of height. However, these results are similar to the gradient we derived for the disk overall. The differences could have arisen from the lack of correction for selection biases in Mikolaitis et al. (2014) and the different abundance scales of the *Gaia*-ESO and GALAH surveys. The [Mg/Fe] histograms shown in Fig. 3 of Mikolaitis et al. (2014) shows that *Gaia*-ESO iDR1 has a larger spread in their abundances compared to GALAH (c.f. Fig 4.5).

An important point to consider is the dependence of [α/M] on [M/H], and the correlation of the latter with respect to vertical height $|z|$. At greater heights above the plane, observed stellar populations become more metal-poor (Fig 4.12), and these stars are typically more α-enhanced. The positive α-gradient over the entire disk is therefore reflective of the fact that more metal-poor, high-α stars become dominant at large heights. For each of the α sub-populations as defined in Fig 4.8, however, the correlation between [α/M] and [M/H] is rather flat, which means that the small positive gradients we measured are intrinsic to these sub-populations.

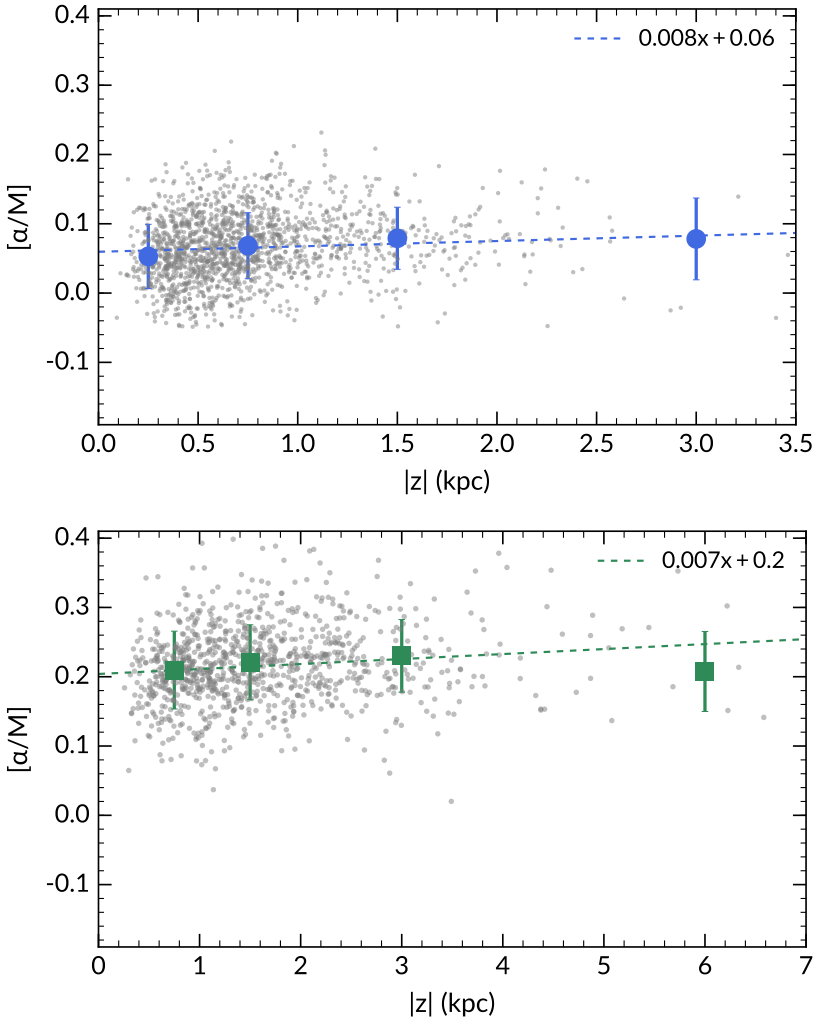

Figure 4.15 Variation of [α/M] with distance from the Galactic plane for each of the high and low-α population. Top panel: vertical abundance gradient for the low-α stars. Bottom panel: vertical abundance gradient of the high-α stars. Both populations show a flat-positive trend. The high-α population shows a higher dispersion in [α/M] values. The trends are fitted over grey data points, over-plotted are averaged values of four height bins and their one sigma error bars. Note that the binned values were not used in the gradient fitting.

Table 4.3 Summary of measured vertical gradients, and intercepts at $|z| = 0$ for disk metallicity and α-abundances.

Population	d[M/H]/dz dex kpc^{-1}	$\sigma_{\mathrm{d[M/H]/d}z}$	$[\mathrm{M/H}]_{(z=0)}$ dex	$\sigma_{[\mathrm{M/H}](z=0)}$	d[α/M]/dz dex kpc^{-1}	$\sigma_{\mathrm{d}[\alpha/\mathrm{M}]/\mathrm{d}z}$	$[\alpha/\mathrm{M}]_{(z=0)}$ dex	$\sigma_{[\alpha/\mathrm{M}](z=0)}$
low-α	−0.18	0.01	−0.02	0.01	+0.008	0.002	0.06	0.002
high-α	−0.058	0.003	−0.47	0.01	+0.007	0.002	0.20	0.003
All stars	−0.22	0.01	−0.08	0.01	+0.038	0.001	0.08	0.002

4.7 Discussion

The process(es) that created the thick disk have been a central point of discussion in Galactic studies. The very definition of the thick disk has changed since first proposed by Gilmore & Reid (1983), and here we refer to the 'thick disk' as the overall more α-enhanced population as defined in Section 4.3.3 using both chemical and kinematical information. In Section 4.1, we outlined the main scenarios that have been proposed for thick disk formation, and in this section we interpret our results in the context of these scenarios.

In summary, the vertical metallicity and abundance profiles of the disk show that:

(1) The disk overall has a steep negative vertical metallicity gradient.

(2) The low-α population has a similar vertical metallicity gradient to the full disk.

(3) The high-α population, on the other, has a much flatter vertical metallicity gradient.

(4) The α-abundance ratio increases with height in general. At larger heights only the high-α population is present.

(5) Neither the high nor low-α sub-population show a significant vertical alpha abundance ratio gradient.

The vertical metallicity gradient in the high-α population is in contrast with predictions of the direct satellite accretion scenario proposed by Abadi et al. (2003) and the fast internal evolution model of Bournaud et al. (2009). While both of these scenarios could result in a chemically distinct thick disk, they also predict a uniform vertical metallicity distribution, or a lack of vertical metallicity gradient. Brook et al. (2004, 2005) proposed that the thick disk formed via merging of gas-rich clumps at high redshift, prior to the formation of the thin disk. Their model predicts an old, α-enhanced thick disk that matches observations. However, their thick disk also shows no vertical metallicity gradient, in contrast to our results.

The heating of an existing disk by small satellite mergers can create a thick-disk like vertical structure (e.g., Quinn & Goodman 1986, Quinn et al. 1993, Kazantzidis et al. 2008, Villalobos & Helmi 2008). The vertical metallicity gradient of the existing disk could be preserved in the thick disk, however this can also be affected by the interplay between radial migration and radial metallicity gradients (e.g., Kawata et al. 2018). Bekki & Tsujimoto (2011) modelled the kinematics and chemistry of stars formed by minor mergers in detail, and showed that a fast star formation rate in the thick disk results in α-enhanced stars. The steep vertical metallicity gradient of the pre-existing disk flattens over time, but qualitatively it is steeper in the inner Galaxy, consistent with the observations of Hayden et al. (2014). However, the final thick disk gradient is essentially flat at the solar circle, which is not what we observe. Furthermore, disk flaring is expected in such a heating scenario. For the high-α stars, Bovy et al. (2016) did not observe any flaring in their mono-abundance populations (MAPs). However, Minchev et al. (2015, 2016) argued that mono-age populations always flare in their cosmological simulations, and MAPs (mono-abundance populations) are not

necessarily co-eval. Based on APOGEE abundances and calibrated ages[6], Mackereth et al. (2017) found that mono-age α-enhanced populations do show some flaring, albeit with a smaller amplitude compared to the low-α population. Further observational and model constraints from stellar ages and flaring of the high-α stars are thus needed to understand the importance of minor mergers in thick disk formation.

The secular radial migration (Sellwood & Binney 2002) process was proposed by Schönrich & Binney (2009) as the sole explanation for the thick disk (but this remains controversial, see e.g., Minchev & Famaey 2010, Vera-Ciro et al. 2014). Stars in the inner galaxy are formed fast and migrated outwards to create the α-enhanced population at large scale heights. Since radial migration is more likely to affect older stars, a negative vertical metallicity gradient, and a positive [α/M] gradient are expected. Schönrich & McMillan (2017) obtain $\mathrm{d[M/H]/d}z \approx -0.2\,\mathrm{dex\,kpc^{-1}}$ for the full nearby disk in their analytical model (which included inside-out disk formation), in agreement with our observations. Loebman et al. (2011) also reported a similar vertical gradient of $\approx$−0.18 dex kpc^{-1} in their N-body simulation with extensive radial migration. Both of these values are consistent with our measurements of the full disk and low-α population, even though Loebman et al. (2011) did not calibrate their model to reproduce the Milky Way.

Radial migration signatures are observed in the metallicity distribution function (MDF) of disk stars at different Galactocentric radii. Hayden et al. (2015) observed that at small heights above the plane, the skewness of MDFs changes from negative in the outer galaxy (skewed towards metal-poor stars) to positive (skewed towards metal rich stars) in the inner galaxy. In contrast, the high-α population's MDF remain constant at all locations. Loebman et al. (2016) showed that these observations can be qualitatively explained by radial migration in their simulation. The change in skewness of the disk MDFs at different radii could be due to an increased fraction of migrated stars beyond $\approx$5 kpc, such that more metal rich stars are migrated to larger R_{GC}. As the high-α stars formed within a small region and a few Gyrs in a well mixed environment, their chemical content are similar and thus the MDF remains constant at all Galactic locations. Loebman et al. (2016) found a small vertical metallicity gradient in their simulated high-α population of $\approx$−0.03 dex kpc^{-1}. This is half the value observed in our study. Further investigation of the vertical metallicity and abundance gradients for the high-α stars in radial migration models will help to determine the extent to which it affects this population.

Bird et al. (2013) was able to produce a Milky Way-like galaxy with an old, vertically extended population much like the Galactic thick disk using the "Eris" cosmological simulation suite. The effects of the active merger phase at early times (redshift > 3), secular heating, and radial migration on the present-day galaxy were examined. They found that stars born during the merger phase have larger scale heights and shorter scale lengths, and younger populations form progressive thinner and longer structures. This gradual transit-

[6]Ages from Martig et al. (2016a), calibrated on APOGEE DR12 C and N abundance ratios.

ion from a kinematically hot and thick disk to a colder, thinner disk was dubbed 'upside down' formation (see also Samland & Gerhard 2003). Interestingly, secular heating and radial migration did not have a large impact on the final properties of each coeval population. Rather, the trends are established at formation, suggesting that the thick disk-like component was born thick. Similarly, Stinson et al. (2013) and Brook et al. (2012) concluded that their α-enhanced, older populations were born kinematically hot, and that the early disk settles into a thin component. The settling process of the galaxies and fast formation of the old, α-enhanced and vertically extended populations in these simulations could produce the vertical metallicity and abundance profiles observed in this work. It was shown by Wisnioski et al. (2015) that the observed velocity dispersion of Hα gas in galaxies at high redshift decreases with time, providing further indication that disk galaxies were born thick at redshifts of $z = 1 - 2$.

While the cosmological models mentioned above heavily rely on the condition that disk galaxies like the Milky Way had a quiescent merger history, there is observational evidence that this may be true for the Galaxy (Ruchti et al. 2015, Casagrande et al. 2016). However, the metallicity and α-abundance gradients in these simulations have not been studied in detail.

Although we observe an overall continuity in the vertical metallicity profile, we see two distinct α-enhancement tracks as a function of $|z|$, which have implications for the star formation history of the disk. Haywood et al. (2013, 2016) proposed two different star formation epochs for the high and low-α stars. By comparing their chemical evolution model (Snaith et al. 2015) with APOGEE data, Haywood et al. (2016) proposed that the star formation rate dropped significantly at ages of 10 Gyr before increasing again at about 7 Gyr to a lower maximum value. This could indicate the transition between thick to thin disk formation. However, the authors note that due to the strict continuity of the stellar abundances, the gas supply must not have decreased during this period of time. Similarly, Brook et al. (2012) found that the star formation rate decreased slightly at around 7 Gyr, near the epoch of thin disk formation in their simulation. This idea was also explored by the two-infall model proposed by Chiappini et al. (1997), who argued for a decreased star formation rate between the epochs of halo-thick disk and thin disk formation, and proposed a shorter formation timescale for the halo/thick disk of 1 Gyr. Future work that incorporate stellar ages (e.g., from the GALAH/K2 overlap) will be able to rigorously test these scenarios and provide additional constraints on the formation time-scale of the thick disk.

4.8 Conclusion

We have determined the vertical profiles of metallicity and α-abundances in the Galactic disk using data from the GALAH first internal data release. We analysed in total 3191 giants from the GALAH pilot and main surveys, extending up to 4 kpc in height above the plane, within a small range of Galactocentric distance ($7.9 \lesssim R_{\rm GC} \lesssim 9.5$ kpc). The precise metallicity and abundance measurements of GALAH allow us to reliably define 'thick' and 'thin' disk populations using chemistry and radial velocities. The GALAH magnitude limits in the estimated V-band translate to a dependency in $(J-K)$ colour and magnitudes. We corrected for the selection effects for targets from the pilot and main surveys separately by population synthesis using BaSTI isochrones.

The vertical metallicity gradient of the entire disk is -0.22 ± 0.01 dex kpc^{-1}, which is in agreement with recent estimates from large spectroscopic surveys such as SEGUE and APOGEE. The low-α population, or the thin disk, also exhibits a steep negative vertical metallicity gradient d[M/H]/d$z = -0.18 \pm 0.01$ dex kpc^{-1}. The more enhanced α population, which we identify as the thick disk, is found to have a shallower vertical gradient d[M/H]/dz of -0.058 ± 0.003 dex kpc^{-1}. We note again that our data do not probe the metal-poor extension of the thick disk, however, the vertical gradients observed here are similar in amplitude to those of previous studies. Overall, our results confirm some conclusions reached by earlier studies, despite differences in target selection, spatial coverage and abundance scales. The discrepancies were likely caused by uncorrected selection effects in some cases, and the many different definitions in the literature of high-α, or thick disk stars.

As expected, [α/M] increases as a function of $|z|$, with the low-α population occupying lower heights on average. The vertical [α/M] profile at the solar circle shows that there are two over-densities, with the discontinuity most clearly seen around $|z| = 1$ kpc. We find that the both low and high-α sub-populations have a flat vertical [α/M] gradient. Similarly, Ruchti et al. (2011) also found flat vertical gradients for individual α-abundances at the metal-poor end of the α-enhanced population. For the low-α population the gradient can be explained by radial migration playing an important role in the evolution of the thin disk. The negative vertical metallicity gradient of the high-α population indicates that formation scenarios which produce uniform 'thick disk' vertical metallicity gradients are not responsible for its formation. The vertical [M/H] gradient observed in this work and elsewhere could have arisen from a settling phase of the disk as suggested by Samland & Gerhard (2003) and Bird et al. (2013), minor heating episodes such as in the models of Kazantzidis et al. (2008), Villalobos & Helmi (2008), or caused by radial migration (Schönrich & Binney 2009, Loebman et al. 2011). Mergers cause flaring of the disk, which is seen in the low-α population in the analysis of Bovy et al. (2016), but not in the high-α population. However, Mackereth et al. (2017) have since shown that coeval high-α populations do indeed show flaring, but much less than the low-α stars. On the other hand, the α-abundances of both sub-populations are distinct and nearly constant at all heights, indicating that they are formed in very

different conditions.

Accurate distances and proper motion from *Gaia* DR2 will allow for an even more accurate and detailed analysis of the chemistry and kinematics of the high-α population, not only for the GALAH pilot survey but also the larger GALAH main sample. This will give us a clearer and more definitive picture of the formation and evolution of the Milky Way thick disk.

Acknowledgements. We thank Michael R. Hayden for helpful discussions regarding APOGEE results, and the anonymous referee for comments that improved the clarity of this manuscript. LD and MA acknowledge funding from the Australian Government through ARC Laureate Fellowship FL110100012. LD, KCF and RFGW acknowledge support from ARC grant DP160103747. LC gratefully acknowledges support from the Australian Research Council (grants DP150100250, FT160100402). DMN was supported by the Allan C. and Dorothy H. Davis Fellowship. DS is the recipient of an Australian Research Council Future Fellowship (project number FT1400147). TZ acknowledges financial support from the Slovenian Research Agency (research core funding No. P1-0188). Part of this research was supported by the Munich Institute for Astro- and Particle Physics (MIAPP) of the DFG cluster of excellence "Origin and Structure of the Universe". This publication makes use of data products from the Two Micron All Sky Survey, which is a joint project of the University of Massachusetts and the Infrared Processing and Analysis Center/California Institute of Technology, funded by the National Aeronautics and Space Administration and the National Science Foundation; and data products from the Wide-field Infrared Survey Explorer, which is a joint project of the University of California, Los Angeles, and the Jet Propulsion Laboratory/California Institute of Technology, funded by the National Aeronautics and Space Administration.

I have loved the stars too truly to be fearful of the night.

Sarah Williams

5

Metallicity and alpha enhancement along the Galactic bulge minor axis

This chapter is a modified version of the paper 'HERBS I: Metallicity and alpha-enhancement along the Galactic bulge minor axis' by Duong, L., Asplund, M., Nataf, D. M., et al., 2018, submitted to Monthly Notices of the Astronomical Society.

To better understand the origin and evolution of the Milky Way bulge, we have conducted a survey of bulge red giant branch and clump stars using HERMES on the Anglo-Australian Telescope. We targeted ARGOS survey stars with pre-determined bulge memberships, covering the full metallicity distribution function. The spectra have signal-to-noise ratios comparable to, and were analysed using the same methods as the GALAH survey. In this work we present the survey design, stellar parameters, distribution of metallicity and alpha-element abundances along the minor bulge axis at latitudes $b = -10°, -7.5°$ and $-5°$. Our analysis of ARGOS stars indicates that the centroids of ARGOS metallicity components should be located $\approx$0.09 dex closer together. The vertical distribution of α-element abundances is consistent with the varying contributions of the different metallicity components. Closer to the plane, alpha abundance ratios are lower as the metal-rich population dominates. At higher latitudes, the alpha abundance ratios increase as the number of metal-poor stars increases. However, we find that the trend of alpha-enrichment with respect to metallicity is independent of latitude. Comparison of our results with those of GALAH DR2 revealed that for [Fe/H] $\gtrsim -0.8$, the bulge shares the same abundance trend as the high-α disk population. However, the metal-poor bulge population ([Fe/H] $\lesssim -0.8$) show enhanced alpha abundance ratios compared to the disk/halo. These observations point to a fairly rapid chemical evolution in the bulge, and that the metal-poor bulge population does not share the same similarity with the disk as the more metal-rich populations.

5.1 Introduction

Despite its prominent role in the formation and evolution of the Galaxy, the bulge is perhaps the least understood stellar population. The bulge is host to a great diversity of stars, with up to five peaks in its metallicity distribution function (Ness et al. 2013a, Bensby et al. 2017), including some of the oldest stars in the Galaxy (see e.g., Howes et al. 2015; and Nataf 2016, Barbuy et al. 2018 for a review). It is also a major Galactic component, comprising 30% of the Milky Way's total mass (Portail et al. 2015, Bland-Hawthorn & Gerhard 2016). Studies of the bulge are therefore essential for understanding the formation and evolution of the Milky Way, and by inference, other spiral galaxies.

Galaxy bulges are typically referred to either as a 'classical' or 'pseudo'-bulge (Kormendy & Kennicutt 2004). Classical bulges are thought to have formed via rapid dissipative collapse consistent with λCDM cosmological predictions (White & Rees 1978, Tumlinson 2010, Rahimi et al. 2010). The properties of classical bulges largely mirror that of elliptical galaxies: they consist of old stars with random stellar motions. On the other hand, pseudobulges, formed via secular evolution are flatter in shape, contain younger stars and show evidence of cylindrical rotation (Kormendy & Kennicutt 2004). While most nearby galaxies appear to have a pseudobulge, some contain both types of bulges (Fisher & Drory 2011, Erwin et al. 2015). The traditional view of the Galactic bulge is that it is exclusively old (>10 Gyr), based on the observed colour-magnitude diagram in multiple fields (e.g., Zoccali et al. 2003, Clarkson et al. 2008). Using *Hubble Space Telescope* photometry, Clarkson et al. (2011) and Bernard et al. (2018) estimated the young stellar population (<5 Gyr) in the bulge to be <3.4% and 11%, respectively[1]. Early detailed abundance studies of the bulge corroborated this view: bulge giants are typically overabundant in α-elements such as O, Si and Ti, but especially so in Mg (e.g., McWilliam & Rich 1994, Zoccali et al. 2006, Lecureur et al. 2007). Fulbright et al. (2007) suggested that the abundances of bulge stars plateau at [Mg/Fe] = 0.3 dex even at super-solar metallicity, and the bulge has a separate chemical enrichment to the disk in the solar neighbourhood. Furthermore, multiple authors found a vertical metallicity gradient in the bulge (Minniti et al. 1995, Zoccali et al. 2008). Together these results were interpreted as signatures of a classical bulge population, formed early and rapidly via mergers or dissipational collapse prior to the formation of the disk (e.g., Matteucci & Brocato 1990).

[1]Despite the overall small fraction of young stars in the bulge, Bernard et al. (2018) found a significant fraction (30-40%) of super-solar metallicity stars to be younger than 5 Gyr. Bensby et al. (2013) and Haywood et al. (2016) also discussed the possibility of young stars masquerading as an old turn off in colour-magnitude diagrams due to a lack of metallicity information in photometric studies.

The discovery of a significant fraction of young (<5 Gyr), relatively metal-rich ([Fe/H] > -0.4) microlensed bulge turn-off and subgiant stars thus came as a surprise (Bensby et al. 2013, 2017)[2]. The presence of such stars would be inconsistent with the classical scenario and instead point to disk-instabilities channelling stars from the disk into the bulge (e.g., Athanassoula 2005, Martinez-Valpuesta & Gerhard 2013, Di Matteo et al. 2014, Fragkoudi et al. 2018). Abundance studies now suggest that the Milky Way bulge and thick disk share strong chemical similarities. Meléndez et al. (2008) found that the α-abundance trends in the bulge follow that of the local thick disk. Alves-Brito et al. (2010) reached the same conclusion from their re-analysis of Fulbright et al. (2007); as have many recent studies (Gonzalez et al. 2011, Johnson et al. 2014, Ryde et al. 2016, Bensby et al. 2017). However, Bensby et al. (2017) observed that their microlensed bulge stars lie in the upper envelope of the thick disk, implying that the bulge may have experienced a faster chemical enrichment than typical thick disk stars in the solar neighbourhood. An increasing number of kinematic studies show that the bulge rotates cylindrically (Kunder et al. 2012, Ness et al. 2013b, Zoccali et al. 2014, Ness et al. 2016b, Molaeinezhad et al. 2016), which is also evidence against a primarily classical bulge population. Furthermore, infra-red imaging reveal that the bulge is 'boxy', or X-shaped (Dwek et al. 1995, Ness & Lang 2016), and the split red clump observed in photometric studies is often attributed to this X-structure (McWilliam & Zoccali 2010, Wegg & Gerhard 2013, Nataf et al. 2015, Gonzalez et al. 2015a, Zasowski et al. 2016, Ciambur et al. 2017)[3]. The most recent observational evidence thus point to a primarily pseudobulge population in the Milky Way.

The metallicity distribution function (MDF) of the bulge has proven to be complex, that there is not yet a consensus on the metallicity range (see Barbuy et al. 2018 for a review). Many studies have shown that it is composed of multiple components (e.g., Babusiaux et al. 2010, Hill et al. 2011, Ness et al. 2013a, Zoccali et al. 2017, Rojas-Arriagada et al. 2017, García Pérez et al. 2018). In particular, Ness et al. (2013a) showed that there are up to five components based on ≈14 000 bulge red-giant stars. They associated stars with [Fe/H] ≈ -0.5 with the inner thick disk, while the more metal-rich populations with mean [Fe/H] = -0.2 and $+0.2$ differ in their kinematics such that stars with the highest metallicity are more prominent near the plane. Ness et al. (2013a) concluded that these metal-rich populations originated in different parts of the early thin disk due to bar-induced disk instabilities. The strength of each MDF component vary with latitude, manifesting as the vertical metallicity gradient seen in earlier studies. Thus, the vertical metallicity gradient cannot be interpreted as a signature of merger or dissipative collapse bulge formation (Zoccali et al. 2008, Babusi-

[2]Barbuy et al. (2018) argued that due to large uncertainties in the distances of microlensed dwarfs, at least some of these young stars are not part of the bulge, but foreground disk stars.

[3]See Lee et al. (2015), Joo et al. (2017) for a different interpretation of the double red clump in relation to the X-shaped morphology of the Galactic bulge. In addition, López-Corredoira (2016, 2017) observed an absence of the X-structure in the young, main sequence bulge population and Mira variables.

aux et al. 2010, Ness et al. 2013a, Rojas-Arriagada et al. 2017). In agreement with Ness et al. (2013a), Bensby et al. (2017) found five peaks in their MDF for a much smaller sample of microlensed bulge dwarfs and subgiants, four of which matched the ARGOS MDF peaks. The sample age distribution of microlensed bulge stars also shows multiple peaks that could be interpreted as star formation episodes in the bulge. Bensby et al. (2017) suggested that the peaks at 11 and 8 Gyr could be the onset of the thick and thin disks; and at 6 and 3 Gyr could be associated with the younger parts of the thin disk/Galactic bar.

It is possible that a classical bulge component exists in the Milky Way despite mounting evidence for a predominantly pseudobulge population. Studies have shown that fields at latitudes $|b|$ >5 have a combination of X-shaped and classical bulge orbits (Ness et al. 2012, Uttenthaler et al. 2012, Pietrukowicz et al. 2015). In addition, the most metal-poor bulge RR Lyrae stars do not show characteristics of the boxy bulge, such as cylindrical rotation (Dékány et al. 2013, Kunder et al. 2016). Spatial and kinematic results from the GIBS survey (Zoccali et al. 2017) indicate that the metal-poor population of the bulge is centrally concentrated and rotates more slowly than the metal-rich population, although the authors do not argue strongly for a classical component. If such a component did exist, disentangling it from those originated in the disk may be very challenging (Saha 2015). Schiavon et al. (2017) have shown that chemical abundances can serve as a powerful diagnostic for identifying sub-populations in the bulge, having found possible evidence of a dissolved globular clusters using APOGEE abundances.

Studies of the bulge have previously been hindered by high extinction in the bulge region, and the faintness of bulge stars. The sample sizes are typically small if observed at high resolving power (e.g., Johnson et al. 2014, Jönsson et al. 2017, Bensby et al. 2017). While alpha abundance trends are well established for bulge stars with results from the GIBS, *Gaia*-ESO and APOGEE surveys (Gonzalez et al. 2015b, Rojas-Arriagada et al. 2017, Schultheis et al. 2017), information on other elements, especially the neutron-capture elements, are still scarce (Johnson et al. 2012, Van der Swaelmen et al. 2016). In this paper, we present the HERMES Bulge Survey (HERBS), which was designed to be in synergy with the GALAH survey (De Silva et al. 2015). Here we aim to provide a large chemical inventory for stars in the bulge by leveraging the wavelength coverage of the HERMES spectrograph, which allows us to obtain chemical abundances for up to 28 elements, including the light, alpha, iron-peak and heavy elements. In addition, we will be using similar spectroscopic analysis method and linelist to the GALAH survey, which facilitates a consistent comparison of the chemical properties of bulge and disk stars.

5.2 Data description

5.2.1 Target selection

For our observations, we selected giants and red clump stars from the analysed sample of the ARGOS survey (Freeman et al. 2013, Ness et al. 2013a). ARGOS stars were selected to

be between magnitude $K = 11.5$–14 from the 2MASS catalogue (Skrutskie et al. 2006), with J, K magnitude errors <0.06 and all quality flags = 0 (Freeman et al. 2013). To exclude most dwarfs, a colour cut in $(J-K)_0 = 0.38$ was made; each of the ARGOS field was de-reddened using the Schlegel et al. (1998) reddening map. The magnitude and colour selection of ARGOS aimed to minimise very cool and metal-rich giants, but at the same time include very metal-poor giants (Freeman et al. 2013). Any remaining foreground dwarfs are excluded after the ARGOS stellar parameters analysis based on their surface gravity.

In order to exclude background and foreground giants, distances were used to infer $|R_{\rm GC}|$ for each star. Ness et al. (2013a) computed stellar distances by assuming that stars between $\log(g) = 1.8$–3.2 and $T_{\rm eff} = 4500$–5300 K are clump giants, and have absolute magnitude $M_K = -1.61 \pm 0.22$ (Alves 2000). For stars that are not located near the clump, M_K is obtained by matching stellar parameters with the closest point on a grid of 10 Gyr BaSTI isochrones. The error of red clump based distances is ≈15%, and ≈38% for isochrone based distances. Ness et al. (2013a) noted that their red clump sample could be contaminated with non-clump giants, but this contamination should be small. Furthermore, a small subset of their sample shows that isochrone only and red clump only distances return consistent results (Ness et al. 2013a). The ARGOS study defined the bulge region to be within Galactocentric radius $|R_{\rm GC}| \leq 3.5$ kpc.

This study aims to obtain a thorough chemical inventory of red clump and giant stars, probing the different sub-populations found by (Ness et al. 2013a) and their variation with latitude. We have therefore made use of the ARGOS $R_{\rm GC}$ and [Fe/H] measurements to select stars that most likely reside in the bulge region, i.e. those with $|R_{\rm GC}| \leq 3.5$ kpc, and gave greater weights to more metal-poor/metal-rich stars in the selection process. We achieved this by allocating ≈100% of ARGOS stars at low and high metallicity, and ≈50% else where. This ensures that we cover the entire metallicity range and all sub-populations in each field, especially increasing the relative fraction of metal-poor stars.

Because the integration time required for faint bulge stars is much greater for HERMES than AAOmega (see the next section for details), we could only observe a few ARGOS fields to complete the project in a feasible time frame. Fig. 2.3 shows locations of the observed fields (shaded blue), which includes three ARGOS fields along the minor axis at $(\ell, b) = (0, 5)$; $(\ell, b) = (0, -7.5)$; $(\ell, b) = (0, -10)$. In addition to the ARGOS fields, we observed the field $(\ell, b) = (2, -3)$, which was selected due to its relative low extinction and it being covered by K2, which could in principle provide accurate age estimates from asteroseismology (e.g., Silva Aguirre et al. 2015). We also added suitable bulge metal-poor candidates ($[{\rm Fe/H}]_{\rm EMBLA} < -1.5$) from the EMBLA survey (Howes et al. 2016) to fields (0,−10) and (0,−5).

5.2.2 Observations

The observations were taken using the HERMES spectrograph (Sheinis et al. 2015) on the 2dF system of the Anglo-Australian Telescope. The pilot survey, which targeted field $(0, -7.5)$ was completed in August 2014, and observations of the remaining fields were completed between May 2015 and June 2016.

The 2dF system contains two observing plates that cover a 2° diameter field of view. Each 2dF plate has a set of 400 optical fibres, each of them two arcseconds in diameter. Of these, eight fibres are dedicated to bright guide stars to maintain field position accuracy, 25 fibres are allocated to measuring sky variation across the field and typically ≈350–360 science objects were observed per field. Sky locations were chosen by visually inspecting DSS images of each field for blank regions. The instrument, HERMES (High Efficiency and Resolution Multi-Element Spectrograph), enables spectra of four wavelength intervals to be observed simultaneously: 4713–4903 Å (blue CCD); 5648–5873 Å (green CCD); 6478–6737 Å (red CCD) and 7585–7887 Å (IR CCD). The wavelength coverage of HERMES has been optimised for accurate stellar parameters and abundance measurements, including Balmer lines in the blue and red CCDs. At the nominal resolution of $\lambda/\Delta\lambda \approx 28000$, HERMES can deliver abundances for up to 28 elements, including Li, O, Na, Mg, Al, Si, K, Ca, Sc, Ti, V, Cr, Mn, Co, Ni, Cu, Zn, Rb, Sr, Y, Zr, Ru, Ba, La, Sm, Ce, Nd and Eu. Combined with the high multiplexity of 2dF/AAT, HERMES is a powerful tool for detail abundance studies of Galactic stellar populations.

While the optical wavelength coverage of HERMES provides a large number of abundances and accurate parameters, it is also a draw back for bulge observations. Due to the faintness of bulge stars and high extinction in this region, we require significantly longer integration times compared to, for example ARGOS and APOGEE, to achieve the required signal-to-noise ratio (SNR) for precise parameters and abundances. As stated in the previous section, ARGOS stars have 2MASS K magnitude 11.5–14, or an approximate V magnitude of 15–17 in the field $(\ell, b) = (0, -7.5)$. In contrast, typical GALAH targets have V magnitude of 12–14. We aimed to have the same data quality as the GALAH survey, which attains median SNR ≈ 100 per resolution element, or ≈50 per pixel, for the green CCD (Martell et al. 2017). To determine the required integration time, we observed field $(\ell, b) = (0, -7.5)$ over three consecutive nights and determined the signal-to-noise of co-added spectra in real time. This field has an apparent red clump magnitude of $V \approx 16$, and after 10 hours of observing time we reached the desired signal-to-noise. We scaled this time to estimate the required observing time of all other fields based on their apparent red clump magnitudes.

The long integration times meant that we must re-configure each field throughout the night to maintain position accuracy. To do this efficiently, we allocated the same set of stars to both 2dF plates, and alternated between them. Observing intervals are split into 30-minutes exposures to minimise the effect of cosmic rays. Calibration frames (fibre flats

Table 5.1 The estimated V-magnitude and median SNR of each bulge field.

Field (ℓ, b)	RC $V_{\rm mag}$	Exp time (hours)	$\rm SNR_B$ (pixel^{-1})	$\rm SNR_G$ (pixel^{-1})	$\rm SNR_R$ (pixel^{-1})
$(0, -5)$	17.4	17	20	34	46
$(0,-7.5)$	16.3	10	32	51	65
$(0, -10)$	16.0	08	30	40	53

and ThXe arc frames) were taken either immediately before or after each exposure. Most of the observations were carried out in dark time, some during grey time. Lastly, due to the faint signals of our targets, we chose to observe in the `NORMAL` CCD read-out mode, to minimise read noise while maintaining reasonable overhead time.

Due to the large fraction of time lost (because of poor weather) over the course of this project, we were not able to complete the observations of fields $(0,-5)$ and $(2,-3)$. The $(0,-5)$ field is lacking some 10 hours, and $(2,-3)$ requires approximately 25 additional hours. For this reason, we do not include the $(\ell, b) = (2, -3)$ field in our analysis as the signal-to-noise of this field would be insufficient to derive accurate stellar parameters and abundances.

The integration time and median SNR in the blue, green and red CCDs of the minor axis fields are given in Table 5.1. We were able to achieve similar signal-to-noise to the GALAH survey for the pilot field at $(\ell, b) = (0, -7.5)$ and $(0, -10)$. The median SNR for field $b = -5^\circ$ is much lower, because we were not able to complete the planned observations for this field.

5.3 Data reduction

Each 30 minute observing block returns a data frame consisting of ≈380 spectra (including sky fibres). The data frames were reduced using the standard 2dF reduction package 2dfdr v6.46[4]. The software subtracts bias level using the overscan, performs flat-field corrections, calibrates the wavelength using ThXe arclines and subtracts sky. For sky subtraction, we used the throughput mode, in which we calibrated the fibre throughput using strong sky-lines in the IR arm of HERMES. The reduced frames were checked by eye for consistency and data quality. Frames with low SNR due to clouds, or very poor seeing ($>$ 2 arcseconds) were excluded after the reduction stage.

2dfdr outputs the calibrated spectra in 400-apertures images, with additional extensions: the fibre table that matches the fibre number to each object and the variance extension. All frames observed within the same night and plate are averaged, weighted by the

[4]www.aao.gov.au/science/software/2dfdr

variance extension. The flux of each spectrum is given by:

$$flux = \frac{\sum_{i=1}^{n} \left(f_i \sigma_i^{-2} \right)}{\sum_{i=1}^{n} \sigma_i^{-2}} \tag{5.1}$$

Here f_i and σ_i are the flux and error of an individual spectrum, and n is the number of spectra to be combined. The corresponding variance of the combined spectrum is given by:

$$variance = \frac{1}{\sum_{i=1}^{n} \sigma_i^{-2}} \tag{5.2}$$

To correct for the telluric absorption, we convolved the NOAO atlas (Hinkle et al. 2000) to HERMES resolving power ($\mathcal{R}$ = 28 000). The atlas is scaled to match the typical absorption level at Siding Spring, and shifted by the barycentric velocity of each star. The wavelength points corresponding to telluric lines have their errors increased by the inverse of the telluric absorption level. Spectral pixels affected by tellurics have much lower weights and therefore will not contribute significantly to the spectral synthesis analysis (Section 5.4). Thereafter, each object spectrum is corrected for their barycentric velocity, interpolated onto a common wavelength grid and combined using the same averaging method described above. Examples of reduced spectra can be found in Fig. 5.1.

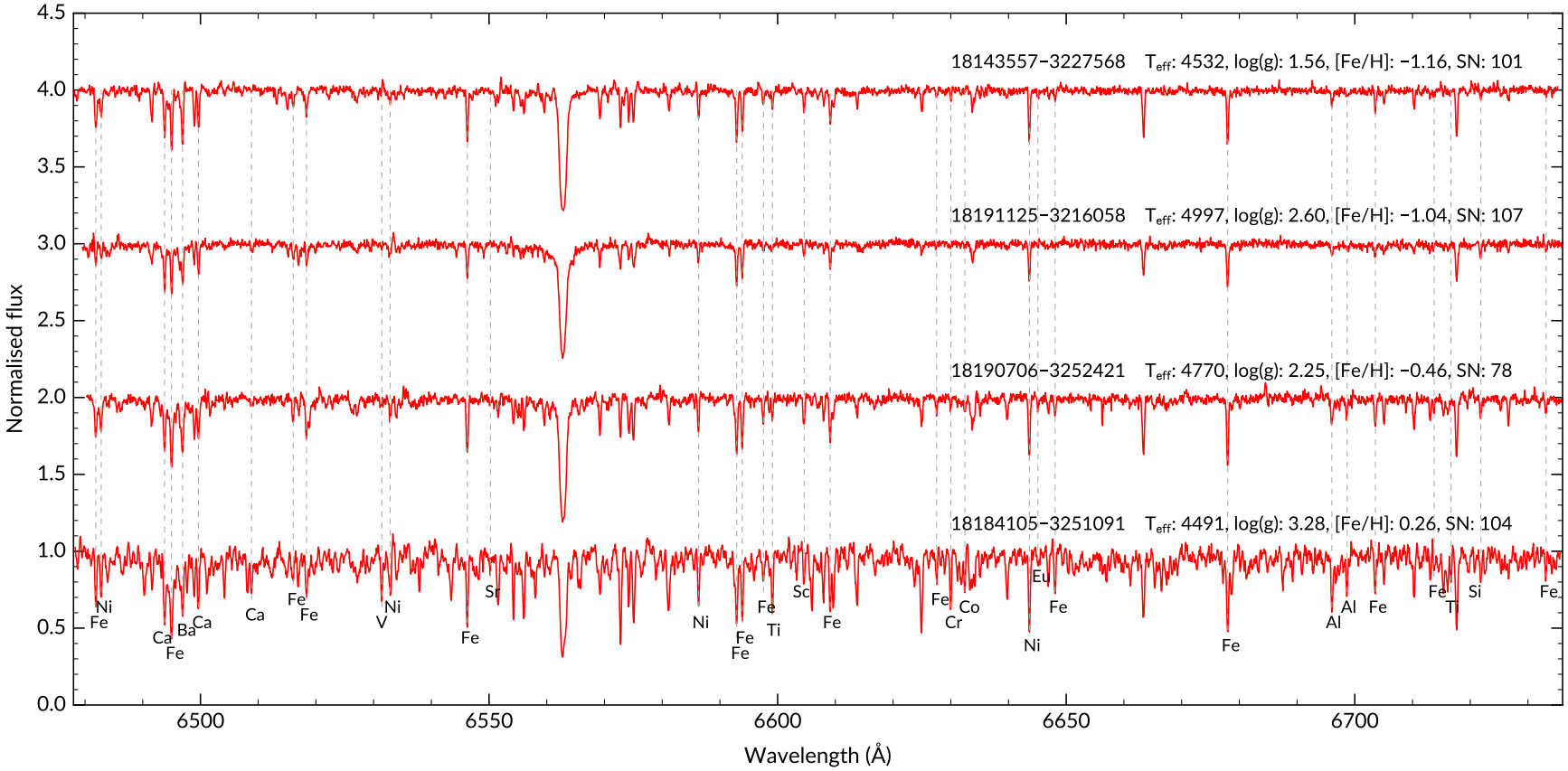

Figure 5.1 Example HERMES spectra in the 'red' wavelength region (which includes the Hα line), normalised and shifted to rest using the GUESS code (Section 2.5). The stars' 2MASS identification, SNR (per pixel) and SME-derived parameters are shown. Most of the lines used for stellar parameters and abundance analysis are have been labelled.

5.4 Spectroscopic analysis

5.4.1 Stellar parameters

The stellar parameters and abundances pipeline and linelist we adopt is the same as that used in Data Release 2 of the GALAH survey (Buder et al. 2018). The atomic data is based on the *Gaia*-ESO survey linelist (Heiter et al. 2015b), consisting of mainly blend-free lines with reliable log(*gf*) values for stellar parameter determination. However, some background blending lines have slightly different *gf* values compared to the *Gaia*-ESO linelist, as they were changed to improve clearly discrepant fits to the HERMES Arcturus and Solar spectra.

For spectral synthesis, we used the code SME (*Spectroscopy Made Easy*) v360 (Valenti & Piskunov 1996, Piskunov & Valenti 2017). In this analysis we implement the 1D, LTE MARCS model atmospheres (Gustafsson et al. 2008). The atmospheric models uses spherical geometry with $1M_{\odot}$ for $\log g \leq 3.5$, and plane parallel otherwise. During the parameter determination stage, we implement non-LTE corrections from Amarsi et al. (2016b) for Fe I lines.

Each spectrum is divided into several ≈10 Å wide segments containing lines relevant to stellar parameter determination. For this step, there are 20 segments containing line masks for Fe, Ti and Sc. SME synthesises the initial model based on the GUESS stellar parameters and radial velocity. In this first iteration, each segment is normalised using a linear function. SME then synthesises lines of Hα and Hβ; neutral and ionised lines of Sc, Ti, and Fe to determine $T_{\rm eff}$, $\log g$, [M/H][5], $v \sin i$ (rotational velocity) and $v_{\rm rad}$. The free SME parameter $v_{\rm rad}$ is used to bring the model and data spectra to a common wavelength grid. The value of this parameter is typically in line with the radial velocity uncertainty. $v_{\rm rad}$ is computed independently of other parameters and the same value is used to correct all segments.

SME solves for the minimum χ^2 using the Levenberg-Marquardt algorithm. The χ^2 parameter is computed for selected regions following the formula:

$$\chi^2 = \frac{\sum \left(\frac{spectrum-model}{variance}\right)^2 \times spectrum}{N_{\rm lpts} - N_{\rm free} - N_{\rm seg}} \tag{5.3}$$

Where $N_{\rm lpts}$ is the number of line pixels; $N_{\rm free}$ is the number of free parameters and $N_{\rm seg}$ is the number of segments. Final parameters from the first cycle are used to build the initial model in the second cycle, which is then used to re-normalise each segment. SME goes through the same iteration process, optimising χ^2 until convergence is achieved (when $\Delta\chi^2 \leq 10^{-3}$).

[5]The [M/H], or metallicity parameter is the iron abundance of the best-fit model atmosphere. In our case, this value is very close to the true iron abundance derived from iron lines only. For the purpose of notation consistency when comparing with other studies, we refer to [M/H] as [Fe/H] in subsequent sections.

Macro-turbulence ($v_{\rm mac}$) cannot be set as a free parameter for HERMES spectra without causing additional scatter in the results. This is due to the degeneracy between $v_{\rm mac}$ and $v \sin i$ at HERMES resolution. We therefore set all $v_{\rm mac}$ values to zero, which effectively incorporates $v_{\rm mac}$ into our $v \sin i$ estimates. Similarly, micro-turbulence (ξ_t) is determined by temperature-dependent formulas that were calibrated for the *Gaia*-ESO survey (Smiljanic et al. 2014). For giants ($\log g \leq 4.2$) we adopt:

$$\xi_t = 1.1 + 1.0 \times 10^{-4} \times (T_{\rm eff} - 5500) + 4 \times 10^{-7} \times (T_{\rm eff} - 5500)^2 \tag{5.4}$$

The resolving power of HERMES is variable across the CCD image, in both the dispersion and aperture axes. A stable median value can be estimated by interpolating each segment with pre-computed resolution maps from Kos et al. (2017); this solution is implemented for the GALAH survey (Buder et al. 2018). However, since our spectra are combined from different fibres, we cannot recover the resolution information. Thus, for the SME analysis, we adopted $\lambda/\Delta\lambda$ = 28 000 throughout. The synthetic spectra are convolved with a Gaussian instrumental broadening kernel.

Overall our spectroscopic analysis returned fairly accurate stellar parameters for *Gaia* benchmark standards, and our reduction method provided similar results to the GALAH reduction pipeline (for details see Appendix A.1). We found no significant offset in our effective temperature or surface gravity compared to reference values derived by Jofré et al. (2014) and Heiter et al. (2015a). The temperature offset is 40 K with standard deviation of 90 K; the surface gravity offset is 0.02 dex with standard deviation of 0.25 dex. The metallicity, however, shows an offset of -0.12 with standard deviation 0.08 dex. The metallicity offset is the same as that reported by the GALAH survey (Sharma et al. 2018). To remain consistent with GALAH, we have added $+0.1$ dex to all of our metallicity values. The standard deviation of the difference between our results and that of benchmark stars can be taken as typical uncertainties in the parameters $T_{\rm eff}$ (90 K), $\log g$ (0.25 dex) and [Fe/H] (0.08 dex).

Fig 5.2 shows the *Kiel* diagram for all minor axis fields. The stellar parameters are well represented by 10 Gyr isochrone tracks, which is what one expects for bulge giants. Of the targets observed ($\approx$350 per field), minus possible binaries and those with reduction issues, we have 313 stars analysed for field $(0, -10)$, 13 of which are from the EMBLA survey. For the pilot field $(0, -7.5)$ there are 315 stars in total. Part of the $(0, -5)$ field was unfortunately affected by very strong hydrogen emission (at Hα and Hβ rest wavelengths) from the ISM. This affected the hydrogen line profiles for many stars, and as a result a large fraction of them failed to converge. Therefore, we only have 204 stars in field $(0, -5)$ (two are EMBLA stars), giving us a grand total of 832 stars.

5.4.2 Elemental abundances

After the stellar parameters have been established, they are fixed for each abundance optimisation. Similarly to the parameters, SME optimises the χ^2 parameter to find the best-fit

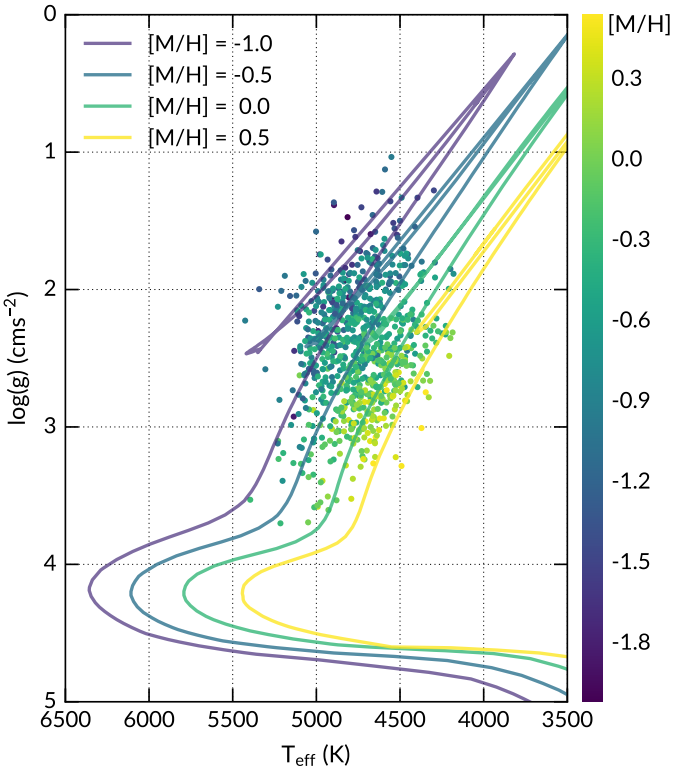

Figure 5.2 The *Kiel* diagram of the full sample (832 stars), over-plotted with 10 Gyr PARSEC isochrones (Marigo et al. 2017) of metallicities indicated in the figure legend.

abundance ratio of each element. Only wavelength pixels within the line masks are used for χ^2-minimisation. During the optimisation stage, SME de-selects blended wavelength points (if any) within the line masks. In this paper, we report on abundances of the alpha elements O, Mg, Si, Ca and Ti. For all elements except Ti, we computed the line-by-line abundances for each element and averaged the individual lines' results, weighted by the abundance ratio uncertainties provided by SME. We do not include in the weighted average abundances that are flagged as upper limits. The Ti abundances are computed with the same lines also used for stellar parameters determination, and all lines were fitted at the same time. In addition, non-LTE corrections were applied to the elements O (Amarsi et al. 2016a), Mg (Osorio & Barklem 2016) and Si (Amarsi & Asplund 2017).

For solar normalisation, we used abundances from a HERMES twilight spectrum, which was reduced as per Section 5.3 and analysed in the same manner as a typical star. This ensures that systematic errors (such as uncertain $\log(gf)$ values) are mostly removed. The solar parameters we derived and adopted for abundance syntheses are: $T_{\rm eff}$ = 5735 K, $\log g$ = 4.3 dex, [Fe/H] = -0.02 dex, $\nu_{\rm mic}$ = 1.1 km s^{-1}. These parameters are different to the nominal solar values from Prša et al. (2016), but they are consistent within our estimated uncertainties. We normalised the single-line abundance ratios before computing the weighted average values for each element, such that:

$$[\mathrm{X/Fe}] = [\mathrm{X/Fe}]_{*} - [\mathrm{X/Fe}]_{\odot,\mathrm{HERMES}} \tag{5.5}$$

The alpha abundances presented here are not particularly sensitive to temperature, as shown in Fig. A.2. We do not see any appreciable trends with $T_{\rm eff}$ for the elements O, Si, and Ti. However, linear trends can be seen for Mg and Ca, which are also observed in GALAH data (Buder et al. 2018). While we note these issues, we do not apply empirical corrections to abundance-temperature trends, as the underlying physics is yet to be understood, and should be investigated further.

5.5 ARGOS comparison and metallicity distribution functions

As noted earlier, we selected most of our bulge stars from the ARGOS survey, which was observed with the AAOmega spectrograph ($\lambda/\Delta\lambda$ =11 000). Fig. 5.3 and 5.4 show the comparison between our parameters and that of ARGOS for stars in common. In Fig 5.3, the differences are plotted as histograms: the biases (median of the difference) are shown for $T_{\rm eff}$, $\log g$ and [Fe/H]. The 1σ values were computed using the median absolute deviation (MAD) method, in order to exclude outliers. This comparison shows small offsets between the two studies. The σ value of Δ[Fe/H] is consistent with the combined HERBS and ARGOS metallicity uncertainties, and the overall bias is negligible. Even though ARGOS effective temperatures were determined using photometry ($J-K_0$ colours), they agree remarkably well with our values, and the MAD value is smaller than our estimated uncertainties. Surface gravity shows a small 0.14 dex offset, but the σ value is also smaller than

both studies' combined $\log g$ uncertainties.

Fig 5.4 shows the same differences as Fig. 5.3, but as functions of ARGOS stellar parameters. In this figure, trends as a function of parameters are apparent. The trend in temperature could have been caused by the photometric calibration that was used to determine ARGOS effective temperatures. In general, stars with higher ARGOS $T_{\rm eff}$ and $\log g$ are estimated to be cooler, and have lower surface gravity in our analysis. For [Fe/H], there is a mild linear trend, which is not apparently dependent on $T_{\rm eff}$ or $\log g$. The trend in Δ[Fe/H] can be described as:

$$\Delta[\mathrm{Fe/H}] = -0.190(0.013) \times [\mathrm{Fe/H}]_{\rm ARGOS} - 0.04(0.01) \tag{5.6}$$

In Equation 5.6, the numbers in parentheses indicate the uncertainties of the slope and intercept. The trend indicates that metal-rich ARGOS stars are estimated to be slightly more metal-poor in our analysis, and vice versa.

The metallicity distribution for each minor-axis field is shown in Fig. 5.5. Here we have also over-plotted the Gaussian distributions corresponding to each ARGOS component A–D; A being the most metal-rich, D the most metal-poor. As indicated above, our analysis suggests a slight compression of the ARGOS MDF. In Fig. 5.5, we have shifted the centroids of these components according to Equation 5.6 to reflect this compression.

On the whole, our MDF appears flatter and wider compared to the ARGOS MDF, however this is to be expected, as our selection function prioritised the most metal-rich and metal-poor stars. The selection criteria we employed have allowed for a larger fraction of metal-poor star to be observed. Approximately 12% of the stars have [Fe/H] ≤ -1, compared to the typical fraction of 4–5% (Ness et al. 2013a, Rojas-Arriagada et al. 2017).

There are discussions in the literature regarding the number of metallicity components in the bulge, with some authors arguing for a two-component bulge metallicity distribution with much larger dispersions (Gonzalez et al. 2015b, Rojas-Arriagada et al. 2017, Schultheis et al. 2017), rather than three components with narrow dispersions (Ness et al. 2013a, García Pérez et al. 2018). As there are strong selection effects associated with our MDF, we are not able to directly address this issue. However, our analysis indicates that the ARGOS component centroids should be located $\approx$0.09 dex closer together. This difference is sufficiently small that for fields $(0, -5)$ and $(0, -10)$, the ARGOS components remain distinct given their narrow dispersions. However, for field $(0, -7.5)$, the centroid of component A is within 1.5σ of component B's centroid, meaning that there is a possibility components A and B are not distinct in field $b = -7.5°$.

It is worth noting that the number of metallicity components may not be indicative of how many distinct populations reside in the Galactic bulge. Indeed, the N-body dynamical model of Fragkoudi et al. (2018) found that even though their bulge population originated from three different disk components, the final MDF is best described by two Gaussian curves with larger dispersions than the original disk components.

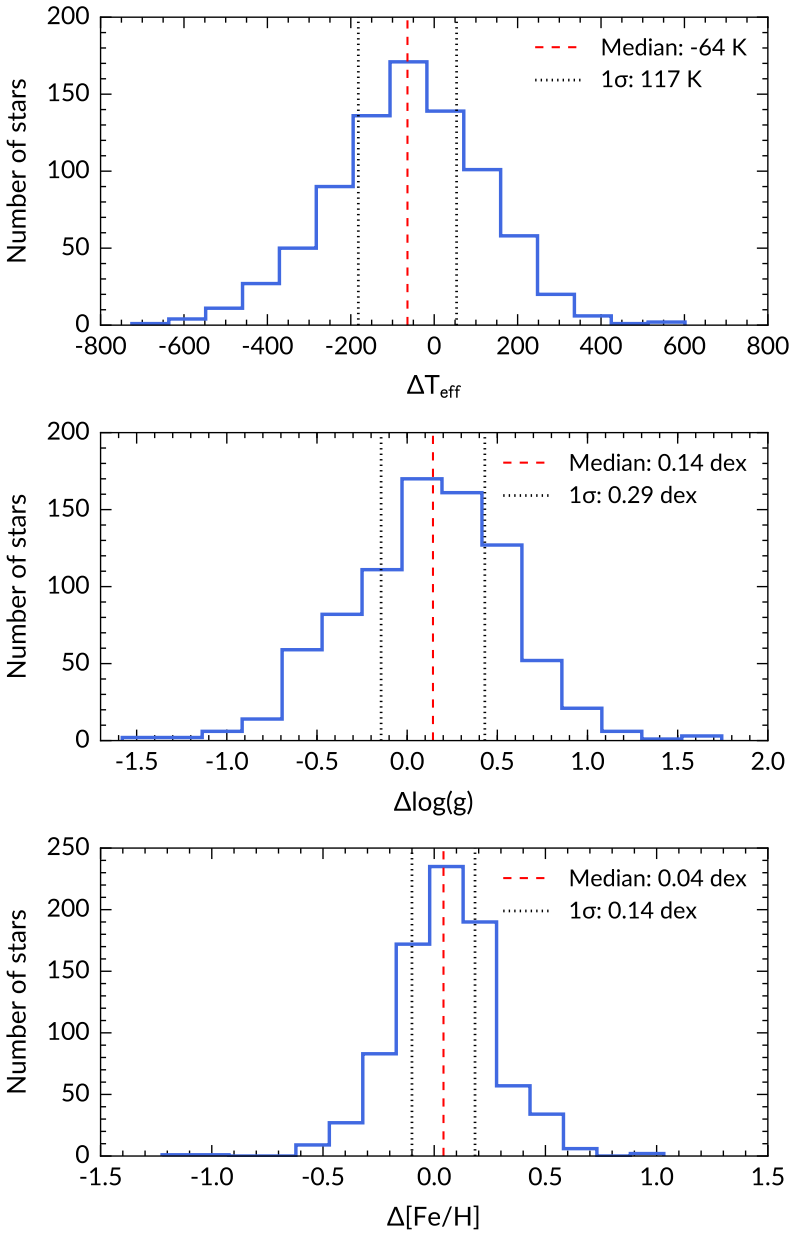

Figure 5.3 Histogram comparison between parameters derived in this work and those of ARGOS for stars in common. The differences are shown as (HERBS – ARGOS). The 1σ levels (dotted lines) are median absolute deviations (MAD), which are more robust against outliers.

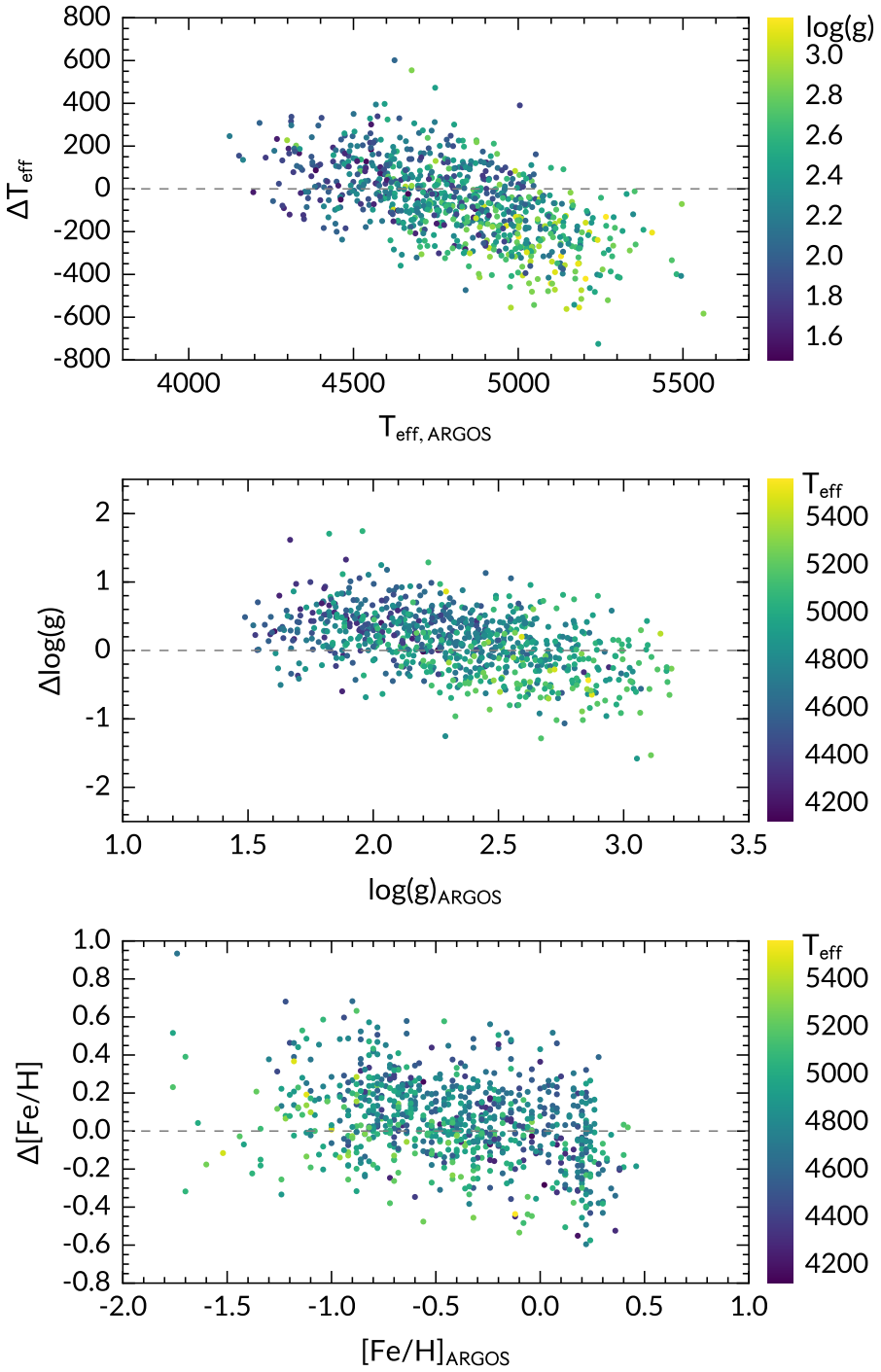

Figure 5.4 The same (HERBS – ARGOS) differences as Fig. 5.3, but plotted as a function of ARGOS stellar parameters, colour-coded by $T_{\rm eff}$ or $\log g$. Lighter colours represent warmer stars with higher surface gravities.

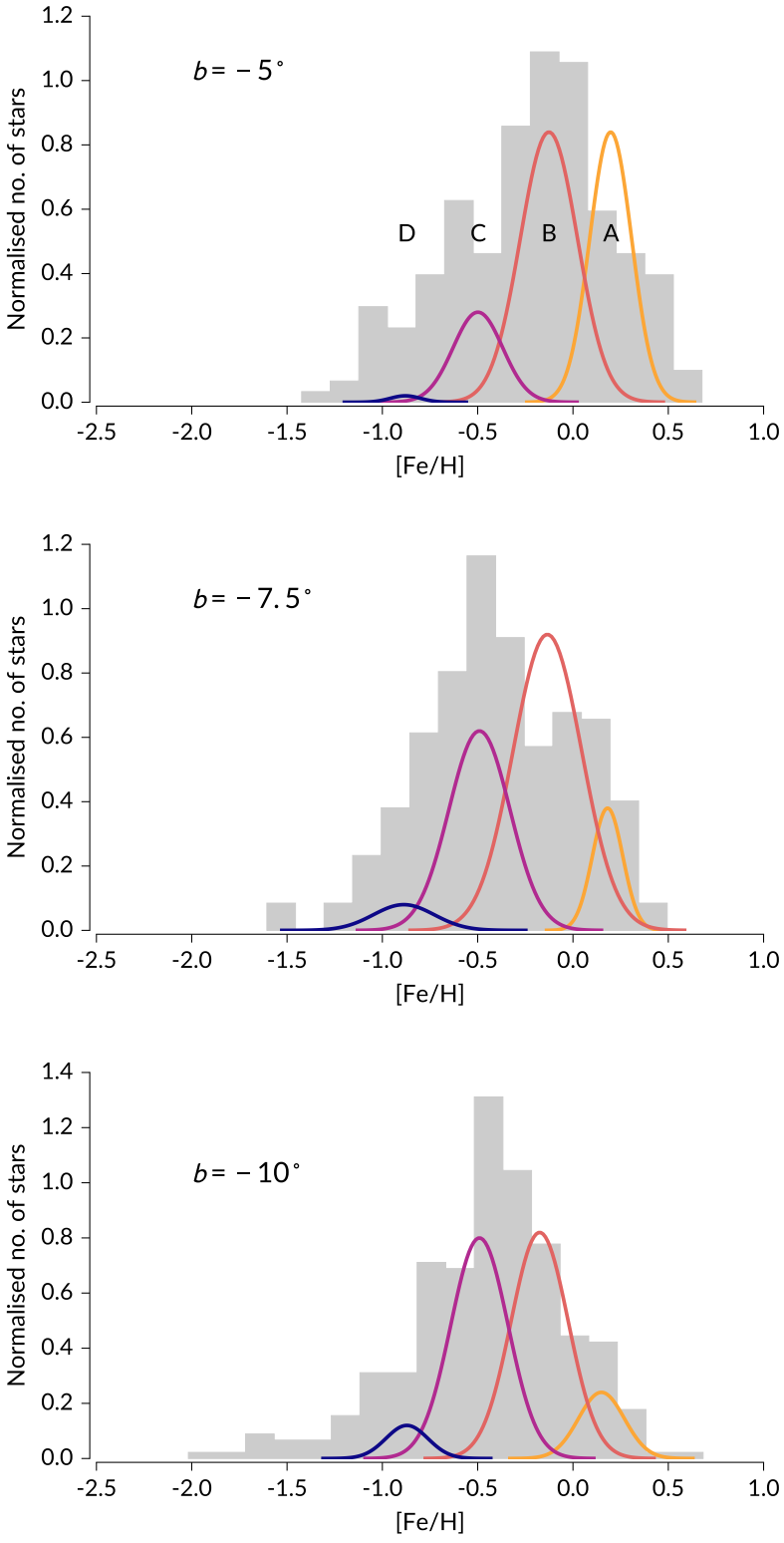

Figure 5.5 The metallicity distribution functions (grey histograms) for the minor axis fields. Overplotted for comparison are ARGOS metallicity components A–D (corresponding to most metal-rich to most metal-poor). The ARGOS centroids have been shifted according to Equation 5.6. The amplitude of each component has been multiplied by a factor of two to better match the distributions presented here, but their relative weights remain the same.

5.6 α-element abundances

The alpha elements are often associated with rapid SNeII enrichment, and are thus useful indicators of formation/evolution timescales for the different Galactic components (Tinsley 1979, Matteucci & Brocato 1990). Fig 5.6 shows the alpha abundances from this study compared to recent high-resolution spectroscopic studies of bulge *field* stars in the literature. For this exercise we have included Bensby et al. (2013, 2017), Johnson et al. (2014) and Gonzalez et al. (2015b). The Bensby et al. (2017) study includes all microlensed bulge dwarfs in Bensby et al. (2013), however we use oxygen abundance ratios from Bensby et al. (2013), which is not available in the later study. The microlensed dwarfs were observed with the VLT/UVES spectrograph; KECK/HIRES spectrograph or Magellan/MIKE spectrograph ($\mathcal{R} \approx 40\,000$–$90\,000$). Both Johnson et al. (2014) and Gonzalez et al. (2015b) provided individual abundances for a large number of bulge giants observed with the VLT/GIRAFFE spectrograph ($\mathcal{R} \approx 22\,500$), but at different wavelength settings. All literature samples considered are smaller, but have on average higher SNR than our sample. Furthermore, only the oxygen abundance ratios from Bensby et al. (2013) were computed assuming non-LTE. All studies assumed LTE in their abundance analysis. On the whole, the scatter in HERBS abundance ratios are larger than the comparison samples and what could be expected from abundance ratio uncertainties from χ^2-square fitting. This indicates that the χ^2-square errors may be underestimated. We describe the trends of each element below.

- **Oxygen** The oxygen abundance trend is largely in agreement with literature studies, but with much larger scatter. We used the O I line at 7772 Å, which is the strongest line of the triplet used by Bensby et al. (2013)[6]. Given that the line strength of the oxygen triplet is weaker in giants than in dwarfs, and the lower SNR of our spectra, it is not surprising that our scatter is larger than that of Bensby et al. (2013). In addition, the plateau of [O/Fe] is not as well defined as in other works, but [O/Fe] decreases as a function of metallicity, from [Fe/H] ≈ -0.4 dex. As other authors have commented, the average oxygen abundance ratio is higher, and the decline of [O/Fe] with metallicity is steeper than that of other alpha elements (Bensby et al. 2013, Johnson et al. 2014). This indicates that aside from SNeIa contribution of iron, other mechanisms may have affected the decrease in [O/Fe], such as stellar mass loss (McWilliam et al. 2008, McWilliam 2016).

- **Magnesium** Similarly to oxygen, magnesium largely follows the same trend as literature studies, but with larger scatter. This could largely be attributed to the low SNR of our spectra. It is also apparent that the mean [Mg/Fe] of this study is lower than that of other studies by ≈0.15 dex. Although Johnson et al. (2014), Gonzalez et al. (2015b)

[6]It made little difference to [O/Fe] whether we use all three lines of the oxygen triplet, or just the 7772 Å line. As the other two lines of the triplet are significantly weaker (therefore often undetectable) in our spectra, we chose to use only the 7772 Å line.

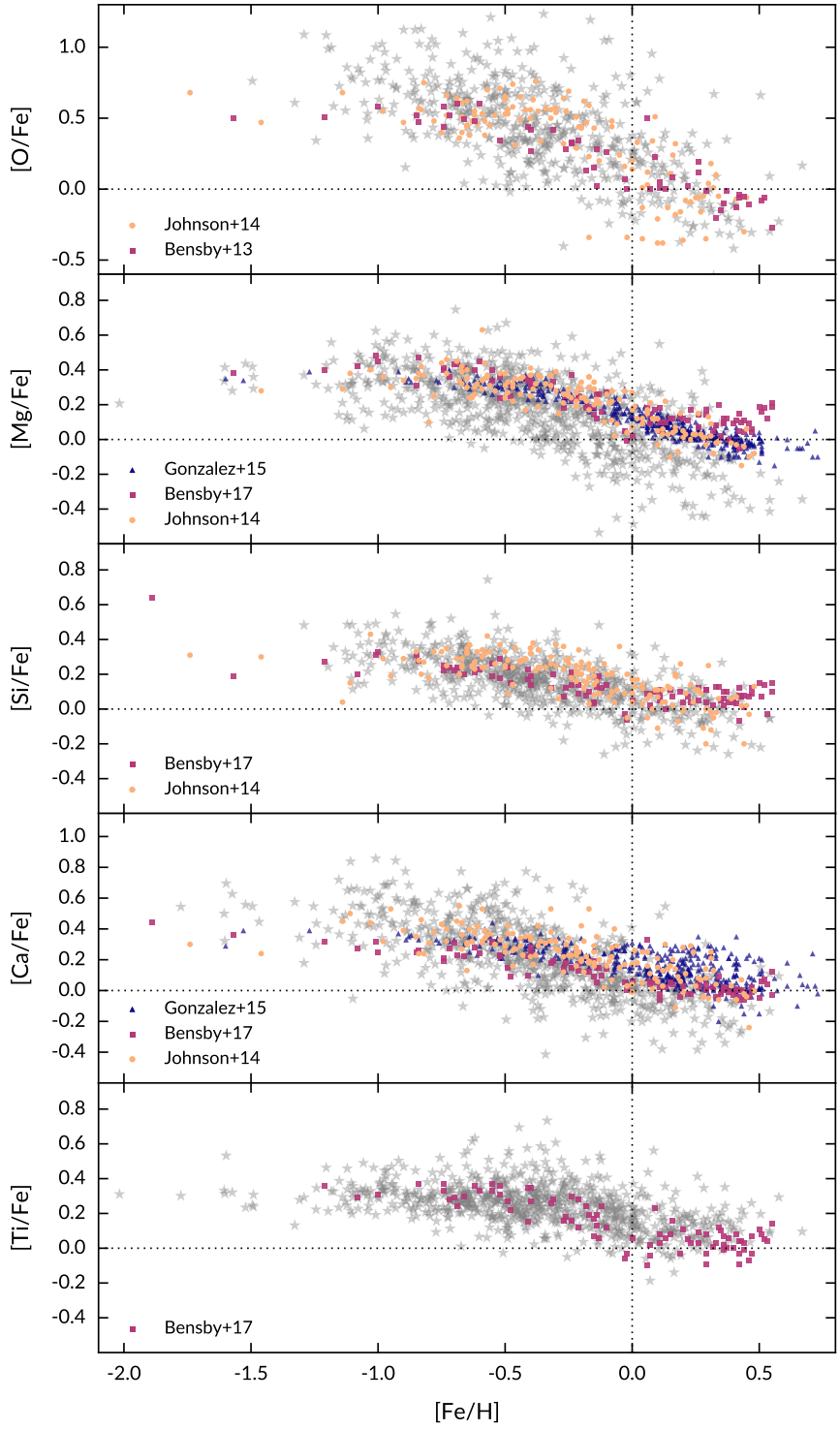

Figure 5.6 Abundance ratios for the alpha elements from this work (grey stars) compared to literature studies. The abundance trends derived here are largely in agreement with the literature. In particular, Si, Ca and Ti seem to follow the same trend and similar abundance scale to the microlensed dwarfs (Bensby et al. 2017). However, for the elements O and Mg, our scatter is considerably larger than other studies. See text for details.

and Bensby et al. (2017) analysed different types of stars, using different methods, their abundance trends and scale agree well up to solar metallicity. At [Fe/H] ≈ 0, Bensby et al. (2017) showed a flattening trend for [Mg/Fe], while Johnson et al. (2014) and Gonzalez et al. (2015b) showed continued decrease as a function of [Fe/H]. Our results are in line with the latter trend.

- **Silicon** For Si, our abundance trend seems to follow that of Bensby et al. (2017), but with slightly larger scatter. Johnson et al. (2014) estimated on average higher [Si/Fe] compared to this work and Bensby et al. (2017) at [Fe/H] < 0 dex. All three studies are in agreement that [Si/Fe] flattens at super-solar metallicity to approximately the solar value, however Bensby et al. (2017) observe slightly more enhanced [Si/Fe] in this regime.

- **Calcium** For Ca, the general abundance trend is consistent with all three literature samples. However, at sub-solar metallicity, our [Ca/Fe] values are in agreement with Johnson et al. (2014) and Gonzalez et al. (2015b), which are on the mean higher than those reported by Bensby et al. (2017). Both Johnson et al. (2014) and Gonzalez et al. (2015b) find enhanced [Ca/Fe] at super-solar metallicity, but Gonzalez et al. (2015b) reported rather large uncertainties for [Ca/Fe] in this regime. Here, our results seem to be in good agreement with Bensby et al. (2017), with [Ca/Fe] flattening to solar value for [Fe/H] > 0. However, there is a small offset (0.05 dex, ours being lower) between our results and that of Bensby et al. (2017). The scatter in our [Ca/Fe] measurements is also higher than other studies.

- **Titanium** The [Ti/Fe] trend derived here is in good agreement with Bensby et al. (2017), but different from the trends established for giants by e.g., Alves-Brito et al. (2010) and Gonzalez et al. (2011). Both the microlensed dwarfs and our giants show that [Ti/Fe] decreases to near-solar value at [Fe/H] ≈ 0 and flattens at super-solar metallicity, consistent with the behaviours of silicon and calcium. However, our [Ti/Fe] values remain enhanced by $\lesssim$0.1 dex compared to Bensby et al. (2017) at super-solar metallicity.

In summary, the alpha abundances derived in this work follow the same trend as some of the most recent, high signal-to-noise, high-resolution studies of bulge stars. For oxygen and magnesium, our results show considerably larger scatter (approximately twice) compared to literature studies, and an offset in the mean magnesium abundances. However, [Si/Fe], [Ca/Fe] and [Ti/Fe] show comparable scatter and abundance scale to other studies. For both O and Mg, a plateau can be seen from [Fe/H] $\lesssim -0.5$, and the abundances of both elements decrease as function of [Fe/H] above solar metallicity. Si, Ca and Ti show similar trends, flattening to near-solar or solar values for [Fe/H] ≥ 0. This behaviour at super-solar metallicity was seen as unique to microlensed bulge dwarfs (e.g., Johnson et al. 2014), however we confirm that this is not the case. A plateau at [X/Fe] ≈ 0.3 dex can be seen for Si

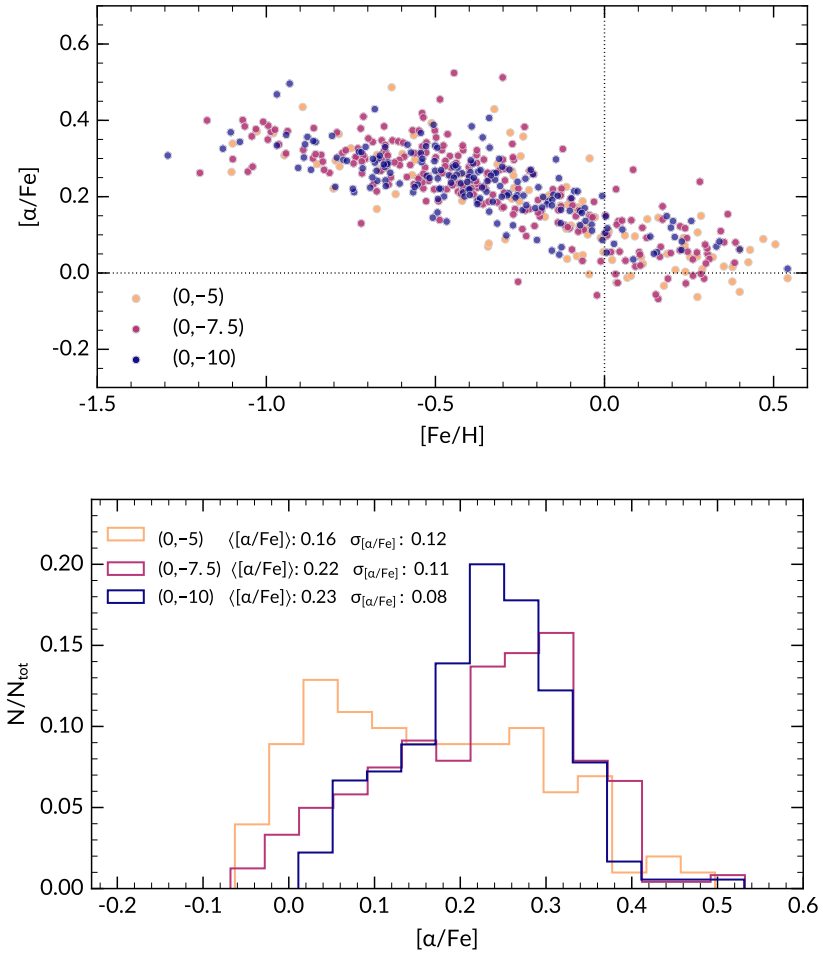

Figure 5.7 Left panel: the weighted average of Mg, Si, Ca and Ti ([α/Fe]) as a function of [Fe/H] for the three minor axis fields. Right panel: the corresponding histograms of [α/Fe] at different latitudes. The mean [α/Fe] values and standard deviations are given for each field. Overall [α/Fe] increases with latitude, but the dispersion seems to be smaller at the highest latitude ($b = -10$).

and Ti, from [Fe/H] $\lesssim -0.5$. Finally, although the abundance trends are largely consistent with the literature, there are some inconsistencies in terms of abundance scale at different metallicity regimes.

5.6.1 Variation with latitude

As the contribution of metallicity components change with latitude, such that the metal-rich component dominates near the plane, one would expect a vertical gradient in [α/Fe] in the opposite sense: that the low-α population dominates near the plane, and the high-α population dominates away from the plane. This has been observed by Gonzalez et al. (2011) for their bulge giants located near the minor axis, at Baade's window and $(\ell, b) = (0.21, -6)$ and $(0, -12)$. More recently, Fragkoudi et al. (2018) showed that a positive [α/Fe] gradient is also present in their N-body simulation, where the bulge population originated from three disk components.

The same conclusion can be drawn from Fig. 5.7, which shows the distribution of [α/Fe] for bulge fields observed in this work. We used the weighted average of the elements Mg, Si, Ca and Ti to determine [α/Fe]. Oxygen was excluded because it may have a different chemical evolution history to the other alpha elements, as discussed in the previous section. The weighted average [α/Fe] is mostly influenced by Si and Ti, which are the most precisely measured elements. We do not report [α/Fe] values for [Fe/H] < -1.5 because most of the elemental abundances cannot be measured at this metallicity regime.

We observe that the mean [α/Fe] indeed shifts towards higher values at higher latitudes. However, the median value and shape of [α/Fe] change sharply between $b = -5^\circ$ and $b = -7.5^\circ$. Closer to the plane, the distribution is fairly uniform, but away from the plane, it is positively skewed (towards higher [α/Fe] values). The alpha abundance distributions of $b = -7.5^\circ$ and $b = -10^\circ$ are similar in shape and mean value, however $b = -7.5^\circ$ have slightly larger dispersion. These observations can be explained by the relative contributions of different metallicity components observed by ARGOS: the fraction of the most metal-rich (low-α) component drops significantly between $b = -5^\circ$ and $b = -7.5^\circ$, whereas the component contributions are similar for fields $b = -7.5^\circ$ and $b = -10^\circ$ (Ness et al. 2013b). Qualitatively, our results are consistent with that of Gonzalez et al. (2011) (see their Figure 15), although our MDF is biased, which could affect the [α/Fe] distribution function. An interesting point to note is that there is a hint of decreasing $\sigma_{[\alpha/\mathrm{Fe}]}$ as a function of latitude, which can also be seen for southern APOGEE bulge fields near the minor axis (see Fragkoudi et al. 2018, Figure 12).

While an increase in the mean [α/Fe] with distance from the plane is expected (Gonzalez et al. 2011, Fragkoudi et al. 2018), intrinsic vertical abundance gradients of the different bulge metallicity components have not been established. In this work we are well placed to assess the variation with latitude (if any) of each metallicity component, as we have sampled the same range of metallicity at each latitude. For some elements, we are able to measure abundances down to [Fe/H] ≈ -2, but for most elements (and thus [α/Fe]), we are able to probe metallicity components within $-1.5 \lesssim$ [Fe/H] $\lesssim 0.5$.

For each latitude, we computed the median [X/Fe] at different [Fe/H] bins, in steps of 0.2 dex, shown in Fig. 5.8. Errors in the median [X/Fe] values are computed as the standard error in the mean. Given the uncertainties, we do not observe variations in alpha element abundances across the latitude range covered here for $-1 <$ [Fe/H] < 0. Similarly, Ryde et al. (2016) did not find vertical variations in the alpha abundances of inner bulge stars within two degrees from the Galactic plane. At the low metallicity regime ([Fe/H] < -1), variations between fields $(0, -7.5)$ and $(0, -10)$ can be seen for certain elements (O, Mg and Si). However, the trends are not consistent. These differences more likely caused by the higher uncertainties in abundance measurements and smaller samples for [Fe/H] < -1. At the metal-rich regime ([Fe/H] > 0), for all alpha elements except calcium, the abundances of field $(0, -10)$ are enhanced compared to field $(0, -5)$. This can be seen most clearly for [α/Fe], but is much less certain for [O/Fe]. We note, however, that there are fewer stars at

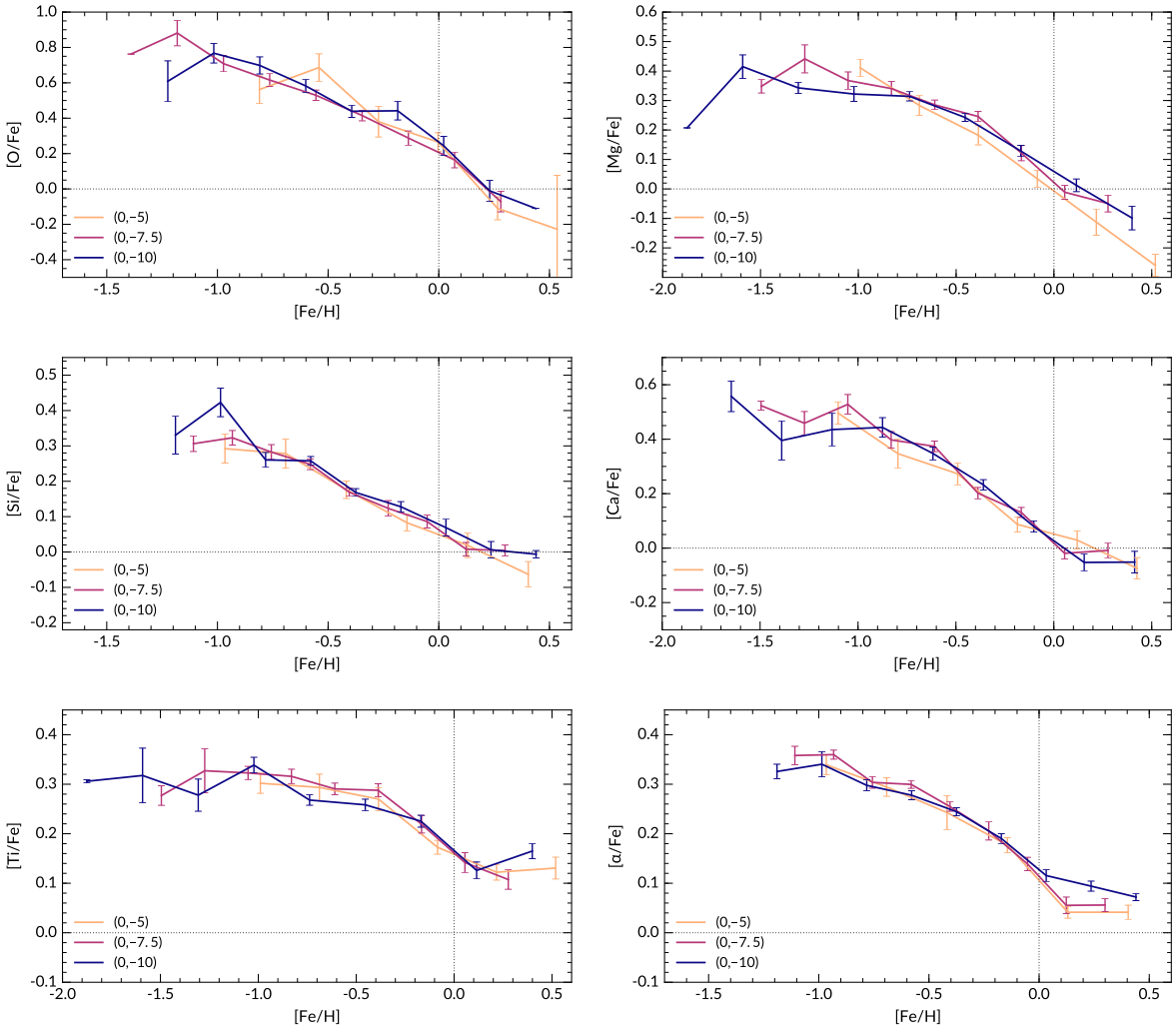

Figure 5.8 The median trends of each α-element, and the weighted average [α/Fe] at different latitudes. Median points are computed for [Fe/H] bins of ≈0.2 dex in width. The error bars are the standard deviation in the mean.

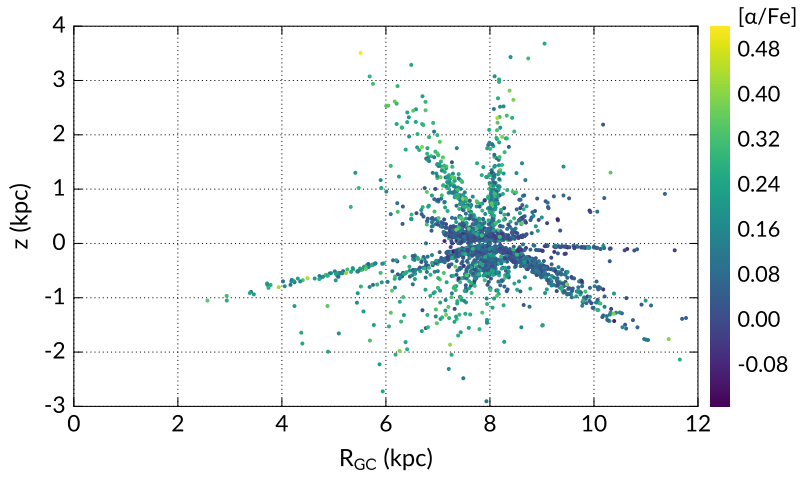

Figure 5.9 The distribution of GALAH giants in $R_{\rm GC}$-z plane. We assumed $R_\odot = 8$ kpc. Most of the stars are concentrated in the solar neighbourhood. Due to the survey observing strategy, only a very small fraction of the sample is located in the inner galaxy. Few stars are located at $|z| \geq 4$ kpc, they are not shown here.

the high metallicity regime, especially for field $(0, -10)$.

The lack of vertical alpha abundance gradient in each metallicity component for [Fe/H] < 0 is indicative of fast bulge evolution. Similarly, it has been shown that the high-α disk population (commonly referred to as the thick disk) does not exhibit a vertical [α/Fe] gradient (Ruchti et al. 2011, Mikolaitis et al. 2014, Duong et al. 2018).

5.6.2 Comparison with GALAH DR2

Because this work uses the same lines, atomic data and spectral analysis technique as the GALAH survey, systematic differences and offsets are minimal (see Appendix A.1). Although differences are expected due to our independent reduction and lower S/N, our bulge sample allows for a consistent comparison with disk/halo stars from the GALAH survey DR2 (Buder et al. 2018). To avoid intrinsic offsets in the abundance ratios of different stellar types, we restricted the GALAH sample to approximately same parameters space as that shown in Fig. 5.2: $T_{\rm eff} \approx 4000$–5000 K and $\log g \approx 3.5$–1.5 cms^{-2}. For a fair comparison, we only used results determined by SME, i.e., the reference results used to train *The Cannon*. The GALAH training set is of high fidelity and signal-to-noise, with mean SNR of ≈100 per pixel for the green CCD. Due to the survey observing strategy, most GALAH stars are in the outer disk. Assuming $R_\odot = 8$ kpc, over 90% of the comparison sample are located at $R_{\rm GC} > 7$ kpc and 80% are in the solar neighbourhood ($7 < R_{\rm GC} < 9$ kpc). The $R_{\rm GC}$-z distribution of GALAH giants is shown in Fig. 5.9.

We determined the component membership of the GALAH disk stars based on their weighted average [α/Fe], which shows the clearest separation between the disk components. We separated the low and high-α populations of the disk guided by the 'gap' in the [α/Fe]

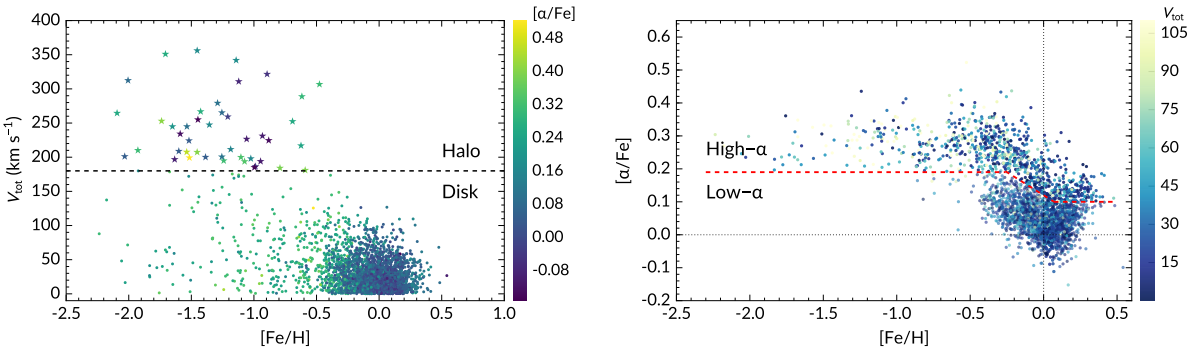

Figure 5.10 Definitions of stellar populations in the GALAH sample. Left panel: $V_{\rm tot}$ as a function of metallicity. The dotted line shows $V_{\rm tot} = 180$ km s^{-1}, which separates the halo from the disk components. Right panel: The [α/Fe] distribution of GALAH disk stars; stars above the dashed line is defined as the high-α population, and below the dashed line is the low-α population.

distribution. The separation is shown in Fig 5.10. At the metal-poor regime ([Fe/H] ≤ -1), there is substantial overlap between the metal-weak thick disk and halo in velocities, metallicity and abundances (e.g., Reddy & Lambert 2008). To identify halo stars, we relied on the space velocities U, V, W, computed using *Gaia* DR2 parallaxes and proper motions (Gaia Collaboration et al. 2016, 2018). The solar motion is corrected by adapting $(U, V, W)_\odot = (11.1, 12.24, 7.25)$ from Schönrich et al. (2010). Fig 5.10 shows the total velocity $V_{\rm tot} \equiv \sqrt{U^2 + V^2 + W^2}$ as a function of [Fe/H]. We designated those with $V_{\rm tot} > 180$ km s^{-1} as likely halo stars (e.g., Nissen & Schuster 2010).

Fig 5.11 shows the comparison of bulge and disk/halo abundance trends for the five alpha elements and weighted average [α/Fe]. Our abundance trends and scale are mostly compatible with GALAH, as we would expect. We note that our [Mg/Fe] trend does not resemble the GALAH trend as do the other elements. This may be due to the different Mg lines used in this study and GALAH (we omitted a magnesium line at 4730 Å due to blending). For this reason, we do not show the comparison for [α/Fe], as this average would be affected by the systematic difference between our and GALAH [Mg/Fe] ratios.

Overall the bulge trend follows that of the high-α disk component for [Fe/H] $\gtrsim -0.8$. The bulge abundances remain enhanced compared to the low-α component also at the metal-rich regime. However, both Mg and Ca abundance ratios show little difference between the low-α disk and bulge, especially at high metallicity. However, we note the high and low-α disks are not easily separated in the GALAH [Mg/Fe] and [Ca/Fe] distributions, perhaps due to the lower precision of these measurements (see Buder et al. (2018) for details). Except for Mg and Ca, the rest of the alpha elements (O, Si, Ti) show behaviours that are in line with the conclusion of many previous works: that the bulge and high-α disk population shares a similar chemical evolution (Meléndez et al. 2008, Alves-Brito et al. 2010, Johnson et al. 2014, Rojas-Arriagada et al. 2017, Jönsson et al. 2017, Bensby et al. 2017). There is thus good evidence to support a disk origin for bulge stars with [Fe/H] > -0.8. We

Table 5.2 The median [X/Fe] of the disk/halo and bulge at [Fe/H] $\lesssim -0.8$ for each alpha element.

Abundance ratio	Bulge median	Disk median
[O/Fe]	0.73 ± 0.07	0.55 ± 0.07
[Mg/Fe]	0.35 ± 0.04	0.25 ± 0.04
[Si/Fe]	0.30 ± 0.03	0.20 ± 0.04
[Ca/Fe]	0.49 ± 0.05	0.27 ± 0.06
[Ti/Fe]	0.33 ± 0.03	0.22 ± 0.03

note that McWilliam (2016) concluded the bulge is enhanced in [Mg/Fe] compared to the thick disk by examining several literature studies, however this comparison may be affected by systematic offsets between bulge RGB and thick disk main-sequence stars.

The metal-poor bulge population ([Fe/H] $\lesssim -0.8$), however, appears to be enhanced in some alpha elements compared to the thick disk and halo by ≈ 0.1 dex. This result is less conclusive for [Si/Fe], where the scatter at low metallicity is higher than other elements. Table 5.2 shows the median for disk and bulge alpha abundance ratios at [Fe/H] $\lesssim -0.8$ (averaged over three metallicity bins).

The enhanced alpha abundance ratios suggest a slightly higher star formation rate (SFR) for the metal-poor bulge population, as the initial mass function (IMF) of the bulge has shown to be consistent with that of the local disk (e.g., Calamida et al. 2015, Wegg et al. 2017). The metal-poor bulge population also has distinctive kinematics signatures: Ness et al. (2013b) found that stars with [Fe/H] < -1 have a different rotation profile to the metal-rich stars, and Zoccali et al. (2017) showed that their metal-poor bulge stars rotate more slowly. This would suggest that the metal-poor population may not share the same disk origin as the more metal-rich populations.

5.7 Conclusion

In this work, we have successfully obtained stellar parameters and α-element abundances for 832 RGB stars at latitudes $b = -5°, -7.5°, -10°$ along the minor axis of the Galactic bulge. The majority of our sample are ARGOS survey stars with pre-determined bulge memberships. ARGOS stars were selected based on metallicity so that we observe higher relative fractions of the metal-rich and metal-poor bulge populations.

According to our analysis of stars in common with ARGOS, the metallicity scale reported by Ness et al. (2013a) should be compressed; i.e., we obtain slightly higher [Fe/H] for metal-poor ARGOS stars, and vice versa. Our results suggest that along the minor axis, the spacing between ARGOS MDF component centroids should be $\approx$0.09 dex closer. The effect of this is most apparent in field $(0, -7.5)$, where primary ARGOS components A and B become almost indistinguishable. However, the ARGOS components remain distinct (given measured ARGOS dispersions) for fields $(0, -5)$ and $(0, -10)$.

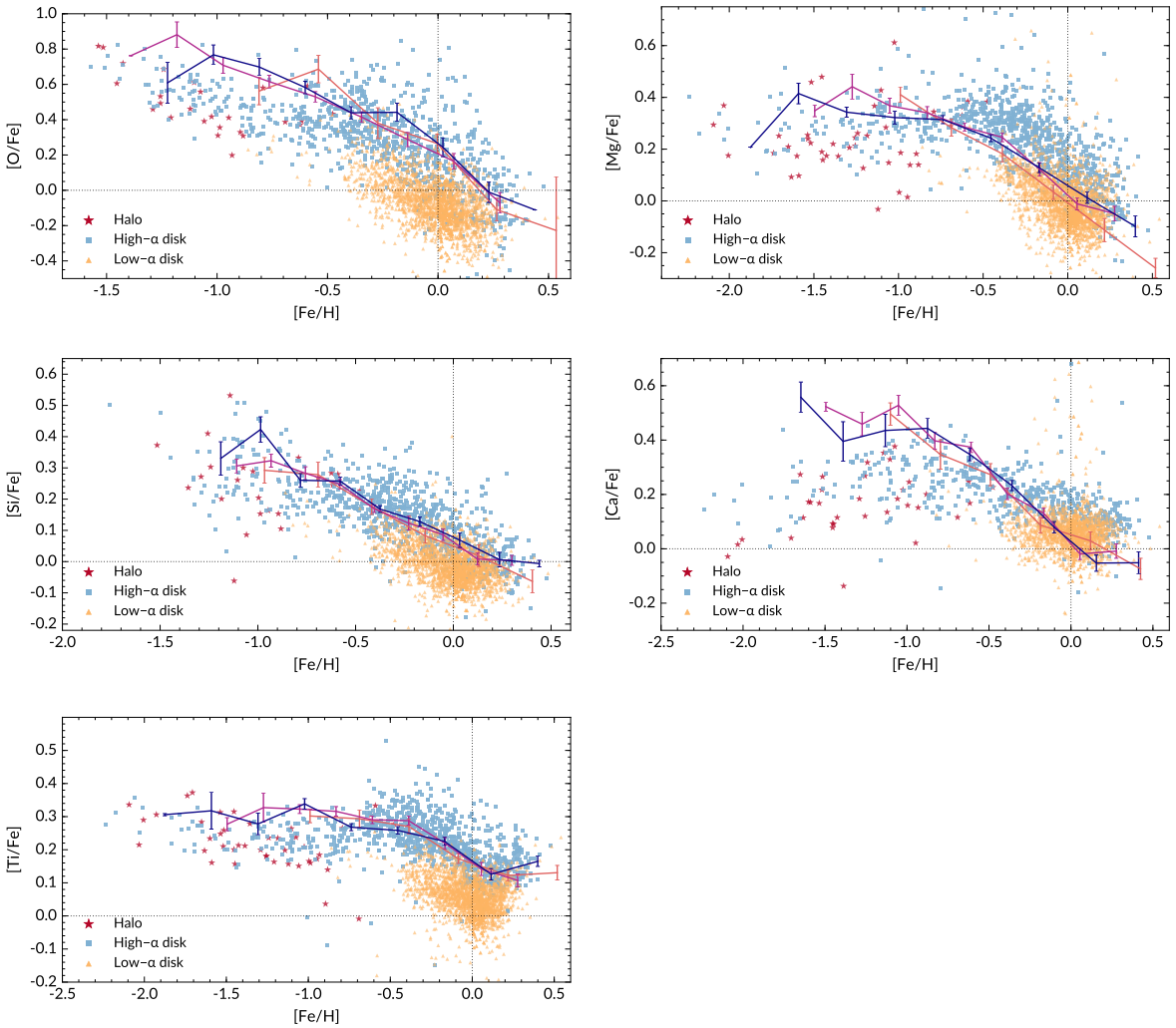

Figure 5.11 Comparison of the abundance trends in the Galactic bulge and disk/halo. The data points are training set giants from GALAH DR2, separated into the disk and halo components as described in the text. The solid lines are median abundance trends of three bulge fields along the minor axis (colours have the same meaning as in Fig 5.8).

The optical wavelength range and resolving power of the HERMES spectrograph allowed us to measure chemical abundances for up to 28 elements, including the alpha elements O, Mg, Si, Ca and Ti. In general, we find that the [X/Fe] vs [Fe/H] trends of these elements follow that of previous works at similar resolving power. We also observe similar trends to the microlensed dwarfs sample from Bensby et al. (2017), which was observed at much higher resolving power but is limited to less than 100 stars. Within the scatter of the datasets, we confirm that there are no significant systematic differences between the bulge giants and microlensed dwarfs, except for [Ca/Fe] from [Fe/H] < -0.5, where our median [Ca/Fe] is higher by up to 0.2 dex. In addition, our [Mg/Fe] values decrease as a function of [Fe/H] and do not flatten at super-solar metallicity. We find that the mean value of [α/Fe] increases with increasing distance from the plane, which is expected as the metal-poor component dominates at high latitudes. We also find that the [α/Fe] dispersion is smaller at higher latitudes.

Our metallicity coverage allowed assessment of the vertical variation in alpha abundances of the different bulge metallicity components. Within uncertainties, the abundance ratios remain uniform with height for most metallicity bins. At the metal-rich regime ([Fe/H] > 0), there is evidence of enhanced alpha-abundances in field $(0, -10)$, which is most conclusive for [α/Fe] (weighted average of Mg, Ca, Si, Ti). However, this conclusion is uncertain for individual elements, and does not seem to hold true for [Ca/Fe]. The bulge abundance trends appear to follow that of the high-α disk population, and are enhanced compared to the low-α disk population at super solar metallicities. However, the more metal-poor bulge population ([Fe/H] $\lesssim -0.8$) is enhanced compared to thick disk and halo stars at the same metallicity.

The lack of vertical abundance variation for different metallicity components and abundance trends similar to the high-α, or thick disk population, both point to fast chemical enrichment in the bulge (e.g., Friaça & Barbuy 2017). Furthermore, the metal-poor bulge population may have experienced a different evolution, as we observe that it is enhanced in alpha abundances compared to the high-α disk population. This may be compatible with previous findings that the metal-poor population has distinct kinematics compared to the metal-rich population, and indicates that the bulge does not just consist of stars originating from the disk. We further explore the chemical evolution of the bulge and its connection to the disk in the next paper of this series, which will focus on the abundances light, iron peak and heavy elements.

Acknowledgements. LD, MA and KCF acknowledge funding from the Australian Research Council (projects FL110100012 and DP160103747). LD gratefully acknowledges a scholarship from Zonta International District 24. DMN was supported by the Allan C. and Dorothy H. Davis Fellowship. LMH was supported by the project grant 'The New Milky Way' from the Knut and Alice Wallenberg foundation. MA's work was conducted as part of the research by Australian Research Council Centre of Excellence for All Sky Astrophysics in 3 Dimensions (ASTRO 3D), through project number CE170100013. Part of this research was conducted at the Munich Institute for Astro- and Particle Physics (MIAPP) of the DFG cluster of excellence "Origin and Structure of the Universe".

This publication makes use of data products from the Two Micron All Sky Survey, which is a joint project of the University of Massachusetts and the Infrared Processing and Analysis Center/California Institute of Technology, funded by the National Aeronautics and Space Administration and the National Science Foundation. We acknowledge the use of data from the European Space Agency (ESA) mission *Gaia* (https://www.cosmos.esa.int/gaia), processed by the *Gaia* Data Processing and Analysis Consortium (DPAC, https://www.cosmos.esa.int/web/gaia/dpac/consortium). Funding for the DPAC has been provided by national institutions, in particular the institutions participating in the *Gaia* Multilateral Agreement. The GALAH survey is based on observations made at the Australian Astronomical Observatory, under programmes A/2013B/13, A/2014A/25, A/2015A/19, A/2017A/18. We acknowledge the traditional owners of the land on which the AAT stands, the Gamilaraay people, and pay our respects to elders past and present.

If you wish to make an apple pie from scratch,
you must first invent the universe.

Carl E Sagan

6

Populations in the Galactic bulge: detailed abundances

This chapter is a modified version of the paper 'HERBS II: Detailed chemical composition of Galactic bulge stars' by Duong, L., Asplund, M., Nataf, D. M., et al., 2018, submitted to Monthly Notices of the Astronomical Society.

This work explores the detailed chemistry of the Milky Way bulge using the HERMES spectrograph on the Anglo-Australian Telescope. Here we present the abundance ratios of 13 elements for 832 red giant branch and clump stars along the minor bulge axis at latitudes $b = -10°, -7.5$ and $-5°$. Our results show that none of the abundance ratios vary significantly with latitude. We also observe disk-like [Na/Fe] abundance ratios, which indicates the bulge does not contain numerous helium-enhanced populations as observed in some globular clusters. Helium enhancement is therefore not the likely explanation for the double red-clump observed in the bulge. We confirm that bulge stars mostly follow abundance trends observed in the disk. However, this similarity is not confirmed across for all elements and metallicity regimes. The more metal-poor bulge population at [Fe/H] $\lesssim -0.8$ is enhanced in the elements associated with core collapse supernovae (SNeII). In addition, the [La/Eu] abundance ratio suggests higher *r*-process contribution, and likely higher star formation in the bulge compared to the disk. This highlights the complex evolution in the bulge, which should be investigated further, both in terms of modelling; and with additional observations of the inner Galaxy.

6.1 Introduction

The bulge region of the Milky Way is a complex system that has been the focus of many recent Galactic studies (see Nataf 2016, Barbuy et al. 2018 and references therein). Once thought to be an exclusively old, classical bulge, much evidence has emerged suggesting it is a pseudo-bulge, formed via disk instability. Infrared images of the Galactic bulge show its X-shaped morphology, which is supported by the double clump seen in photometric studies and kinematic studies confirmed that it rotates cylindrically (Dwek et al. 1995, McWilliam & Zoccali 2010, Kunder et al. 2012, Ness et al. 2013b, Nataf et al. 2015, Ness & Lang 2016). Furthermore, the chemistry of the bulge, in particular, the abundances of alpha elements[1] largely follow the thick disk trend (Meléndez et al. 2008, Alves-Brito et al. 2010, Gonzalez et al. 2011, Johnson et al. 2014, Bensby et al. 2017, Rojas-Arriagada et al. 2017, Jönsson et al. 2017).

There are, however, hints in the data indicating that bulge stars may have experienced a slightly different chemical evolution to the thick disk. Based on their high-resolution data of bulge microlensed dwarfs and turn-off stars, Bensby et al. (2013, 2017) found evidence that the 'knee' of the bulge, or the metallicity at which [α/Fe] begins to decline, is more metal-poor compared to the local thick disk. Because the alpha elements are thought to be produced in massive stars ($M \geq 8\ M_{\odot}$) with short lifetimes, this suggests faster chemical enrichment of the bulge region (e.g. Tinsley 1979, Matteucci & Brocato 1990). By comparing the alpha abundances of stellar samples from many different studies, McWilliam (2016) found offsets between the bulge and the thick disk, such that the bulge is more enhanced in the alpha elements. However, this conclusion is still under debate: the difference between the thick disk alpha knee and bulge is small, and may not be significant given measurement errors (Bensby et al. 2017, Rojas-Arriagada et al. 2017). Furthermore, offsets found between independent bulge and disk studies may well be due to the variations in linelists, atomic data and analysis techniques (Haywood et al. 2018).

Abundance measurements for element groups other than the alpha elements are also crucial to our understanding of chemical evolution in the Galactic bulge. The light elements Na and Al have unique anti-correlation signatures with respect to O and Mg, respectively, which can inform the origin of bulge stars (Gratton et al. 2012, Bastian & Lardo 2018, and references therein). It has also been demonstrated that, for globular clusters, relatively high [Na/Fe] indicates a helium-enhanced stellar population (e.g., Carretta et al. 2010, Dupree et al. 2011). In addition, the bulge [Al/Fe] vs [Fe/H] trend is similar to the alpha elements, which indicate that aluminium is produced in massive stars and will therefore provide formation time-scale constraints.

The iron-peak elements, although part of the same group, typically do not share the same production site and for some elements there are large discrepancies between predicted and observed abundance ratios (e.g. Romano et al. 2010). The abundance ratios of iron-

[1]Typically, alpha elements are O, Mg, Si, Ca, Ti, see e.g. Burbidge et al. (1957).

peak elements also display different trends with metallicity, not necessarily tracking iron. Scandium is thought to be produced mostly in massive stars (Woosley & Weaver 1995), and shares a similar behaviour to the alpha elements. Cu is also thought to be produced in massive stars but follows an interesting, non-alpha trend, both in the Galactic disk and bulge (Woosley & Weaver 1995, Reddy et al. 2006, Romano & Matteucci 2007, Johnson et al. 2014). However, Cu abundance measurements for bulge field stars are rare in the literature, with results from Johnson et al. (2014) being the only data available. On the other hand, Cr, Mn, Co and Ni are produced via silicon burning processes (Woosley & Weaver 1995), but their correlation with metallicity can be very different (e.g. Johnson et al. 2014, Bensby et al. 2017).

Neutron-capture elements are produced via the *r*- (rapid) or *s*- (slow) process. The *r*-process is thought to trace rapid enrichment timescales, as one of the possible formation sites is core-collapsed supernovae, or SNeII (see e.g. Woosley et al. 1994; Sneden et al. 2008 and references therein). The merging of neutron stars is now more favoured as the likely production site of the *r*-process (e.g., Thielemann et al. 2017, Côté et al. 2018). The *s*-process occurs in low- and intermediate-mass AGB stars, with lifetimes up to several Gyrs (e.g., Karakas & Lattanzio 2014). Neutron-capture elements are produced by a combination of both *s*- and *r*- processes. For certain elements, the contribution from one process is much greater the other, thus they are referred to as '*r*-process' or '*s*-process' elements. Commonly studied neutron-capture elements are Ba and Eu, which in the Sun have ≈85% and ≈5% *s*-process contribution, respectively (Sneden et al. 2008, Bisterzo et al. 2014).

There are a few gaps in the literature regarding the abundance trends of bulge stars. One is that few measurements exist for metal-poor stars between $-2 \leq$ [Fe/H] ≤ -1, while an extensive study of extremely metal-poor stars have been conducted by (Howes et al. 2015, 2016). Additionally, the number of stars with abundance measurements for elements other than alpha is still relatively small. This is mainly due to difficulties with observing faint, reddened bulge targets at high resolution. As outlined above, having abundances of other elements, such as the light and neutron-capture elements will be informative for the formation/evolution timescale of the Galactic bulge. The HERMES Bulge Survey (HERBS) was designed to address some of these gaps. As detailed in Chapter 5 (hereafter Paper I), we made use of the extensive wavelength coverage of the HERMES spectrograph, which can provide abundances for up to 28 elements. The high multiplexity of the 2dF/AAT 2 system (≈350 science objects observed in a single exposure) allows for longer integration times and thus adequate signal to noise ratio (S/N) for abundance determination. One advantage of HERBS is its compatibility with abundance measurements of the GALAH survey, which targeted disk and halo stars. By using the same atomic data and analysis method, we are able to eliminate many systematic offsets that may affect the bulge-disk comparison.

In Paper I, we have presented the HERBS survey and detailed the data analysis. There we also provided the stellar parameters and abundance ratios of five alpha elements (O, Mg, Si, Ca, Ti) for 832 bulge giants. In this paper we present and discuss the results of 13 more

elements from different nucleosynthesis channels: the light elements Na and Al; iron-peak elements Ni, Mn, Cu, Cr, Co, Sc; neutron capture elements La, Nd, Eu, Ce and Zr.

6.2 Data description and analysis

The details of data selection, observation, reduction and analysis for the stellar sample presented here have been discussed in Paper I, which the reader is referred to for more information. Briefly, the majority of the sample are red giant and red clump stars with confirmed bulge membership from the ARGOS survey (Freeman et al. 2013, Ness et al. 2013a). The 2MASS K_s magnitude range of ARGOS stars is 11–14. Our sample also includes 15 bulge stars from the EMBLA survey (Howes et al. 2016), which were added to help increase the number of metal-poor stars. We were able to probe the full metallicity range of the bulge, from [Fe/H] ≈ 0.5 to [Fe/H] ≈ -2. The minor axis fields $(\ell, b) = (0, -10)$; $(0, -7.5)$ and $(0, -5)$ were observed with the HERMES spectrograph, at resolving power $\mathcal{R} \approx 28000$. The four wavelength intervals covered by HERMES are 4713–4903 Å (blue CCD); 5648–5873 Å (green CCD); 6478–6737 Å (red CCD) and 7585–7887 Å (IR CCD).

All spectra were reduced with the standard HERMES reduction software 2dfdr v6.46[2]. Additional data processing (barycentric correction, telluric correction, co-adding) were done with custom PYTHON scripts. We used the GUESS code, which is also used by the GALAH survey, to determine radial velocities and estimate initial stellar parameters (Kos et al. 2017). The final stellar parameters were obtained with the spectral synthesis software *Spectroscopy Made Easy* (Valenti & Piskunov 1996, Piskunov & Valenti 2017) using 1D LTE MARCS model atmospheres (Gustafsson et al. 2008). Starting from initial estimates, SME solves for best-fit stellar parameters by optimising χ^2 through an iterative process. During the stellar parameter determination stage, we implement non-LTE corrections from Amarsi et al. (2016b) for Fe I lines. All lines and atomic data used to derive stellar parameters are the same as that used in GALAH survey DR2 (Buder et al. 2018). In total there are 313 stars in field $(0, -10)$, 313 stars in $(0, -7.5)$ and 204 stars in field $(0, -5)$ with reliable stellar parameters.

Elemental abundance ratios were determined by SME after stellar parameters have been established, also using χ^2-optimisation. Pre-determined wavelength regions covering each line (line masks) are given for each element. During the optimisation stage, SME computes a model spectrum based on the stellar parameters and atomic data given, and de-selects blended wavelength points within line masks. We have used the same atomic data as the GALAH survey, and where possible, the exact same lines. However, we performed line-by-line synthesis, whereas GALAH optimised all lines simultaneously for each element. In our analysis, we discovered that certain lines show problematic behaviour, such as spuriously high abundances at the metal-poor and metal-rich regimes owing either to unknown blends

[2]www.aao.gov.au/science/software/2dfdr

or possible non-LTE effects. To provide as accurate results as possible, we excluded these lines from the final abundance ratios. While every effort was made to be consistent with the GALAH survey, some of the linelist changes we implemented could not be adopted in time for the GALAH Data Release 2. As the result, GALAH would have used more lines than we did here for some elements. We discuss this further in Section 6.4. The full list of lines we used in this analysis is given in Appendix B.

To compute the final abundance ratios, we averaged line-by-line abundances (normalised to solar values), weighted by measurement uncertainties. We do not include abundances that are flagged as upper limits in the weighted average. For solar normalisation, we used abundance ratios from a HERMES twilight spectrum, which was reduced and analysed in the same manner as a typical star (see Paper I for details). This ensures systematic errors, such as uncertain $\log(gf)$ values are mostly removed. For Na and Al, we took into account departures from LTE using the computations by Lind et al. (2011) and Nordlander & Lind (2017), respectively. For all other elements, abundance ratios were computed assuming LTE. Although HERMES wavelength coverage in principle allows 28 elements to be measured, we have had to omit a number of elements for various reasons, as outlined below:

- The light element Li can only be measured with lines that are too weak for reliable abundance determination, at least for the RGB stars in this study.
- The light element K (7699 Å) show very strong temperature dependency, and large scatter likely caused by non-LTE effects and interstellar absorption that are unaccounted for.
- The iron-peak elements V and Zn only have lines in the blue arm of HERMES. Since this arm has the lowest S/N and is most affected by background blends, the abundance ratios show large scatter and/or unexpected trends.
- The abundance ratios of neutron-capture elements Rb (7800 Å), Sr (6550 Å), and Sm (4854.5 Å) can only be determined with a single, weak line at HERMES resolving power. In particular the Rb line is blended by a neighbouring Si I line. Upon inspection of spectral syntheses, it is evident that the measurements are not reliable, especially not at low S/N.
- Yttrium lines are blended or fall in regions where continuum determination is very difficult. The scatter in [Y/Fe] is ≈ 1 dex. We are not confident that these results are reliable.
- Similar to GALAH survey, our results for neutron-capture element Ba show more than 1 dex scatter for both the 5854 and 6497 Å lines at all metallicities. To date we have not found the reason for this behaviour, but it is unexpected and requires further investigation.

For most elements, the abundance ratios reported below do not show effective temperature dependence. Only the elements Mn and Co show significant trends with $T_{\rm eff}$, but they are known to be affected by non-LTE effects (Bergemann & Gehren 2008, Bergemann et al. 2010). More details can be found in Appendix A.2.

6.3 Abundance trends

In this section we discuss the [X/Fe] trends with respect to metallicity. We were able to measure abundances of most elements for [Fe/H] ≥ -1.5. For each element, we compare our results with recent high-resolution measurements for bulge field stars that span a similar metallicity range. For elements where none, or only one bulge sample is available, abundance ratios for disk stars have been included for reference. The literature samples below all assume LTE in their abundance calculations.

6.3.1 Light elements

- **Sodium** Our [Na/Fe] trend is similar to what Bensby et al. (2017) observed for microlensed dwarfs, but with larger scatter (due to lower resolution and S/N). [Na/Fe] values are enhanced low metallicities, decreasing to solar as [Fe/H] increases, and increases to above solar again for [Fe/H] > 0. This behaviour indicates that sodium is at least partly produced in massive stars, as [Na/Fe] decreases with metallicity in the sub-solar regime (Woosley & Weaver 1995). The results from Johnson et al. (2014) (also for RGB stars) show a different behaviour, where [Na/Fe] is under-abundant at the metal-poor regime. Since Johnson et al. (2014) have shown that the discrepancy is not likely due to the non-LTE corrections from Lind et al. (2011), the cause may be different lines/atomic data used.

- **Aluminium** The Al abundance trend is basically the same as the alpha elements, in agreement with Johnson et al. (2014) and Bensby et al. (2017). [Al/Fe] is enhanced by +0.4 dex at low metallicities and decreases with increasing [Fe/H]. This trend has also been observed by other authors for disk stars, and indicates SNeII origin for Al (e.g., Reddy et al. 2006, Bensby et al. 2014). There is an apparent offset of $\approx$0.1 dex around solar metallicity between our abundance ratios and that of the literature samples.

While Na and Al show disk-like behaviour in our metallicity regime, Howes et al. (2016) observed particularly low abundance ratios for these two elements for extremely metal-poor bulge stars.

6.3.2 Iron-peak elements

- **Scandium** To the best of our knowledge, only our study so far has provided scandium abundance trend for bulge field stars over a large metallicity range (but see also Grat-

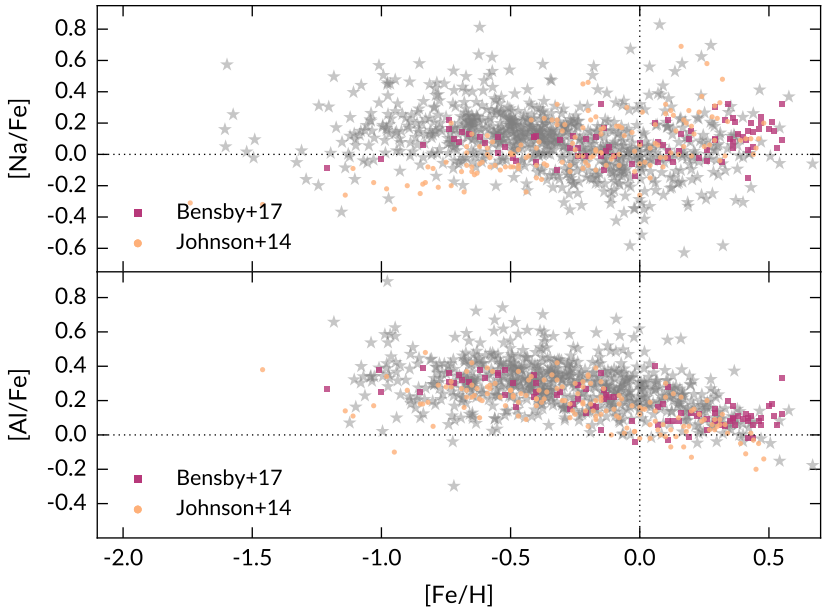

Figure 6.1 The [X/Fe] vs [Fe/H] trends for the light elements Al and Na from this work (grey stars). Shown for comparison are bulge field stars from Johnson et al. (2014) and Bensby et al. (2017).

ton et al. 2006, Casey & Schlaufman 2015, Howes et al. 2016). The Sc abundance ratios follow a well defined, alpha-like trend, in good agreement with results from Battistini & Bensby (2015) for the local disk. The [Sc/Fe] enhancement at low metallicities is not as high as observed in aluminium and the alpha elements (at maximum [Sc/Fe] ≈ 0.2 dex), but we do see a decrease in [Sc/Fe] with metallicity, reaching solar values at [Fe/H] ≈ 0. This behaviour is indicative of scandium production in massive stars, as suggested by Woosley & Weaver (1995).

- **Chromium** [Cr/Fe] ratios show very little scatter, and follow the same trend as observed by Johnson et al. (2014) and Bensby et al. (2017). [Cr/Fe] remains constant (at solar value) across the entire metallicity range.

- **Manganese** Unfortunately we were not able to measure manganese for many stars more metal-rich than [Fe/H] $= -0.5$. All Mn lines are in the blue arm of HERMES, which has the lowest S/N, and are susceptible to blends at higher metallicities. The abundances that we can measure show much larger scatter than those from Barbuy et al. (2013) (bulge giants) and Battistini & Bensby (2015) (disk dwarfs). However, the general trend is similar: that [Mn/Fe] increases linearly as a function of metallicity, and rises to [Mn/Fe] = 0 at super solar metallicity. Note that Battistini & Bensby (2015) observed a very different [Mn/Fe] vs [Fe/H] trend when non-LTE corrections are applied. The NLTE manganese abundances become essentially flat, and remain sub-solar at all metallicities.

- **Cobalt** Co is another iron-peak element that shows alpha-like behaviour, as shown by

Battistini & Bensby (2015) for disk main-sequence stars. The alpha-like trend is much less pronounced in our [Co/Fe] values, which tracks iron for [Fe/H] > -0.5, and only show a slight increase at lower metallicities. Our results are in good agreement with Battistini & Bensby (2015). We do not observe the enhanced [Co/Fe] ratios around solar metallicity as did Johnson et al. (2014).

- **Nickel** The mean [Ni/Fe] observed here is in agreement with Johnson et al. (2014), but slightly enhanced compared to Bensby et al. (2017). The [Ni/Fe] trend is reminiscent of [Na/Fe]: for both elements the abundance ratios are approximately solar between $-0.5 <$ [Fe/H] < 0 and increase as a function of metallicity at the super-solar regime. However, nickel does not show strong enhancement at the metal-poor regime and the abundance ratios basically remain constant between $-1 <$ [Fe/H] < 0.

- **Copper** The copper abundance trend in the bulge is not well established; Johnson et al. (2014) was the only study that measured copper abundance ratios for bulge field stars that cover a wide metallicity range. The copper abundance pattern we observe here is similar to that of Johnson et al. (2014): [Cu/Fe] increases as a function of metallicity for $-1 <$ [Fe/H] < -0.5, remains approximately constant between $-0.5 <$ [Fe/H] < 0, but appears to increase with metallicity at the super-solar regime. This is consistent with disk [Cu/Fe] measurements from Reddy et al. (2006). However, Johnson et al. (2014) observe a +0.4 dex enhancement in [Cu/Fe] around $-0.5 <$ [Fe/H] < 0, which may be due to blended copper lines in their analysis (McWilliam 2016).

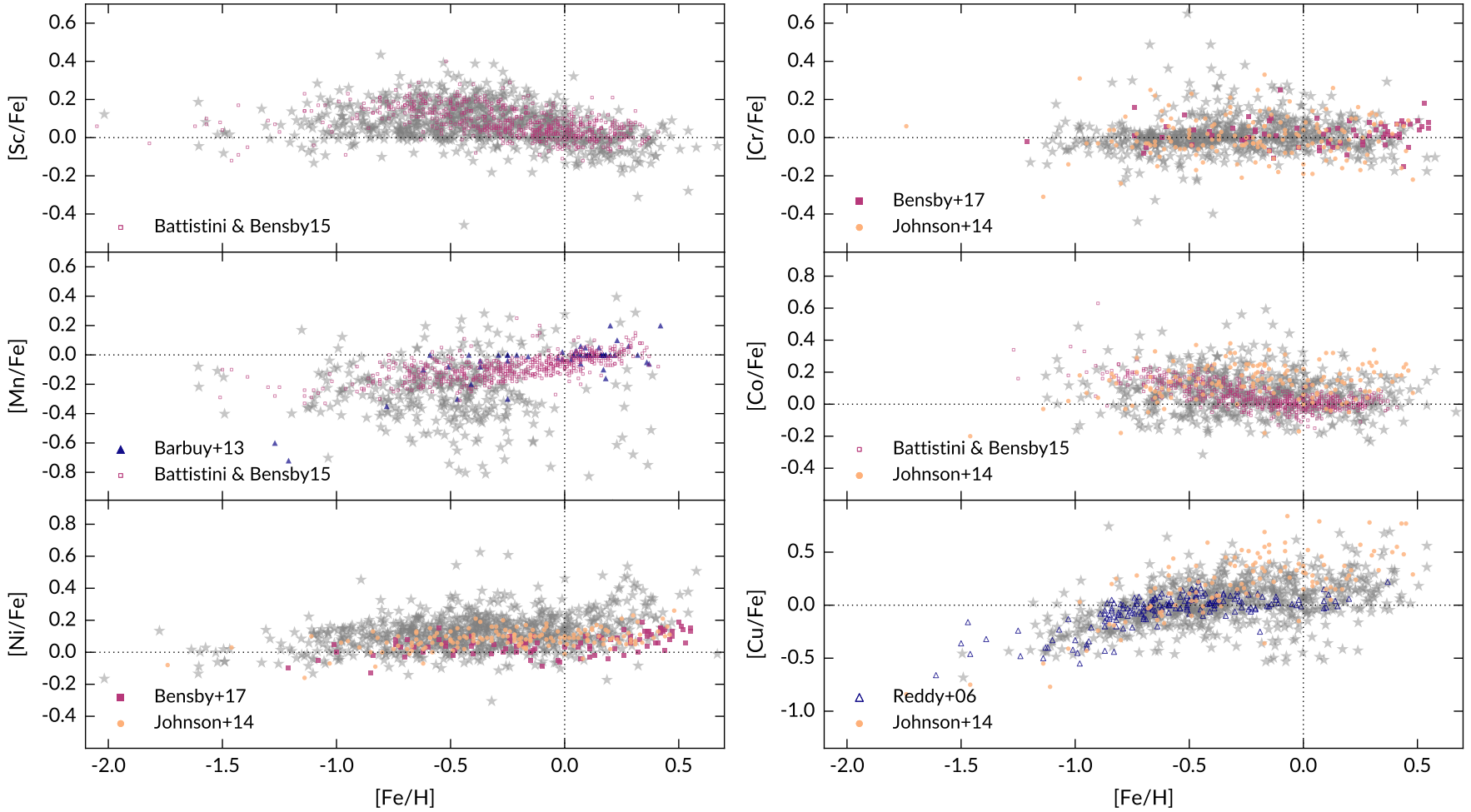

Figure 6.2 The [X/Fe] vs [Fe/H] trends for the iron-peak elements from this work (grey stars). Where few, or no bulge data for field stars can be compared against, data from studies of disk stars are included for reference (Battistini & Bensby 2015, Reddy et al. 2006).

6.3.3 Neutron capture elements

The five neutron capture abundance ratios we report here contains the *r*-process element Eu; three elements with high *s*-process contribution La, Ce, Nd and Zr (Bisterzo et al. 2014).

The abundance ratios of *s*-process elements La and Nd do not show strong variations with metallicity. In particular [La/Fe] remains solar at the metal-rich regime, and increases slightly for [Fe/H] < -0.5 (up to [La/Fe] ≈ 0.2). This is in line with the [La/Fe] trend observed by Simmerer et al. (2004). Battistini & Bensby (2016), on the other hand, reported relatively under-abundant [La/Fe] for disk stars at super-solar metallicity. Our results are not in agreement with Johnson et al. (2012), who show, on the mean, sub-solar [La/Fe] for [Fe/H] > -0.8. For [Nd/Fe], the trend observed in this work is similar to that of Battistini & Bensby (2016): the abundance ratios increase from sub-solar at [Fe/H] > 0 to [Nd/Fe] ≈ 0.2 at the metal-poor regime. Johnson et al. (2012) found the same trend, but their abundance ratios show quite large scatter around solar metallicity. The [Ce/Fe] ratios we measure remain at around solar value for [Fe/H] < 0. However, at super-solar metallicity, we observe enhanced cerium abundance ratios. Increasing [Ce/Fe] with metallicity could suggest a contributing blend that has not been accounted for in one for more of our Ce lines. At sub-solar metallicity, our [Ce/Fe] abundance ratios agree well with Battistini & Bensby (2016). The flat [X/Fe] trends of La, Nd and Ce reflect high *s*-process contribution from low mass AGB stars (Travaglio et al. 1999, Travaglio et al. 2004, Karakas & Lattanzio 2014). Since these stars have longer lifetimes and begin to contribute at higher metallicities, the yields of La, Nd and Ce increase with [Fe/H] and therefore we do not observe a steep decline in [X/Fe].

The lanthanum and europium and zirconium abundance ratios show linear correlations with metallicity, decreasing as metallicity increases. However, the [La/Fe] slope that we observe is relatively shallow. We observe a strong slope for both europium and zirconium, but [Eu/Fe] is enhanced compared to [Zr/Fe]. This observation is broadly in agreement with both Johnson et al. (2012) and Battistini & Bensby (2016). However, note that our [Zr/Fe] values show much larger scatter at super-solar metallicity, and are almost ≈ 0.2 dex under-abundant compared to Battistini & Bensby (2016). Our [Eu/Fe] values also show much larger scatter than the literature samples. The [Eu/Fe] trend is similar to the alpha elements and aluminium, and indicates a possible SNeII origin for this element. Our results suggest a [Eu/Fe] plateau at [Fe/H] $\lesssim 0.5$ dex for the bulge. It is worth noting that the decline of [Zr/Fe] with metallicity observed here (and by Johnson et al. 2012, Battistini & Bensby 2016) is steeper than the other *s*-process elements, despite Zr having similar *s*-process fraction to Nd. This may suggest a higher *r*-process contribution to zirconium yields than expected (see also McWilliam 2016).

The abundance trends we observed for La, Nd and Eu agree qualitatively with Van der Swaelmen et al. (2016), who reported neutron-capture abundance ratios for 56 red giants in the bulge. The cerium abundance ratios from that work are very high/low at low/high

metallicities. Furthermore, Van der Swaelmen et al. (2016) reported lower [Eu/Fe] values compared to our results and the comparison samples shown in Fig 6.3.

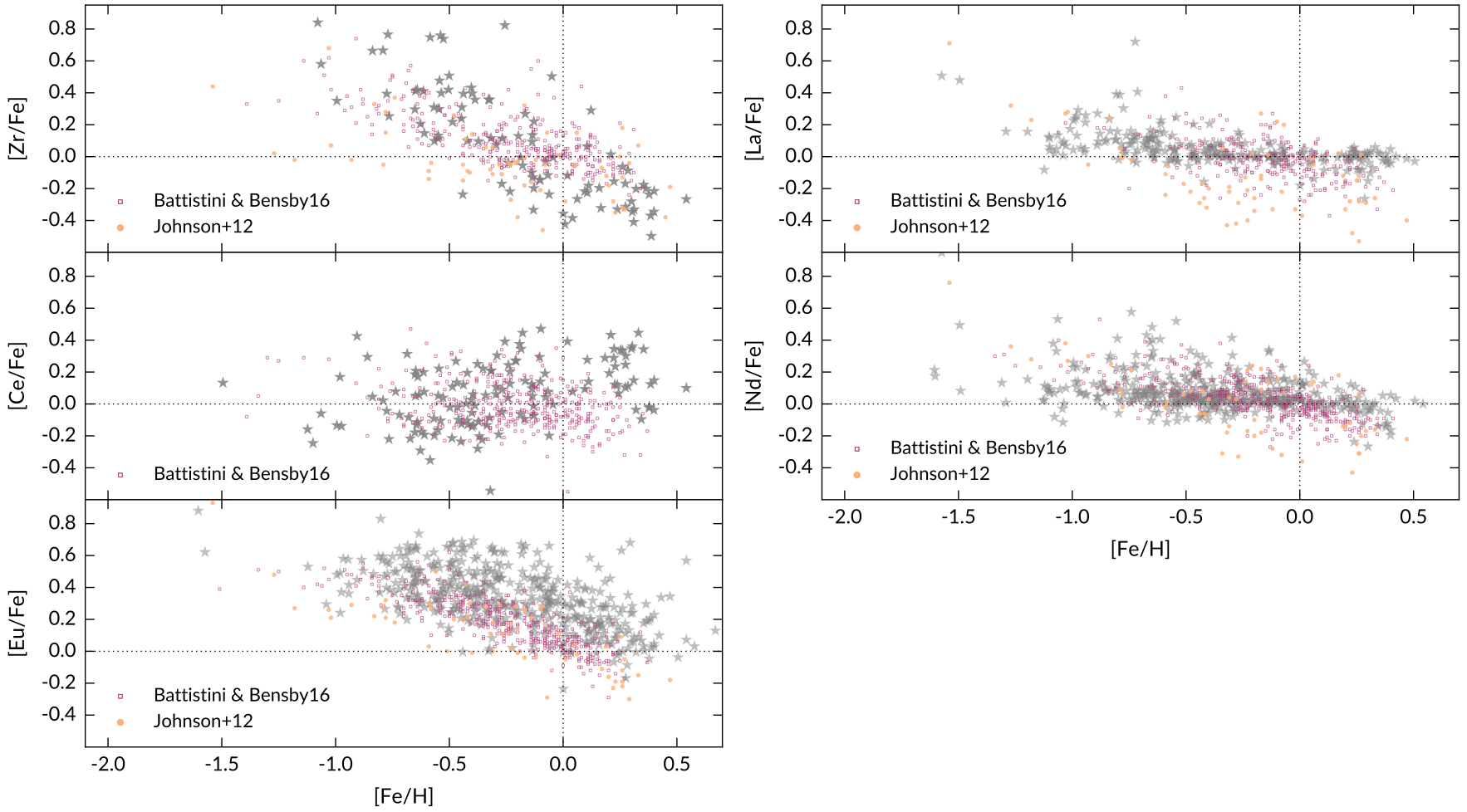

Figure 6.3 The [X/Fe] vs [Fe/H] trends for the neutron-capture elements from this work (grey stars). Where few, or no bulge data for field stars can be compared against, disk data from Battistini & Bensby (2016) are included for reference.

6.4 Latitude variation and comparison to the disk and halo

The aim of this section is to identify and discuss the similarities and differences between the chemistry of the bulge and other Galactic components. Such comparison can give insights on how the bulge formed and evolved (e.g., McWilliam 2016, Haywood et al. 2018). As mentioned previously, we strived to be as consistent as possible with the GALAH survey when conducting our analysis. This is to facilitate a consistent comparison between the bulge and other Galactic components observed by GALAH. However, in this study we decided to remove certain lines from the GALAH linelist that show unexpected trends, or prominent blends. Because we used the same analysis techniques and atomic data, our results are still mostly consistent with GALAH (see Paper I). For some elements, however, the removal of these lines caused discrepancies between this work and the GALAH survey. For example, we observe systematic differences in [Sc/Fe] abundance ratios, where our results are ≈0.15 dex lower than GALAH values, as shown in Fig 6.4. The likely reason for this is our removal of a scandium line that showed very enhanced abundance ratios at all metallicities, and a strong increase in [Sc/Fe] with with increasing [Fe/H]. We note that the majority of GALAH dwarf stars do not deviate significantly from the trend reported by Battistini & Bensby (2015), suggesting that the issue mainly manifests in giants (see Fig. 23 of Buder et al. 2018). We therefore cannot provide conclusions for [Sc/Fe] in terms of its connection to other Galactic components. Furthermore, we do not provide a comparison for the element Nd, as these abundance ratios were not released as part of GALAH Data Release 2.

In the sections below, we have selected GALAH disk and halo giants with similar stellar parameters to our bulge sample for comparison. We also used the same definition as in Paper I to assign disk/halo membership. The median bulge abundance trends and standard errors were calculated for [Fe/H] bins that are ≈0.2 dex wide. Here, data points that lie more than two sigma from the median were omitted so that metallicity bins with few data points are not affected by outliers. The median bulge abundance trends are also used to assess whether or not different bulge populations show latitude-dependent variations. Mn, Zr and Ce are excluded entirely from this exercise because we have too few data points to compute mean abundance trends. We note that Zr and Ce abundance ratios were also not available in the GALAH dataset.

6.4.1 Light elements

For both Na and Al, we do not observe significant systematic latitude variations at fixed metallicity given the standard errors. The two disk populations (low and high-α) are not distinguishable by their [Na/Fe] abundances, but some distinction can be seen in [Al/Fe]. The high-α population is also enhanced in [Al/Fe] compared to the low-α population. Our comparison shows that the disk and bulge basically have the same [Na/Fe] trends for [Fe/H] ≥ -1 (see also Alves-Brito et al. 2010). At metallicities lower than -1, there is a difference

between the bulge and thick disk/halo: the bulge [Na/Fe] remain enhanced, meanwhile, [Na/Fe] decrease to sub-solar values for the thick disk and halo. In addition, we find that the aluminium abundances in the bulge is generally enhanced compared to the low-α disk, and is consistent with the behaviour of the high-α disk. From [Fe/H] ≈ -0.8, the bulge abundance trends lie above the thick disk. This has also been observed in the alpha elements (see Chapter 5). The few halo stars in the GALAH sample show very large scatter in [Al/Fe].

It has been confirmed by many authors that aluminium is produced in massive stars, and the [Al/Fe] trend closely resemble that the alpha elements. The so-called 'zig-zag' [Na/Fe] trend can be understood if Na is produced in massive stars, but the yield is metal-dependent (i.e., increasing with [Fe/H]) (McWilliam 2016, Bensby et al. 2017). If both aluminium and sodium are primarily produced in SNeII, then it appears that the metal-poor bulge population ([Fe/H] < -0.8) contains excess SNeII ejecta compared to the disk and halo.

The [Na/Fe] and [Al/Fe] ratios we measured here do not show the anti-correlation signature with [O/Fe] and [Mg/Fe], as often observed in globular clusters. We could expect stars with globular cluster chemistry in our sample, since Schiavon et al. (2017) found nitrogen-rich bulge stars that may have originated from a dissolved globular cluster in APOGEE data. It is unclear, however, if these stars could be distinguished in our abundance space: while the [Al/Fe]-[N/Fe] correlation was observed, the [Al/Fe]-[Na/Fe] correlation was not confirmed by Schiavon et al. (2017).

[Na/Fe], He-enhancement and the double red clump

The double red clump (double RC), or the presence of a faint and bright red clump population was confirmed by multiple authors from photometric surveys (e.g., McWilliam & Zoccali 2010, Nataf et al. 2015). The double RC is typically associated with the X-shaped morphology of the bulge, but this is not without contention. Lee et al. (2015) and Joo et al. (2017) argue that double clump can arise from two populations with different helium content, such that the helium-enhanced population manifests as a brighter red clump branch. This would be similar to multiple stellar populations with distinct helium abundances observed in globular clusters (GCs) (e.g., D'Antona et al. 2010, Dupree et al. 2011). Because helium-enhanced populations in GCs also show strong sodium enhancement (e.g., Carretta et al. 2010), one would expect to observe the same [Na/Fe] enhancement in the bulge. At high latitudes a long the minor axis (e.g. $b = -10°$), we should also see a higher fraction of sodium-rich stars than at lower latitudes according to the model of Lee et al. (2015). In contrast, our results here show that [Na/Fe] is very much uniform at all latitudes. Joo et al. (2017) also cited the larger spread in bulge [Na/Fe] measurements (Johnson et al. 2014) compared to the disk/halo as evidence that the bulge may contain more helium-rich stars. But this conclusion is based on multiple studies which could have large systematic offsets and differences in their intrinsic precision. Both Bensby et al. (2017) and this work have shown that the spread in bulge and disk sodium abundances are comparable for stars that

are homogeneously analysed. In theory, helium enhancement similar to the phenomenon observed in globular clusters may be able to explain the split red clump in the bulge, but this explanation is not supported by our [Na/Fe] measurements. However, it is still possible for the bulge RC to contain populations with different He content.

6.4.2 Iron-peak elements

Within errors, the iron-peak elements mostly show uniform abundance ratios as a function of latitude, as shown in Fig 6.4. Scandium exhibits slight latitude variations around solar metallicity, where field $(0, -10)$ has higher [Sc/Fe] than the other fields. However, this may be due to the small number of stars in each bin at high metallicities. We do not observe differences between bulge and disk abundances for cobalt[3]. Both the bulge and disk show a rather flat [Co/Fe] trend, with a modest increase at low metallicities. Although we show the GALAH [Sc/Fe] ratios against our results, the large systematic difference prevents us from making a meaningful comparison.

The GALAH survey was able to measure [Cr/Fe] at much lower metallicity than we could (due to higher S/N of GALAH stars), but with larger scatter. For all stars with < -1 [Fe/H] < 0.2, where we could measure [Cr/Fe], the bulge abundance ratios follow the same trend as the disk, which remains constant at all metallicities. However, GALAH disk stars may have slightly enhanced mean [Cr/Fe] (by $\approx$0.05 dex) compared to bulge stars. This perhaps indicate a small zero point error in GALAH results. We note that the GALAH [Cr/Fe] ratios begin to decrease with metallicity for [Fe/H] < -1, and at [Fe/H] ≈ -1, the mean GALAH [Cr/Fe] seems to be slightly lower than ours. However, this conclusion is less certain due to the lack of bulge data points at this metallicity regime.

For nickel, the bulge abundance ratios are in agreement with that of the disk. There is a difference compared to GALAH disk/halo stars in the metal-poor regime ([Fe/H] < -0.8). Here the bulge is enhanced in [Ni/Fe] by up to 0.2 dex compared to the disk and halo. This enhancement at low metallicity is qualitatively similar to the behaviour of [Na/Fe] we observed in the previous section. As McWilliam (2016) noted, enhanced [Ni/Fe] in the metal-poor bulge population could indicate more SNeII material in their birth environment. Some halo stellar populations that are deficient in SNeII products, such as the alpha elements, also show relatively lower [Ni/Fe] ratios (e.g., Nissen & Schuster 2010). From $-0.8 \lesssim$ [Fe/H] $\lesssim -0.5$, the bulge has slightly enhanced [Ni/Fe] compared to the disk (by 0.05 dex). But this is similar to the typical abundance ratio uncertainties of $\approx$0.04 dex.

The bulge copper abundance ratios follow the same trend as the GALAH sample. For all stars with [Fe/H] ≥ -0.8, there is no noticeable difference between the mean [Cu/Fe] of the bulge and the disk. In addition, both populations clearly show increasing [Cu/Fe]

[3]We note that the high-α and low-α disks differ in their mean [Co/Fe] by 0.05 dex, smaller than the typical abundance uncertainties (0.08 dex). Because the two disk populations overlap substantially, and extend the same range, we did not discuss them separately.

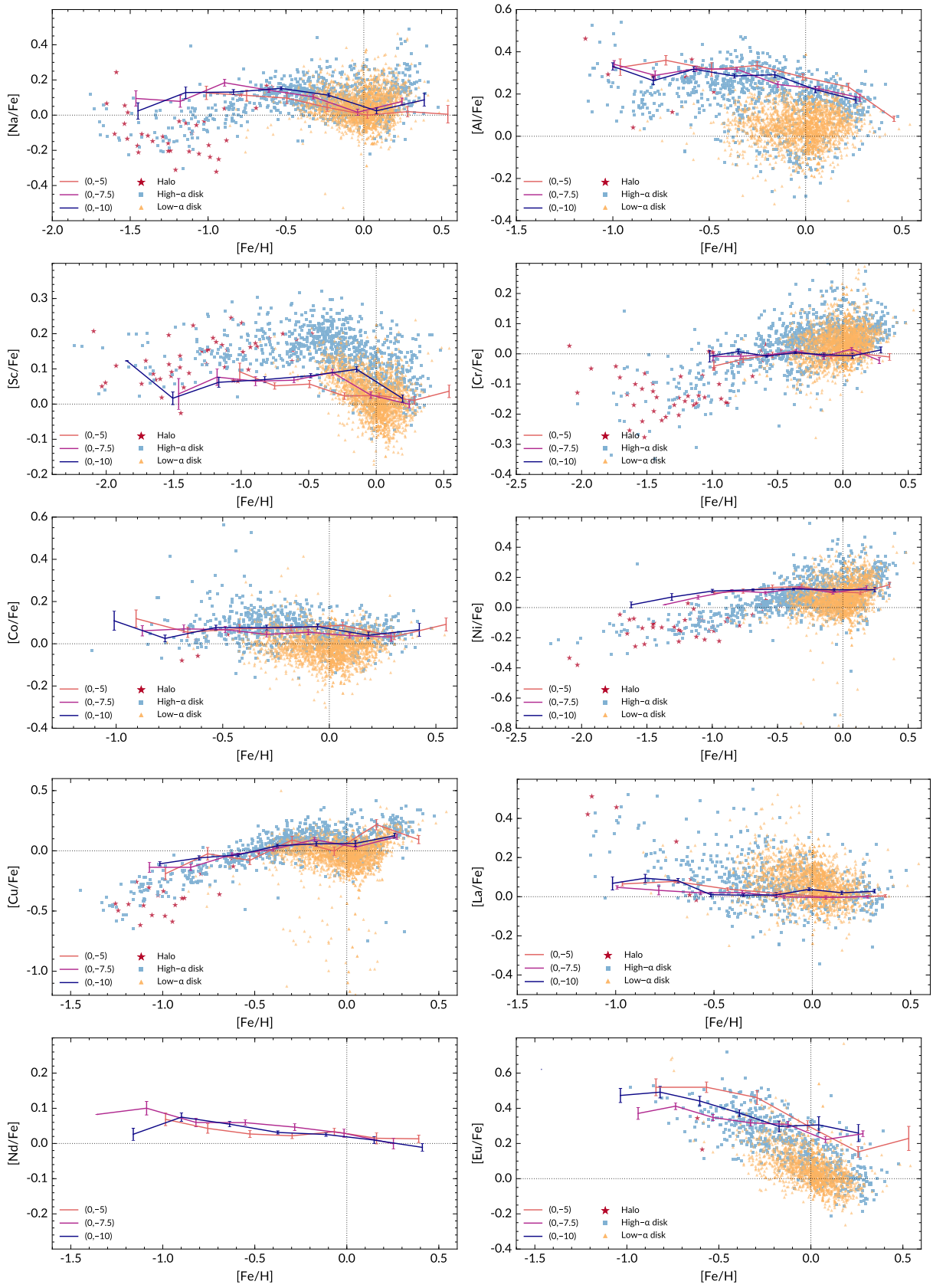

Figure 6.4 Comparison of the bulge and GALAH disk/halo sample for light, iron-peak and neutron-capture elements. The solid lines indicate median bulge trends at three minor-axis latitudes. While the GALAH [Sc/Fe] ratios are plotted here, we *do not* compare our results with GALAH due to systematic offsets (see text for details).

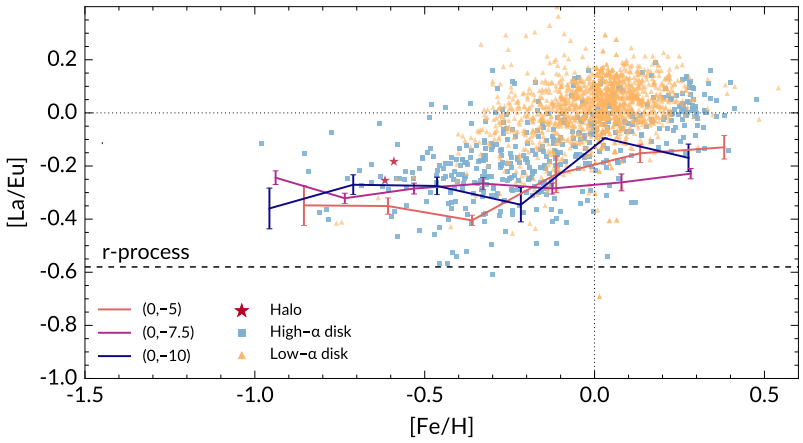

Figure 6.5 The *s*/*r*-process ratio in the bulge and disk/halo. The solid lines indicate median bulge trends at three minor-axis latitudes. The dashed line shows the pure *r*-process ratio from Bisterzo et al. (2014).

at super-solar metallicity. At $-1 \lesssim$ [Fe/H] $\lesssim -0.8$, it appears that the bulge [Cu/Fe] median trends lie just above disk/halo stars. However, the disk and halo samples are relatively sparse in this metallicity range and the difference is not significant when errors in the median bulge trends are taken into account. The variation of [Cu/Fe] with metallicity suggests that copper is produced via the weak *s*-process in massive stars, and its yield increases with metallicity (e.g., Romano & Matteucci 2007). As mentioned previously, Johnson et al. (2014) reported enhanced [Cu/Fe] around [Fe/H] ≥ -0.5. This lead McWilliam (2016) to tentatively conclude that the bulge may have higher copper yields than the local disk, and therefore higher overall star formation rate. Our observations confirm that this is not the case. If the bulge copper abundance ratios are at all enhanced compared to the disk, this would be limited only to the metal-poor population with [Fe/H] $\lesssim -0.8$.

6.4.3 Neutron capture elements

As can be seen in Fig 6.4, no consistent trend with latitude is observed for La, Nd and Eu. We could not compare our [Nd/Fe] values with GALAH because they were not available as part of the survey data release. However, our [La/Fe] trend seems to be consistent with the GALAH disk sample. Both the disk and bulge show flat [La/Fe] with metallicity, but the disk has larger scatter. We also note that at sub-solar metallicity, the disk [La/Fe] is ≈ 0.1 dex higher than the bulge. This is interesting, given that the disk sample from Battistini & Bensby (2016) does not show this enhancement compared to our results. In this case we used the same La lines as GALAH, so there should not be any systematic offsets. The higher [La/Fe] abundance ratios in the disk could indicate more efficient *s*-process compared to the bulge. There are too few halo data points for us to make a comparison, and the scatter in [La/Fe] is very large for halo stars.

Table 6.1 The median [X/Fe] of the disk/halo and bulge at [Fe/H] $\lesssim -0.8$ for some light and iron-peak elements. See text for details.

Abundance ratio	Bulge median	Disk median
[Na/Fe]	0.14 ± 0.06	-0.06 ± 0.06
[Al/Fe]	0.34 ± 0.05	0.19 ± 0.09
[Cr/Fe]	-0.02 ± 0.02	-0.11 ± 0.03
[Ni/Fe]	0.07 ± 0.03	-0.03 ± 0.03

Table 6.2 The median [La/Eu] of the disk/halo and bulge at different metallicity bins. The median and error in the mean are shown. See text for details.

Metallicity range	Bulge median	Disk median
$0.2 <$ [Fe/H] < 0.4	-0.16 ± 0.02	0.02 ± 0.01
$0.0 <$ [Fe/H] < 0.2	-0.26 ± 0.04	0.034 ± 0.003
$-0.2 <$ [Fe/H] < 0.0	-0.30 ± 0.03	-0.017 ± 0.005
$-0.4 <$ [Fe/H] < -0.2	-0.28 ± 0.03	-0.12 ± 0.01

For the *r*-process element Eu, our comparison with the GALAH sample indicates that the bulge is enhanced in [Eu/Fe] compared to the disk for [Fe/H] $\gtrsim -0.4$. At lower metallicities, the disk sample becomes quite sparse and bulge [Eu/Fe] ratios begin to show very large scatter. This is probably the reason why for all stars with [Fe/H] $\lesssim -0.4$, we can find no difference between the disk and bulge samples. We only used one of the two Eu lines in the GALAH linelist, but the line that we discarded is very weak, and if anything this line would have contributed even higher Eu abundances.

In Fig 6.5, we show the *s*/*r*-process ratio for our bulge sample and the GALAH disk/halo sample using [La/Eu] abundance ratios. Overall we observe a consistent trend with previous works, that the [La/Eu] ratio in both the disk and bulge increase as a function of metallicity (McWilliam & Zoccali 2010, Johnson et al. 2012, Van der Swaelmen et al. 2016). However, the bulge [La/Eu] ratios are markedly lower than in the disk (see Table 6.2), closer to the pure *r*-process ratio from Bisterzo et al. (2014). At sub-solar metallicity, the bulge is more similar to the high-α disk population. From solar metallicity and above, the GALAH sample consists of mostly low-α disk stars, which appear to have higher *s*-process contribution. However, we should mention that Battistini & Bensby (2016) found no distinction between their high and low-α disk population, and their [La/Eu] ratios are similar to that of our bulge sample.

6.5 Conclusion

As part of the HERBS survey, this work reports abundances for 13 elements in the light, iron-peak and neutron-capture families, in addition to the five alpha elements reported in Paper I. For most of the elements, we can measure abundances to $0.5 \lesssim$ [Fe/H] $\lesssim -1.5$. We assessed the abundance trends at different latitudes along the minor axis and compared the chemistry of bulge stars with disk/halo stars from the GALAH survey. In addition to comparing only stars with similar parameters, the same atomic data and analysis method is used in this work and GALAH. This removes the major systematic offsets between the two sets of results, even though there are some variations between the two pipelines.

In general, we find that the [X/Fe] vs [Fe/H] trends follow that of previous studies (of both disk and bulge stars) at similar or higher resolving power. For the bulge in particular, we do not observe enhanced copper and cobalt abundances, nor did we observe sub-solar [La/Fe] and [Zr/Fe] in the bulge as did Johnson et al. (2014). The majority of our iron-peak elements agree quite well with abundances from Battistini & Bensby (2015), who studied main-sequence and sub-giant stars in the local disk. For the heavy elements, there are notable differences in the [La/Fe] and [Ce/Fe] trends between this work and the Battistini & Bensby (2016) disk sample.

Of the neutron-capture elements, we observed rather flat trends in La, Ce and Nd, confirming the high *s*-process contribution to the yields of these elements. The *s*-process element Zr shows a steep decline with metallicity that is comparable to Eu. This observation is in agreement with other studies in the literature, and may also suggest that Zr has a higher *r*-process contribution than expected. [Eu/Fe] decrease with metallicity similarly to the alpha elements. A plateau can be seen at [Fe/H] ≈ -0.5 dex, after which the Eu abundance ratios decrease rapidly.

We do not observe consistent latitude-dependent variations in any of the elements. The uniformity of [Na/Fe] with latitude, and the lack of a Na-enhanced population indicate that the double RC observed in the bulge is not due to helium enhancement similar to that observed in globular clusters. Compared the disk/halo samples from GALAH, the overarching observation is that the bulge follows the same abundance trends as the disk. For Al, which behaves like an alpha element, the bulge is enhanced compared to the low-α disk population. There are also differences between the Galactic components at low metallicity for some elements. In particular, the more metal-poor bulge population ([Fe/H] $\lesssim -0.8$) appears to have enhanced Na, Al, Ni and possibly Cu abundance ratios compared to the disk. In the previous paper of this series, the metal-poor population also showed enhanced [X/Fe] for the majority of the alpha elements. Because these elements likely have SNeII origin, our results suggest that this population contains more SNeII material (relative to SNIa) than the more metal-rich bulge population. For all stars with [Fe/H] ≥ -0.8, the bulge seems to the share the same chemical evolution as the disk for the light, alpha and iron-peak elements. However, the neutron-capture elements La and Eu indicates that the

r-process was more dominant in the bulge than in the disk. This result indicates perhaps a higher star formation rate in the bulge compared to the disk.

Although we confirm chemical similarities between the disk and bulge for most elements, there are also differences indicating that the stellar population with [Fe/H] $\lesssim -0.8$ has distinct chemistry to the disk/halo at the same metallicity. Furthermore, the neutron-capture elements show that the bulge may have experienced higher star formation rate than the disk. Recently, many studies in the literature have asserted that the metal-rich ([Fe/H] $\gtrsim 0.20$) bulge stars are largely the product of a dynamically buckled inner thin disk (see e.g., Di Matteo et al. 2015, Fragkoudi et al. 2018; and Nataf 2017 for a review). This is supported by the similarity between thin disk and bulge abundance ratios (e.g., Bensby et al. 2013, 2017). However, we have demonstrated that this similarity is not confirmed across the chemical abundance space spanned by our investigation. Differences can be seen not only for neutron-capture elements La and Eu, but also for Al. In addition, Paper I shows that the elements O and Ti follows the thick disk trend at high metallicity, and remain enhanced compared to the thin disk.

These conclusions further highlight the complex evolution in the bulge, which should be investigated further both in terms of alternative models (e.g., Inoue & Saitoh 2012) and more extensive observational coverage of the inner Galaxy.

Acknowledgements. LD, MA and KCF acknowledge funding from the Australian Research Council (projects FL110100012 and DP160103747). LD gratefully acknowledges a scholarship from Zonta International District 24. DMN was supported by the Allan C. and Dorothy H. Davis Fellowship. MA's work was conducted as part of the research by Australian Research Council Centre of Excellence for All Sky Astrophysics in 3 Dimensions (ASTRO 3D), through project number CE170100013. Part of this research was conducted at the Munich Institute for Astro- and Particle Physics (MIAPP) of the DFG cluster of excellence "Origin and Structure of the Universe". This publication makes use of data products from the Two Micron All Sky Survey, which is a joint project of the University of Massachusetts and the Innfrared Processing and Analysis Center/California Institute of Technology, funded by the National Aeronautics and Space Administration and the National Science Foundation. The GALAH survey is based on observations made at the Australian Astronomical Observatory, under programmes A/2013B/13, A/2014A/25, A/2015A/19, A/2017A/18. We acknowledge the traditional owners of the land on which the AAT stands, the Gamilaraay people, and pay our respects to elders past and present.

If you find yourself at sea in a small unlighted boat alone in the darkness of a cloudless night, and if you gaze into the darkness of the space between the stars, then keep wide awake. And if your mind is full of wonder and your heart is full of peace, there is a chance that you will understand.

John L Dobson

7 Conclusion

The Milky Way is a benchmark system that is central to our understanding of how spiral galaxies form and evolve. Properties of Galactic stellar populations, such as their kinematics, metallicity and elemental abundances have revealed important processes in the Galaxy's assembly history. Over the last few decades, our knowledge of the Galaxy has undergone an evolution itself as new evidence emerge from increasingly larger stellar samples and more accurate measurements. In particular, there is now growing consensus on the origin of two major and controversial Galactic components that are closely linked: the thick disk and the bulge. However, many evolutionary aspects of these components are not completely understood, but necessary to fully establish the assembly history of the Milky Way.

This thesis examined the Galactic disk and bulge in order to better understand the processes from which they originate. To this end, we observed a large number of Galactic stars using the HERMES spectrograph on the 4 metre Anglo Australian Telescope. The spectrograph delivers high-resolution spectra ($\mathcal{R} \equiv \lambda/\Delta\lambda = 28000$), covering four optical wavelength regions, each approximately 250 Å wide. This allowed us to obtain accurate stellar parameters and relative abundances for up to 28 elements, which provided important insights on the evolution of the Galaxy.

Like many spiral galaxies in the local group, the Milky Way appears to contain two disk components: a high density population that resides close to the plane (thin disk), and a more sparse component that occupies large heights above the Galactic plane (thick disk). The Galactic 'thin' and 'thick' disks show differences in kinematics, metallicity and elemental abundances, but can be most easily distinguished by the [α/Fe][1] abundance ratios.

[α/Fe] is defined as the average of alpha-capture elements, which are typically O, Mg,

[1]In Chapter 4, [α/Fe] was denoted [α/M], as metallicity was denoted [M/H]. Thereafter, we used [α/Fe] and [Fe/H] to denote the same values, as this notation is more often used in the literature.

Si, Ca and Ti (Burbidge et al. 1957). Because the alpha elements are produced in core-collapsed supernovae (SNeII) which have short lifetimes, relatively high [α/Fe] indicates more rapid formation timescales (e.g., Tinsley 1979, Matteucci & Brocato 1990). The 'thick' disk is markedly more enhanced in [α/Fe], which means that its evolution was much faster than that of the 'thin' disk. However, the origin of the Galactic thick disk has been a subject of intense debate ever since it was discovered. Some of the most discussed scenarios are disk heating by minor mergers and radial migration of stars from the inner to the outer Galaxy. Our disk study aimed to address the still contentious properties of the thick disk and interpret our results in the context of Galactic disk evolution.

As part of the GALAH pilot survey, we targeted disk stars in the direction of Galactic anti-rotation at $\ell \approx 270°$, and five latitudes $b \approx -16°, -22°, -28°, -34°$, and $-42°$. By observing fields at high latitudes, we were able to obtain a larger fraction of thick disk stars, especially at greater heights above the plane. The final sample contains 3191 giants, extending up to 4 kpc in height and concentrated within 1.5 kpc around the solar radius. This allowed us to reliably determine the vertical metallicity and α-abundance profiles of the disk and its components.

We assigned thin and thick disk membership using likelihood probabilities from a Gaussian mixture model computed for the combined metallicity, [α/Fe] and kinematic distribution. After correcting for magnitude and colour selection effects, we found a steep vertical metallicity gradient for the entire disk: $\mathrm{d[M/H]}/\mathrm{d}z = -0.22 \pm 0.01$ dex kpc^{-1}. This value is in agreement with recent estimates from large spectroscopic surveys such as SEGUE and APOGEE, noting that our sample covers a larger range in height above the plane than most literature studies. The thin disk, or low-α population, also shows a steep negative vertical metallicity gradient, with $\mathrm{d[M/H]}/\mathrm{d}z = -0.18 \pm 0.01$ dex kpc^{-1}. The thick disk, or [α/Fe]-enhanced population, is found to have a shallow vertical metallicity gradient of -0.058 ± 0.003 dex kpc^{-1}. The vertical metallicity gradient of the thin disk is similar in amplitude to those of previous studies. For the thick disk, we established that there is a vertical metallicity gradient, however it is shallower than reported by some studies in the literature. Both of the disk components have rather flat vertical [α/Fe] gradients. We measured $\mathrm{d[\alpha/Fe]}/\mathrm{d}z = 0.008 \pm 0.002$ dex kpc^{-1} for the thin disk, and $\mathrm{d[\alpha/Fe]}/\mathrm{d}z = 0.007 \pm 0.002$ dex kpc^{-1} for the thick disk. Furthermore, the vertical [α/Fe] profile of the Milky Way disk is not continuous: two over-densities corresponding to the high- and low-α components can be observed.

The negative vertical metallicity gradient of the thin disk is indicative of radial migration being an important process for its evolution. As for the thick disk, the observed metallicity gradient rules out formation scenarios that produce a uniform vertical metallicity distribution. The gradient observed in this work could have arisen from a settling phase of the disk, minor merger episodes, or caused by radial migration. However, Aumer et al. (2016) found that in their standard model, outwardly-migrating stars are not responsible for thick disk formation. Mergers cause flaring of the disk, but the high-α population shows little

to no flaring (Bovy et al. 2016, Mackereth et al. 2017). Recent cosmological simulations and studies of disk galaxies at high redshift indicate that disks are born thick and settle over time into a thin component. A decrease in star formation rate at an early epoch (e.g., due to a merger episode or bar formation) could be the reason for the different chemistry of thick and thin disk stars. This scenario would be qualitatively consistent with the thick disk properties observed in this work and other works in the literature. However, the vertical metallicity and [α/Fe] distributions of galactic disks in cosmological simulations have not been studied in detail. It is essential that these are established in order to confirm the origin of the Milky Way thick disk.

High resolution abundance studies have shown that the evolution of the Galactic disk, especially the thick disk, also have implications for the origin of the bulge. Meléndez et al. (2008), Alves-Brito et al. (2010), Bensby et al. (2013) showed that the alpha-element abundance ratios of bulge stars were similar to the thick disk, not significantly higher as previously believed (e.g., Fulbright et al. 2007). To date, multiple studies have confirmed this similarity. In addition, the metallicity distribution of the bulge has been shown to be complex, consisting of up to five components that may have arisen from disk populations (e.g., Ness et al. 2013a, Bensby et al. 2017). This suggests the bulge was formed via disk instability, a secular process. Other evidence, such as cylindrical rotation and infrared images showing a boxy, X-shaped structure, also point to a secular origin for the Milky Way bulge. However, although the chemistry of the thick disk and bulge are similar, differences have emerged in the abundance ratios of alpha, light and neutron-capture elements. Unfortunately there are no definitive conclusions regarding the chemistry of the bulge, or indeed if it is at all different to the disk. This is largely due to the scarcity of abundance measurements for elements other those of the alpha group, and relatively small number of bulge stars with a comprehensive chemical inventory.

To gain a better understanding of the Galactic bulge and how it is related to the disk, we observed giant branch and red clump stars along the minor axis, at latitudes $b = -5°, -7.5°, -10°$. The majority of our targets were selected from the ARGOS survey, which have predetermined bulge memberships (Freeman et al. 2013, Ness et al. 2013a). Our selection function prioritised the metal-poor ($[\mathrm{Fe/H}]_{\mathrm{ARGOS}} \leq -0.8$) and metal-rich ($[\mathrm{Fe/H}]_{\mathrm{ARGOS}} \geq 0.2$) populations, such that close to 100% of these populations were observed. The intermediate bulge components were given ≈50% allocation. This selection ensured that there are enough stars at all metallicity regimes to establish bulge abundance trends.

We successfully derived stellar parameters for 832 stars, as well as measured abundance ratios for 18 elements covering the light, alpha-capture, iron-peak and neutron-capture nucleosynthesis channels. In Chapters 5 and 6, we presented stellar parameters and [X/Fe] vs [Fe/H] trends for the elements Na, Al, O, Mg, Si, Ca, Sc, Ti, V, Cr, Mn, Co, Ni, Cu, Zr, La, Nd and Eu. In general, the abundance trends we observed are not drastically different to previous bulge studies at higher, or similar resolving power (albeit much smaller sample sizes). Where the bulge trends are not well established, such as for some iron-peak and

neutron-capture elements, we found that our results are largely in agreement with the high-resolution disk study by Battistini & Bensby (2015, 2016). Some notable bulge abundance trends we found are [Cu/Fe] and [Co/Fe], which are not enhanced as suggested by previous studies. In addition, the neutron capture abundance ratios [La/Fe], [Ce/Fe] and [Nd/Fe] all show relatively flat trends with metallicity, which confirms the high *s*-process contribution to the production of these elements. Also thought to be an *s*-process element, Zr shows significantly steeper decline with metallicity, suggesting that the *r*-process contribution is greater than expected.

Our wide metallicity coverage allowed us to assess vertical variations in the abundance ratios of bulge metallicity components. Within uncertainties, we found that [X/Fe] remain uniform with height at fixed metallicity. At the metal-rich regime ([Fe/H] > 0), the alpha-abundances of field $(0, -10)$ may be enhanced. This is most conclusive for [α/Fe] (weighted average of Mg, Ca, Si, Ti), but uncertain for individual alpha elements. The [Na/Fe] abundance ratios are uniform with latitude, and we did not observe stars with relatively enhanced [Na/Fe]. Although a helium-enhanced population has been suggested as an alternative interpretation of the double red clump observed in the bulge, studies of globular clusters show that such a population would also have high [Na/Fe] values. Our observations therefore do not support helium enhancement as the likely explanation for the double red clump.

The bulge study was conducted in synergy with the GALAH survey. Not only did we use the same instrument, we also used the same spectroscopic analysis technique and atomic data. Where possible, the exact same lines were used to derive elemental abundances. This was so that we could compare the disk and bulge populations in a consistent manner. However, during our analysis we discovered that some lines in the GALAH linelist were problematic and had to be removed. This seems to have caused large systematic differences between our results and that of GALAH for the elements Mg and Sc. For the rest of the elements, our comparison indeed confirms the overall similarity of abundance trends in the disk and bulge. However, the population with [Fe/H] $\lesssim -0.8$, has higher abundance ratios for most of the alpha elements, also for Na, Al, Ni and possibly Cu. These elements are thought to be produced in massive stars, which are progenitors of SNeII. Our results would suggest that this bulge population contains relatively more SNeII material. In addition, the [La/Eu] abundance ratio indicates higher *r*-process contribution in the bulge.

Overall, our observations advocate for fast chemical enrichment in the bulge. For many of the elements that have SNeII origin, such as the alpha elements and aluminium, the bulge has enhanced abundance ratios compared to the thin disk. Furthermore, the metal-poor bulge population appears to have distinct chemistry, and possibly distinct kinematics compared to the metal-rich population as observed by other studies. While the similarity between the Galactic disk and bulge is evident, we conclude that it is possible not all bulge stars have disk origin, and that the star formation rate in the bulge is higher than that of the disk.

7.1 Future outlook

This work has characterised properties of the Galactic disk and bulge, to better understand the formation and evolution of both components, and how they may be related to each other. The vertical metallicity and [α/Fe] profiles we observed in the Galactic thick disk have placed further constraints on its formation scenario. However, additional information from cosmological and galactic chemical evolution models are needed to confirm the origin of the thick disk. Since our work was published, accurate distances and proper motions from the *Gaia* survey have become available for a large number of GALAH stars. One could now perform a more accurate analysis of thick disk kinematics, which would reveal further details about its evolution.

The bulge study provides perhaps the largest sample of bulge stars, with the most comprehensive chemical inventory yet. Our results highlight the complexity of bulge chemistry, and raise additional questions. It is not clear that the bulge and disk have identical chemistry. The metal-poor bulge population ([Fe/H] $\lesssim -0.8$) seems to have different chemistry to disk stars at the same metallicity. Moving forward, further development or scrutiny into bulge formation models via disk instability may be able to shed some light on this observation. Furthermore, it would be beneficial to compare the abundance ratios measured in this work with chemical evolution models that consider a composite bulge. This will help to constrain the conditions in which the Galactic bulge was formed.

It is possible to extend the bulge study, first and foremost to complete observations for the K2 field. Many of the stars in this field have been observed by K2 Campaign 9, and may soon have asteroseismic measurements. This will allow masses, and thus fairly accurate ages, to be computed for bulge stars in this field. *The Cannon* can then be used to transfer age labels from the K2 field to our other bulge fields (e.g., Ness et al. 2016a). Ages can also be derived using hydrogen line profiles, which is well suited to HERMES spectra (Bergemann et al. 2016). Such information would be very valuable for the study of bulge evolution when combined with our chemical inventory.

At the beginning of this thesis, we were entering a new era for Galactic Archaelogy: stellar samples are larger than ever before, and their measured properties are highly accurate and precise thanks to improved and new analysis techniques. With this information, we have been able to characterise the properties of Galactic components, and better understand their evolution. In the near future, up-coming surveys such as WEAVE, 4MOST, MOONS and APOGEE-2 will provide high-resolution spectra for even larger stellar samples, especially for the inner Galaxy. As next generation telescopes such as the GMT come online, the possibility to study not only the Milky Way, but also its satellites and nearby galaxies in close detail will become a reality. And at that time, we would be a step closer to establishing a complete theory of galaxy formation and evolution in a ΛCDM universe.

Bibliography

Abadi, M. G., Navarro, J. F., Steinmetz, M., and Eke, V. R., 2003, Simulations of galaxy formation in a ΛCold Dark Matter Universe II. The fine structure of simulated galactic disks, *The Astrophysical Journal*, 597:21.

Ade, P. A. R., Aghanim, N., Arnaud, M., Ashdown, M., Aumont, J., et al., 2016, Planck 2015 Results XIII. Cosmological parameters, *Astronomy & Astrophysics*, 594:A13.

Adibekyan, V. Z., Sousa, S. G., Santos, N. C., Delgado Mena, E., González Hernández, J. I., et al., 2012, Chemical abundances of 1111 FGK stars from the HARPS GTO planet search program. Galactic stellar populations and planets, *Astronomy & Astrophysics*, 545:A32.

Adibekyan, V. Z., Santos, N. C., Sousa, S. G., and Israelian, G., 2011, A new α-enhanced super-solar metallicity population, *Astronomy & Astrophysics*, 535:L11.

Adibekyan, V. Z., Figueira, P., Santos, N. C., Hakobyan, A. A., Sousa, S. G., et al., 2013, Kinematics and chemical properties of the Galactic stellar populations, *Astronomy & Astrophysics*, 554:A44.

Allend Prieto, C., Beers, T. C., Wilhelm, R., Newberg, H. J., Rockosi, C. M., et al., 2006, A spectroscopic study of the ancient Milky Way: F-and G-type stars in the third data release of the Sloan Digital Sky Survey, *The Astrophysical Journal*, 636:804.

Alonso, A., Arribas, S., and Mart, C., 1999, The effective temperature scale of giant stars (F0–K5) II . Empirical calibration of $T_{\rm eff}$ versus colours and [Fe/H], *Astronomy & Astrophysics Supplement Series*, 140:261.

Alves, D. R., 2000, *K*-band calibration of the red clump luminosity, *The Astrophysical Journal*, 539:732.

Alves-Brito, A., Meléndez, J., Asplund, M., Ramírez, I., and Yong, D., 2010, Chemical similarities between Galactic bulge and local thick disk red giants: O, Na, Mg, Al, Si, Ca, and Ti, *Astronomy & Astrophysics*, 513:A35.

Amarsi, A. M. and Asplund, M., 2017, The solar silicon abundance based on 3D non-LTE calculations, *Monthly Notices of the Royal Astronomical Society*, 464:264.

Amarsi, A. M., Asplund, M., Collet, R., and Leenaarts, J., 2015, The Galactic chemical evolution of oxygen inferred from 3D non-LTE spectral-line-formation calculations, *Monthly Notices of the Royal Astronomical Society*, 454:L11.

Amarsi, A. M., Asplund, M., Collet, R., and Leenaarts, J., 2016, Non-LTE oxygen line formation in 3D hydrodynamic model stellar atmospheres, *Monthly Notices of the Royal Astronomical Society*, 455:3735.

Amarsi, A. M., Lind, K., Asplund, M., Barklem, P. S., and Collet, R., 2016, Non-LTE line formation of Fe in late-type stars III. 3D non-LTE analysis of metal-poor stars, *Monthly Notices of the Royal Astronomical Society*, 463:1518.

Anguiano, B., Zucker, D. B., Scholz, R. D., Grebel, E. K., Seabroke, G., et al., 2015, Identification of globular cluster stars in RAVE data I. Application to stellar parameter calibration, *Monthly Notices of the Royal Astronomical Society*, 451:1229.

Arzoumanian, Z., Holmberg, J., and Norman, B., 2005, An astronomical pattern-matching algorithm for computer-aided identification of whale sharks Rhincodon typus, *Journal of Applied Ecology*, 42:999.

Asplund, M., Nordlund, A., Trampedach, R., Prieto, C. A., and Stein, R. F., 2000, Line formation in solar granulation I. Fe line shapes, shifts and asymmetries, *Astronomy & Astrophysics*, 742:729.

Asplund, M., 2005, New light on stellar abundance analyses: departures from LTE and homogeneity, *Annual Review of Astronomy and Astrophysics*, 43:481.

Asplund, M., Grevesse Nicolas, Jacques, S. A., and Scott, P., 2009, The chemical composition of the Sun, *Annual Review of Astronomy and Astrophysics*, 47:481.

Astraatmadja, T. L. and Bailer-Jones, C. A. L., 2016, Estimating distances from the prallaxes III. Distances of two million stars in the *Gaia* DR1 catalogue, *The Astrophysical Journal*, 833:119.

Athanassoula, E., 2005, On the nature of bulges in general and of box/peanut bulges in particular: input from N-body simulation, *Monthly Notices of the Royal Astronomical Society*, 358:1477.

Aumer, M., Binney, J., and Schönrich, R., 2016, The quiescent phase of galactic disc growth, *Monthly Notices of the Royal Astronomical Society*, 459:3326.

Baade, W., 1944, The resolution of Messier 32, NGC 205, and the central region of the Andromeda nebula, *The Astrophysical Journal*, 100:137.

Babusiaux, C., Gómez, A., et al. Hill, V., Gomez, A., Hill, V., et al., 2010, Insights on the Milky Way bulge formation from the correlations between kinematics and metallicity, *Astronomy & Astrophysics*, 519:A77.

Barbuy, B., Hill, V., Zoccali, M., Minniti, D., Renzini, A., et al., 2013, Manganese abundances in Galactic bulge red giants, *Astronomy & Astrophysics*, 559:A5.

Barbuy, B., Chiappini, C., and Gerhard, O., 2018, Chemodynamical history of the Galactic bulge, *Annual Review of Astronomy and Astrophysics*, 56:223.

Bartašiūtė, S., Aslan, Z., Boyle, R. P., Kharchenko, N. V., Ossipkov, L. P., et al., 2003, Stellar populations of the Galactic disk: metallicity distribution and kinematics, *Baltic Astronomy*, 12:539.

Bastian, N. and Lardo, C., 2018, Multiple stellar populations in globular clusters, *Annual Review of Astronomy and Astrophysics*, 56:83.

Battistini, C. and Bensby, T., 2015, The origin and evolution of the odd-Z iron-peak elements Sc, V, Mn, and Co in the Milky Way stellar disk, *Astronomy & Astrophysics*, 577: A9.

Battistini, C. and Bensby, T., 2016, The origin and evolution of *r*- and *s*-process elements in the Milky Way stellar disk, *Astronomy & Astrophysics*, 586:A49.

Beers, T. C., Carollo, D., Ivezić, Ž., An, D., Chiba, M., et al., 2012, The case for the dual halo of the Milky Way, *The Astrophysical Journal*, 746:34.

Bekki, K. and Tsujimoto, T., 2011, Origin of chemical and dynamical properties of the Galactic thick disk, *The Astrophysical Journal*, 738:4.

Bensby, T., Alves-Brito, A., Oey, M. S., Yong, D., and Meléndez, J., 2011, A first constraint on the thick disk scale length: differential radial abundances in K giants at galactocentric radii 4, 8, and 12 kpc, *The Astrophysical Journal*, 735:L46.

Bensby, T., Yee, J., Feltzing, S., Johnson, J., Gould, A., et al., 2013, Chemical evolution of the Galactic bulge as traced by microlensed dwarf and subgiant stars V. Evidence for a wide age distribution and a complex MDF, *Astronomy & Astrophysics*, 549:A147.

Bensby, T., Feltzing, S., and Oey, M. S., 2014, Exploring the Milky Way stellar disk: A detailed elemental abundance study of 714 F and G dwarf stars in the solar neighbourhood, *Astronomy & Astrophysics*, 562:A71.

Bensby, T., Feltzing, S., Gould, A., Yee, J., Johnson, J., et al., 2017, Chemical evolution of the Galactic bulge as traced by microlensed dwarf and subgiant stars VI. Age and abundance structure of the stellar populations in the central sub-kpc of the Milky Way, *Astronomy & Astrophysics*, 605:A89.

Bergemann, M. and Gehren, T., 2008, NLTE abundances of Mn in a sample of metal-poor stars, *Astronomy & Astrophysics*, 492:823.

Bergemann, M., Pickering, J. C., and Gehren, T., 2010, NLTE analysis of Co I/Co II lines in spectra of cool stars with new laboratory hyperfine splitting constants, *Monthly Notices of the Royal Astronomical Society*, 401:1334.

Bergemann, M., Ruchti, G. R., Serenelli, A., Feltzing, S., Alves-Brito, A., et al., 2014, The *Gaia*-ESO Survey: radial metallicity gradients and age-metallicity relation of stars in the Milky Way disk, *Astronomy & Astrophysics*, 565:A89.

Bergemann, M., Serenelli, A., Schönrich, R., Ruchti, G., Korn, A., et al., 2016, The *Gaia*-ESO Survey: Hydrogen lines in red giants directly trace stellar mass, *Astronomy & Astrophysics*, 594:A120.

Bernard, E. J., Schultheis, M., Di Matteo, P., Hill, V., Haywood, M., et al., 2018, Star formation history of the Galactic bulge from deep HST imaging of low reddening windows, *Monthly Notices of the Royal Astronomical Society*, 477:3507.

Bessell, M., Bloxham, G., Schmidt, B., Keller, S., Tisserand, P., et al., 2011, SkyMapper filter set: design and fabrication of large-scale optical filters, *Publications of the Astronomical Society of the Pacific*, 123:789.

Bird, J. C., Kazantzidis, S., Weinberg, D. H., Guedes, J., Callegari, S., et al., 2013, Inside out and upside down: Tracing the assembly of a simulated disk galaxy using mono-age stellar populations, *The Astrophysical Journal*, 773:43.

Bisterzo, S., Travaglio, C., Gallino, R., Wiescher, M., and Käppeler, F., 2014, Galactic chemical evolution and solar *s*-process abundances: dependence on the ^{13}C-pocket structure, *The Astrophysical Journal*, 787:10.

Blackwell, D. E., Shallis, M. J., and Selby, M. J., 1979, The infrared flux method for determining stellar angular diameters and effective temperatures, *Monthly Notices of the Royal Astronomical Society*, 188:847.

Bland-Hawthorn, J. and Gerhard, O., 2016, The Galaxy in context: structural, kinematic & integrated properties, *Annual Review of Astronomy and Astrophysics*, 54:529.

Bland-Hawthorn, J., Krumholz, M. R., and Freeman, K., 2010, The long-term evolution of the Galactic disk traced by dissolving star clusters, *The Astrophysical Journal*, 713:166.

Bland-Hawthorn, J., Kos, J., Betters, C. H., Silva, G. D., O'Byrne, J., et al., 2017, Mapping the aberrations of a wide-field spectrograph using a photonic comb, *Optics Express*, 25: 15614.

Boeche, C., Siebert, A., Piffl, T., Just, A., Steinmetz, M., et al., 2014, Chemical gradients in the Milky Way from the RAVE data II. Giant stars, *Astronomy & Astrophysics*, 568:A71.

Böhm-Vitense, E., 1958, Über die wasserstoffkonvektionszone in sternen verschiedener effektivtemperaturen und leuchtkräfte. Mit 5 textabbildungen, *Zeitschrift für Astrophysik*, 46:108.

Bournaud, F., Elmegreen, B. G., and Martig, M., 2009, The thick disks of spiral galaxies as relics from gas-rich, turbulent, clumpy disks at high redshift, *The Astrophysical Journal*, 707:L1.

Bovy, J., Rix, H.-W., and Hogg, D. W., 2012, The Milky Way has no distinct thick disk, *The Astrophysical Journal*, 751:131.

Bovy, J., Rix, H.-W., Liu, C., Hogg, D. W., Beers, T. C., et al., 2012, The spatial structure of mono-abundance sub-populations of the Milky Way disk, *The Astrophysical Journal*, 753: 148.

Bovy, J., Rix, H.-W., Schlafly, E. F., Nidever, D. L., Holtzman, J. A., et al., 2016, The stellar population structure of the Galactic disk, *The Astrophysical Journal*, 823:30.

Brewer, J. M., Fischer, D. A., Basu, S., Valenti, J. A., and Piskunov, N., 2015, Accurate gravities of F, G, and K stars from high resolution spectra without external constraints, *The Astrophysical Journal*, 805:126.

Brook, C. B., Stinson, G. S., Gibson, B. K., Kawata, D., House, E. L., et al., 2012, Thin disc, thick disc and halo in a simulated galaxy, *Monthly Notices of the Royal Astronomical Society*, 426:690.

Brook, C. B., Kawata, D., Gibson, B. K., and Freeman, K. C., 2004, The emergence of the thick disk in a Cold Dark Matter Universe, *The Astrophysical Journal*, 612:894.

Brook, C. B., Gibson, B. K., Martel, H., and Kawata, D., 2005, The emergence of the thick disk in a CDM Universe II. Colors and abundance patterns, *The Astrophysical Journal*, 630: 298.

Brown, A. G. A., Vallenari, A., Prusti, T., de Bruijne, J. H., Mignard, F., et al., 2016, *Gaia* Data Release 1. Summary of the astrometric, photometric, and survey properties, *Astronomy & Astrophysics*, 595:A2.

Buder, S., Asplund, M., Duong, L., Kos, J., Lind, K., et al., 2018, The GALAH Survey: Second data release, *Monthly Notices of the Royal Astronomical Society*, 478:4513.

Bullock, J. S. and Boylan-Kolchin, M., 2017, Small scale challenges to the ΛCDM paradigm, *Annual Review of Astronomy and Astrophysics*, 55:343.

Burbidge, E. M., Burbidge, G. R., Fowler, W. A., and Hoyle, F., 1957, Synthesis of the elements in stars, *Review of Modern Physics*, 29:547.

Burkert, A., Truran, J. W., and Hensler, G., 1992, The collapse of our Galaxy and the formation of the Galactic disk, *The Astrophysical Journal*, 391:651.

Burnett, B. and Binney, J., 2010, Stellar distances from spectroscopic observations: a new technique, *Monthly Notices of the Royal Astronomical Society*, 407:339.

Burstein, D., 1979, Structure and origin of S0 galaxies III. The luminosity distribution perpendicular to the plane of the disks in S0's, *The Astrophysical Journal*, 234:829.

Calamida, A., Sahu, K. C., Casertano, S., Anderson, J., Cassisi, S., et al., 2015, New insights on the Galactic bulge initial mass function, *The Astrophysical Journal*, 810:8.

Cannon, A. J. and Pickering, E. C., 1901, Spectra of bright Southern stars photographed with the 13-inch Boyden telescope, *Annals of The Astronomical Observatory of Harvard College*, 28:135.

Carney, B. W., Lee, J.-W., and Dodson, B., 2005, Infrared photometry of NGC 6791, *The Astronomical Journal*, 129:656.

Carollo, D., Beers, T. C., Lee, Y. S., Chiba, M., Norris, J. E., et al., 2007, Two stellar components in the halo of the Milky Way, *Nature*, 450:1020.

Carretta, E., Bragaglia, A., Gratton, R. G., Lucatello, S., Bellazzini, M., et al., 2010, Detailed abundances of a large sample of giant stars in M54 and in the Sagittarius nucleus, *Astronomy & Astrophysics*, 520:A95.

Casagrande, L. and VandenBerg, D. A., 2014, Synthetic stellar photometry I. General considerations and new transformations for broad-band systems, *Monthly Notices of the Royal Astronomical Society*, 444:392.

Casagrande, L., Ramírez, I., Meléndez, J., Bessell, M., and Asplund, M., 2010, An absolutely calibrated $T_{\rm eff}$ scale from the infrared flux method. Dwarfs and subgiants, *Astronomy & Astrophysics*, 512:54.

Casagrande, L., Schönrich, R., Asplund, M., Cassisi, S., Ramírez, I., et al., 2011, New constraints on the chemical evolution of the solar neighbourhood and Galactic disc(s), *Astronomy & Astrophysics*, 530:A138.

Casagrande, L., Aguirre, V. S., Stello, D., Huber, D., Serenelli, A. M., et al., 2014, Strömgren survey for Asteroseismology and Galactic Archaeology: Let the SAGA begin, *The Astrophysical Journal*, 787:110.

Casagrande, L., Silva Aguirre, V., Schlesinger, K. J., Stello, D., Huber, D., et al., 2016, Measuring the vertical age structure of the Galactic disc using asteroseismology and SAGA, *Monthly Notices of the Royal Astronomical Society*, 455:987.

Casey, A. R. and Schlaufman, K. C., 2015, Chemistry of the most metal-poor stars in the Bulge and the $z \gtrsim 10$ Universe, *The Astrophysical Journal*, 809:110.

Casey, A. R., Hawkins, K., Hogg, D. W., Ness, M., Rix, H.-W., et al., 2017, The RAVE-on catalog of stellar atmospheric parameters and chemical abundances for chemo-dynamic studies in the *Gaia* era, *The Astrophysical Journal*, 840:59.

Chen, Y. Q., Zhao, G., Carrell, K., and Zhao, J. K., 2011, The metallicity gradient of the thick disk based on red horizontal-branch stars from SDSS DR8, *The Astronomical Journal*, 142: 184.

Cheng, J. Y., Rockosi, C. M., Morrison, H. L., Lee, Y. S., Beers, T. C., et al., 2012, A short scale length for the α-enhanced thick disk of the Milky Way: Evidence from low-latitude SEGUE data, *The Astrophysical Journal*, 752:51.

Chiappini, C., Matteucci, F., and Gratton, R., 1997, The chemical evolution of the Galaxy: The two-infall model, *The Astrophysical Journal*, 477:765.

Chiappini, C., Anders, F., Rodrigues, T. S., Miglio, A., Montalbán, J., et al., 2015, Young [α/Fe]-enhanced stars discovered by CoRoT and APOGEE: What is their origin?, *Astronomy & Astrophysics*, 576:L12.

Chiba, M. and Beers, T. C., 2000, Kinematics of metal-poor stars in the Galaxy III. Formation of the stellar halo and thick disk as revealed from a large sample of nonkinematically selected stars, *The Astronomical Journal*, 119:2843.

Ciambur, B. C., Graham, A. W., and Bland-Hawthorn, J., 2017, Quantifying the (X/peanut)-shaped structure of the Milky Way - new constraints on the bar geometry, *Monthly Notices of the Royal Astronomical Society*, 471:3988.

Ciucă, I., Kawata, D., Lin, J., Casagrande, L., Seabroke, G., et al., 2018, The vertical metallicity gradients of mono-age stellar populations in the Milky Way with the RAVE and *Gaia* data, *Monthly Notices of the Royal Astronomical Society*, 475:1203.

Clarkson, W. I., Sahu, K. C., Anderson, J., Rich, R. M., Smith, T. E., et al., 2011, The first detection of Blue Straggler stars in the Milky Way bulge, *The Astrophysical Journal*, 735:37.

Clarkson, W., Sahu, K., Anderson, J., Smith, T. E., Brown, T. M., et al., 2008, Stellar proper motions in the Galactic bulge from deep *Hubble Space Telescope* ACS WFC photometry, *The Astrophysical Journal*, 684:1110.

Comerón, S., Salo, H., Janz, J., Laurikainen, E., and Yoachim, P., 2015, Galactic archaeology of a thick disc: Excavating ESO 533-4 with VIMOS, *Astronomy & Astrophysics*, 584:A43.

Côté, B., Fryer, C. L., Belczynski, K., Korobkin, O., Chruślińska, M., et al., 2018, The origin of *r*-process elements in the Milky Way, *The Astrophysical Journal*, 855:99.

Dalcanton, J. J. and Bernstein, R. A., 2002, A structural and dynamical study of late-type, edge-on galaxies II. Vertical color gradients and the detection of ubiquitous thick disks, *The Astronomical Journal*, 124:1328.

Dalton, G., Trager, S., Abrams, D. C., Bonifacio, P., Aguerri, J. A. L., et al., 2016, Final design and progress of WEAVE: the next generation wide-field spectroscopy facility for

the William Herschel Telescope, *Proc. SPIE: Ground-based and Airborne Instrumentation for Astronomy VI*, 9908:99081G.

D'Antona, F., Ventura, P., Caloi, V., D'Ercole, A., Vesperini, E., et al., 2010, Terzan 5: An alternative interpretation for the split horizontal branch, *The Astrophysical Journal*, 715: L63.

de Jong, R. D., Sartoretti, P., Schnurr, O., Schwope, A., Bauer, S., et al., 2011, 4MOST – 4-metre Multi-Object Spectroscopic Telescope, *The Messenger*, 145:14.

de Laverny, P., Recio-Blanco, A., Worley, C. C., and Plez, B., 2012, The AMBRE project: A new synthetic grid of high-resolution FGKM stellar spectra, *Astronomy & Astrophysics*, 544:A126.

De Silva, G. M., Sneden, C., Paulson, D. B., Asplund, M., Bland-Hawthorn, J., et al., 2006, Chemical homogeneity in the Hyades, *The Astronomical Journal*, 131:455.

De Silva, G. M., Freeman, K. C., Asplund, M., Bland-Hawthorn, J., Bessell, M. S., et al., 2007, Chemical homogeneity in Collinder 261 and implications for chemical tagging, *The Astronomical Journal*, 133:1161.

De Silva, G. M., Freeman, K. C., Bland-Hawthorn, J., Martell, S., Wylie de Boer, E., et al., 2015, The GALAH survey: scientific motivation, *Monthly Notices of the Royal Astronomical Society*, 449:2604.

de Vaucouleurs, G., 1970, The case for a hierarchical cosmology, *Science*, 167:1203.

Dékány, I., Minniti, D., Catelan, M., Zoccali, M., Saito, R. K., et al., 2013, VVV survey near-infrared photometry of known bulge RR Lyrae stars: the distance to the Galactic center and absence of a barred distribution of the metal-poor population, *The Astrophysical Journal*, 776:L19.

Dempster, A. P., Laird, N. M., and Rubin, D. B., 1977, Maximum likelihood from incomplete data via the EM algorithm, *Journal of the Royal Statistical Society: Series B*, 39:1.

Di Matteo, P., Haywood, M., Damme, L. V., Combes, F., Hall, A., et al., 2014, Mapping a stellar disk into a boxy bulge: The outside-in part of the Milky Way bulge formation, *Astronomy & Astrophysics*, 567:A122.

Di Matteo, P., Gómez, A., Haywood, M., Combes, F., Lehnert, M. D., et al., 2015, Why the Milky Way's bulge is not only a bar formed from a cold thin disk, *Astronomy & Astrophysics*, 577:A1.

Dierickx, M., Klement, R., Rix, H.-W., and Liu, C., 2010, Observational evidence from SDSS for a merger origin of the Milky Way's thick disk, *The Astrophysical Journal*, 725: L186.

Drimmel, R. and Spergel, D. N., 2001, Three-dimensional structure of the Milky Way disk: The distribution of stars and dust beyond 0.35 $R_{\odot}$, *The Astrophysical Journal*, 556:181.

Duong, L., Freeman, K. C., Asplund, M., Casagrande, L., Buder, S., et al., 2018, The GALAH survey: properties of the galactic disc(s) in the solar neighbourhood, *Monthly Notices of the Royal Astronomical Society*, 476:5216.

Dupree, A. K., Strader, J., and Smith, G. H., 2011, Direct evidence for an enhancement of helium in giant stars in Omega Centauri, *The Astrophysical Journal*, 728:155.

Dwek, E., Arendt, R. G., Hauser, M. G., Kelsall, T., Lisse, C. M., et al., 1995, Morphology, near-infrared luminosity, and mass of the Galactic bulge from COBE DIRBE observations, *The Astrophysical Journal*, 445:716.

Edvardsson, B., Andersen, J., Gustafsson, B., Lambert, D. L., Nissen, P. E., et al., 1993, The chemical evolution of the Galactic disk part one - analysis and results, *Astronomy & Astrophysics*, 275:101.

Eggen, O. J., Lynden-Bell, D., and Sandage, A. R., 1962, Evidence from the motions of old stars that the Galaxy collapsed, *The Astrophysical Journal*, 136:748.

Erwin, P., Saglia, R. P., Fabricius, M., Thomas, J., Nowak, N., et al., 2015, Composite bulges: the coexistence of classical bulges and discy pseudo-bulges in S0 and spiral galaxies, *Monthly Notices of the Astronomical Society*, 4077:4039.

Feng, Y. and Krumholz, M. R., 2014, Early turbulent mixing as the origin of chemical homogeneity in open star clusters, *Nature*, 513:523.

Fisher, D. B. and Drory, N., 2011, Demographics of bulge types within 11 Mpc and implications for galaxy evolution, *The Astrophysical Journal*, 733:L47.

Forbes, J., Krumholz, M., and Burkert, A., 2012, Evolving gravitationally unstable disks over cosmic time: implications for thick disk formation, *The Astrophysical Journal*, 754: 48.

Fragkoudi, F., Di Matteo, P., Haywood, M., Schultheis, M., Khoperskov, S., et al., 2018, The disc origin of the Milky Way bulge. Dissecting the chemo-morphological relations using N-body simulations and APOGEE, *Astronomy & Astrophysics*, 616:A180.

Frebel, A. and Norris, J. E., 2015, Near-field cosmology with metal-poor stars, *Annual Review of Astronomy and Astrophysics*, 53:631.

Freeman, K. and Bland-Hawthorn, J., 2002, The new Galaxy, *Annual Review of Astronomy and Astrophysics*, 40:487.

Freeman, K., Ness, M., Wylie-de Boer, E., Athanassoula, E., Bland-Hawthorn, J., et al., 2013, ARGOS - II. The Galactic bulge survey, *Monthly Notices of the Royal Astronomical Society*, 428:3660.

Freeman, K. C., 1970, On the disks of spiral and S0 galaxies, *The Astrophysical Journal*, 160: 811.

Friaça, A. C. S. and Barbuy, B., 2017, Tracing the evolution of the Galactic bulge with chemodynamical modelling of alpha-elements, *Astronomy & Astrophysics*, 598:A121.

Fuhrmann, K., 2008, Nearby stars of the Galactic disc and halo - IV, *Monthly Notices of the Royal Astronomical Society*, 384:173.

Fuhrmann, K., Chini, R., Kaderhandt, L., and Chen, Z., 2016, On the local stellar populations, *Monthly Notices of the Royal Astronomical Society*, 464:2610.

Fulbright, J. P., McWilliam, A., and Rich, R. M., 2007, Abundances of Baade's window giants from Keck HIRES spectra II. The alpha and light odd elements, *The Astrophysical Journal*, 661:1152.

Gaia Collaboration, Prusti, T., de Bruijne, J. H. J., Brown, A. G. A., Vallenari, A., et al., 2016, The *Gaia* mission, *Astronomy & Astrophysics*, 595:A1.

Gaia Collaboration, Brown, A. G. A., Vallenari, A., Prusti, T., de Bruijne, J. H. J., et al., 2018, *Gaia* Data Release 2. Summary of the contents and survey properties, *arXiv preprint: 1804.09365*.

Gao, X., Lind, K., Amarsi, A. M., Buder, S., Dotter, A., et al., 2018, The GALAH survey: verifying abundance trends in the open cluster M67 using non-LTE modelling, *Monthly Notices of the Royal Astronomical Society*, 481:2666.

García Pérez, A. E., Prieto, C. A., Holtzman, J. A., Shetrone, M., Mészáros, S., et al., 2016, ASPCAP: the APOGEE stellar parameters and abundances pipeline, *The Astronomical Journal*, 151:144.

García Pérez, A. E., Ness, M., Robin, A. C., Martinez-Valpuesta, I., Sobeck, J., et al., 2018, The bulge metallicity distribution from the APOGEE survey, *The Astrophysical Journal*, 852:91.

Genovali, K., Lemasle, B., Bono, G., Romaniello, M., Fabrizio, M., et al., 2014, On the fine structure of the Cepheid metallicity gradient in the Galactic thin disk, *Astronomy & Astrophysics*, 566:A37.

Genovali, K., Lemasle, B., da Silva, R., Bono, G., Fabrizio, M., et al., 2015, On the α-element gradients of the Galactic thin disk using Cepheids, *Astronomy & Astrophysics*, 580:A17.

Gilmore, G. and Reid, N., 1983, New light on faint stars III. Galactic structure towards the South Pole and the Galactic thick disc, *Monthly Notices of the Royal Astronomical Society*, 202:1025.

Gilmore, G., Randich, S., Asplund, M., Binney, J., Bonifacio, P., et al., 2012, The *Gaia*-ESO public spectroscopic survey, *The Messenger*, 147:25.

Gilmore, G., Wyse, R. F. G., and Jones, B. J., 1995, A determination of the thick disk chemical abundance distribution: implications for galaxy evolution, *The Astronomical Journal*, 109:1095.

Gilmore, G., Wyse, R. F. G., and Norris, J. E., 2002, Deciphering the last major invasion of the Milky Way, *The Astrophysical Journal*, 574:L39.

Gonzalez, O. A., Rejkuba, M., Zoccali, M., Hill, V., Battaglia, G., et al., 2011, Alpha element abundances and gradients in the Milky Way bulge from FLAMES-GIRAFFE spectra of 650 K giants, *Astronomy & Astrophysics*, 530:A54.

Gonzalez, O. A., Zoccali, M., Debattista, V. P., Alonso-García, J., Valenti, E., et al., 2015, Reinforcing the link between the double red clump and the X-shaped bulge of the Milky Way, *Astronomy & Astrophysics*, 583:L5.

Gonzalez, O. A., Zoccali, M., Vasquez, S., Hill, V., Rejkuba, M., et al., 2015, The GIRAFFE Inner Bulge Survey (GIBS) II. Metallicity distributions and alpha element abundances at fixed Galactic latitude, *Astronomy & Astrophysics*, 562:A66.

Grand, R. J. J., Bustamante, S., Gómez, F. A., Kawata, D., Marinacci, F., et al., 2017, Origin of chemically distinct discs in the Auriga cosmological simulations, *ArXiv preprint:1708.07834*.

Gratton, R. G., Carretta, E., Matteucci, F., and Sneden, C., 2000, Abundances of light elements in metal-poor stars IV. [Fe/O] and [Fe/Mg] ratios and the history of star formation in the solar neighborhood, *Astronomy & Astrophysics*, 358:671.

Gratton, R. G., Lucatello, S., Bragaglia, A., Carretta, E., Momany, Y., et al., 2006, Na-O anticorrelation and HB III. The abundances of NGC 6441 from FLAMES-UVES spectra, *Astronomy & Astrophysics*, 455:271.

Gratton, R. G., Carretta, E., and Bragaglia, A., 2012, Multiple populations in globular clusters., *Astronomy and Astrophysics Review*, 20:50.

Gray, D. F. *The observation and analysis of stellar photospheres*. Cambridge University Press, Third edition, 2005.

Grevesse, N., Asplund, M., and Sauval, A. J., 2007, The solar chemical composition, *Space Science Review*, 130:105.

Gustafsson, B., Edvardsson, B., Eriksson, K., Jorgensen, U. G., Nordlund, A., et al., 2008, A grid of MARCS model atmospheres for late-type stars I. Methods and general properties, *Astronomy & Astrophysics*, 486:951.

Hawkins, K., Masseron, T., Jofré, P., Gilmore, G., Elsworth, Y., et al., 2016, An accurate and self-consistent chemical abundance catalogue for the APOGEE/*Kepler* sample, *Astronomy & Astrophysics*, 594:A43.

Hayden, M. R., Holtzman, J. A., Bovy, J., Majewski, S. R., Johnson, J. A., et al., 2014, Chemical cartography with APOGEE: large-scale mean metallicity maps of the Milky Way disk, *The Astronomical Journal*, 147:116.

Hayden, M. R., Bovy, J., Holtzman, J. A., Nidever, D. L., Bird, J. C., et al., 2015, Chemical cartography with APOGEE: Metallicity distribution functions and the chemical structure of the Milky Way disk, *The Astrophysical Journal*, 808:132.

Haywood, M., 2008, Radial mixing and the transition between the thick and thin Galactic discs, *Monthly Notices of the Royal Astronomical Society*, 388:1175.

Haywood, M., Di Matteo, P., Snaith, O., and Lehnert, M. D., 2015, Clues to the formation of the Milky Way's thick disk, *Astronomy & Astrophysics*, 579:A5.

Haywood, M., Lehnert, M. D., Di Matteo, P., Snaith, O., Schultheis, M., et al., 2016, When the Milky Way turned-off the lights: APOGEE provides evidence of star formation "quenching" in our Galaxy, *Astronomy & Astrophysics*, 589:A66.

Haywood, M., Di Matteo, P., Lehnert, M., Snaith, O., Fragkoudi, F., et al., 2018, Phylogeny of the Milky Way's inner disk and bulge populations: Implications for gas accretion, (the lack of) inside-out thick disk formation, and quenching, *arXiv preprint: 1802.09887*.

Haywood, M., Matteo, P. D., Lehnert, M. D., Katz, D., and Gómez, A., 2013, The age structure of stellar populations in the solar vicinity - Clues of a two-phase formation history of the Milky Way disk, *Astronomy & Astrophysics*, 560:A109.

Heiter, U., Jofré, P., Gustafsson, B., Korn, A. J., Soubiran, C., et al., 2015, *Gaia* FGK benchmark stars : Effective temperatures and surface gravities, *Astronomy & Astrophysics*, 582: A49.

Heiter, U., Lind, K., Asplund, M., Barklem, P. S., Bergemann, M., et al., 2015, Atomic and molecular data for optical stellar spectroscopy, *Physica Scripta*, 90:054010.

Hekker, S., Elsworth, Y., Mosser, B., Kallinger, T., Basu, S., et al., 2013, Asteroseismic surface gravity for evolved stars, *Astronomy & Astrophysics*, 556:A59.

Hill, V., Lecureur, A., Gómez, A., Zoccali, M., Schultheis, M., et al., 2011, The metallicity distribution of bulge clump giants in Baade's window, *Astronomy & Astrophysics*, 534:A80.

Hinkle, K., Wallace, L., Valenti, J., and Harmer, D. *Visible and Near Infrared atlas of the Arcturus spectrum 3727-9300 Å*. Astronomical Society of the Pacific, 2000.

Ho, A. Y. Q., Ness, M. K., Hogg, D. W., Rix, H.-W., Liu, C., et al., 2016, Survey cross-clibration with The Cannon: APOGEE-scale stellar labels from LAMOST spectra, *arXiv pre-print: 1602.00303v2*.

Hogg, D. W., Casey, A. R., Ness, M., Rix, H.-W., Foreman-Mackey, D., et al., 2016, Chemical tagging can work: identification of stellar phase-space structures purely by chemical-abundance similarity, *The Astrophysical Journal*, 833:262.

Holtzman, J. A., Shetrone, M., Johnson, J. A., Prieto, C. A., and Anders, F., 2015, Abundances, stellar parameters, and spectra from the SDSS-III/APOGEE survey, *The Astronomical Journal*, 150:148.

Howes, L. M., Casey, A. R., Asplund, M., Keller, S. C., Yong, D., et al., 2015, Extremely metal-poor stars from the cosmic dawn in the bulge of the Milky Way, *Nature*, 527:484.

Howes, L. M., Asplund, M., Keller, S. C., Casey, A. R., Yong, D., et al., 2016, The EMBLA survey - metal-poor stars in the Galactic bulge, *Monthly Notices of the Royal Astronomical Society*, 460:884.

Huber, D., Zinn, J., Bojsen-Hansen, M., Pinsonneault, M., Sahlholdt, C., et al., 2017, Asteroseismology and *Gaia*: Testing scaling relations using 2200 *Kepler* stars with TGAS parallaxes, *The Astrophysical Journal*, 844:102.

Ibata, R., Mouhcine, M., and Rejkuba, M., 2009, An HST/ACS investigation of the spatial and chemical structure and sub-structure of NGC 891, a Milky Way analogue, *Monthly Notices of the Royal Astronomical Society*, 395:126.

Inoue, S. and Saitoh, T. R., 2012, Natures of a clump-origin bulge: a pseudo-bulge like but old metal-rich bulge, *Monthly Notices of the Royal Astronomical Society*, 422:1902.

Jofré, P., Heiter, U., Soubiran, C., Blanco-Cuaresma, S., Worley, C. C., et al., 2014, *Gaia* FGK benchmark stars: Metallicity, *Astronomy & Astrophysics*, 564:A133.

Johnson, C. I., Rich, R. M., Kobayashi, C., and Fulbright, J. P., 2012, Constraints on the formation of the galactic bulge from Na, Al, and heavy-element abundances in Plaut's field, *The Astrophysical Journal*, 749:175.

Johnson, C. I., Rich, R. M., Kobayashi, C., Kunder, A., and Koch, A., 2014, Light, alpha, and Fe-peak element abundances in the Galactic bulge, *The Astronomical Journal*, 148:67.

Jönsson, H., Ryde, N., Schultheis, M., and Zoccali, M., 2017, Abundances of disk and bulge giants from high-resolution optical spectra II. O, Mg, Ca, and Ti in the bulge sample, *Astronomy & Astrophysics*, 598:A101.

Joo, S.-J., Lee, Y.-W., and Chung, C., 2017, New insight on the origin of the double red clump in the Milky Way bulge, *The Astrophysical Journal*, 840:98.

Jurić, M., Ivezić, Ž., Brooks, A., Lupton, R. H., Schlegel, D., et al., 2008, The Milky Way tomography with SDSS I. Stellar number density distribution, *The Astrophysical Journal*, 673:864.

Kafle, P. R., Sharma, S., Lewis, G. F., Robotham, A. S. G., and Driver, S. P., 2018, The need for speed: Escape velocity and dynamical mass measurements of the Andromeda galaxy, *Monthly Notices of the Royal Astronomical Society*, 475:4043.

Karakas, A. I. and Lattanzio, J. C., 2014, The Dawes Review 2: Nucleosynthesis and stellar yields of low- and intermediate-mass single stars, *Publications of the Astronomical Society of Australia*, 31:e030.

Katz, D., Soubiran, C., Cayrel, R., Barbuy, B., Friel, E., et al., 2011, Probing the Galactic thick disc vertical properties and interfaces, *Astronomy & Astrophysics*, 525:A90.

Kawata, D., Grand, R. J. J., Gibson, B. K., Casagrande, L., Hunt, J. A. S., et al., 2017, Impacts of a flaring star-forming disc and stellar radial mixing on the vertical metallicity gradient, *Monthly Notices of the Royal Astronomical Society*, 464:702.

Kawata, D., Allende Prieto, C., Brook, C. B., Casagrande, L., Ciucă, I., et al., 2018, Metallicity gradient of the thick disc progenitor at high redshift, *Monthly Notices of the Royal Astronomical Society*, 473:867.

Kazantzidis, S., Bullock, J. S., Zentner, A. R., Kravtsov, A. V., and Moustakas, L. A., 2008, Cold Dark Matter substructure and galactic disks I. Morphological signatures of hierarchical satellite accretion, *The Astrophysical Journal*, 688:254.

Kjeldsen, H. and Bedding, T. R., 1995, Amplitudes of stellar oscillations: the implications for asteroseismology, *Astronomy & Astrophysics*, 293:87.

Kollmeier, J. A., Zasowski, G., Rix, H.-W., Johns, M., Anderson, S. F., et al., 2017, SDSS-V: Pioneering Panoptic Spectroscopy, *arXiv preprint: 1711.03234*.

Kordopatis, G., Recio-Blanco, A., de Laverny, P., Gilmore, G., Hill, V., et al., 2011, A spectroscopic survey of thick disc stars outside the solar neighbourhood, *Astronomy & Astrophysics*, 535:A107.

Kordopatis, G., Wyse, R. F., Chiappini, C., Minchev, I., Anders, F., et al., 2017, Cardinal kinematics I. Rotation fields of the APOGEE survey, *Monthly Notices of the Royal Astronomical Society*, 467:469.

Kormendy, J. and Kennicutt, R. C., 2004, Secular evolution and the formation of pseudobulges in disk galaxies, *Annual Review of Astronomy and Astrophysics*, 42:603.

Kormendy, J., Drory, N., Bender, R., and Cornell, M. E., 2010, Bulgeless giant galaxies challenge our picture of galaxy formation by hierarchical clustering, *The Astrophysical Journal*, 723:54.

Kos, J., Lin, J., Zwitter, T., Žerjal, M., Sharma, S., et al., 2017, The GALAH survey: the data reduction pipeline, *Monthly Notices of the Royal Astronomical Society*, 464:1259.

Kos, J., Bland-Hawthorn, J., Freeman, K., Buder, S., Traven, G., et al., 2018, The GALAH survey: chemical tagging of star clusters and new members in the Pleiades, *Monthly Notices of the Royal Astronomical Society*, 473:4612.

Kunder, A., Koch, A., Michael Rich, R., de Propris, R., Howard, C. D., et al., 2012, The Bulge Radial Velocity Assay (BRAVA) II. Complete sample and data release, *The Astronomical Journal*, 143:57.

Kunder, A., Rich, R. M., Koch, A., Storm, J., Nataf, D. M., et al., 2016, Before the bar: kinematic detection of a spheroidal metal-poor bulge component, *The Astrophysical Journal*, 821:L25.

Kunder, A., Kordopatis, G., Steinmetz, M., Zwitter, T., McMillan, P. J., et al., 2017, The Radial Velocity Experiment (RAVE): Fifth data release, *The Astronomical Journal*, 153:75.

Lecureur, A., Hill, V., Zoccali, M., Barbuy, B., Gómez, A., et al., 2007, Oxygen, sodium, magnesium, and aluminium as tracers of the Galactic bulge formation, *Astronomy & Astrophysics*, 465:799.

Lee, Y.-W., Joo, S.-J., and Chung, C., 2015, The Milky Way without X: An alternative interpretation of the double red clump in the Galactic bulge, *Monthly Notices of the Royal Astronomical Society*, 453:3907.

Li, Z.-Y. and Shen, J., 2012, The vertical X-shaped structure in the Milky Way: Evidence from a simple boxy bulge model, *The Astrophysical Journal*, 757:L7.

Lind, K., Asplund, M., and Barklem, P. S., 2009, Departures from LTE for neutral Li in late-type stars, *Astronomy & Astrophysics*, 503:541.

Lind, K., Asplund, M., Barklem, P. S., and Belyaev, A. K., 2011, Non-LTE calculations for neutral Na in late-type stars using improved atomic data, *Astronomy & Astrophysics*, 528: A103.

Lind, K., Bergemann, M., and Asplund, M., 2012, Non-LTE line formation of Fe in late-type stars II. 1D spectroscopic stellar parameters, *Monthly Notices of the Royal Astronomical Society*, 427:50.

Lind, K., Melendez, J., Asplund, M., Collet, R., and Magic, Z., 2013, The lithium isotopic ratio in very metal-poor stars, *Astronomy & Astrophysics*, 554:A96.

Lind, K., Koposov, S. E., Battistini, C., Marino, A. F., Ruchti, G., et al., 2015, The *Gaia*-ESO Survey: A globular cluster escapee in the Galactic halo, *Astronomy & Astrophysics*, 575: L12.

Liu, F., Asplund, M., Ram, I., Yong, D., and Mel, J., 2014, A high-precision chemical abundance analysis of the HAT-P-1 stellar binary: constraints on planet formation, *Monthly Notices of the Royal Astronomical Society*, 442:L51.

Liu, F., Yong, D., Asplund, M., Ramírez, I., and Meléndez, J., 2016, The Hyades open cluster is chemically inhomogeneous, *Monthly Notices of the Royal Astronomical Society*, 457:3934.

Loebman, S. R., Roškar, R., Debattista, V. P., Ivezić, Ž., Quinn, T. R., et al., 2011, The genesis of the Milky Way's thick disk via stellar migration, *The Astrophysical Journal*, 737:8.

Loebman, S. R., Debattista, V. P., Nidever, D. L., Hayden, M. R., Holtzman, J. A., et al., 2016, Imprints of radial migration of the Milky Way's metallicity distribution functions, *The Astrophysical Journal*, 818:L6.

López-Corredoira, M., 2016, A case against an X-shaped structure in the Milky Way young bulge, *Astronomy & Astrophysics*, 593:A66.

López-Corredoira, M., 2017, Absence of an X-shaped Structure in the Milky Way bulge Using Mira variable Stars, *The Astrophysical Journal*, 836:218.

Luo, A.-L., Zhao, Y.-H., Zhao, G., Deng, L.-C., Liu, X.-W., et al., 2015, The first data release (DR1) of the LAMOST regular survey, *Research in Astronomy and Astrophysics*, 15:1095.

Ma, X., Hopkins, P. F., Wetzel, A. R., Kirby, E. N., Angl, D., et al., 2017, The structure and dynamical evolution of the stellar disc of a simulated Milky Way-mass galaxy, *Monthly Notices of the Royal Astronomical Society*, 467:2430.

Mackereth, J. T., Bovy, J., Schiavon, R. P., Zasowski, G., Cunha, K., et al., 2017, The age–metallicity structure of the Milky Way disc using APOGEE, *Monthly Notices of the Royal Astronomical Society*, 471:3057.

Magic, Z., Collet, R., Asplund, M., Trampedach, R., Hayek, W., et al., 2013, The STAGGER-grid: A grid of 3D stellar atmosphere models I. Methods and general properties, *Astronomy & Astrophysics*, 557:A26.

Majewski, S. R., Zasowski, G., and Nidever, D. L., 2011, Lifting the dusty veil with near- and mid-infrared photometry I. Description and applications of the Rayleigh-Jeans color excess method, *The Astrophysical Journal*, 739:25.

Majewski, S., Schiavon, R., Frinchaboy, P., Allende Prieto, C., Barkhouser, R., et al., 2015, The Apache Point Observatory Galactic Evolution Experiment (APOGEE), *arXiv preprint: 1509.05420*.

Marigo, P., Girardi, L., Bressan, A., Rosenfield, P., Aringer, B., et al., 2017, A new generation of PARSEC-COLIBRI stellar isochrones including the TP-AGB phase, *The Astrophysical Journal*, 835:77.

Marsakov, V. A. and Borkova, T. V., 2006, Formation of Galactic subsystems in light of the magnesium abundance in field stars : the thin disk, *Astronomy Letters*, 32:376.

Martell, S. L., Sharma, S., Buder, S., Duong, L., Schlesinger, K. J., et al., 2017, The GALAH survey: observational overview and *Gaia* DR1 companion, *Monthly Notices of the Royal Astronomical Society*, 465:3203.

Martig, M., Rix, H. W., Aguirre, V. S., Hekker, S., Mosser, B., et al., 2015, Young α-enriched giant stars in the solar neighbourhood, *Monthly Notices of the Royal Astronomical Society*, 451:2230.

Martig, M., Fouesneau, M., Rix, H. W., Ness, M., Mészáros, S., et al., 2016, Red giant masses and ages derived from carbon and nitrogen abundances, *Monthly Notices of the Royal Astronomical Society*, 456:3655.

Martig, M., Minchev, I., Ness, M., Fouesneau, M., and Rix, H.-W., 2016, A radial age gradient in the geometrically thick disk of the Milky Way, *The Astrophysical Journal*, 831:139.

Martinez-Valpuesta, I. and Gerhard, O., 2013, Metallicity gradients through disk instability: a simple model for the Milky Way's boxy bulge, *The Astrophysical Journal*, 766:L3.

Mashonkina, L., Gehren, T., Travaglio, C., and Borkova, T., 2003, Mg, Ba and Eu abundances in thick disk and halo stars, *Astronomy & Astrophysics*, 397:275.

Matteucci, F. and François, P., 1989, Galactic chemical evolution: abundance gradients of individual elements, *Monthly Notices of the Astronomical Society*, 239:885.

Matteucci, F. and Brocato, E., 1990, Metallicity distribution and abundance ratios in the stars of the Galactic bulge, *The Astrophysical Journal*, 365:539.

Maury, A. C. and Pickering, E. C., 1896, Spectra of bright stars photographed with the 11-inch Draper telescope, *Annals of The Astronomical Observatory of Harvard College*, 28: 1.

McWilliam, A. and Rich, R. M., 1994, The first detailed abundance analysis of Galactic bulge K giants in Baade's window, *The Astrophysical Journal Supplement Series*, 91:749.

McWilliam, A., Matteucci, F., Ballero, S., Rich, R. M., Fulbright, J. P., et al., 2008, The evolution of oxygen and magnesium in the bulge and disk of the Milky Way, *The Astronomical Journal*, 136:367.

McWilliam, A., 2016, The chemical composition of the galactic bulge and implications for its evolution, *Publications of the Astronomical Society of Australia*, 33:e040.

McWilliam, A. and Zoccali, M., 2010, Two red clumps and the X-shaped Milky Way bulge, *The Astrophysical Journal*, 724:1491.

Meléndez, J., Asplund, M., Alves-Brito, A., Cunha, K., Barbuy, B., et al., 2008, Chemical similarities between Galactic bulge and local thick disk red giant stars, *Astronomy & Astrophysics*, 484:L21.

Michalik, D., Lindegren, L., and Hobbs, D., 2015, The *Tycho–Gaia* astrometric solution. How to get 2.5 million parallaxes with less than one year of *Gaia* data, *Astronomy & Astrophysics*, 574:A115.

Mikolaitis, Š., Hill, V., Recio–Blanco, A., de Laverny, P., Allende Prieto, C., et al., 2014, The *Gaia*-ESO Survey: the chemical structure of the Galactic discs from the first internal data release, *Astronomy & Astrophysics*, 572:A33.

Minchev, I. and Famaey, B., 2010, A new mechanism for radial migration in galactic disks: spiral-bar resonance overlap, *The Astrophysical Journal*, 722:112.

Minchev, I., Martig, M., Streich, D., Scannapieco, C., de Jong, R. S., et al., 2015, On the formation of galactic thick disks, *The Astrophysical Journal*, 804:L9.

Minchev, I., Steinmetz, M., Chiappini, C., Martig, M., Anders, F., et al., 2016, The relationship between mono-abundance and mono-age stellar populations in the Milky Way disk, *The Astrophysical Journal*, 834:27.

Minniti, D., Olszewski, E. W., Liebert, J., White, S. D. M., Hill, J. M., et al., 1995, The metallicity gradient of the Galactic bulge, *Monthly Notices of the Royal Astronomical Society*, 277: 1293.

Mitschang, A. W., De Silva, G., Zucker, D. B., Anguiano, B., Bensby, T., et al., 2014, Quantitative chemical tagging, stellar ages and the chemo-dynamical evolution of the Galactic disc, *Monthly Notices of the Royal Astronomical Society*, 438:2753.

Molaeinezhad, A., Falcón-Barroso, J., Martínez-Valpuesta, I., Khosroshahi, H. G., Balcells, M., et al., 2016, Establishing the level of cylindrical rotation in boxy/peanut bulges, *Monthly Notices of the Royal Astronomical Society*, 456:692.

Morgan, W. W. and Keenan, P. C., 1973, Spectral classification, *Annual Review of Astronomy & Astrophysics*, 11:29.

Nataf, D. M., 2016, The controversial star-formation history and delium enrichment of the Milky Way bulge, *Publications of the Astronomical Society of Australia*, 33:e023.

Nataf, D. M., 2017, Was the Milky Way bulge formed from the buckling disk instability, hierarchical collapse, accretion of clumps, or all of the above?, *Publications of the Astronomical Society of Australia*, 34:e041.

Nataf, D. M., Udalski, A., Skowron, J., Szymański, M. K., Kubiak, M., et al., 2015, The X-shaped Milky Way bulge in OGLE-III photometry and in N-body models, *Monthly Notices of the Royal Astronomical Society*, 447:1535.

Nemec, J. M. and Nemec, A. F. L., 1993, Mixture models for studying stellar populations II. Multivariate finite mixture models, *The Astronomical Journal*, 105:1455.

Ness, M., Freeman, K., Athanassoula, E., Wylie-De-Boer, E., Bland-Hawthorn, J., et al., 2012, The origin of the split red clump in the Galactic bulge of the Milky Way, *The Astrophysical Journal*, 756:22.

Ness, M., Freeman, K., Athanassoula, E., Wylie-de Boer, E., Bland-Hawthorn, J., et al., 2013, ARGOS - III. Stellar populations in the Galactic bulge of the Milky Way, *Monthly Notices of the Royal Astronomical Society*, 430:836.

Ness, M., Freeman, K., Athanassoula, E., Wylie-de Boer, E., Bland-Hawthorn, J., et al., 2013, ARGOS - IV. The kinematics of the Milky Way bulge, *Monthly Notices of the Royal Astronomical Society*, 432:2092.

Ness, M., Hogg, D. W., Rix, H.-W., Martig, M., Pinsonneault, M. H., et al., 2016, Spectroscopic determination of masses (and implied ages) for red giants, *The Astrophysical Journal*, 823:114.

Ness, M., Zasowski, G., Johnson, J. A., Athanassoula, E., Majewski, S. R., et al., 2016, APOGEE kinematics I. Overview of the kinematics of the Galactic bulge as mapped by APOGEE, *The Astrophysical Journal*, 819:2.

Ness, M., Rix, H.-W., Hogg, D. W., Casey, A. R., Holtzman, J., et al., 2018, Galactic doppelgängers: The chemical similarity among field stars and among stars with a common birth origin, *The Astrophysical Journal*, 853:198.

Ness, M. and Lang, D., 2016, The X-shaped bulge of the Milky Way revealed by WISE, *The Astronomical Journal*, 152:14.

Ness, M., Hogg, D. W., Rix, H.-W., Ho, A. Y. Q., and Zasowski, G., 2015, *The Cannon*: a data-driven approach to stellar label determination, *The Astrophysical Journal*, 808:16.

Nidever, D. L., Bovy, J., Bird, J. C., Andrews, B. H., Hayden, M., et al., 2014, Tracing chemical evolution over the extent of the Milky Way's disk with APOGEE red clump stars, *The Astrophysical Journal*, 796:38.

Nissen, P. E. and Schuster, W. J., 2010, Two distinct halo populations in the solar neighborhood. Evidence from stellar abundance ratios and kinematics, *Astronomy & Astrophysics*, 511:L10.

Nissen, P. E., Høg, E., and Schuster, W. J. Surface gravities of metal-poor stars derived from Hipparcos parallaxes. In *Proceedings of the ESA Symposium Hipparcos - Venice '97*, 225, 1997.

Nordlander, T. and Lind, K., 2017, Non-LTE aluminium abundances in late-type stars, *Astronomy & Astrophysics*, 607:A75.

Nordlander, T., Amarsi, A. M., Lind, K., Asplund, M., Barklem, P. S., et al., 2017, 3D NLTE analysis of the most iron-deficient star, SMSS0313-6708, *Astronomy & Astrophysics*, 597: A6.

Norris, J., 1987, Population studies: The nature of the thick disk, *The Astrophysical Journal*, 314:L39.

Oort, J. H., 1926, The stars of high velocity, *Publications of the Kapteyn Laboratory Groningen*, 40:1.

Osorio, Y. and Barklem, P. S., 2016, Mg line formation in late-type stellar atmospheres II. Calculations in a grid of 1D models, *Astronomy & Astrophysics*, 586:A120.

Pedregosa, F., Varoquaux, G., Gramfort, A., Michel, V., Thirion, B., et al., 2011, Scikit-learn: machine learning in Python, *Journal of Machine Learning Research*, 12:2825.

Peebles, P. J. E., 1970, Primeval adiabatic perturbation in an expanding universe, *The Astrophysical Journal*, 162:815.

Pereira, T. M. D., Asplund, M., Collet, R., Thaler, I., Trampedach, R., et al., 2013, How realistic are solar model atmospheres?, *Astronomy & Astrophysics*, 554:A118.

Perryman, M. A. C., Lindegren, L., Kovalevsky, J., Hoeg, E., Bastian, U., et al., 1997, The Hipparcos catalogue, *Astronomy & Astrophysics*, 323:L49.

Pietrinferni, A., Santi, C., Salaris, M., and Castelli, F., 2004, A large stellar evolution database for population synthesis studies I. Scaled solar models and isochrones, *The Astrophysical Journal*, 612:168.

Pietrukowicz, P., Kozłowski, S., Skowron, J., Soszyński, I., Udalski, A., et al., 2015, Deciphering the 3D structure of the old Galactic bulge from the OGLE RR Lyrae stars, *The Astrophysical Journal*, 811:113.

Pinsonneault, M. H., Elsworth, Y., Epstein, C., Hekker, S., Mészáros, S., et al., 2014, The APOKASC catalog: an asteroseismic and spectroscopic joint survey of targets in the *Kepler* fields, *The Astrophysical Journal Supplement Series*, 215:19.

Piskunov, N. and Valenti, J. A., 2017, Spectroscopy Made Easy: Evolution, *Astronomy & Astrophysics*, 597:A16.

Portail, M., Wegg, C., Gerhard, O., and Martinez-Valpuesta, I., 2015, Made-to-measure models of the Galactic box/peanut bulge: stellar and total mass in the bulge region, *Monthly Notices of the Royal Astronomical Society*, 448:713.

Press, W. H. and Schechter, P., 1974, Formation of glaxies and clusters of galaxies by self-similar gravitational condensation, *The Astrophysical Journal*, 187:425.

Prochaska, J. X., Naumov, S. O., Carney, B. W., McWilliam, A., and Wolfe, A. M., 2000, The Galactic thick disk stellar abundances, *The Astronomical Journal*, 120:2513.

Prša, A., Harmanec, P., Torres, G., Journalek, E. M. A., Asplund, M., et al., 2016, Nominal values for selected solar and planetary quantities: IAU 2015 resolution B3, *The Astronomical Journal*, 152:41.

Quillen, A. C., Anguiano, B., De Silva, G., Freeman, K., Zucker, D. B., et al., 2015, The parent populations of six groups identified from chemical tagging in the solar neighbourhood, *Monthly Notices of the Royal Astronomical Society*, 450:2354.

Quinn, P. J. and Goodman, J., 1986, Sinking satellites of spiral systems, *The Astrophysical Journal*, 309:472.

Quinn, P. J., Hernquist, L., and Fullagar, D. P., 1993, Heating of galactic disks by mergers, *The Astrophysical Journal*, 403:74.

Rahimi, A., Kawata, D., Brook, C. B., and Gibson, B. K., 2010, Chemodynamical analysis of bulge stars for simulated disc galaxies, *Monthly Notices of the Royal Astronomical Society*, 401:1826.

Rahimi, A., Carrell, K., and Kawata, D., 2014, Numerical simulation of a possible origin of the positive radial metallicity gradient of the thick disk, *Research in Astronomy and Astrophysics*, 14:1406.

Recio-Blanco, A., de Laverny, P., Kordopatis, G., Helmi, A., Hill, V., et al., 2014, The *Gaia*-ESO Survey: the Galactic thick to thin disc transition, *Astronomy & Astrophysics*, 567:A5.

Reddy, B. E., Lambert, D. L., and Allende Prieto, C., 2006, Elemental abundance survey of the Galactic thick disc, *Monthly Notices of the Royal Astronomical Society*, 367:1329.

Reddy, B. E. and Lambert, D. L., 2008, Searching for the metal-weak thick disc in the solar neighbourhood, *Monthly Notices of the Royal Astronomical Society*, 391:95.

Robin, A. C., Reylé, C., Derrière, S., and Picaud, S., 2003, A synthetic view on structure and evolution of the Milky Way, *Astronomy & Astrophysics*, 409:523.

Rojas-Arriagada, A., Recio-Blanco, A., de Laverny, P., Schultheis, M., Guiglion, G., et al., 2016, The *Gaia*-ESO Survey: separating disk chemical substructures with cluster models, *Astronomy & Astrophysics*, 586:A39.

Rojas-Arriagada, A., Recio-Blanco, A., de Laverny, P., Mikolaitis, Š., Matteucci, F., et al., 2017, The *Gaia*-ESO Survey : Exploring the complex nature and origins of the Galactic bulge populations, *Astronomy & Astrophysics*, 601:A140.

Romano, D. and Matteucci, F., 2007, Contrasting copper evolution in ω Centauri and the Milky Way, *Monthly Notices of the Royal Astronomical Society*, 378:L59.

Romano, D., Karakas, A. I., Tosi, M., and Matteucci, F., 2010, Quantifying the uncertainties of chemical evolution studies II. Stellar yields, *Astronomy & Astrophysics*, 522:A32.

Roškar, R., Debattista, V. P., Quinn, T. R., Wadsley, J., Lancashire, C., et al., 2012, Radial migration in disc galaxies I . Transient spiral structure and dynamics, *Monthly Notices of the Royal Astronomical Society*, 426:2089.

Roškar, R., Debattista, V. P., and Loebman, S. R., 2013, The effects of radial migration on the vertical structure of Galactic discs, *Monthly Notices of the Royal Astronomical Society*, 433:976.

Rubin, V. C. and Ford, W. K., Jr., 1970, Rotation of the Andromeda nebula from a spectroscopic survey of emission regions, *The Astrophysical Journal*, 159:379.

Ruchti, G. R., Read, J. I., Feltzing, S., Serenelli, A. M., Mcmillan, P., et al., 2015, The *Gaia*-ESO Survey: a quiescent Milky Way with no significant dark/stellar accreted disc, *Monthly Notices of the Royal Astronomical Society*, 450:2874.

Ruchti, G. R., Fulbright, J. P., Wyse, R. F. G., Gilmore, G. F., Bienaymé, O., et al., 2011, Observational properties of the metal-poor thick disk of the Milky Way and insights into its origins, *The Astrophysical Journal*, 737:9.

Russell, H. N., 1948, On the distribution of absolute magnitude in Populations I and II, *Publications of the Astronomical Society of the Pacific*, 60:202.

Ryde, N., Schultheis, M., Grieco, V., Matteucci, F., Rich, R. M., et al., 2015, Chemical evolution of the inner 2 degrees of the Milky Way bulge: [α/Fe] trends and metallicity gradients, *The Astronomical Journal*, 151:1.

Saha, K., 2015, Lost in secular evolution: the case of a low mass classical bulge, *The Astrophysical Journal*, 806:L29.

Sales, L. V., Helmi, A., Abadi, M. G., Brook, C. B., Gómez, F. A., et al., 2009, Orbital eccentricity as a probe of thick disc formation scenarios, *Monthly Notices of the Royal Astronomical Society*, 400:L61.

Salpeter, E. E., 1955, The luminosity function and stellar evolution, *The Astrophysical Journal*, 121:161.

Samland, M. and Gerhard, O. E., 2003, The formation of a disk galaxy within a growing dark halo, *Astronomy & Astrophysics*, 399:961.

Scannapieco, C., Wadepuhl, M., Parry, O. H., Navarro, J. F., Jenkins, A., et al., 2012, The Aquila comparison project: the effects of feedback and numerical methods on simulations of galaxy formation, *Monthly Notices of the Royal Astronomical Society*, 423:1726.

Scannapieco, C., White, S. D. M., Springel, V., and Tissera, P. B., 2009, The formation and survival of discs in a ΛCDM universe, *Monthly Notices of the Royal Astronomical Society*, 396:696.

Schiavon, R. P., Zamora, O., Carrera, R., Lucatello, S., Ness, M., et al., 2017, Chemical tagging with APOGEE: Discovery of a large population of nitrogen rich stars in the inner Galaxy, *Monthly Notices of the Royal Astronomical Society*, 465:501.

Schlegel, D. J., Finkbeiner, D. P., and Davis, M., 1998, Maps of dust infrared emission for use in estimation of reddening and cosmic microwave background radiation foregrounds, *The Astrophysical Journal*, 500:525.

Schlesinger, K. J., Johnson, J. A., Rockosi, C. M., Lee, Y. S., Beers, T. C., et al., 2014, The vertical metallicity gradient of the Milky Way disk: transitions in [α/Fe] populations, *The Astrophysical Journal*, 791:112.

Schönrich, R. and Binney, J., 2009, Origin and structure of the Galactic disc(s), *Monthly Notices of the Royal Astronomical Society*, 399:1145.

Schönrich, R. and McMillan, P. J., 2017, Understanding inverse metallicity gradients in galactic discs as a consequence of inside-out formation, *Monthly Notices of the Royal Astronomical Society*, 467:1154.

Schönrich, R., Binney, J., and Dehnen, W., 2010, Local kinematics and the local standard of rest, *Monthly Notices of the Royal Astronomical Society*, 403:1829.

Schönrich, R., Asplund, M., and Casagrande, L., 2011, On the alleged duality of the Galactic halo, *Monthly Notices of the Royal Astronomical Society*, 415:3807.

Schultheis, M., Hayden, M., Nandakumar, G., Cunha, K., Prieto, C. A., et al., 2017, Baade's window and APOGEE: Metallicities, ages, and chemical abundances, *Astronomy & Astrophysics*, 600:A14.

Searle, L. and Zinn, R., 1978, Compositions of halo clusters and the formation of the Galactic halo, *The Astrophysical Journal*, 225:357.

Sellwood, J. A. and Binney, J. J., 2002, Radial mixing in galactic discs, *Monthly Notices of the Royal Astronomical Society*, 336:785.

Sharma, S., Bland-Hawthorn, J., Johnston, K. V., and Binney, J., 2011, *Galaxia*: a code to generate a synthetic survey of the Milky Way, *The Astrophysical Journal*, 730:3.

Sharma, S., Stello, D., Buder, S., Kos, J., Bland-Hawthorn, J., et al., 2018, The TESS-HERMES survey data release 1: high-resolution spectroscopy of the TESS southern continuous viewing zone, *Monthly Notices of the Royal Astronomical Society*, 473:2004.

Sheinis, A., Anguiano, B., Asplund, M., Bacigalupo, C., Barden, S., et al., 2015, First light results from the High Efficiency and Resolution Multi-Element Spectrograph at the Anglo-Australian Telescope, *Journal of Astronomical Telescopes, Instruments, and Systems*, 1:035002.

Shen, J., Rich, R. M., Kormendy, J., Howard, C. D., De Propris, R., et al., 2010, Our Milky Way as a pure-disk galaxy - a challenge for galaxy formation, *The Astrophysical Journal*, 720:L72.

Silva Aguirre, V., Davies, G. R., Basu, S., Christensen-Dalsgaard, J., Creevey, O., et al., 2015, Ages and fundamental properties of Kepler exoplanet host stars from asteroseismology, *Monthly Notices of the Royal Astronomical Society*, 452:2127.

Simmerer, J., Sneden, C., Cowan, J. J., Collier, J., Woolf, V. M., et al., 2004, The rise of the *s*-process in the Galaxy, *The Astrophysical Journal*, 617:1091.

Skrutskie, M. F., Cutri, R. M., Stiening, R., Weinberg, M. D., Schneider, S., et al., 2006, The Two Micron All Sky Survey (2MASS), *The Astronomical Journal*, 131:1163.

Smette, A., Sana, H., Noll, S., Horst, H., Kausch, W., et al., 2015, `Molecfit`: A general tool for telluric absorption correction, *Astronomy & Astrophysics*, 576:A77.

Smiljanic, R., Korn, A. J., Bergemann, M., Frasca, A., Magrini, L., et al., 2014, The *Gaia*-ESO Survey: The analysis of high-resolution UVES spectra of FGK-type stars, *Astronomy & Astrophysics*, 570:A122.

Snaith, O., Haywood, M., Matteo, P. D., Lehnert, M. D., Combes, F., et al., 2015, Reconstructing the star formation history of the Milky Way disc(s) from chemical abundances, *Astronomy & Astrophysics*, 578:A87.

Sneden, C., Cowan, J. J., and Gallino, R., 2008, Neutron-capture elements in the early Galaxy, *Annual Review of Astronomy and Astrophysics*, 46:241.

Springel, V., White, S. D., Jenkins, A., Frenk, C. S., Yoshida, N., et al., 2005, Simulations of the formation, evolution and clustering of galaxies and quasars, *Nature*, 435:629.

Stassun, K. G. and Torres, G., 2016, Evidence for a systematic offset of −0.25 mas in the *Gaia* DR1 prallaxes, *The Astrophysical Journal*, 831:L6.

Steinmetz, M., Zwitter, T., Siebert, A., Watson, F. G., Freeman, K. C., et al., 2006, The Radial Velocity Experiment (RAVE): First data release, *The Astronomical Journal*, 132:1645.

Stello, D., Zinn, J., Elsworth, Y., Garcia, R. A., Kallinger, T., et al., 2017, The K2 Galactic Archaeology program data release I. Asteroseismic results from Campaign 1, *The Astrophysical Journal*, 835:83.

Stinson, G. S., Bovy, J., Rix, H., Brook, C., Roškar, R., et al., 2013, MaGICC thick disc I. Comparing a simulated disc formed with stellar feedback to the Milky Way, *Monthly Notices of the Astronomical Society*, 436:625.

Stonkutė, E., Koposov, S. E., Howes, L. M., Feltzing, S., Worley, C. C., et al., 2016, The *Gaia*-ESO Survey: the selection function of the Milky Way field stars, *Monthly Notices of the Royal Astronomical Society*, 460:1131.

Thielemann, F.-K., Eichler, M., Panov, I. V., and Wehmeyer, B., 2017, Neutron star mergers and nucleosynthesis of heavy elements, *Annual Review of Nuclear and Particle Science*, 67: 253.

Ting, Y.-S., Freeman, K. C., Kobayashi, C., De Silva, G. M., and Bland-Hawthorn, J., 2012, Principal component analysis on chemical abundances spaces, *Monthly Notices of the Royal Astronomical Society*, 421:1231.

Ting, Y.-S., Conroy, C., and Goodman, A., 2015, Prospects for chemically tagging stars in the Galaxy, *The Astrophysical Journal*, 807:104.

Tinsley, B. M., 1979, Stellar lifetimes and abundance ratios in chemical evolution, *The Astrophysical Journal*, 229:1046.

Travaglio, C., Gallino, R., Arnone, E., Cowan, J., Jordan, F., et al., 2004, Galactic evolution of Sr, Y, and Zr: a multiplicity of nucleosynthetic processes, *The Astrophysical Journal*, 601: 864.

Travaglio, C., Galli, D., Gallino, R., Busso, M., Ferrini, F., et al., 1999, Galactic chemical evolution of heavy elements: from barium to europium, *The Astrophysical Journal*, 521: 691.

Tsikoudi, V., 1979, Photometry and structure of lenticular galaxies I. NGC 3115, *The Astrophysical Journal*, 234:842.

Tumlinson, J., 2010, Chemical evolution in hierarchical models of cosmic structure II. The formation of the Milky Way stellar halo and the distribution of the oldest stars, *The Astrophysical Journal*, 708:1398.

Uttenthaler, S., Schultheis, M., Nataf, D. M., Robin, A. C., Lebzelter, T., et al., 2012, Constraining the structure and formation of the Galactic bulge from a field in its outskirts.

FLAMES-GIRAFFE spectra of about 400 red giants around $(l, b) = (0°, -10°)$, *Astronomy & Astrophysics*, 546:A57.

Valenti, J. A. and Piskunov, N., 1996, Spectroscopy Made Easy: a new tool for fitting observations with synthetic spectra, *Astronomy & Astrophysics Supplement Series*, 118:595.

Valenti, J. A. and Fischer, D. A., 2005, Spectroscopic Properties of Cool Stars (SPOCS) I. 1040 F, G, and K Dwarfs from Keck, Lick, and AAT planet search programs, *The Astrophysical Journal Supplement Series*, 159:141.

van der Kruit, P. and Freeman, K., 2011, Galaxy disks, *Annual Review of Astronomy and Astrophysics*, 49:301.

Van der Swaelmen, M., Barbuy, B., Hill, V., Zoccali, M., Minniti, D., et al., 2016, Heavy elements Ba, La, Ce, Nd, and Eu in 56 Galactic bulge red giants, *Astronomy & Astrophysics*, 586:A1.

van Dokkum, P. G., 2001, Cosmic-ray rejection by Laplacian edge detection, *Publications of the Astronomical Society of the Pacific*, 113:1420.

Vera-Ciro, C., D'Onghia, E., Navarro, J., and Abadi, M., 2014, The effect of radial migration on galactic disks, *The Astrophysical Journal*, 794:173.

Villalobos, Á. and Helmi, A., 2008, Simulations of minor mergers I. General properties of thick discs, *Monthly Notices of the Royal Astronomical Society*, 391:1806.

Wegg, C., Gerhard, O., and Portail, M., 2017, The initial mass function of the inner Galaxy measured from OGLE-III microlensing timescales, *The Astrophysical Journal*, 843:L5.

Wegg, C. and Gerhard, O., 2013, Mapping the three-dimensional density of the Galactic bulge with VVV red clump stars, *Monthly Notices of the Royal Astronomical Society*, 435: 1874.

Wetzel, A. R., Hopkins, P. F., and Kim, J.-H., 2016, Reconciling dwarf galaxies with ΛCDM cosmology: simulating a realistic population of satellites around a Milky Way-mass galaxy, *The Astrophysical Journal*, 827:L23.

White, S. D. M. and Rees, M. J., 1978, Core condensation in heavy halos: a two-stage theory for galaxy formation and clustering, *Monthly Notices of the Royal Astronomical Society*, 183: 341.

White, S. D. M. and Frenk, C. S., 1991, Galaxy formation through hierarchical clustering, *The Astrophysical Journal*, 379:52.

Wisnioski, E., Schreiber, N. M. F., Wuyts, S., Wuyts, E., Bandara, K., et al., 2015, The KMOS^{3D} Survey: design, first results, and the evolution of galaxy kinematics from $0.7 \leq z \leq 2.7$, *The Astrophysical Journal*, 209:799.

Woosley, S. E. and Weaver, T. A., 1995, The evolution and explosion of massive stars II. Explosive hydrodynamics and nucleosynthesis, *The Astrophysical Journal Supplement Series*, 181.

Woosley, S. E., Wilson, J. R., Mathews, G. J., Hoffman, R. D., and Meyer, B. S., 1994, The *r*-process and neutrino-heated supernova ejecta, *The Astrophysical Journal*, 433:229.

Wright, E. L., Eisenhardt, P. R. M., Mainzer, A. K., Ressler, M. E., Cutri, R. M., et al., 2010, The Wide-Fied Infrared Survey Explorer (WISE): Mission description and intial on-orbit performance, *The Astronomical Journal*, 140:1868.

Wyse, R. F. G. and Gilmore, G., 1988, The Galactic spheroid: what is Population II?, *The Astronomical Journal*, 95:1404.

Wyse, R. F. G., Gilmore, G., Norris, J. E., Wilkinson, M. I., Kleyna, J. T., et al., 2006, Further evidence of a merger origin for the thick disk: Galactic stars along lines of sight to dwarf spheroidal galaxies, *The Astrophysical Journal*, 639:L13.

Yoachim, P. and Dalcanton, J. J., 2006, Structural parameters of thin and thick disks in edge-on disk galaxies, *The Astronomical Journal*, 131:226.

Yong, D., Carney, B. W., and Friel, E. D., 2012, Elemental abundance ratios in stars of the outer Galactic disk IV. A new sample of open clusters, *The Astronomical Journal*, 144:95.

Yoshii, Y., 1982, Density distribution of faint stars in the direction of the North Galactic pole, *Publications of the Astronomical Society of Japan*, 34:365.

Zasowski, G., Johnson, J. A., Frinchaboy, P. M., Majewski, S. R., Nidever, D. L., et al., 2013, Target selection for the Apache Point Observatory Galactic Evolution Experiment (APOGEE), *The Astronomical Journal*, 146:81.

Zasowski, G., Ness, M. K., García Pérez, A. E., Martinez-Valpuesta, I., Johnson, J. A., et al., 2016, Kinematics in the Galactic bulge with APOGEE II. High-order kinematic moments and comparison to extragalactic bar diagnostics, *The Astrophysical Journal*, 832:132.

Zhang, H. W. and Zhao, G., 2005, Chemical abundances of very metal-poor stars, *Monthly Notices of the Royal Astronomical Society*, 364:712.

Zoccali, M., Renzini, A., Ortolani, S., Greggio, L., Saviane, I., et al., 2003, Age and metallicity distribution of the Galactic bulge from extensive optical and near-IR stellar photometry, *Astronomy & Astrophysics*, 399:931.

Zoccali, M., Lecureur, A., Barbuy, B., Hill, V., Renzini, A., et al., 2006, Oxygen abundances in the Galactic bulge: evidence for fast chemical enrichment, *Astronomy & Astrophysics*, 457:L1.

Zoccali, M., Hill, V., Lecureur, A., Barbuy, B., Renzini, A., et al., 2008, The metal content of bulge field stars from FLAMES-GIRAFFE spectra I. Stellar parameters and iron abundances, *Astronomy & Astrophysics*, 486:177.

Zoccali, M., Gonzalez, O. A., Vasquez, S., Hill, V., Rejkuba, M., et al., 2014, The GIRAFFE Inner Bulge Survey (GIBS) I . Survey description and a kinematical map of the Milky Way bulge, *Astronomy & Astrophysics*, 562:A66.

Zoccali, M., Vasquez, S., Gonzalez, O. A., Valenti, E., Minniti, J., et al., 2017, The GIRAFFE Inner Bulge Survey (GIBS) III. Metallicity distributions and kinematics of 26 Galactic bulge fields, *Astronomy & Astrophysics*, 599:A12.

Zwitter, T., Matijevivc, G., Breddels, M. A., Smith, M. C., Helmi, A., et al., 2010, Distance determination for RAVE stars using stellar models II: Most likely values assuming a standard stellar evolution scenario, *Astronomy & Astrophysics*, 522:A54.

A

Spectroscopic analysis tests

This chapter contains a modified version of supplementary material from Chapters 5 and 6, which have been submitted for publication in Monthly Notices of the Astronomical Society.

A.1 Stellar parameters

To estimate the accuracy of our stellar parameters, we analysed giants and subgiants in the *Gaia* benchmark stars (GBS) sample using the reduction and parameter optimisation pipeline described above. For this purpose we used archive HERMES benchmark observations that were taken for the GALAH survey. To gauge the effects of the difference in reduction methods between our survey (2dfdr-based) and the GALAH survey (IRAF-based), we also compared our benchmark results with that obtained from spectra reduced with the GALAH reduction pipeline. The results are shown in Fig. A.1. We note that the GALAH spectrum of the benchmark giant εFor was not available, but this star is included in the 2dfdr comparison sample. We performed our analysis assuming $\mathcal{R} = 28\,000$. For the IRAF benchmark reductions, adopting either this constant spectral resolution or the resolution map from (Kos et al. 2017) returned near identical results, with temperature differences $\leq$ 30 K, metallicity differences $\leq$ 0.04 dex and surface gravity differences $\leq$ 0.1 dex, all within expected uncertainties.

In general, the differences between the two reduction methods are not significant. For the 2dfdr sample, we observe biases[1] and standard deviations for $T_{\rm eff}$: 40 ± 90 K; $\log g$: 0.02 ± 0.25 dex and [Fe/H]: -0.12 ± 0.08 dex. The IRAF biases and standard deviations for $T_{\rm eff}$, $\log g$ and [Fe/H] are: 100 ± 90 K; -0.06 ± 0.22 dex and -0.05 ± 0.06 dex, respectively. While both sets of results are fairly accurate, spectra from the GALAH reduction pipeline produce

[1]The biases are defined as the median of the difference (SME − benchmark).

slightly more precise $\log g$ and [Fe/H], perhaps due to the tilted PSF correction that increases the resolution and signal-to-noise towards the CCD corners. However, GALAH-reduced spectra return even higher effective temperature for giants compared to our reductions, which already overestimates $T_{\rm eff}$ by 40 K compared to reference values.

For the GALAH reductions, the biases of this giants-only sample is different to that of the full giants and dwarfs benchmark sample analysed by Sharma et al. (2018). Before bias correction, Sharma et al. (2018) quoted biases in $T_{\rm eff}$: 23 ± 112 K; $\log g$: -0.15 ± 0.22 dex and [Fe/H]: -0.12 ± 0.1 dex. Here, we find that neither $\log g$ and [Fe/H] show a strong offset, and the metallicity precision is higher compared to the full sample.

We derived particularly discrepant surface gravity results for the M-giant αCeti. Compared to the benchmark value from Heiter et al. (2015a), this star has $\Delta \log g = 1$ dex, for both 2dfdr and IRAF reductions. The cause of this discrepancy is unclear, seeing as the M-giant αTau with similar parameters does not show this large deviation. This may be a concern that surface gravity determination for $\log g < 1$ dex is challenging with HERMES spectra. The outlier αCeti has been excluded from $\log g$ standard deviation calculations.

Our comparison here shows that 2dfdr-reduced spectra perform just as well as IRAF-reduced spectra, however the IRAF reductions return higher precision for [Fe/H] and $\log g$. We do not see significant biases in effective temperature or surface gravity in our results, and thus do make corrections to these parameters. However, the metallicity is underestimated by our pipeline by -0.12 dex. Similarly to HERMES-GALAH results, we corrected for this metallicity bias by adding +0.1 dex to all of our [Fe/H] values.

A.2 Effective temperature and abundance ratio correlations

Fig. A.2 shows [X/Fe] as a function of temperature for all 18 elements measured for the bulge sample. While most of the abundances were computed in LTE, we do not see significant trends with temperature for the majority of them. [Mg/Fe] and [Ca/Fe] both show positive linear trends with respect to temperature. For calcium, this could be due to non-LTE effects, however the reason for the [Mg/Fe]-$T_{\rm eff}$ correlation is not clear. The non-LTE magnesium abundances of M67 giants observed by GALAH also the same trend with temperature (see Gao et al. 2018, their Fig. 7). [Mn/Fe] also increases linearly with temperature. Manganese abundance ratios are susceptible to non-LTE effects, which is likely the reason for this abundance-temperature trend (Bergemann & Gehren 2008, Battistini & Bensby 2015). The iron-peak element cobalt also shows a positive linear trend, suggesting departure from LTE (Bergemann et al. 2010). However, the non-LTE effect on cobalt is relatively small within our metallicity range, larger effects are observed for metal-poor stars (Bergemann et al. 2010). Zirconium may have a positive correlation with temperature, but this is difficult to assess as we have few data points, and there is a large range in [Zr/Fe].

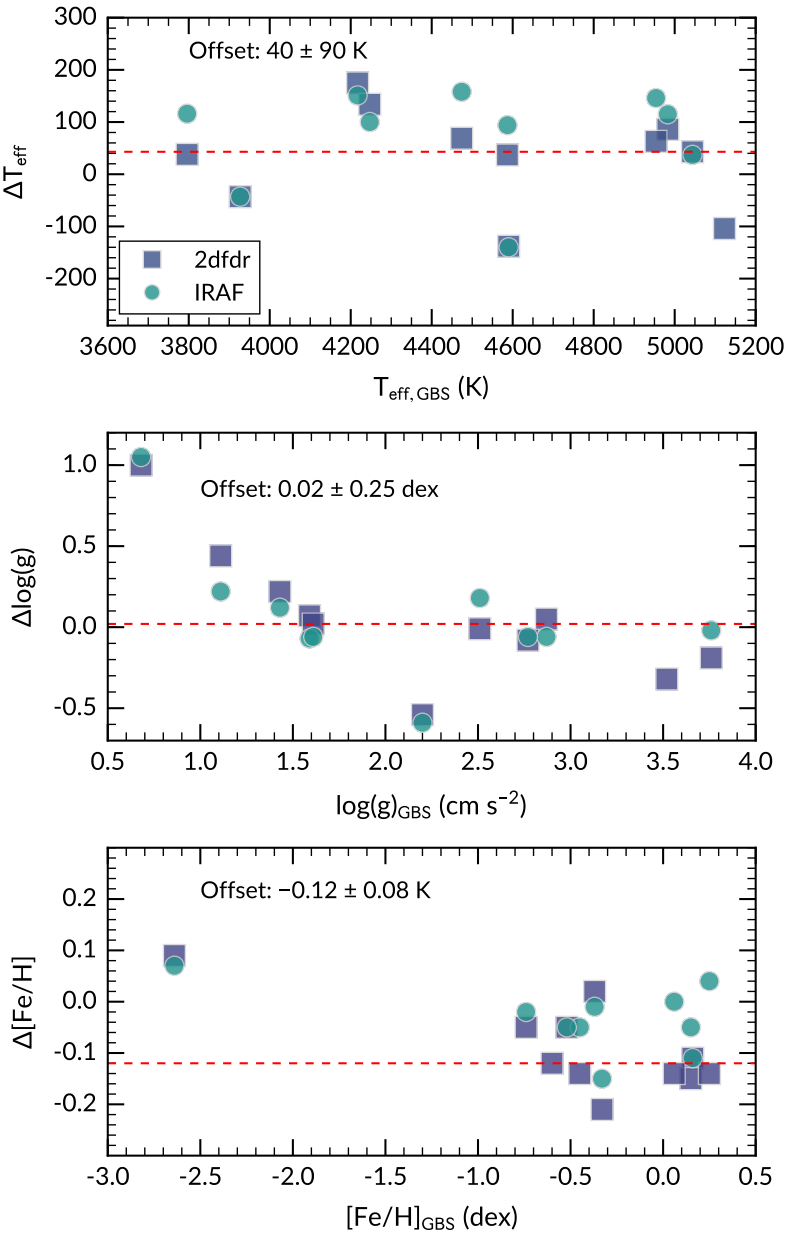

Figure A.1 Comparison of our derived parameters with fundamental $T_{\rm eff}$, $\log g$ (Heiter et al. 2015a) and *Gaia* ESO-derived [Fe/H] (from high resolution UVES spectra, Jofré et al. 2014) for benchmark stars. The squares indicate 2dfdr-based reductions and the circles are results from IRAF-based reductions. The differences are shown as (SME − GBS); the red line indicates biases for 2dfdr-based reductions *only*. The outlier in $\log g$ is the M-giant αCeti.

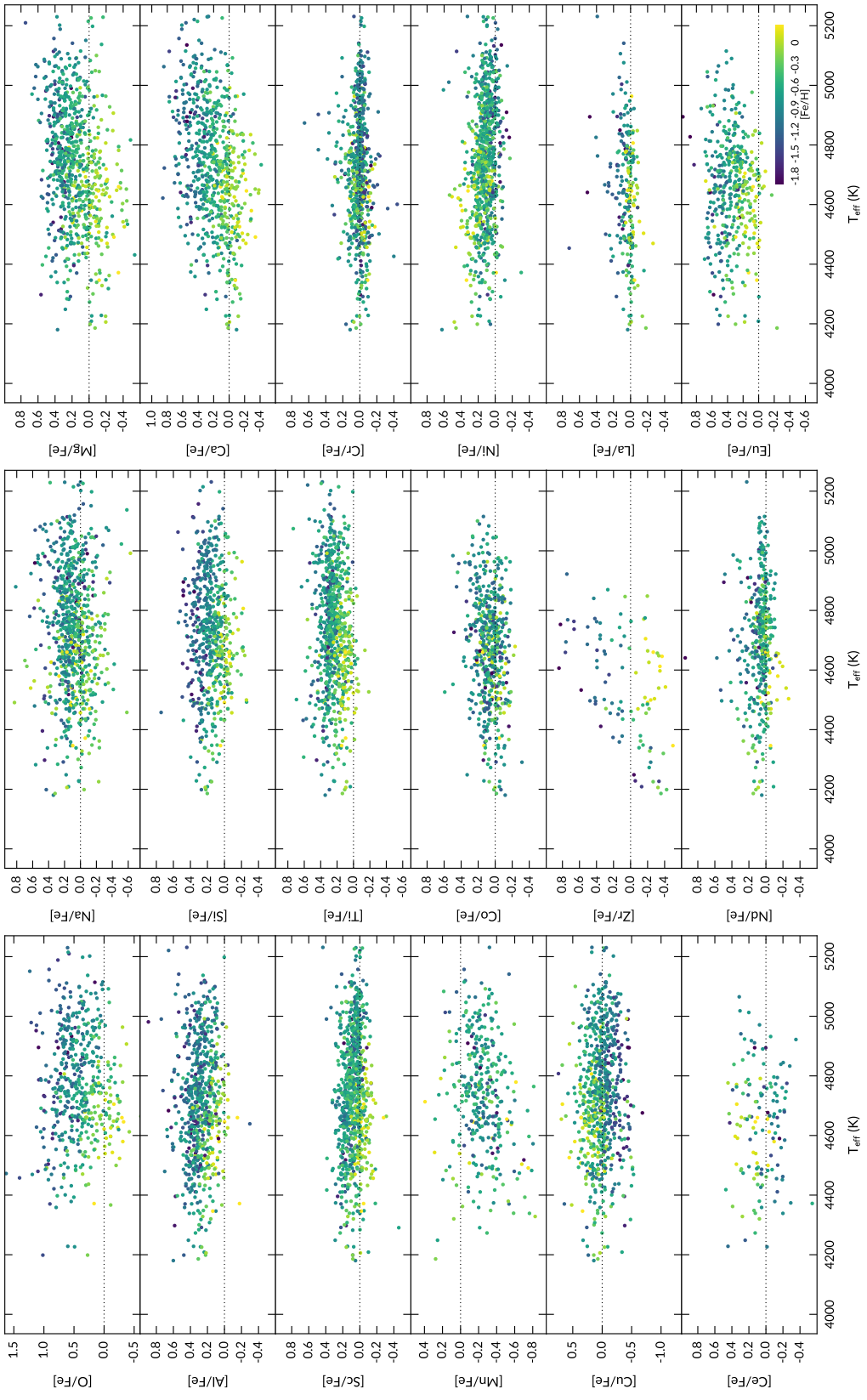

Figure A.2 The $T_{\rm eff}$–[X/Fe] correlations for all 18 elements. The [O/Fe], [Na/Fe], [Al/Fe], [Mg/Fe] and [Si/Fe] abundance ratios are calculated assuming non-LTE. All other elemental abundances were derived assuming LTE. Most elements do not show a strong correlation with temperature. Similar linear trends are observed for [Mg/Fe] and [Ca/Fe], and positive linear trends can be seen for Mn, Co and Zr, although the trend is less significant for Co.

B
Atomic data

This chapter contains a modified version of the supplementary material from chapters 5 and 6, which have been submitted for publication in Monthly Notices of the Astronomical Society.

The tables below contain line data used for the spectroscopic analysis performed in chapters 5 and 6. The atomic data and lines used for stellar parameters analysis are the same as that of the GALAH survey (Buder et al. 2018). However, we omitted some lines in the GALAH linelist for our abundance analysis (details can be found in Section 5.6.2 and Section 6.4).

Table B.1 Line data used for stellar parameters determination.

Species	λ (Å)	log (gf)	EP (eV)	Species	λ (Å)	log (gf)	EP (eV)
Sc I	4743.8300	0.422	1.448	Fe I	5661.3447	-1.756	4.284
Sc I	4753.1610	-1.659	0.000	Fe I	5662.5161	-0.447	4.178
Sc I	5671.8163	-0.290	1.448	Fe I	5679.0229	-0.820	4.652
Sc I	5686.8386	-0.133	1.440	Fe I	5680.2404	-2.480	4.186
Sc I	5717.3070	-0.532	1.440	Fe I	5696.0892	-1.720	4.549
Sc I	5724.1070	-0.661	1.433	Fe I	5701.5442	-2.193	2.559
Sc II	5657.8960	-0.603	1.507	Fe I	5705.4642	-1.355	4.301
Sc II	5667.1490	-1.309	1.500	Fe I	5731.7618	-1.200	4.256
Sc II	5684.2020	-1.074	1.507	Fe I	5732.2960	-1.460	4.991
Sc II	6604.6010	-1.309	1.357	Fe I	5741.8477	-1.672	4.256
Sc II	5669.0420	-1.200	1.500	Fe I	5775.0805	-1.080	4.220
Ti I	4758.1178	0.510	2.249	Fe I	5778.4533	-3.430	2.588
Ti I	4759.2697	0.590	2.256	Fe I	5806.7249	-0.950	4.608
Ti I	4778.2547	-0.350	2.236	Fe I	5809.2174	-1.740	3.884

Table B.1 Continued from previous page.

Species	λ (Å)	log (*gf*)	EP (eV)	Species	λ (Å)	log (*gf*)	EP (eV)
Ti I	4781.7106	-1.950	0.848	Fe I	5811.9144	-2.330	4.143
Ti I	4797.9757	-0.630	2.334	Fe I	5814.8071	-1.870	4.283
Ti I	4801.9016	-3.060	0.818	Fe I	5849.6833	-2.890	3.695
Ti I	4820.4094	-0.380	1.503	Fe I	5853.1483	-5.180	1.485
Ti I	5689.4600	-0.360	2.297	Fe I	5855.0758	-1.478	4.608
Ti I	5716.4500	-0.720	2.297	Fe I	5858.7780	-2.160	4.220
Ti I	5720.4359	-0.900	2.292	Fe I	6481.8698	-2.981	2.279
Ti I	5739.4690	-0.610	2.249	Fe I	6494.9804	-1.268	2.404
Ti I	5866.4513	-0.790	1.067	Fe I	6498.9383	-4.687	0.958
Ti I	6716.6660	-1.370	2.488	Fe I	6546.2381	-1.536	2.759
Ti II	4719.5109	-3.320	1.243	Fe I	6592.9124	-1.473	2.728
Ti II	4764.5247	-2.690	1.237	Fe I	6593.8695	-2.420	2.433
Ti II	4798.5313	-2.660	1.080	Fe I	6597.5592	-0.970	4.795
Ti II	4849.1678	-2.960	1.131	Fe I	6609.1097	-2.691	2.559
Ti II	4865.6104	-2.700	1.116	Fe I	6627.5438	-1.590	4.549
Ti II	4874.0094	-0.860	3.095	Fe I	6648.0796	-5.918	1.011
Fe I	4788.7566	-1.763	3.237	Fe I	6677.9851	-1.418	2.692
Fe I	4793.9614	-3.430	3.047	Fe I	6699.1413	-2.101	4.593
Fe I	4794.3541	-3.950	2.424	Fe I	6703.5660	-3.060	2.759
Fe I	4802.8797	-1.510	3.642	Fe I	6713.7425	-1.500	4.795
Fe I	4808.1478	-2.690	3.251	Fe I	6725.3558	-2.100	4.103
Fe I	4875.8770	-1.900	3.332	Fe I	6733.1503	-1.480	4.638
Fe I	4890.7551	-0.386	2.876	Fe II	4720.1386	-4.480	3.197
Fe I	4891.4921	-0.111	2.851	Fe II	4731.4476	-3.100	2.891
Fe I	5651.4689	-1.900	4.473	Fe II	4833.1916	-5.110	2.657
Fe I	5652.3176	-1.850	4.260				

Table B.2 Line data used for abundance determination. The same Ti lines in table B.1 were used to determine [Ti/Fe].

Species	λ (Å)	log (gf)	EP (eV)	Species	λ (Å)	log (gf)	EP (eV)
O I	7771.9440	0.369	9.146	Co I	6632.4505	-2.726	2.280
Na I	5688.2050	-0.404	2.104	Ni I	5748.3507	-3.240	1.676
Mg I	5711.0880	-1.724	4.346	Ni I	5846.9935	-3.460	1.676
Mg I	7691.5500	-0.783	5.753	Ni I	6482.7983	-2.630	1.935
Al I	6696.0230	-1.569	3.143	Ni I	6532.8730	-3.350	1.935
Al I	6698.6730	-1.870	3.143	Ni I	6586.3098	-2.780	1.951
Si I	5690.4250	-1.773	4.930	Ni I	6643.6303	-2.220	1.676
Si I	5701.1040	-1.953	4.930	Cu I	5782.1554	-2.148	1.642
Si I	5793.0726	-1.963	4.930	Zr I	4805.8700	-0.420	0.687
Ca I	5867.5620	-1.570	2.933	Zr I	4828.0400	-0.640	0.623
Ca I	6499.6500	-0.818	2.523	La II	4716.4400	-1.210	0.772
Sc I	4753.1610	-1.659	0.000	La II	4748.7300	-0.540	0.927
Sc I	5671.8163	-0.290	1.448	La II	4804.0690	-1.870	0.235
Sc I	5686.8386	-0.133	1.440	La II	5805.7700	-1.560	0.126
Sc II	6604.6010	-1.309	1.357	Ce II	4773.9410	-0.390	0.924
Cr I	5719.8150	-1.580	3.013	Nd II	4811.3420	-1.140	0.064
Cr I	5787.9190	-0.083	3.322	Nd II	5740.8580	-0.530	1.160
Cr I	5844.5950	-1.770	3.013	Nd II	5811.5700	-0.860	0.859
Mn I	4761.5060	-0.548	2.953	Eu II	6645.0978	-0.319	1.380
Mn I	4765.8525	-0.445	2.941				

This thesis was typeset using LaTeX, originally developed by Leslie Lamport and based on Donald Knuth's TeX. A template that can be used to format a PhD dissertation with this look & feel has been released under the permissive AGPL license, and can be found online at github.com/suchow/Dissertate or from its lead author, Jordan Suchow, at suchow@post.harvard.edu.